Beauty Meson Decays to Charmonium

A thesis presented

by

Alexey Valerievich Ershov

to

The Department of Physics

in partial fulfillment of the requirements

for the degree of

Doctor of Philosophy

in the subject of

Physics

Harvard University

Cambridge, Massachusetts

May 2001

Thesis advisors
George Brandenburg
Hitoshi Yamamoto

Author
Alexey Valerievich Ershov

Beauty Meson Decays to Charmonium

Abstract

We study decays of beauty (B) mesons into the final states containing charmonium mesons. The data were collected by the CLEO experiment at the Cornell Electron Storage Ring from 1990 to 1999. First, we describe a technique that significantly improves the reconstruction efficiency for decays of J/ψ and $\psi(2S)$ mesons into a pair of leptons. This reconstruction method is used in all the analyses presented in this dissertation. Then we present a study of B decays to the χ_{c1} and χ_{c2} charmonium states and compare our results with the predictions of different theoretical models of charmonium production. After that we report the first observation of the decay $B \to J/\psi\,\phi\,K$, which is the first B meson decay requiring a creation of an additional $s\overline{s}$ quark pair. Then we measure the B^0 and B^+ meson masses from $B^0 \to \psi^{(\prime)}\,K^0_S$ and $B^+ \to \psi^{(\prime)}\,K^+$ decays. The method employed eliminates the dominant systematic uncertainty associated with the previous B meson mass measurements at the e^+e^- colliders and results in a significant improvement in precision. After that we present a study of three B^0 decay modes useful for time-dependent CP asymmetry measurements. In this study we reconstruct $B^0 \to J/\psi\,K^0_S$, $B^0 \to \chi_{c1}\,K^0_S$, and $B^0 \to J/\psi\,\pi^0$ decays. The latter two decay modes are observed for the first time. We describe a $K^0_S \to \pi^0\pi^0$ detection technique and its application to the reconstruction of the decay $B^0 \to J/\psi\,K^0_S$. Then we present a sensitivity study for the measurement of the mixing-induced CP violation in the neutral B meson system (parameter $\sin 2\beta$) at CLEO using the method that requires a measurement of the decay time of only one meson in a $B^0\overline{B}^0$ pair. Finally, we search for direct CP violation in decays $B^\pm \to J/\psi\,K^\pm$ and $B^\pm \to \psi(2S)\,K^\pm$. The results of this search are consistent with the Standard Model expectations and provide the first experimental test of the assumption that direct CP violation is negligible in $B \to \psi^{(\prime)}\,K$ decays.

Contents

Outline and Citations to Previously Published Work

In this thesis we present a collection of analyses of the CLEO experimental data. In each of these analyses we study decays of beauty (B) mesons into the final states containing charmonium mesons. The work described here was performed over a period of three years from 1997 to 2000.

Chapter 1 contains a brief introduction to the CLEO experiment.

Chapter 2, adapted from an internal CLEO note [116], describes a technique that significantly improves the reconstruction efficiency for decays of J/ψ and $\psi(2S)$ mesons into a pair of leptons. This reconstruction method is used in all the other analyses presented in this dissertation.

Chapters 3, 4, 5, 6, and 8 contain the sections called "Analysis summary and results" which are adapted from the published journal articles. The sections called "More details on the analysis" are largely drawn from the internal CLEO notes.

The study of B decays to the χ_{c1} and χ_{c2} charmonia states presented in Chapter 3 was described in an internal CLEO note [117] and published as a Rapid Communication in Physical Review D [118].

The first observation of the decay $B \to J/\psi\,\phi\,K$ presented in Chapter 4 was described in [119] and published in Physical Review Letters [120].

The measurement of the absolute masses of charged and neutral B mesons presented in Chapter 5 was described in [121] and published as a Rapid Communication in Physical Review D [122].

The analyses of the decays $B^0 \to J/\psi\,K^0_S$, $B^0 \to \chi_{c1}\,K^0_S$, and $B^0 \to J/\psi\,\pi^0$ presented in Chapter 6 were described in [123, 124, 125] and published as a Rapid Communication in Physical Review D [126].

The sensitivity study for the measurement of the parameter $\sin 2\beta$ at CLEO presented in Chapter 7 was described in [127].

Finally, the search for direct CP violation in the decays $B^\pm \to J/\psi\,K^\pm$ and $B^\pm \to \psi(2S)\,K^\pm$ presented in Chapter 8 was described in [128] and published in Physical Review Letters [129].

Acknowledgments

I would like to thank all the people who made my 5 years in the graduate school so happy and productive that I am not eagerly looking forward to graduation. One should not be allowed to have such a good time in a graduate school and such a close relationship with his advisors. I would like to thank my thesis advisors — George Brandenburg and Hitoshi Yamamoto — who gave me a complete freedom to decide which analyses to work on and in what order. When I was jumping from one idea to another, they had the courage to believe that I would finish some of the work I started.

George Brandenburg has been a wonderful advisor both on physics and on real-life matters. He deserves much of the credit for the research presented in this thesis. The combination of intelligence with a kind, calm, humorous attitude makes George very pleasant to work with. I also thank George and his wife Ellen for making me feel welcome during my stays at the Brandenburg's Ritz-Carlton.

Hitoshi Yamamoto introduced me to CLEO and has stayed close through e-mail, telephone, and video for the past 3 years when he was thousands of kilometers away. He even flew from Japan for my thesis defense. I did my best to draw on his impressive physics knowledge and intuition. Did I mention that the conversations with Hitoshi on non-physics topics were equally pleasant and instructive?

I owe special thanks to Richard Wilson. He brought me to Harvard and has been a source of wisdom and help ever since. He taught me to look at the big picture and think of physics in a broader context. When I was stuck in Russia without a visa, the first thing I did was to send a message to Richard, with absolute confidence that in no more than 24 hours the consul in Moscow would receive a message persuasively linking Alexey's timely return to the well-being of the American taxpayers. Richard and his wife Andrée are among the most admirable people I have met.

I thank the members of my thesis committee for useful suggestions: the chairman Gary Feldman, George Brandenburg, Hitoshi Yamamoto, and Richard Wilson. I was fortunate to have Gary Feldman as an academic advisor at Harvard. The words of approval and encouragement from him were always important to me. I would also like to thank Masahiro Morii for reading the thesis, giving me useful comments, asking questions at the defense, and enthusiastically signing the thesis acceptance certificate.

The experimental data upon which this dissertation is based are the fruit of collaborative effort of the people who have built and improved the CESR collider and the CLEO detector. I certainly have taken more out of CLEO than I have contributed to it. I feel guilty for not signing up for more service jobs and cabling shifts. I spent 4 out of 5 graduate school years at Cornell's Laboratory of Nuclear Studies. I thank Cornell for warm hospitality and the intellectually stimulating atmosphere of the Wilson Synchrotron Laboratory. Andy Foland, Pablo Hopman, Tony Hill, Petr Gaidarev, Vladimir Savinov, David Asner, Mark Palmer, David Jaffe, Frank Würthwein, Sören Prell, Roy Briere, Yongsheng Gao, and Daniel Kim are some of the people who created this atmosphere around me. Vlatko Balić patiently introduced me to the CLEO technicalities during my first year at Harvard. I thank Vitaliy Fadeyev for his insightful comments on all the analyses in this thesis. Conversations with Ed Thorndike were invariably instructive and enjoyable. It is not surprising that almost any CLEO thesis has his name in the acknowledgments.

The idea of the B^0 mass measurement with $B^0 \to J/\psi K^0_S$ decay came from David Jaffe.

The method of finding the K^0_S flight direction used in the $K^0_S \to \pi^0\pi^0$ reconstruction was suggested by Paul Avery and Lawrence Gibbons. I wrote much of the computer code for $K^0_S \to \pi^0\pi^0$ reconstruction by modifying the routines from XBAL and KNFIT libraries developed by Tomasz Skwarnicki and Paul Avery.

The sensitivity study for the measurement of $\sin 2\beta$ at CLEO presented in Chapter 7 is based upon an idea from Andy Foland. Working on this project in close collaboration with Andy was one of my most pleasant and stimulating experiences on CLEO. In this study I have extensively used the technique and the computer code developed by Sören Prell for his D lifetime analysis. I would also like to acknowledge stimulating discussions with Karl Berkelman, Hitoshi Yamamoto, Lawrence Gibbons, and Pablo Hopman.

The search for direct CP violation presented in Chapter 8 would have been much more difficult were it not for Tony Hill, who calculated the charge-correlated bias of the kaon detection efficiency. I thank Amarjit Soni, Matthias Neubert, Alexey Petrov, Vladimir Savinov, and Frank Würthwein for discussions on the phenomenology of direct CP violation.

Over 4 years, the members of the CLEO paper committees have ensured high quality of my work and made papers (and therefore this thesis) much more readable: Paul Avery, Bill Ford, Sacha Kopp, Andreas Wolf, Stephen Pappas, Todd Pedlar, Mats Selen, Kay Kinoshita, Persis Drell, and Vladimir Savinov. I thank David Jaffe for his suggestions and criticisms on almost all the papers making up this thesis.

I had a privilege to take the excellent courses taught at Harvard by Sidney Coleman, John Huth, Hitoshi Yamamoto, Paul Horowitz, and Thomas Hayes. Thanks to John Oliver for his instruction in theoretical and experimental electronics. Melissa Franklin's charming personality and physics intuition have made our conversations memorable. My encounters with Petar Macsimović have been few but nevertheless are fondly remembered. The warm, friendly, and at the same time highly professional people in the electronics and machine shops have made my work at HEPL enjoyable: Sarah Harder, Jack O'Kane, Nathan Felt, Richard Haggerty, and Steve Sansone (thank you for showing how to change brake pads and cut a Kryptonite lock, now I can do either for a living). Thanks to Guy Sciacca and Mary Lampros for sheltering me from real-life problems.

I would like to express my gratitude to my teachers in Russia and especially to two of the professors in Protvino — Alexandr Mikhailovich Zaitsev and Semyon Solomonovich Gershtein — for teaching me much of the physics I know and being interested in my work at Harvard. I thank Natalya Semyonovna Zvereva, my physics teacher at school, for her encouragement many years ago.

Finally, I thank my family and especially my wife Elena for their support and encouragement.

Unlike the rest of the thesis, this section is being written in a hurry. When the thesis is printed, bound, and submitted to the Registrar's office, I will discover that a few names that certainly have to be in this section are missing. I ask these people to forgive me.

Chapter 1

CLEO experiment

We study B_u and B_d mesons in the data collected at the Cornell Electron Storage Ring (CESR) with two configurations of the CLEO detector called CLEO II [1] and CLEO II.V [2]. The CESR provides symmetric e^+e^- collisions in the energy range of the Υ states, 9 to 11 GeV (Figure 1.1). The $\Upsilon(4S)$ state is the first resonance above the B meson pair production threshold: its mass is only 22 MeV higher than the mass of two B mesons. The $\Upsilon(4S)$ decays almost exclusively [3] to a pair of charged or neutral B mesons, $B^0\overline{B}^0$ or B^+B^-, in nearly equal numbers [4]. The center of mass of a $B\overline{B}$ pair is at rest in the laboratory frame. The B mesons are created with a typical momentum of 310 MeV/c [5]; this value, however, depends on the beam energy. The annihilation of the e^+ and e^- with the same helicities is suppressed by a factor of $M_e/E_{\rm beam}$, therefore the annihilation proceeds through a virtual photon with $J_z = \pm 1$. The B mesons are spin–0 particles, therefore the angular distribution of the B mesons has a $\sin^2\theta$ dependence, where θ is the angle of a B with respect to the beam axis.

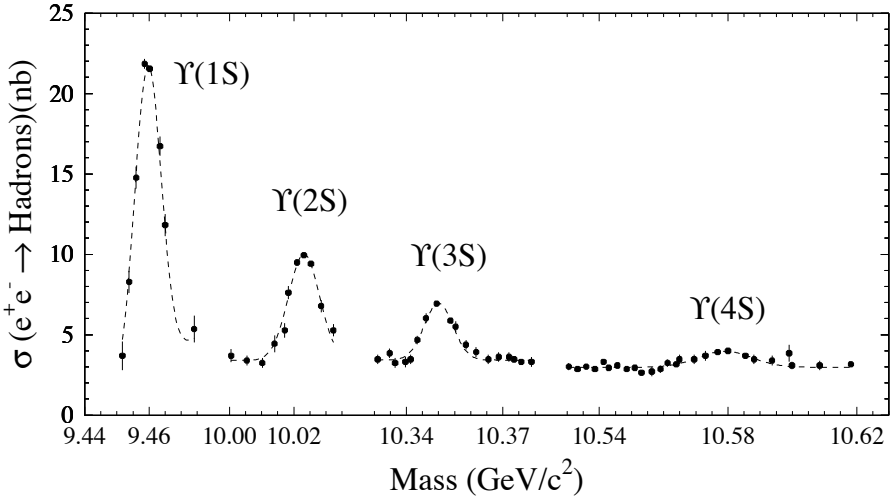

Figure 1.1: The first four Υ resonances.

The fascinating history of CESR and CLEO can be learned from [6]. The main components of our experimental apparatus are briefly described below.

1.1 CESR e^+e^- collider

CESR is a symmetric e^+e^- collider [7] with a circumference of 768 meters, located on campus of Cornell University. Electrons and positrons travel in opposite directions in the same vacuum chamber and are brought to collision in the center of the CLEO detector (Figure 1.2).

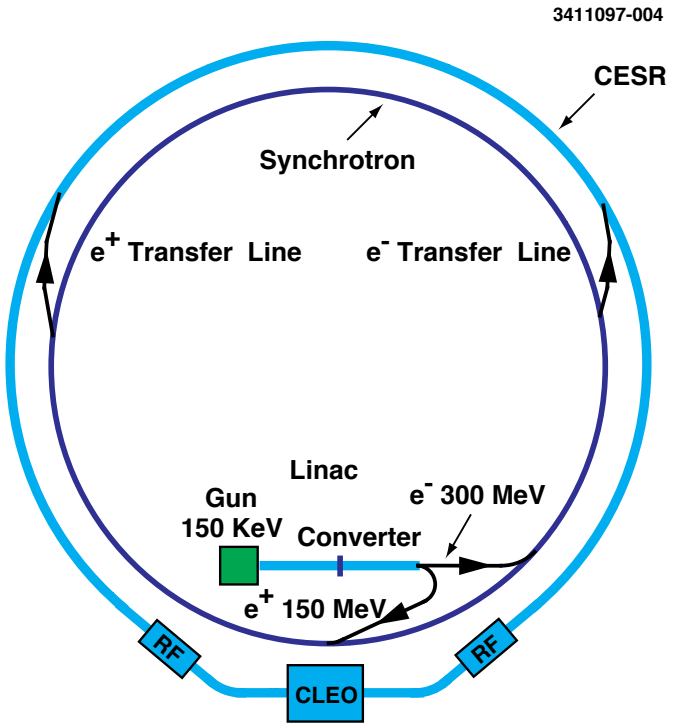

Figure 1.2: The CESR e^+e^- collider.

The major parts of the CESR collider complex are the linear accelerator, the synchrotron, and the storage ring. The linear accelerator (linac) produces both electrons and positrons and provides the first stage of acceleration. Electrons are emitted from a heated cathode and accelerated to 300 MeV before the injection into the synchrotron. Positrons are produced in an intermediate point of the linac by placing a tungsten plate in the way of 140 MeV electrons. The synchrotron accepts the electrons (at 300 MeV) or positrons (150 to 200 MeV) from the linac and accelerates them to their final energy at which they are stored in CESR. When the desired energy is reached, electrons or positrons are transferred to the storage ring.

In CESR the counter-rotating electron and positron beams share a common vacuum chamber. Electrostatic separators are used to displace the electron and positron orbits

so that the collisions of the multiple bunch beams occur only at the single interaction point [8]. The maximum horizontal displacement of the beams from the center of the chamber is about 20 mm. The beam trajectories intersect at the interaction point with a small horizontal crossing angle (± 2 mrad) [9]. By the end of the CLEO II.V data taking in early 1999, CESR operated in 9×4 mode, with 9 trains of 4 closely spaced bunches stored in each beam. Through a series of innovations, the Cornell accelerator physicists steadily increased the peak CESR luminosity over the period of CLEO II and CLEO II.V detector operation: from $1.5 \times 10^{32}\mathrm{cm}^{-2}s^{-1}$ in late 1990 to $8.3 \times 10^{32}\mathrm{cm}^{-2}s^{-1}$ in early 1999 [10, 11].

Each bunch has an approximate Gaussian profile: $\sigma_y \approx 10$ μm in height, $\sigma_x \approx 530$ μm in width, and $\sigma_z \approx 18$ mm along the beam direction When the two beams collide, they create a luminous region (beam spot) which is the overlap of the two colliding bunches. The parameters of the approximate Gaussian profile of the beam spot are: $\sigma_y \approx 6$ μm, $\sigma_x \approx 300$ μm, and $\sigma_z \approx 13$ mm [12, 13]. Note that for unperturbed beams the size of the luminous region is a factor of $\sqrt{2}$ smaller than the single bunch size. Additional reduction in the transverse beam size at the interaction point results from beam-beam interaction (dynamic beta effect described in [12]).

1.2 CLEO detector

CLEO is a general purpose collider detector with barrel geometry and with a solid angle coverage of almost 4π. CLEO's strong features are electromagnetic calorimetry, tracking, and muon identification. Hadron identification capabilities, however, are limited. Cross-sectional views of the CLEO detector are shown in Figures 1.3 and 1.4.

1.2.1 Beam pipe

Particles from the interaction point first pass through the beam pipe before entering the instrumented components of the detector. The CLEO II detector has a 0.5 mm-thick beryllium beam pipe with an inner radius of 3.5 cm. The inner surface is coated with a 25 μm-thick layer of silver to absorb synchrotron radiation. The CLEO II.V configuration has a beryllium beam pipe constructed of two concentric cylinders separated by a 0.5 mm gap through which cooling water is circulated [14]. The inner radius of the beam pipe is 1.9 cm. A 10 μm gold coating is deposited on the inner surface of the beam pipe. The total thickness of the CLEO II.V beam pipe — including gold coating and cooling water — corresponds to 0.6% of a radiation length [15].

1.2.2 Tracking system

In CLEO II the momenta of charged particles are measured in a tracking system consisting of a 6-layer straw tube chamber (`PTL`), a 10-layer precision drift chamber (`VD`), and a 51-layer main drift chamber (`DR`), all operating inside a 1.5 T superconducting solenoidal magnet. The main drift chamber also provides a measurement of the specific ionization, dE/dx, used for particle identification. For CLEO II.V, the straw tube chamber was replaced with a 3-layer silicon vertex detector.

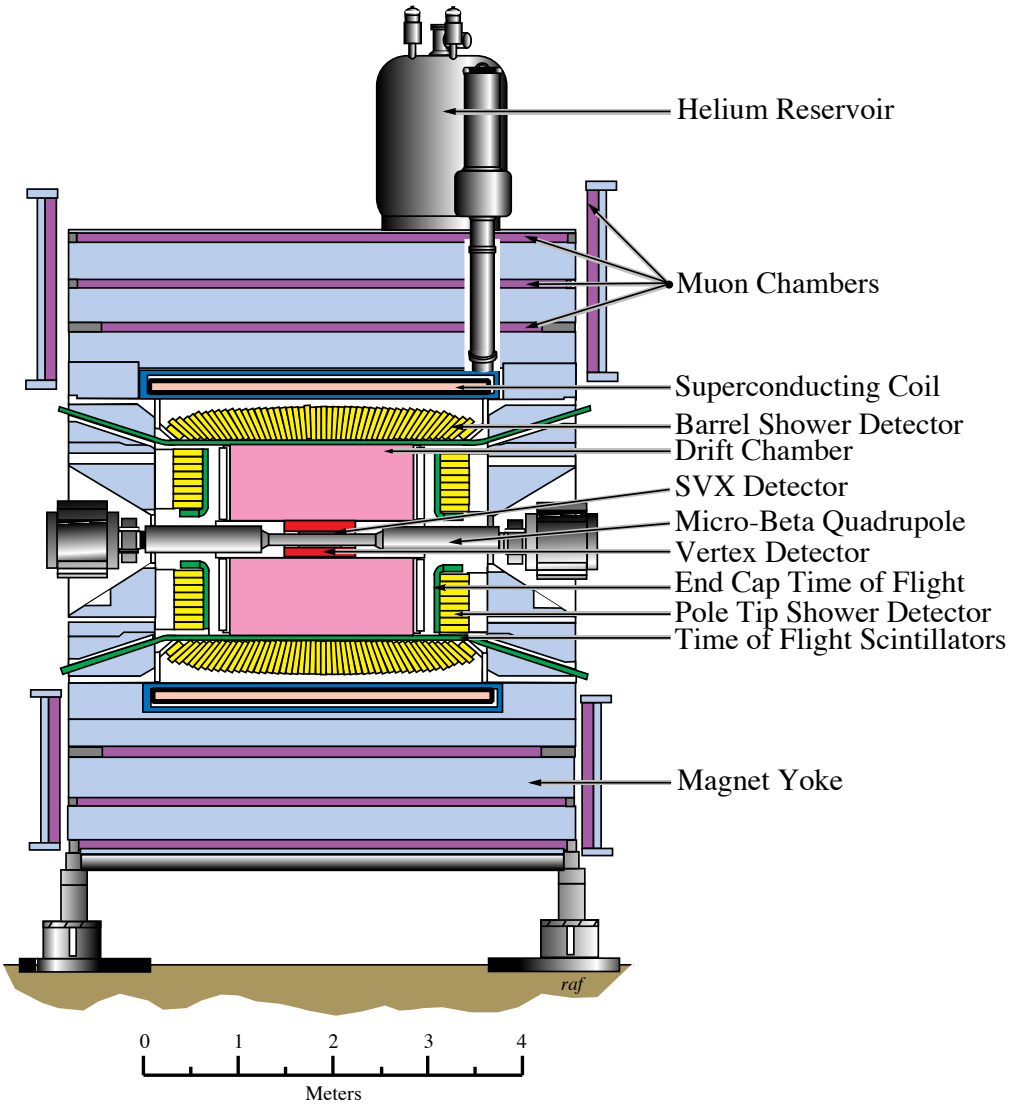

Figure 1.3: The CLEO II.V detector.

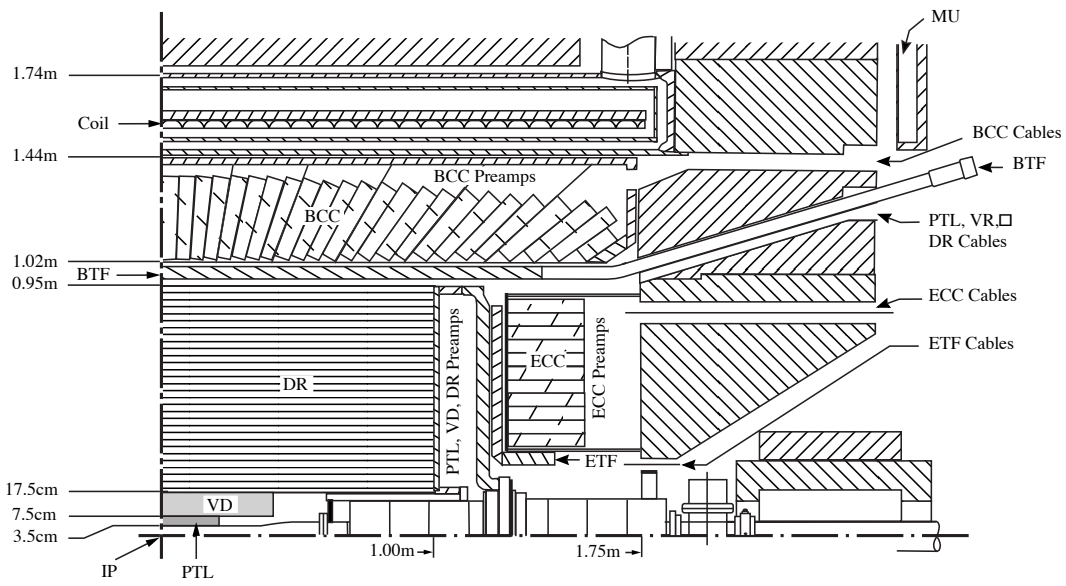

Figure 1.4: One quadrant of the CLEO II detector. Acronyms: `IP` – e^+e^- interaction point; `DR`, `VD`, `PTL` – the outer, intermediate, and inner drift chambers; `TF` – time-of-flight counters, `CC` – crystal calorimeter, and `MU` – muon identification system. Prefixes: `B`= barrel, `E`= endcap.

CLEO II inner drift chamber (precision tracking layers, `PTL`)

The inner tracking detector in CLEO II is a six-layer straw tube chamber occupying the inner volume from a radius of 4.5 to 8 cm (Figures 1.4 and 1.5). It has 64 axial wires per layer. The diameter of the straw tubes ranges from 5 to 7 mm. No longitudinal direction measurements are made with this chamber. In each layer the drift time information is used to make a position measurement with a typical resolution of 50 μm for the tracks traversing the central part of a cell.

CLEO II.V silicon vertex detector (`SVX`)

The inner tracking detector in CLEO II.V is a 3-layer silicon microstrip vertex detector [2] (Figure 1.6). The detector is composed of 300 μm-thick double-sided silicon wafers. Both $r\phi$ and rz information is read out for each of the 96 wafers. The implants on the $r\phi$ side have a pitch of 28 μm, and every fourth implant is read out. The rz implants have a pitch of 100 μm, and every one is instrumented. With the silicon detector the $r\phi$ impact parameter resolution improved by a factor of 2, whereas the rz resolution improved by over an order of magnitude in CLEO II.V compared to CLEO II data. Figure 1.7 shows the intrinsic resolution of the silicon detector as a function of track entrance angle.

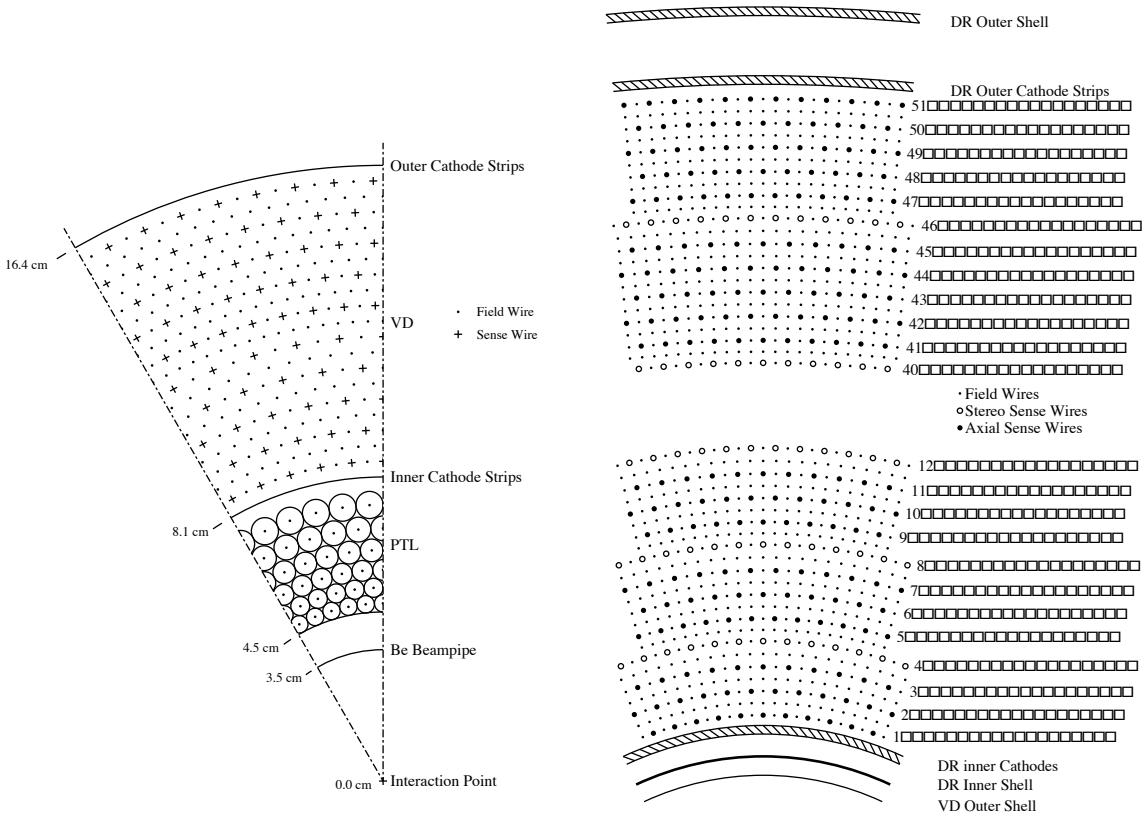

Figure 1.5: Left plot shows the cell structure of the two inner drift chambers (PTL and VD) in the CLEO II configuration. The CLEO II.V detector upgrade includes a new smaller-radius beam pipe and silicon vertex detector replacing the innermost wire chamber (PTL). Right plot shows the cell structure of the main drift chamber (DR).

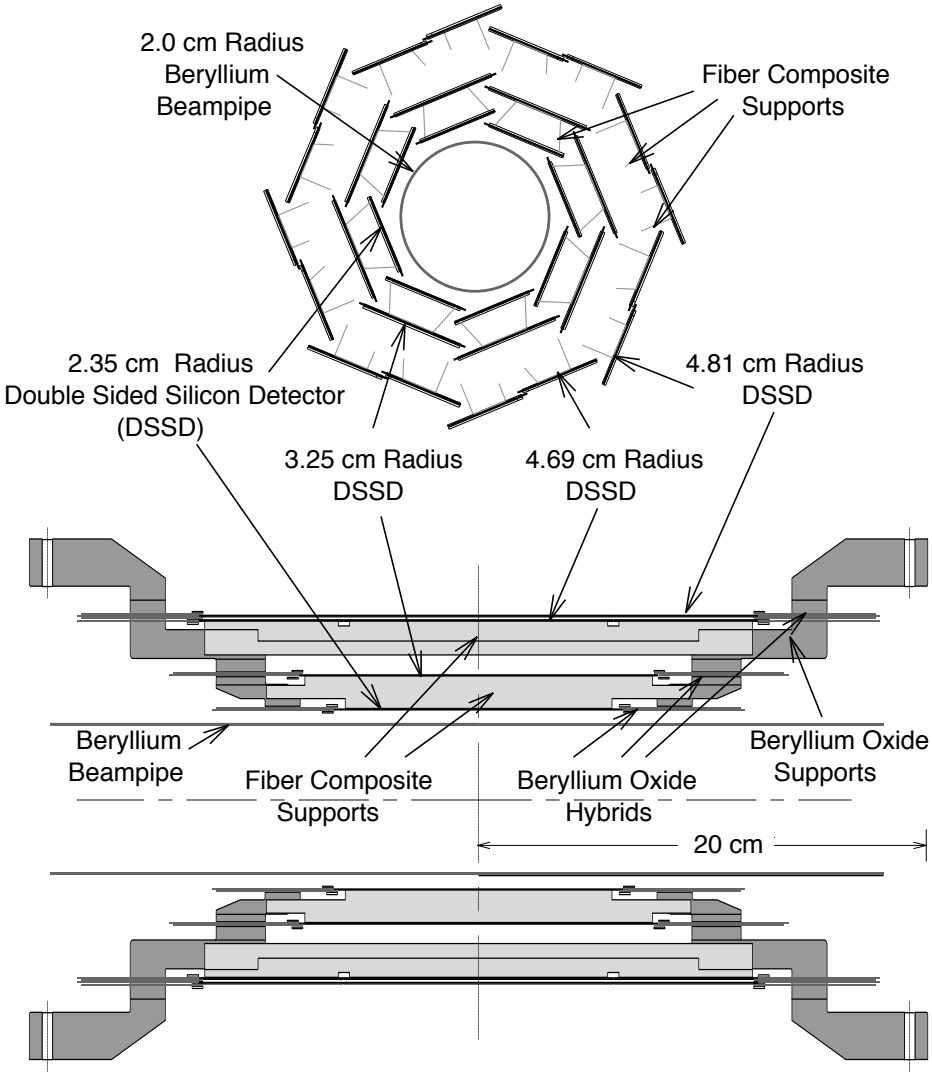

Figure 1.6: The CLEO II.V silicon vertex detector (`SVX`) cross-sectional $r\phi$ view (top) and rz view (bottom).

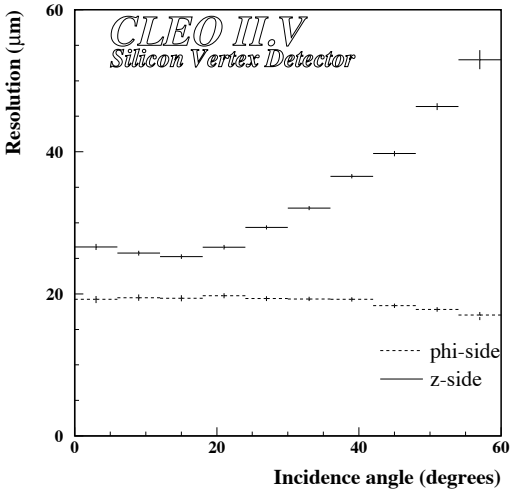

Figure 1.7: Intrinsic silicon detector resolutions as a function of track incidence angle. The zero-angle tracks are perpendicular to the beam direction.

Intermediate drift chamber (VD)

The intermediate drift chamber has a total of 800 sense and 2272 field wires arranged to form 10 layers of hexagonal cells (Figures 1.4 and 1.5). VD extends in radius from 8.1 to 16.4 cm. All layers are axial. The inner 5 layers have 64 cells per layer, whereas the outer 5 layers have 96 cells. The cell size is between 7 and 10 mm. The typical position measurement resolution is 100 μm for the tracks traversing the central part of a cell. Both inner and outer cathode planes are segmented and instrumented to provide rz position measurements with a typical resolution of 1 mm.

Main drift chamber (DR)

The main drift chamber extends in radius from 19 to 91 cm. A total of 12240 sense and 36240 field wires are arranged in a pattern of 51 layers of rectangular cells of nearly equal size (Figures 1.4 and 1.5). The cell size is 14 mm. The typical position measurement resolution is 100 μm for the tracks traversing the central part of a cell. Both inner and outer cathode planes are segmented and instrumented to provide rz position measurements with a typical resolution of 1 mm. Eleven of the 51 DR layers have a 6 degree stereo angle to provide additional z information. In CLEO II.V the gas in the main drift chamber was changed from an argon-ethane to a helium-propane mixture [16]. Multiple scattering is considerably reduced for particles going through the helium-propane mixture. In addition, this mixture makes for more uniform drift isochrones thereby improving the charge collection efficiency from the outer part of a drift cell. The gas mixture change resulted in improved tracking and dE/dx performance of the drift chamber.

1.2.3 Time-of-flight system

The time-of-flight (`TF`) system is used in the trigger, as a tool for particle identification, and as a bunch-finder. This system is located just outside the drift chamber volume (Figures 1.3 and 1.4). The barrel part of the `TF` system comprises 64 counters. Each barrel counter consists of the 5 cm thick bar of plastic scintillator with light pipes leading to the photomultipliers at both ends. Each of the two endcap `TF` subsystems consists of 28 trapezoidal-shaped scintillators. Only one end of each endcap counter is instrumented with a photomultiplier.

1.2.4 Electromagnetic calorimeter

The calorimeter consists of 7800 thallium-doped cesium iodide (CsI) scintillation crystals covering 95% of the solid angle. The barrel part of the calorimeter covers 71% of the solid angle and contains 6144 crystals arranged in 48 rings of 128 crystals. Photons originating at the interaction point strike barrel crystals at nearly normal incidence. Each endcap contains 828 crystals. The layout of crystals is shown in Figures 1.3 and 1.4. The CsI radiation length $X_0 = 1.83$ cm. The crystal dimensions are 5×5 cm in cross-section and 30 cm long ($16X_0$ or 0.8 nuclear interaction lengths). The photon energy resolution parametrizations for barrel and endcap regions are shown in Figure 1.8. Calorimeter performance is degraded by the material the particles have to travel through before reaching the crystals. Therefore the performance varies considerably with polar angle. The central barrel region ($|\cos\theta| < 0.71$) has the smallest amount of material in front of it, about $0.18X_0$, with $0.12X_0$ accounted for by the time-of-flight counters. The material before the endcap calorimeter amounts to $1X_0$, with $1/3X_0$ accounted for by the drift chamber endplate.

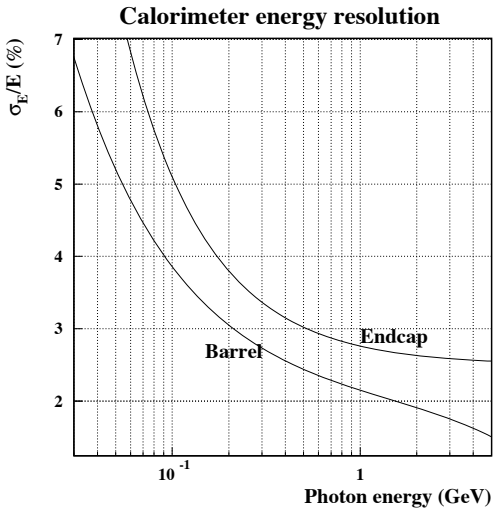

Figure 1.8: Photon energy resolution of the calorimeter as a function of the photon energy.

1.2.5 Solenoidal magnet

The superconducting magnet coil resides outside the crystal calorimeter (Figures 1.3 and 1.4). The solenoid generates a 1.5 T magnetic field which is parallel to the beam axis and is uniform to within 0.2% in the whole tracking volume. A uniform magnetic field is assumed by the tracking software.

1.2.6 Muon identification system

The CLEO muon identification system [17] consists of proportional counters placed at increasing depth in steel absorber (Figure 1.3). The steel absorber is octagonally divided in $r\phi$ plane. The first two of the 36 cm thick layers[1] are the main elements for the magnetic field flux return. The third layer is primarily for the muon identification system. There are three layers of muon chambers in the barrel region ($|\cos\theta| < 0.71$). They are placed at 3, 5, and 7 nuclear interaction lengths (λ_I) for normal incidence tracks. There is also one set of muon chambers outside each endcap that covers the polar angle range of $0.67 < |\cos\theta| < 0.87$. The amount of material in front of the endcap layer of muon counters corresponds to $7\lambda_I$.

1.3 Particle identification

1.3.1 Hadron identification

Hadrons are identified through dE/dx and time-of-flight measurements. The dE/dx information is provided by 49 out of 51 layers of the main drift chamber (`DR`). Figure 1.9 shows dE/dx and time-of-flight measurements for various particle species. Figure 1.10 shows the achieved K/π separation [21].

1.3.2 Electron identification

Electron candidates are identified based on the ratio of the shower energy in the CsI calorimeter to the associated track momentum (E/p), width of the shower in the calorimeter, and dE/dx measurement in the drift chamber. Time-of-flight measurement is used to reject low-momentum antiprotons annihilating in the calorimeter. The information from different devices is combined to form a single discriminating variable for electron identification (`R2ELEC`). By far the most powerful of all discriminating variables is E/p. For $J/\psi \to e^+e^-$ reconstruction, we impose loose electron identification requirements (`R2ELEC` > 0) on both $e^\pm$ candidates. For 1.5 GeV/c tracks pointing to the barrel region, this requirement results in signal efficiency of over 95% and hadron misidentification probability of $\approx 0.5\%$.

1.3.3 Muon identification

Muon candidates are identified based on their ability to penetrate steel absorber and reach the muon chambers. Figure 1.11 shows the muon identification efficiency in barrel and endcap regions for different penetration requirements. For the `DPTHMU` > 3 requirement

[1] Nuclear interaction length of iron is $\lambda_I = 16.8$ cm.

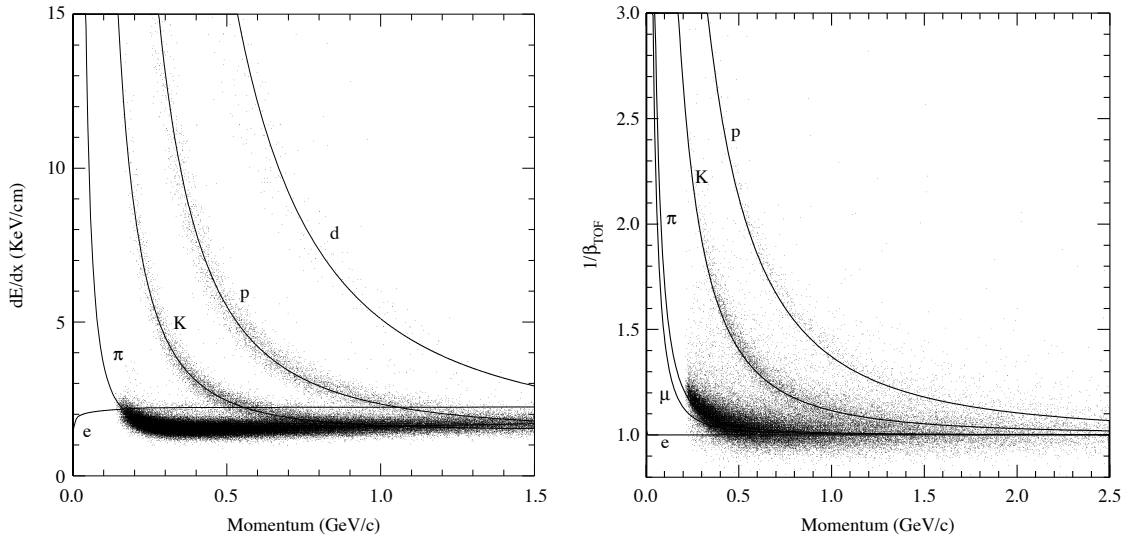

Figure 1.9: The dE/dx (left) and time-of-flight (right) measurements for different particle species. The predicted curves are shown by the solid lines.

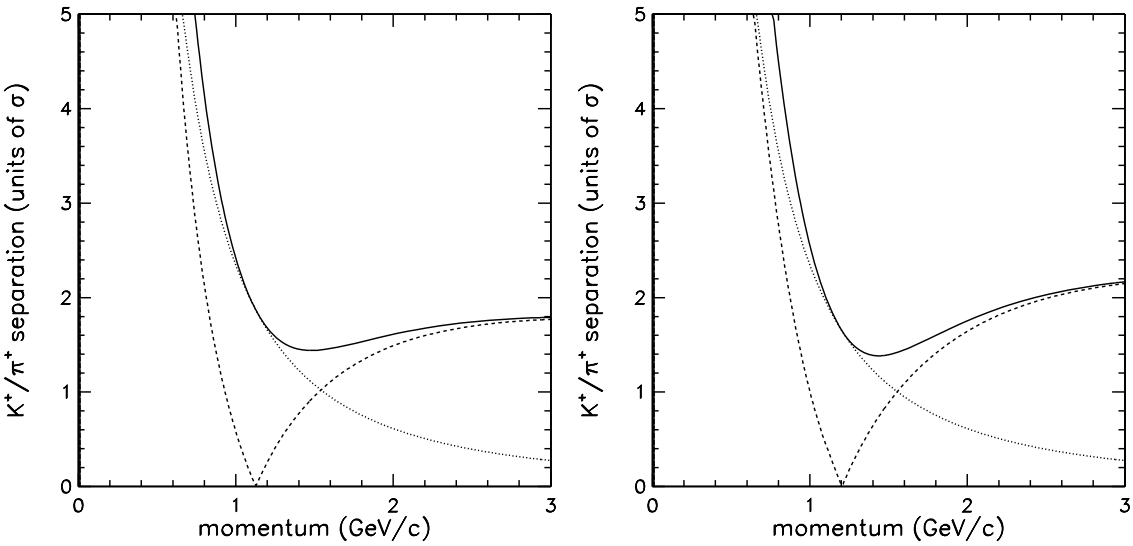

Figure 1.10: Momentum dependence of dE/dx (dashed) and time-of-flight (dotted) K/π separation in CLEO II (left) and CLEO II.V (right). The solid line shows the separation achieved by combining dE/dx and time-of-flight information.

imposed upon 1.5 GeV/c tracks, the misidentification probability is approximately 4% for pions and 5% for kaons.

For $J/\psi \to \mu^+\mu^-$ reconstruction, one of the muon candidates is required to penetrate the steel absorber to a depth greater than 3 nuclear interaction lengths (`DPTHMU` > 3). As described in Section 2.3, we relax the absorber penetration requirement for the second muon candidate if it is not expected to reach a muon chamber either because its energy is too low or because it does not point to a region of the detector covered by the muon chambers. For these muon candidates we require the ionization signature in the CsI calorimeter to be consistent with that of a muon.

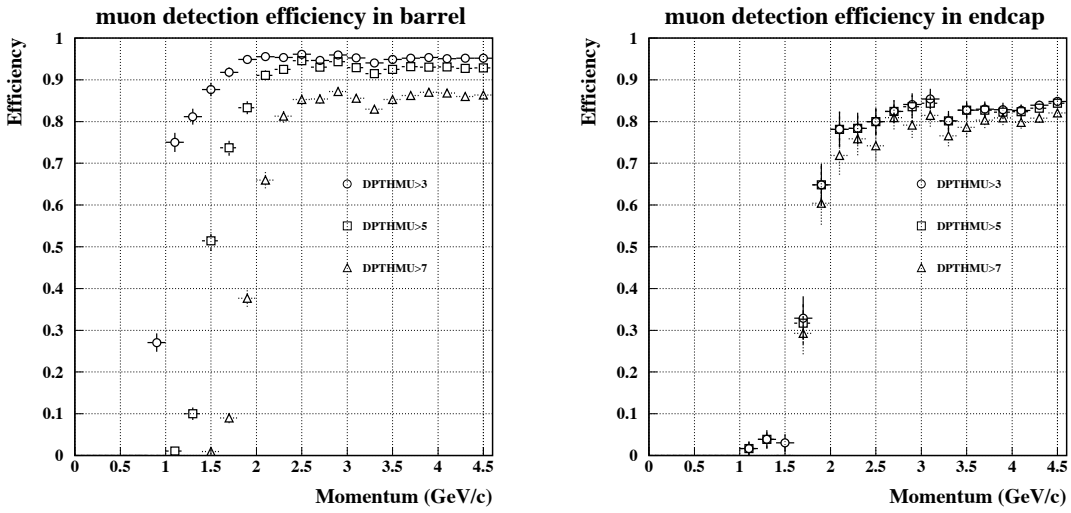

Figure 1.11: Muon detection efficiency in barrel and endcap regions for different penetration requirements. `DPTHMU` is amount of material, in nuclear interaction lengths, penetrated by a muon candidate. The data points were obtained from $e^+e^- \to \mu^+\mu^-\gamma$ events.

1.4 Track fitting

Track fitting is performed using a Kalman filtering technique [18], which was first applied to track fitting by Billoir [19]. The track fit sequentially adds the measurements provided by the tracking system to correctly take into account multiple scattering and energy loss of a particle in the detector material. For each physical track, separate fits are performed using 5 different particle hypotheses: e, μ, π, K, and p. At CLEO the Billoir fitter is a final track fitter. It is not used for pattern recognition, i.e. for finding tracks. In addition to optimally estimating the track parameters at the point of closest approach to the e^+e^- interaction point, the Billoir fitter also calculates covariance matrices for the track parameters.

1.5 $K^0_S \to \pi^+\pi^-$ reconstruction

CLEO has a sophisticated software [20] for finding K^0_S, Λ, and converted photons. The algorithm uses full power of the Billoir track fitter. The first guess on the K^0_S vertex position is obtained by overlapping two oppositely-charged tracks in $r-\phi$ plane. Daughter $\pi^\pm$ tracks are then refit by Billoir fitter, taking into account the decay vertex position to correct for multiple scattering and ionization in the detector material. Then the K^0_S candidate is built from two tracks with a vertex constraint, using the first guess on the vertex position as a starting point.

1.6 Normalized variables

We extensively use normalized variables, taking advantage of well-understood track and photon-shower four-momentum covariance matrices to calculate the expected resolution for each combination. For example, the normalized $J/\psi \to \mu^+\mu^-$ mass is defined as $[M(\mu^+\mu^-) - M_{J/\psi}]/\sigma(M)$, where $M_{J/\psi}$ is the world average value of the J/ψ mass and $\sigma(M)$ is the calculated mass resolution for that particular $\mu^+\mu^-$ combination. The normalized variables naturally take into account non-uniformity of the detector: some tracks and showers are better measured than others. Also, the use of the normalized variables allows the same candidate selection criteria to be applied to the data collected with the CLEO II and CLEO II.V detector configurations. In Figure 1.12 we compare $J/\psi \to \mu^+\mu^-$ mass and normalized mass lineshapes for CLEO II and CLEO II.V simulated events. The $M(\mu^+\mu^-) - M_{J/\psi}$ distributions differ significantly, whereas normalized mass distributions are virtually indistinguishable.

The Billoir track fitter uses hit resolution parametrizations extracted from data. The fitter, however, employs χ^2 fits and Gaussian approximations for hit resolution and multiple scattering. Shower covariance matrices are also calculated using Gaussian parametrizations of the calorimeter resolution. Of course, there are non-Gaussian tails in real life. Although the distributions of the normalized variables are significantly closer to being well described by a single Gaussian than the corresponding non-normalized distributions, still they are not perfect unit Gaussians (with mean of 0 and σ=1) as they should ideally be. Therefore the full Monte Carlo simulation is used whenever we decide on the selection criteria. Based on simulation, we often multiply the calculated combination-by-combination uncertainties by a global scale factor to make the normalized distribution look more like a unit Gaussian.

1.7 B candidate selection variables ΔE and $M(B)$

Due to energy and momentum conservation in the reaction $e^+e^- \to \Upsilon(4S) \to B\overline{B}$, the energy of each B meson should be equal to the beam energy, and the absolute momentum of each B meson can be calculated as $p(B) = \sqrt{E^2_{\rm beam} - M^2_B}$. We select fully reconstructed B candidates by means of two observables.

The first observable is the difference between the energy of the B candidate and the beam energy, $\Delta E \equiv E(B) - E_{\rm beam}$. The ΔE resolution is dominated by the resolution in

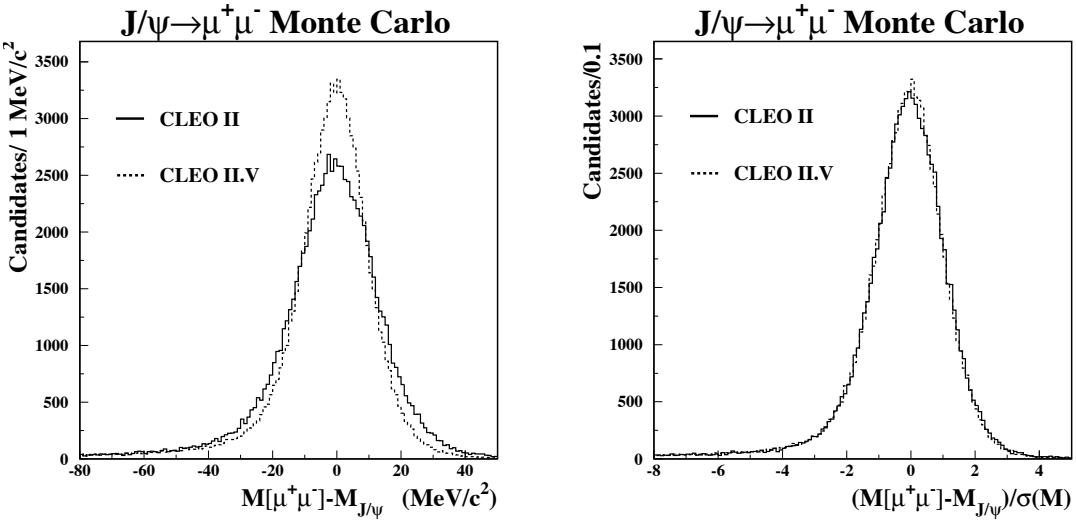

Figure 1.12: The distribution of mass difference $M(\mu^+\mu^-) - M_{J/\psi}$ (left) and normalized mass $[M(\mu^+\mu^-) - M_{J/\psi}]/\sigma(M)$ (right) for $J/\psi \to \mu^+\mu^-$ decays selected from simulated event samples. CLEO II (CLEO II.V) events are represented by solid (dashed) line. Solid and dashed histograms are normalized to have the same area.

the $E(B)$ term which accounts for the uncertainties in the track and shower measurements.

The second observable is the beam-constrained B mass, $M(B) \equiv \sqrt{E^2_{\rm beam} - p^2(B)}$. Often we also use $M_{\rm bc}$ notation for beam-constrained mass. If CESR were always running *exactly* at the $\Upsilon(4S)$ peak, then we could use $p(B)$ instead of $M(B)$. For some datasets, however, the average beam energy deviates by as much as 2 MeV from the nominal peak energy. Therefore it is necessary to use $M(B)$ to trace the beam energy variations. The CESR beam energy spread is $\delta E/E \simeq 7 \times 10^{-3}$ per beam, which corresponds to the center-of-mass energy spread for the colliding beams of $\sqrt{2} \cdot 7 \times 10^{-3} \cdot 5290$ MeV $= 2 \times 2.6$ MeV. This beam energy spread dominates the $M(B)$ resolution:

$$\sigma[M(B)] = \frac{E_{\rm beam}}{M(B)} \cdot \sigma(E_{\rm beam}) \oplus \frac{p(B)}{M(B)} \cdot \sigma[p(B)] \approx \sigma(E_{\rm beam}).$$

The beam-constrained mass is shifted by $[5.290\ {\rm GeV} - E_{\rm beam}]$ for off-$\Upsilon(4S)$ runs to correctly reproduce the shape of continuum background.

We use normalized variables $\Delta E/\sigma(\Delta E)$ and $|M(B) - M_B|/\sigma(M)$ for candidate selection. The reported ΔE uncertainties usually have to be multiplied by a factor of 1.1 to 1.2 to make the normalized distribution look more like a unit Gaussian for simulated signal events.

Table 1.1: Production cross-sections in e^+e^- collisions at the $\Upsilon(4S)$ resonance (Figure 1.1).

$e^+e^- \to$	Cross-section (nb)
$b\overline{b}$	1.05
$c\overline{c}$	1.30
$s\overline{s}$	0.35
$u\overline{u}$	1.39
$d\overline{d}$	0.35
total hadronic	4.44
$\tau^+\tau^-$	0.94
$\mu^+\mu^-$	1.16

1.8 Data sample

The data used in this thesis were recorded over a period of almost ten years between 1990 and 1999. In most analyses we use the full CLEO II and CLEO II.V datasets corresponding to 9.2 fb^{-1} of e^+e^- data taken at the $\Upsilon(4S)$ resonance (Figure 1.1) and 4.6 fb^{-1} taken 60 MeV below the $\Upsilon(4S)$ resonance (off-$\Upsilon(4S)$ sample). These data contain the information about the decays of 9.7×10^6 $B\overline{B}$ meson pairs. Two thirds of the data were collected with the CLEO II.V detector installed in the fall of 1995.

The data sample comprises 21 individual data sets marked `4S2-4S9`, `4SA-4SG` for CLEO II, and `4SH-4ST` (no `4SO`) for CLEO II.V. The data set boundaries were designed to mark the interruptions — such as extended shutdowns and hardware modifications — in periods of stable data taking; some of the big CLEO II.V data sets, however, were arbitrarily subdivided for calibration purposes. The integrated luminosities of the individual data sets range from 98 pb^{-1} (`4SD`) to 1.6 fb^{-1} (`4ST`).

Table 1.1 lists hadronic as well as $\tau^+\tau^-$ and $\mu^+\mu^-$ production cross-sections at the $\Upsilon(4S)$ peak [22].

1.9 Monte Carlo simulation

We use simulated event samples (Monte Carlo) to determine reconstruction efficiency, estimate background, or extract a signal shape for some distribution. The production of Monte Carlo samples occurs in 3 steps:

1. Physical process generator called `QQ` simulates an $\Upsilon(4S) \to B\overline{B}$ or a continuum $e^+e^- \to q\overline{q}$ event and decays unstable particles. The probabilities of decays are taken from tables that are periodically updated to reflect our current best knowledge. Quark fragmentation is handled by JETSET program [23].

2. The decay history output of the `QQ` event generator is passed to `CLEOG`, a GEANT-based [24] package which simulates the passage of a particle through the detector material.

3. Finally, the simulated events are processed with the same reconstruction programs as used for real data.

Several samples of simulated events are widely used throughout the thesis:

1. *Generic $B\overline{B}$ Monte Carlo sample:* a sample of simulated $\Upsilon(4S) \to B\overline{B}$ events, where both B mesons are allowed to decay generically, i.e. into all available final states. This sample was produced by the central CLEO Monte Carlo farm. The statistics correspond to about 4 times the data, although this value varies depending on the analysis.

2. *High-statistics generic $B\overline{B}$ Monte Carlo sample:* this sample was designed to look like a J/ψ skim of simulated generic $B\overline{B}$ events. It includes the events with true $J/\psi \to \ell^+\ell^-$ decays as well as the ones contributing to the background under the J/ψ peak. The statistics correspond to about 31 times the data.

3. *Generic continuum Monte Carlo sample:* a sample of simulated generic $e^+e^- \to q\overline{q}$ continuum events produced by the central CLEO Monte Carlo farm. The statistics of the sample correspond to about 5 times the on-$\Upsilon(4S)$ data.

Other samples of simulated events will be introduced in the course of the discussion.

Chapter 2

Improvements in reconstruction of $J/\psi \to \ell^+\ell^-$

2.1 Abstract

The J/ψ mesons are detected through their dilepton decays in all the analyses presented in this thesis. In this chapter we describe the improvements upon the traditional reconstruction procedure.

We show that the detection of the bremsstrahlung photons in the crystal calorimeter improves the $J/\psi \to e^+e^-$ reconstruction efficiency by approximately 25% without adding more background.

We also show how to increase the $J/\psi \to \mu^+\mu^-$ reconstruction efficiency by relaxing the absorber penetration requirement for a muon candidate if it is not expected to reach a muon chamber either because its energy is too low or because it does not point to a region of the detector covered by the muon chambers. For these muon candidates we require the ionization signature in the crystal calorimeter to be consistent with that of a muon.

2.2 $J/\psi \to e^+e^-$

2.2.1 How much radiation is there?

The internal bremsstrahlung in $J/\psi \to e^+e^-\gamma$ decay as well as the bremsstrahlung in the detector material produces a long radiative tail in the e^+e^- invariant mass distribution (Figure 2.1) and impedes efficient J/ψ detection. Figure 2.2 shows a real $B^0 \to J/\psi K^0_S$ event which would have been lost because a very energetic (840 MeV) bremsstrahlung photon was produced either in $J/\psi \to e^+e^-\gamma$ decay or in the passage of the electron through the detector material.

The internal bremsstrahlung spectrum is given by [25, 26]

$$\frac{d\Gamma(J/\psi \to \ell^+\ell^-\gamma)}{dE^*_\gamma d\cos\theta} = \frac{2\alpha}{\pi}\Gamma(J/\psi \to \ell^+\ell^-)\frac{1}{E^*_\gamma}\left(1 - \frac{2E^*_\gamma}{M_{J/\psi}}\right)\frac{\beta^3 sin^2\theta}{\beta_0(1-\beta^2\cos^2\theta)^2}, \qquad (2.1)$$

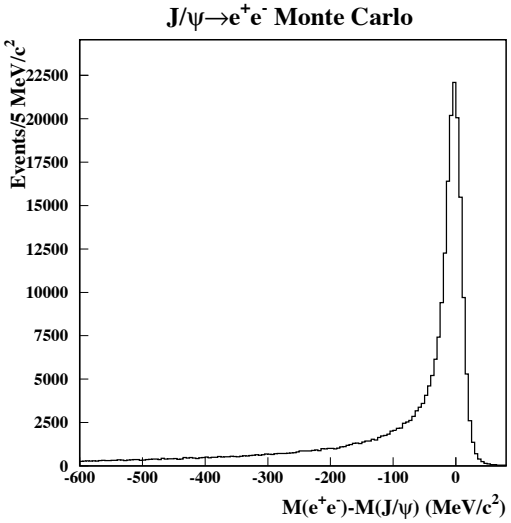

Figure 2.1: The $\Delta M \equiv M(e^+e^-) - M_{J/\psi}$ distribution for $J/\psi \to e^+e^-$ candidates reconstructed from a sample of simulated events. No bremsstrahlung photon recovery is attempted.

where E^*_γ is the photon energy in the J/ψ rest frame, θ is the angle between the photon and one lepton in the dilepton rest frame, α is the fine structure constant, $\beta = \sqrt{1 - \frac{4m_\ell^2}{M^2_{J/\psi} - 2M_{J/\psi}E^*_\gamma}}$, is the lepton velocity in the dilepton rest frame, and $\beta_0 = \sqrt{1 - \frac{4m_\ell^2}{M^2_{J/\psi}}}$ is the value of β for $E^*_\gamma = 0$. Integration over the angle θ yields

$$\begin{aligned} \frac{d\Gamma(J/\psi \to \ell^+\ell^-\gamma)}{dE^*_\gamma} &= \frac{\alpha}{\pi}\Gamma(J/\psi \to \ell^+\ell^-)\frac{1}{E^*_\gamma}\left(1 - \frac{2E^*_\gamma}{M_{J/\psi}}\right) \times \\ &\times \frac{\beta}{\beta_0}\left[\frac{1+\beta^2}{\beta}\ln\left(\frac{1+\beta}{1-\beta}\right) - 2\right]. \end{aligned} \tag{2.2}$$

The E760 experiment measured the rate for internal bremsstrahlung $\frac{Br(J/\psi \to e^+e^-\gamma)}{Br(J/\psi \to e^+e^-)} = 14.7 \pm 2.2\%$ for $E^*_\gamma > 100$ MeV [26], which is in good agreement with the QQ prediction of 15.5%. The relative importance of internal and detector bremsstrahlung is estimated from simulation. Table 2.1 lists the fraction of $J/\psi \to e^+e^-$ candidates in the tail of the $\Delta M \equiv M(e^+e^-) - M_{J/\psi}$ distribution (Figure 2.1) with and without internal bremsstrahlung. Roughly 2/3 of the efficiency loss arises from the $e^\pm$ radiation in the detector material.

2.2.2 Bremsstrahlung photon recovery

Both internal and detector bremsstrahlung photons are emitted very close to the direction of the parent electron or positron. For our purposes we do not have to discriminate

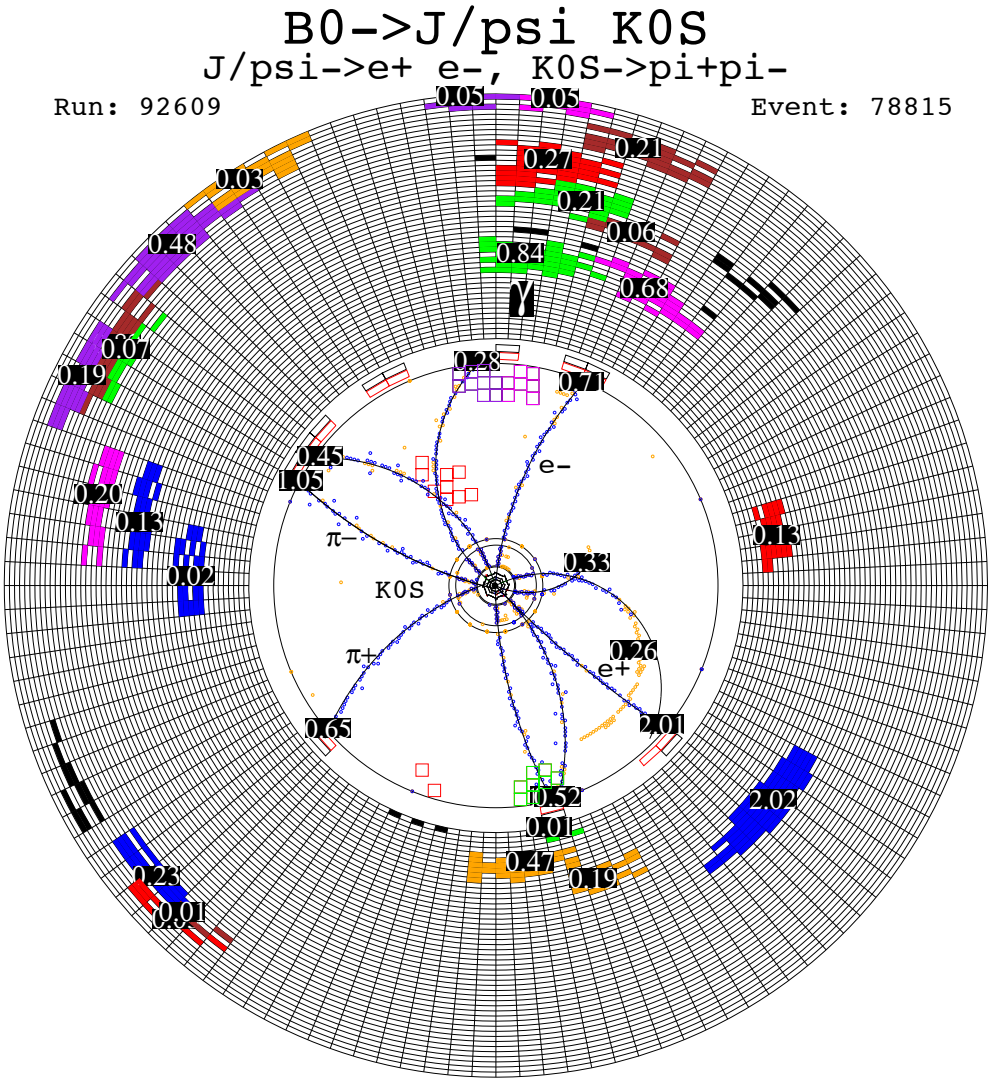

Figure 2.2: A $B^0 \to J/\psi K^0_S$ event in CLEO II.V data. The very energetic (840 MeV) bremsstrahlung photon at 12 o'clock (marked γ) was produced either in $J/\psi \to e^+e^-\gamma$ decay or in the passage of the electron through the detector material. Without the bremsstrahlung photon recovery the calculated e^+e^- invariant mass is approximately 70 standard deviations away from the J/ψ mass peak.

Table 2.1: The fraction of $J/\psi \to e^+e^-$ candidates in the tail of the $\Delta M \equiv M(e^+e^-) - M_{J/\psi}$ distribution as determined from simulation (Figure 2.1). The values in parentheses were obtained by switching off the decay radiation (internal bremsstrahlung). As expected, the rate of the detector bremsstrahlung is higher for CLEO II.V configuration.

Dataset	Fraction of J/ψ candidates in tail of ΔM distribution	
	tail $\Delta M < -50$ MeV/c^2	tail $\Delta M < -100$ MeV/c^2
CLEO II	38%(23%)	29%(16%)
CLEO II.V	45%(31%)	35%(24%)
CLEO II+II.V	43%(28%)	33%(21%)

between the photons produced in internal or detector bremsstrahlung because in CLEO II and CLEO II.V detectors essentially all the material (beam pipe, silicon detector layers, and drift chamber interfaces) is located close to the interaction point compared to the size of the main drift chamber. The magnetic field deflects electrons and positrons so that the showers produced in the calorimeter by the bremsstrahlung photon and by the $e^\pm$ parent are usually well separated.

To recover the bremsstrahlung photons we:

- Select the photon showers with energies greater than 10 MeV which are not matched to any charged track and have at most one nearby shower (the $e^\pm$ shower).
- From these photons we select the one with the smallest opening angle with respect to the direction of the $e^\pm$ track evaluated at the interaction point and then require this opening angle to be smaller than 5° (Figure 2.3).

Our search for the bremsstrahlung photons has three possible outcomes:

1. No showers satisfy our requirements, then $M(e^+(\gamma)e^-(\gamma)) \equiv M(e^+e^-)$.
2. A shower accompanying one of the $e^\pm$ tracks is found, then $M(e^+(\gamma)e^-(\gamma)) \equiv M(e^+e^-\gamma)$ (Figure 2.4).
3. Two showers (one for each $e^\pm$ track) are found, then $M(e^+(\gamma)e^-(\gamma)) \equiv M(e^+\gamma e^-\gamma)$ (Figure 2.5).

The net effect of adding the bremsstrahlung photons can be seen in Figure 2.6. In Figure 2.7 we show the scatter plot for $M(e^+(\gamma)e^-(\gamma)) - M_{J/\psi}$ vs. $M(e^+e^-) - M_{J/\psi}$ for $\Upsilon(4S)$ data. In this figure one can see:

- The "recovery" band: addition of photon(s) improves $J/\psi \to e^+e^-$ mass peak;
- The barely noticeable "loss" band: addition of photon(s) kicks good combinations from $J/\psi \to e^+e^-$ mass peak;
- The "no change" band: no photons were added, therefore $M(e^+(\gamma)e^-(\gamma)) \equiv M(e^+e^-)$.

The effect of the bremsstrahlung photon detection on the $J/\psi \to e^+e^-$ reconstruction efficiency will be discussed in Section 2.4.

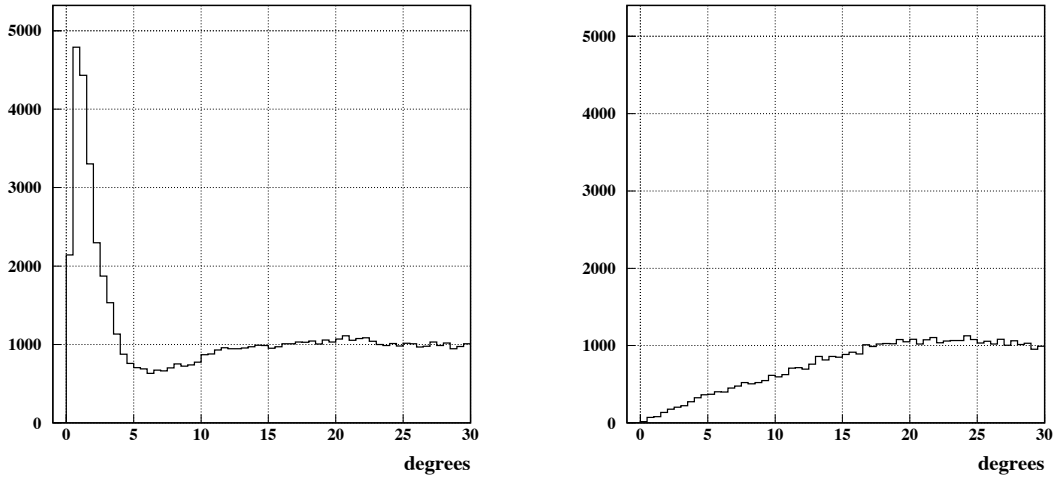

Figure 2.3: Angle between a track and the closest shower not matched to any track. Left (right) histogram represents the distribution for tagged $e^{\pm}$ ($\mu^{\pm}$) tracks from $J/\psi \to e^+e^-$ ($J/\psi \to \mu^+\mu^-$) decays in the sample of simulated generic $B\overline{B}$ events.

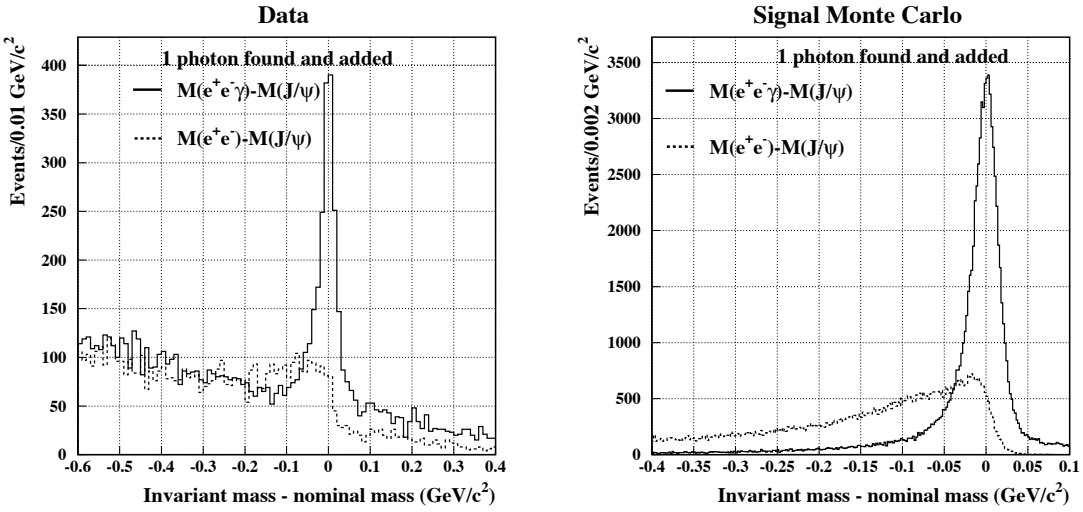

Figure 2.4: The $J/\psi \to e^+e^-$ mass peak with one bremsstrahlung photon detected and added. The solid line shows $M(e^+e^-\gamma) - M_{J/\psi}$ distribution; the dashed line shows $M(e^+e^-) - M_{J/\psi}$ distribution for the same events. Left plot represents $\Upsilon(4S)$ data, whereas right plot is obtained from simulated $J/\psi \to e^+e^-$ decays.

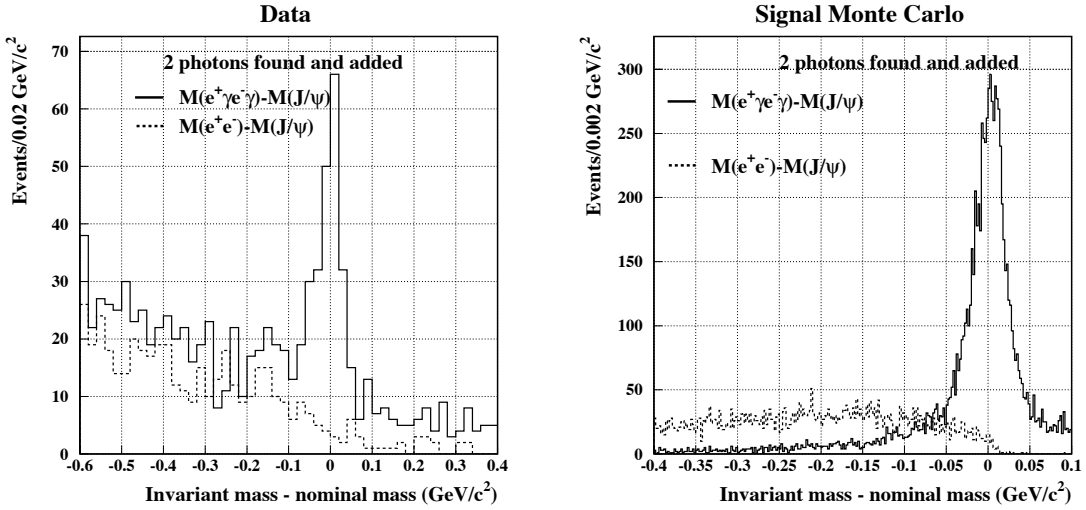

Figure 2.5: The $J/\psi \to e^+e^-$ mass peak with two bremsstrahlung photons detected and added. The solid line shows $M(e^+\gamma e^-\gamma) - M_{J/\psi}$ distribution; the dashed line shows $M(e^+e^-) - M_{J/\psi}$ distribution for the same events. Left plot represents $\Upsilon(4S)$ data, whereas right plot is obtained from simulated $J/\psi \to e^+e^-$ decays.

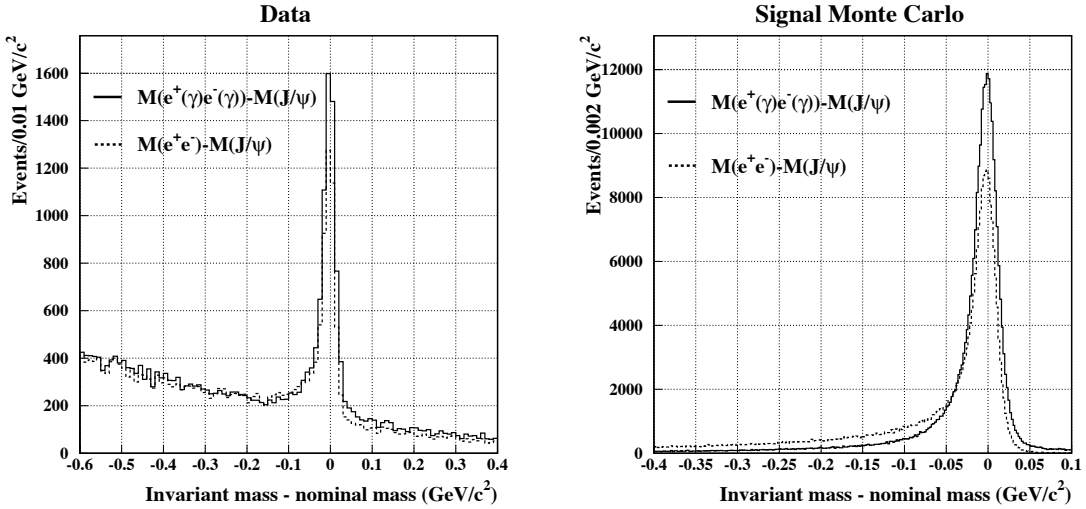

Figure 2.6: The $J/\psi \to e^+e^-$ mass peak with zero to two bremsstrahlung photons detected and added. The solid line shows $M(e^+(\gamma)e^-(\gamma)) - M_{J/\psi}$ distribution; the dashed line shows $M(e^+e^-) - M_{J/\psi}$ distribution for the same events. Left plot represents $\Upsilon(4S)$ data, whereas right plot is obtained from simulated $J/\psi \to e^+e^-$ decays.

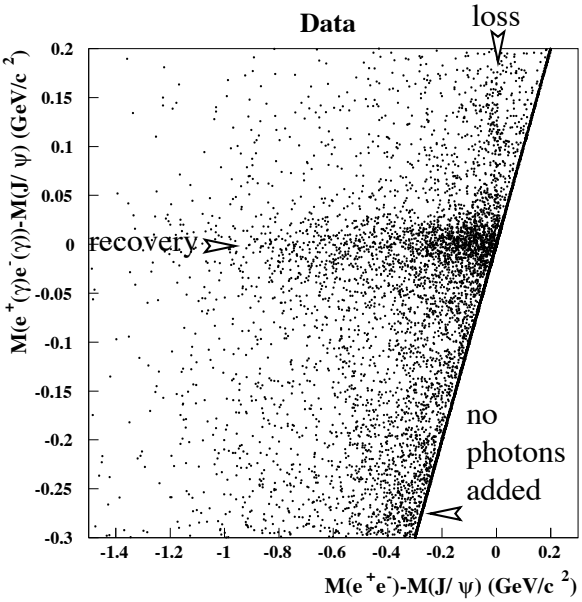

Figure 2.7: Relationship between $M(e^+(\gamma)e^-(\gamma)) - M_{J/\psi}$ and $M(e^+e^-) - M_{J/\psi}$ for data with zero to two bremsstrahlung photons detected and added. "Recovery", "loss" and "no change" bands described in the text are visible.

2.3 $J/\psi \to \mu^+\mu^-$

2.3.1 Radiation in $J/\psi \to \mu^+\mu^-$

In our energy range the muon bremsstrahlung in the detector material is negligible. However, the internal bremsstrahlung rate is not much smaller for $J/\psi \to \mu^+\mu^-$ compared to $J/\psi \to e^+e^-$. Figure 2.8 shows that the $J/\psi \to \mu^+\mu^-$ mass lineshape is visibly altered by the decay radiation.

Should we try to recover the bremsstrahlung photons in $J/\psi \to \mu^+\mu^-$? The distributions of $d\Gamma(J/\psi \to e^+e^-\gamma)/dE^*_\gamma$ and $d\Gamma(J/\psi \to \mu^+\mu^-\gamma)/dE^*_\gamma$, calculated using Equation 2.2, are shown in Figure 2.9. If $E^*_\gamma \ll M_{J/\psi}$, then $\beta \simeq 1 - 2\frac{m_\ell^2}{M_{J/\psi}^2}$, and from Equation 2.2 we obtain

$$\frac{d\Gamma(J/\psi \to e^+e^-\gamma)/dE^*_\gamma}{d\Gamma(J/\psi \to \mu^+\mu^-\gamma)/dE^*_\gamma} \approx \frac{1 + 2\ln(\frac{m_e}{M_{J/\psi}})}{1 + 2\ln(\frac{m_\mu}{M_{J/\psi}})} \approx 2.9.$$

The E760 experiment measured $\frac{Br(J/\psi \to e^+e^-\gamma)}{Br(J/\psi \to e^+e^-)} = 14.7 \pm 2.2\%$ for $E^*_\gamma > 100$ MeV [26]. Therefore $\frac{Br(J/\psi \to \mu^+\mu^-\gamma)}{Br(J/\psi \to \mu^+\mu^-)} \approx 5\%$ for $E^*_\gamma > 100$ MeV which is in good agreement with the QQ prediction of 4.9%.

However, a difficulty arises when we take a look at the angular distribution of the

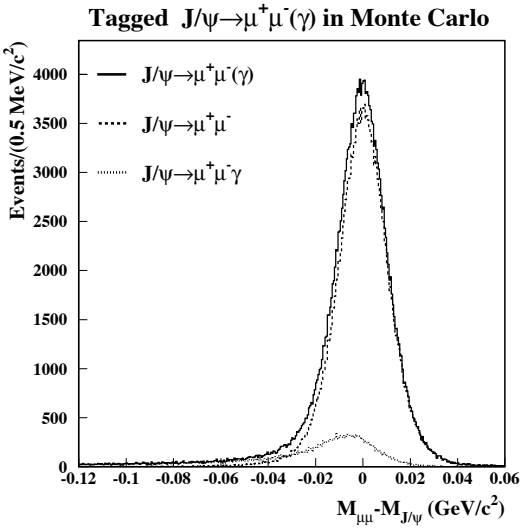

Figure 2.8: Distribution of $M(\mu^+\mu^-) - M_{J/\psi}$ for simulated $B \to J/\psi X$, $J/\psi \to \mu^+\mu^-$ decays. The dashed (dotted) line represents contribution from events generated with (without) internal bremsstrahlung photon in the final state, whereas the solid line represents the sum of both contributions. The soft-photon energy cut-off for internal bremsstrahlung is 1 MeV.

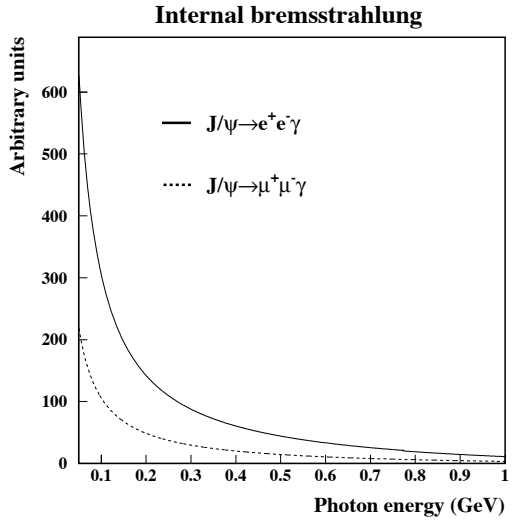

Figure 2.9: Internal bremsstrahlung rate for $J/\psi \to e^+e^-$(solid line) compared to $J/\psi \to \mu^+\mu^-$(dotted line). The distributions were computed using Equation 2.2.

bremsstrahlung photons as given by Equation 2.1:

$$\frac{d\Gamma(J/\psi \to \ell^+\ell^-\gamma)}{d\cos\theta} \propto \frac{(1-\cos^2\theta)}{(1-\beta^2\cos^2\theta)^2}. \tag{2.3}$$

The maximum of the $d\Gamma/d\theta$ distribution is at $\theta_{\max} \approx \sqrt{3}m_\ell c^2/E_\ell$, where m_ℓ and E_ℓ are the mass and typical energy of the lepton. We obtain $\theta_{\max} \approx 0.03^\circ$ for electrons and $\theta_{\max} \approx 7^\circ$ for muons (Figure 2.10). Such an angular distribution of the bremsstrahlung photons in $J/\psi \to \mu^+\mu^-\gamma$ decay makes the photon recovery much more difficult because these photons are no longer concentrated in a narrow cone around the parent track. We therefore do not attempt to recover the bremsstrahlung photons for $J/\psi \to \mu^+\mu^-$.

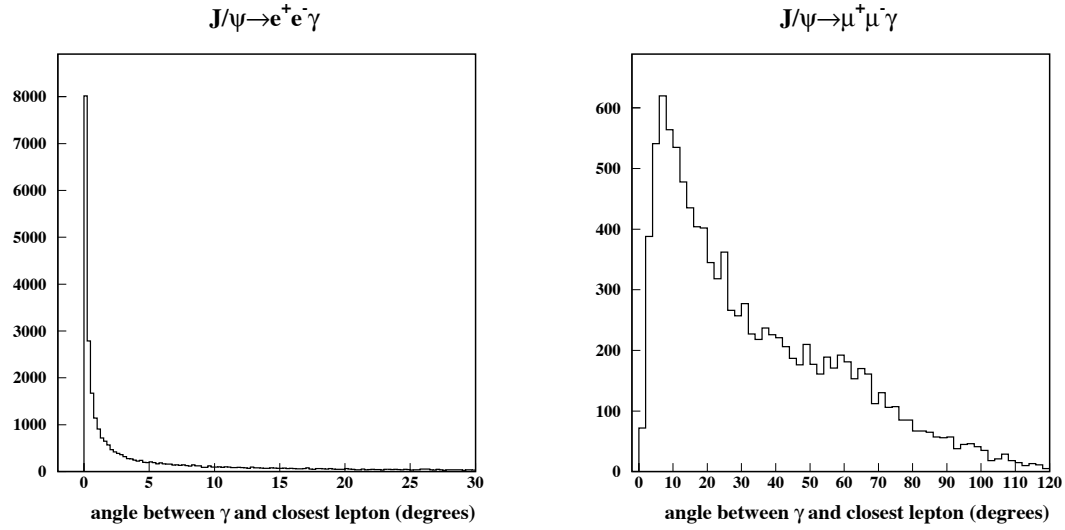

Figure 2.10: The angle between the internal bremsstrahlung photon ($E_\gamma > 10$ MeV) and the closest lepton for $J/\psi \to e^+e^-\gamma$ (left) and $J/\psi \to \mu^+\mu^-\gamma$ (right). The distribution is produced by the QQ event generator.

2.3.2 Use of crystal calorimeter for muon identification

Two approaches have been traditionally applied at CLEO to reconstruction of $J/\psi \to \mu^+\mu^-$ decay:

1. Both muon candidates are positively identified by the muon system [27, 28].
2. Only one muon is identified [29, 30].

The advantage of the first approach is low background. The advantages of the second approach are higher reconstruction efficiency and reduced systematic uncertainty associated with muon identification.

We would like to find a middle ground between these two approaches. Namely, we would like to increase the $J/\psi \to \mu^+\mu^-$ detection efficiency without being swamped

by background. To accomplish that, we will use crystal calorimeter information. Muons typically leave a narrow trail of ionization and deposit approximately 200 MeV of energy in the crystal calorimeter. Hadrons, on the other hand, quite often undergo a nuclear interaction in a CsI crystal whose length corresponds to $0.8\lambda_I$. Andy Foland and Darin Acosta have successfully used the calorimeter information to find K_L^0's [31] and to reject muons [32].

The detailed information on whether the particular muon candidate is expected to reach a muon chamber with high probability is calculated by the CLEO muon identification software [33]. Unfortunately, this information is not currently stored for all the tracks of interest. This is why for the same purpose we use cruder requirements based only on the momentum and polar angle of a muon candidate track.

Looking at the picture of the CLEO detector (Figure 1.3), we divide all the tracks into 3 groups according to the value of cosine of the track polar angle with respect to the beam axis ($\cos\theta$):

1. $|\cos\theta| < 0.71$.— Track points to the barrel muon chambers.
2. $0.71 < |\cos\theta| < 0.85$.— Track points to the end-cap muon chambers.
3. $|\cos\theta| > 0.85$.— Track points to the region of the detector not covered by any muon chambers.

The momentum spectrum of the muons from $B \to J/\psi X$, $J/\psi \to \mu^+\mu^-$ decays is shown in Figure 2.11. The muon identification efficiency plots for barrel and endcap regions are shown in Figure 1.11. Essentially all the muons from J/ψ decays can reach the first layer of the barrel muon chambers (`DPTHMU` $= 3$ for $\cos\theta = 0$). However, to reach the end-cap muon chamber a track needs to traverse about seven nuclear absorption lengths (Figure 2.12).

We always require one of the two muon candidates to be identified by the muon system (`DPTHMU` > 3). The second muon candidate should satisfy one of the following three requirements:

1. `DPTHMU` > 3 (see Figure 2.14).
2. 1.0 GeV/c< $|P_\mu| < 1.8$ GeV/c, the track is matched to a minimum ionization shower in the calorimeter, and the track projects into the acceptance of the end-cap muon chambers ($0.71 < |\cos\theta| < 0.85$) (see left plot in Figure 2.13).
3. $|P_\mu| > 1.0$ GeV/c, the track is matched to a minimum ionization shower in the calorimeter, and the track does not project into the acceptance of the muon chambers ($|\cos\theta| > 0.85$) (see right plot in Figure 2.13).

The calorimeter shower is consistent with being produced by a minimum ionizing particle if there is a good match between track and shower, shower energy is between 160 and 300 MeV, there are no nearby showers, and the shower is narrow. The total reconstructed $J/\psi \to \mu^+\mu^-$ sample is shown in Figure 2.15.

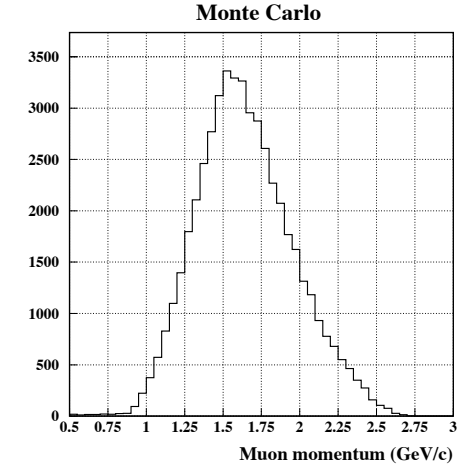

Figure 2.11: Momentum spectrum of the muons from simulated $B \to J/\psi X$, $J/\psi \to \mu^+\mu^-$ decays.

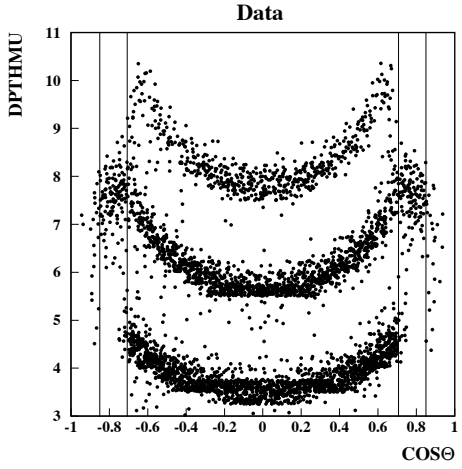

Figure 2.12: Absorber penetration depth `DPTHMU` as a function of the polar angle for inclusive muon candidates in data. Vertical lines are drawn at $\cos\theta = \pm 0.71$ and $\cos\theta = \pm 0.85$

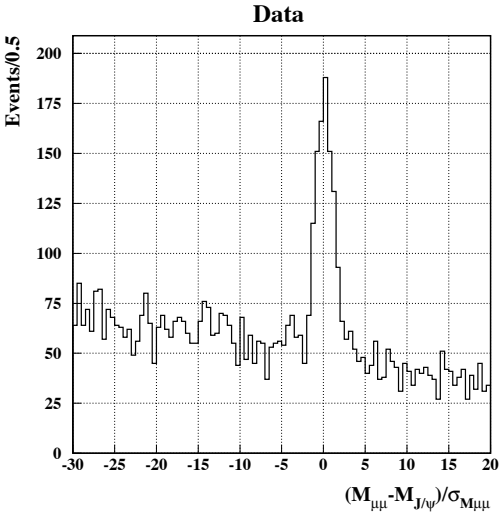

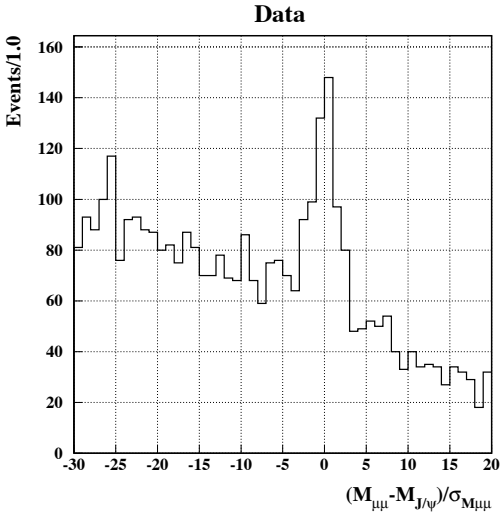

Figure 2.13: Normalized $\mu^+\mu^-$ invariant mass distribution for the salvaged $J/\psi \to \mu^+\mu^-$ candidates in $\Upsilon(4S)$ data. One of the muon candidates does not have `DPTHMU` > 3.0, but its ionization signature in the calorimeter is consistent with that of a muon. In left plot the non-identified muon candidates point to the end-cap muon chamber but do not have enough energy to penetrate the absorber in front of the chamber. In right plot the non-identified muon candidates do not project into the acceptance of the muon chambers.

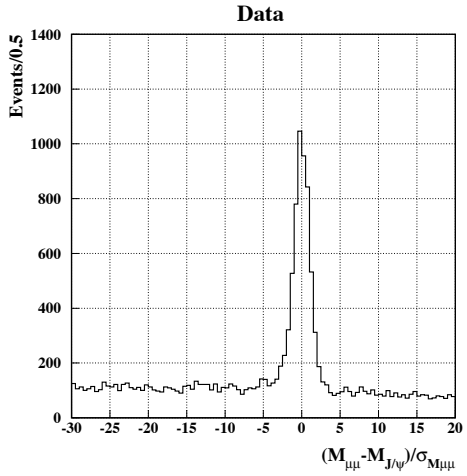

Figure 2.14: Normalized $\mu^+\mu^-$ invariant mass distribution for the $J/\psi \to \mu^+\mu^-$ candidates in $\Upsilon(4S)$ data. Both muon candidates are identified by the muon system (DPTHMU > 3.0).

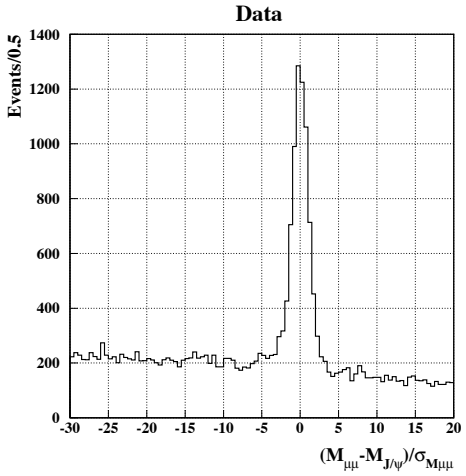

Figure 2.15: Total reconstructed $J/\psi \to mu^+\mu^-$ sample: the sum of three histograms shown in Figures 2.14 and 2.13.

2.4 Calculation of the increase in efficiency

We use normalized mass distributions (Figure 2.16) and define the signal regions to be from -10 to $+3$ for the $J/\psi \to e^+e^-$ and from -4 to $+3$ for the $J/\psi \to \mu^+\mu^-$ candidates. In this study we use full CLEO II dataset and 4.7 fb^{-1} of CLEO II.V $\Upsilon(4S)$ data (4SH-4SS datasets). We find that the detection of the bremsstrahlung photons in the crystal calorimeter improves the $J/\psi \to e^+e^-$ reconstruction efficiency by $(24.4 \pm 0.6)\%$. The corresponding efficiency increase for the simulated events is 24.0%. The efficiency increase equals 17% for CLEO II data and 29% for CLEO II.V data. This difference is expected if we consider that CLEO II.V detector has more material inside the main drift chamber. There is no significant increase in background rate for the $J/\psi \to e^+e^-$ channel. The resulting $J/\psi \to e^+e^-$ reconstruction efficiency, determined without any requirement on the invariant mass, is approximately 67%.

We observe that new selection criteria for muon candidates result in an increase of $(19.9 \pm 0.6)\%$ in the reconstruction efficiency for the $J/\psi \to \mu^+\mu^-$. The corresponding efficiency increase for the simulated events is 21.0%. However, this procedure increases the number of background combinations under $J/\psi \to \mu^+\mu^-$ peak by 80% when the continuum is not subtracted and by 60% with continuum subtraction. Such an increase in the background rate can be tolerated in most analyses presented in this dissertation. The resulting $J/\psi \to \mu^+\mu^-$ reconstruction efficiency, determined without any requirement on the invariant mass, is approximately 59%.

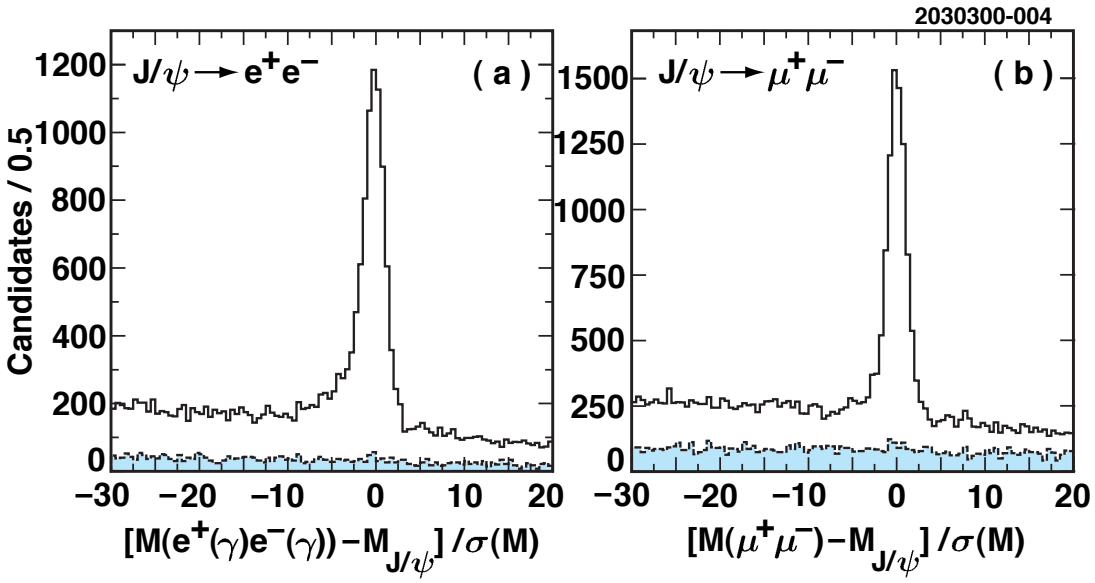

Figure 2.16: Normalized invariant mass of the (a) $J/\psi \to e^+e^-$ and (b) $J/\psi \to \mu^+\mu^-$ candidates in data. The momentum of the J/ψ candidates is required to be less than 2 GeV/c, which is slightly above the maximal J/ψ momentum in $B \to J/\psi\,\pi$ decays. The shaded histogram represents the luminosity-scaled data taken 60 MeV below the $\Upsilon(4S)$ showing the level of background from non-$B\overline{B}$ events. Full CLEO II and CLEO II.V data set was used to produce these plots.

Chapter 3

Study of χ_{c1} and χ_{c2} meson production in B meson decays

3.1 Abstract

Using a sample of 9.7×10^6 $B\overline{B}$ meson pairs, we study B decays to the χ_{c1} and χ_{c2} charmonium states, which are reconstructed via their radiative decays to J/ψ. We first measure the branching fraction for inclusive χ_{c1} production in B decays to be $\mathcal{B}(B \to \chi_{c1}X) = (4.14 \pm 0.31 \pm 0.40) \times 10^{-3}$, where the first uncertainty is statistical and the second one is systematic. We derive the branching fractions for direct χ_{c1} and χ_{c2} production in B decays by subtracting the known contribution of the decay chain $B \to \psi(2S)X$ with $\psi(2S) \to \chi_{c1,2}\gamma$. We obtain $\mathcal{B}[B \to \chi_{c1}(\text{direct})X] = (3.83 \pm 0.31 \pm 0.40) \times 10^{-3}$. No statistically significant signal for χ_{c2} production is observed. Using the Feldman-Cousins approach, we determine the 95% confidence intervals to be $[0.2, 2.0] \times 10^{-3}$ for $\mathcal{B}(B \to \chi_{c2}X)$, $[0.0, 1.7] \times 10^{-3}$ for $\mathcal{B}[B \to \chi_{c2}(\text{direct})X]$, and $[0.00, 0.44]$ for the ratio $\Gamma[B \to \chi_{c2}(\text{direct})X]/\Gamma[B \to \chi_{c1}(\text{direct})X]$. We also measure the branching ratio $\Gamma[B \to \chi_{c2}(\text{direct})X_s]/\Gamma[B \to \chi_{c1}(\text{direct})X_s]$ for different X_s configurations by reconstructing B decays into exclusive final states with J/ψ, γ, a kaon, and up to four pions. For all the X_s configurations we observe a strong χ_{c1} signal yet no statistically significant χ_{c2} signal. We discuss how our results compare with the predictions of different theoretical models of charmonium production.

3.2 Introduction

The recent measurements of charmonium production in various high-energy physics reactions have brought welcome surprises and challenged our understanding both of heavy-quark production and of quarkonium bound state formation. The CDF and D0 measurements [34] of a large production rate for charmonium at high transverse momenta (P_T) were in sharp disagreement with the then-standard color-singlet model. The charmonium production involves physics at both perturbative and nonperturbative energy scales and provides one of the more manageable processes for QCD calculations. Theoretical understanding of the charmonium production is crucial, for example, for the interpretation of

results in the search for quark-gluon plasma, where a particular J/ψ suppression pattern provides the most prominent signal for the onset of deconfinement [35, 36]. Inclusive B decays to charmonia offer another means by which theoretical predictions may be confronted with experimental data. A measurement of the χ_{c2}-to-χ_{c1} production ratio in B decays provides an especially clean test of charmonium production models.

We will now turn to brief discussion of the theoretical frameworks used for the calculations of charmonium production [37].

3.2.1 Color-singlet model

This is indeed only a phenomenological model, and there is no limit in which it reproduces the full QCD calculation [38]. Applied to B decays, the charmonium production mechanism is the decay at short distances of a b quark into a color-singlet $c\overline{c}$ pair plus other quarks and gluons, with the c and $\overline{c}$ produced in an appropriate angular momentum state and with vanishing relative momentum. For example, J/ψ mesons are born only from $c\overline{c}$ pairs in a ${}^3S_1^{(1)}$ state. We use a notation ${}^{2S+1}L_J^{(C)}$, where S, L, and J refer to spin, orbital, and total angular momentum, whereas $C = 1, 8$ refers to a color-singlet or color-octet configurations of the $c\overline{c}$ pair. The $V - A$ current $\overline{c}\gamma_\mu(1-\gamma_5)c$ cannot create a $c\overline{c}$ pair in a ${}^{2S+1}L_J = {}^3P_2$ state [39], therefore the decay $B \to \chi_{c2}X$ is forbidden at leading order in α_s in color-singlet model [40]. The color-singlet model prediction is about a factor of 50 below the observed rate of high-P_T J/ψ and $\psi(2S)$ production at the Tevatron [34]. Also, the color-singlet contribution is thought to be [41] a factor of 5–10 below the observed inclusive J/ψ production rate in B meson decays [28].

3.2.2 Nonrelativistic QCD approach

Non-Relativistic QCD (NRQCD) is an effective field theory approximating full QCD. The development of the NRQCD factorization framework [42] has put the calculations of the inclusive charmonium production onto a rigorous footing. The state-of-the-art NRQCD calculations for B decays to charmonia can be found in [41]. The B decay rate to a particular charmonium state H is expressed as

$$\Gamma(B \to H + X) = \sum_n C(b \to c\overline{c}[n] + x)\langle \mathcal{O}^H[n]\rangle, \tag{3.1}$$

where

$$n \in \{{}^3S_1^{(1,8)},\ {}^1S_0^{(1,8)},\ {}^3P_{0,1,2}^{(1,8)},\ {}^1P_1^{(1,8)},\ \ldots\}.$$

The $C(b \to c\overline{c}[n] + x)$ functions are independent of the charmonium state H and describe the production of a $c\overline{c}$ pair in a state n at short distances. These functions can be calculated perturbatively as an expansion in α_s. The long-distance matrix elements $\langle \mathcal{O}^H[n]\rangle$ describe the probabilities for a $c\overline{c}$ pair in the state n to bind into the meson H. These matrix elements cannot be calculated perturbatively, but they are independent of a particular charmonium production process, therefore one can relate Tevatron, HERA, and CLEO data. The matrix elements $\langle \mathcal{O}^H[n]\rangle$ are arranged according to their order in v, the typical relative velocity of the c and $\overline{c}$ quarks within the bound state H. Therefore Equation 3.1 is a double expansion in v^2 and α_s. The color-singlet model is recovered from Equation 3.1 by dropping all the

terms except one color-singlet term. For example, the only surviving contribution to J/ψ production is from $c\overline{c}$ pairs produced in ${}^3S_1^{(1)}$ configuration. The leading order (LO) in α_s calculations of $C(b \to c\overline{c}[n] + x)$ functions for $B \to \chi_{cJ}X$ decays may be found in [43]; the relative χ_{c2} and χ_{c1} production rates are estimated to be $\chi_{c1} : \chi_{c2} \approx 1 : 1.3$. The next-to-leading-order (NLO) calculations can be found in [41]. The authors of [41] argue that NLO calculation of the color-singlet contribution to χ_{c1} production is unreliable, therefore the NRQCD calculations cannot yet produce sharp quantitative predictions for the χ_{c2}-to-χ_{c1} production ratio in B decays. We can, however, consider two limiting cases. If the color-octet mechanism dominates in $B \to \chi_{cJ}X$ decays, then the χ_{c2}-to-χ_{c1} production ratio should be 5:3 because the color-octet contribution is proportional to $2J + 1$. On the contrary, if the color-singlet contribution dominates, then χ_{c2} production should be strongly suppressed relative to χ_{c1} production. The NRQCD calculations are able to account for the observed high-P_T charmonium production cross sections by including the color-octet production mechanisms. A serious problem for NRQCD is the recent CDF measurement of the J/ψ and $\psi(2S)$ polarization [44]. NRQCD predicts that high-P_T J/ψ and $\psi(2S)$ should be dominantly transversely polarized, and this polarization should increase with P_T [38], whereas CDF observes no significant polarization.

3.2.3 Color-evaporation model

In this model, color is effectively ignored with the reasoning that the exchange and emission of soft gluons destroys any correlation between the color and the spin state of the $c\overline{c}$ pair and the observed charmonium hadron. The color-evaporation model differs from the NRQCD approach [42] in its treatment of the color exchange between the $c\overline{c}$ pair and the underlying event. In NRQCD formalism, multiple gluon exchanges with the $c\overline{c}$ pair are suppressed by powers of v, whereas the color-evaporation model assumes that these low-energy interactions can take place through multiple soft-gluon exchanges [45]. The color-evaporation model accommodates high-P_T charmonium production at the Tevatron [45] and predicts an absence of polarization in agreement with the CDF measurement [44]. The model predicts the $B \to \chi_{c1,2}X$ rate to be proportional to $2J + 1$, and therefore the χ_{c2}-to-χ_{c1} production ratio to be $5 : 3$ [46].

3.3 Analysis summary and results

We use 9.2 fb^{-1} of e^+e^- data taken at the $\Upsilon(4S)$ resonance and 4.6 fb^{-1} taken 60 MeV below the $\Upsilon(4S)$ resonance (off-$\Upsilon(4S)$ sample). We reconstruct the $\chi_{c1,2}$ radiative decays to J/ψ. The branching fractions for the $\chi_{c1,2} \to J/\psi\,\gamma$ decays are, respectively, $(27.3 \pm 1.6)\%$ and $(13.5 \pm 1.1)\%$, whereas the branching fraction for the $\chi_{c0} \to J/\psi\,\gamma$ decay is only $(0.66 \pm 0.18)\%$ [48]. In addition, the χ_{c0} production rate in B decays is expected to be smaller than the $\chi_{c1,2}$ rates [41, 43]. We therefore do not attempt to measure χ_{c0} production in this analysis. We require the normalized mass to be between -6 and $+3$ for the $J/\psi \to e^+e^-$ candidates and between -4 and $+3$ for the $J/\psi \to \mu^+\mu^-$ candidates (Figure 2.16). The momentum of the J/ψ candidates is required to be less than 2 GeV/c, which is slightly above the maximal J/ψ momentum in B decays.

Photon candidates for $\chi_{c1,2} \to J/\psi\,\gamma$ reconstruction must be detected in the central angular region of the calorimeter ($|\cos\theta_\gamma| < 0.71$), where our detector has the best energy resolution. Most of the photons in $\Upsilon(4S) \to B\overline{B}$ events come from π^0 decays. We therefore discard those photon candidates which, when paired with another γ in the event, produce a normalized $\pi^0 \to \gamma\gamma$ mass between -3 and $+2$ (Section 3.4.1).

3.3.1 Analysis of inclusive $B \to \chi_{c1,2}X$ decays

In the first part of this work, called the inclusive analysis, we investigate $B \to \chi_{c1,2}X$ decays reconstructing only the J/ψ and the γ.

Fit procedure

We determine the χ_{c1} and χ_{c2} yields in a binned maximum-likelihood fit to the distribution of the mass difference $M(J/\psi\gamma) - M(J/\psi)$ (Figure 3.1a), where $M(J/\psi)$ is the measured mass of a J/ψ candidate. The excellent electromagnetic calorimeter allows us to resolve the χ_{c1} and χ_{c2} peaks. The $M(J/\psi\gamma) - M(J/\psi)$ mass-difference resolution is 8 MeV/c^2 and is dominated by the resolution of photon energy. The bin width in the fit is 1 MeV/c^2. The χ_{c1} and χ_{c2} signal shapes are fit with templates extracted from the Monte Carlo simulation (Section 3.4.2); only the template normalizations are free in the fit. The background in the fit is approximated by a 5th-order Chebyshev polynomial, chosen as the minimal-order polynomial that fits the background well in the "35 times the data" sample of simulated $\Upsilon(4S) \to B\overline{B}$ events. All the polynomial coefficients are allowed to float in the fit. The χ_{c1} and χ_{c2} signal yields in the $\Upsilon(4S)$ data are $N^{\rm ON}(\chi_{c1}) = 672 \pm 47(\text{stat})$ and $N^{\rm ON}(\chi_{c2}) = 83 \pm 37(\text{stat})$. The maximum-likelihood fit is discussed in more detail in Section 3.4.3. Goodness-of-fit tests are discussed in Section 3.4.4. The χ_{c1} and χ_{c2} yields in off-$\Upsilon(4S)$ data are both consistent with zero: $N^{\rm OFF}(\chi_{c1}) = 4 \pm 7(\text{stat})$ and $N^{\rm OFF}(\chi_{c2}) = 1 \pm 7(\text{stat})$ (Section 3.4.5). Subtracting the contributions from non-$B\overline{B}$ continuum events, we obtain the total inclusive $B \to \chi_{c1}X$ and $B \to \chi_{c2}X$ event yields $N(B \to \chi_{c1}X) = 664 \pm 49(\text{stat})$ and $N(B \to \chi_{c2}X) = 81 \pm 39(\text{stat})$.

χ_{c2} signal significance

Taking into account the systematic uncertainties associated with the fit, we determine the $B \to \chi_{c2}X$ signal yield significance to be 2.0 standard deviations (σ). The significance is defined in the Gaussian approximation by dividing the signal mean by the associated uncertainty. The uncertainty in χ_{c2} yield is dominated by the statistical uncertainty of the fit (Figure 3.1). This statistical uncertainty quantifies a possible background fluctuation. The number of background events is large, therefore a Gaussian is a good approximation for the number of observed χ_{c2} events. Subtracting the known contribution of the decay chain $B \to \psi(2S)X$ with $\psi(2S) \to \chi_{c2}\gamma$ and accounting for the associated systematic uncertainty, we likewise determine the significance of the evidence for the decay $B \to \chi_{c2}(\text{direct})X$ to be only 1.4σ (Section 3.4.8).

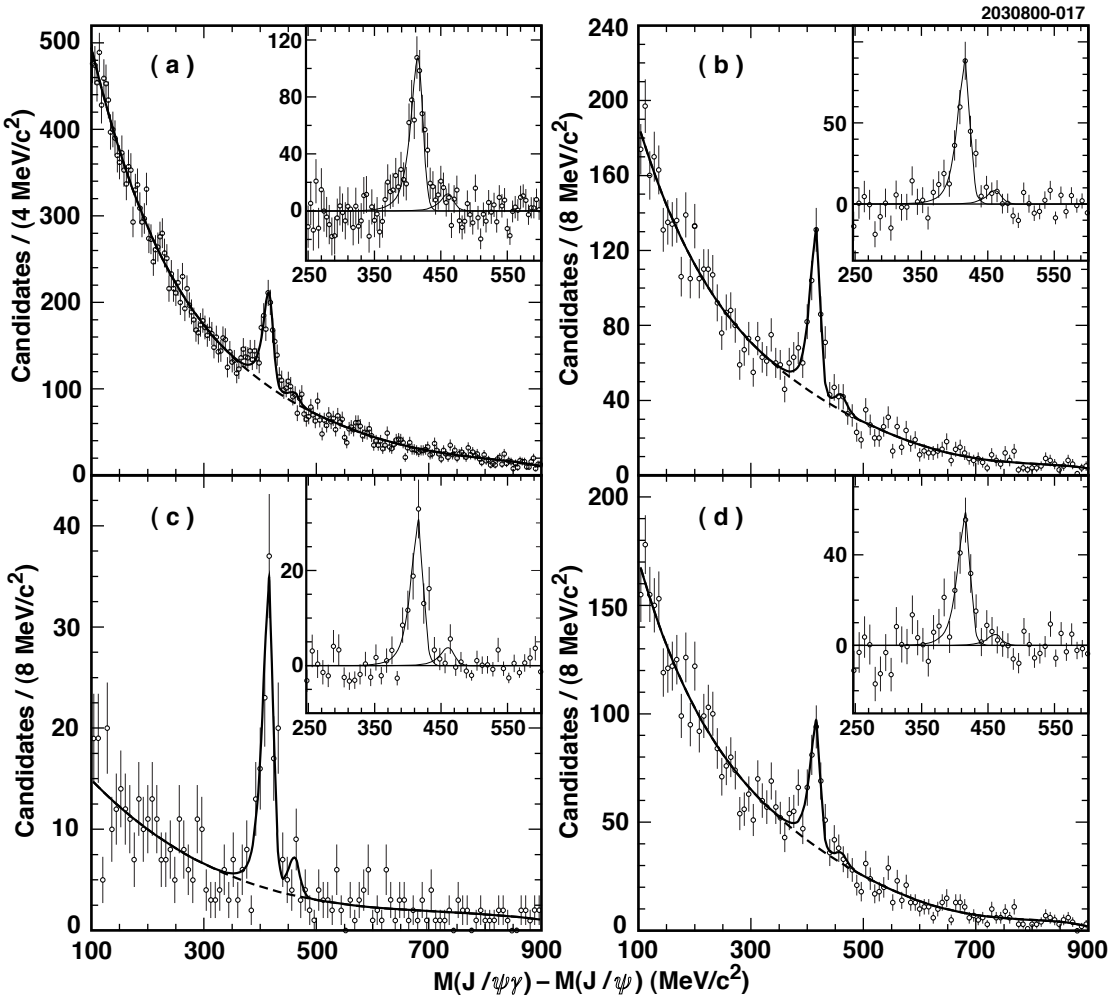

Figure 3.1: The $M(J/\psi\gamma) - M(J/\psi)$ distribution in the $\Upsilon(4S)$ data (points with error bars). Plot (a) is for inclusive $J/\psi\gamma$ combinations, whereas plots (b), (c), and (d) are for those $J/\psi\gamma$ combinations that reconstruct to a $B \to J/\psi\gamma X_s$ decay with the X_s composition corresponding to samples A, B, and C described in the text. The fit function is shown by a solid line with the background component represented by a dashed line. The insets show the background-subtracted distributions with the χ_{c1} and χ_{c2} fit components represented by a solid line.

Calculation of branching fractions

To calculate the branching fractions $\mathcal{B}(B \to \chi_{c1,2}X)$, we use the measured signal yields $N(B \to \chi_{c1,2}X)$, the reconstruction efficiencies, the number of produced $B\overline{B}$ pairs, and the daughter branching fractions. The reconstruction efficiencies, determined from the simulation, are (25.7±0.2)% for χ_{c1} and (26.6±0.2)% for χ_{c2} (Section 3.4.6). The efficiencies do not include daughter branching fractions, and the quoted uncertainties are due to the size of our $B \to \chi_{c1,2}X$ simulation samples. For the calculation of the rates for the decays $B \to \chi_{c1,2}(\text{direct})X$, we make an assumption that the only other source of $\chi_{c1,2}$ production in B decays is the decay chain $B \to \psi(2S)X$ with $\psi(2S) \to \chi_{c1,2}\gamma$. The 95% confidence intervals are calculated using the Feldman-Cousins approach [49]. The resulting branching fractions are listed in Table 3.1. More details on the calculation of $\mathcal{B}(B \to \chi_{c1,2}(\text{direct})X)$ are given in Sections 3.4.7 and 3.4.8. Taking into account correlations between the uncertainties, we obtain the branching ratio $\Gamma[B \to \chi_{c2}(\text{direct})X]/\Gamma[B \to \chi_{c1}(\text{direct})X] = 0.18 \pm 0.13 \pm 0.04$; the 95% C.L. upper limit on the ratio is 0.44 (Section 3.4.9). The assumed value of the ratio $\mathcal{B}(\chi_{c1} \to J/\psi\gamma)/\mathcal{B}(\chi_{c2} \to J/\psi\gamma)$ is discussed in Section 3.4.10.

Table 3.1: Branching fractions for inclusive B decays to χ_{c1} and χ_{c2}.

Branching fraction or ratio	Measured value	95% confidence interval [49]
$\mathcal{B}(B \to \chi_{c1}X)$	$(4.14 \pm 0.31 \pm 0.40) \times 10^{-3}$	—
$\mathcal{B}[B \to \chi_{c1}(\text{direct})X]$	$(3.83 \pm 0.31 \pm 0.40) \times 10^{-3}$	—
$\mathcal{B}(B \to \chi_{c2}X)$	$(0.98 \pm 0.48 \pm 0.15) \times 10^{-3}$	$[0.2; 2.0] \times 10^{-3}$
$\mathcal{B}[B \to \chi_{c2}(\text{direct})X]$	$(0.71 \pm 0.48 \pm 0.16) \times 10^{-3}$	$[0.0; 1.7] \times 10^{-3}$
$\frac{\Gamma[B \to \chi_{c2}(\text{direct})X]}{\Gamma[B \to \chi_{c1}(\text{direct})X]}$	$0.18 \pm 0.13 \pm 0.04$	$[0.0; 0.44]$

3.3.2 Systematic uncertainties in the inclusive analysis

The systematic uncertainties are listed in Table 3.2. The sources of the uncertainty can be grouped into three categories:

Fit procedure.— This category includes the uncertainties due to our choice of the signal and background shapes as well as the bin size. To fit the χ_{c1} and χ_{c2} signal, we use the templates extracted from the simulation. We therefore are sensitive to imperfections in the simulation of the photon energy measurement. The systematic uncertainties associated with the simulation of the calorimeter response are estimated by comparing the $\pi^0 \to \gamma\gamma$ invariant mass lineshapes for inclusive π^0 candidates in the data and in the simulated event samples (Appendix A). Then the χ_{c1} and χ_{c2} signal shape templates are modified accordingly in order to determine the resulting uncertainty in the signal yields. To estimate the uncertainty associated with the calorimeter energy scale, we shift the χ_{c1} and χ_{c2} templates in the fit by ± 0.6 MeV/c^2. The uncertainty due to time-dependent variations of the calorimeter energy scale is small compared to the overall energy scale uncertainty. To estimate the uncertainty due to the calorimeter energy resolution, we change the width of the χ_{c1} and χ_{c2} templates by ±4%. The uncertainty in the background shape is probed by fitting the background with a template extracted from high-statistics samples of simulated $\Upsilon(4S) \to B\overline{B}$ and non-$B\overline{B}$

continuum events; only the template normalization, not its shape, is allowed to float in the fit. The systematic uncertainties associated with the fit procedure are discussed in more detail in Sections 3.4.11, 3.4.12, and 3.4.13.

Efficiency calculation.— This category includes the uncertainties in the number of produced $B\overline{B}$ pairs, tracking efficiency, photon detection efficiency, lepton detection efficiency, and model-dependence and statistical uncertainty of the $B \to \chi_{c1,2}X$ simulation. The $\chi_{c1,2}$ polarization affects the photon energy spectrum. We define the helicity angle θ_h to be the angle between the γ direction in the χ_c rest frame and the χ_c direction in the B frame. We assume a flat $\cos\theta_h$ distribution in our simulation. The systematic uncertainty associated with this assumption is estimated by comparing the reconstruction efficiencies in the simulated event samples with $I(\theta_h) \propto \sin^2\theta_h$ and $I(\theta_h) \propto \cos^2\theta_h$ angular distributions (Section 3.4.14). Parity is conserved in the decays $\chi_{c1,2} \to J/\psi\gamma$, so the helicity angle distribution contains only even powers of $\cos\theta_h$. Another source of uncertainty is our modeling of the X system in the $B \to \chi_{c1,2}X$ simulation. Photon detection efficiency depends on the assumed model through the χ_c momentum spectrum and the π^0 multiplicity of the final state. In our simulation, we assume that X is either a single K or one of the higher K resonances; we also include the decay chain $B \to \psi(2S)X$ with $\psi(2S) \to \chi_{c1,2}\gamma$. To estimate the systematic uncertainty, we compare the $\chi_c \to J/\psi\gamma$ detection efficiency extracted using this sample with the efficiency in the sample where we assume that X is either a $K^\pm$ or $K^0_S \to \pi^+\pi^-$ (Section 3.4.15). A cross-check for the π^0 veto is described in Section 3.4.16.

Assumed branching fractions.— This category includes the uncertainties on the various branching fractions assumed in our calculations. We use the following values of the branching fractions for the secondary decays: $\mathcal{B}(J/\psi \to \ell^+\ell^-) = (5.894 \pm 0.086)\%$ [50], $\mathcal{B}(\chi_{c1} \to J/\psi\gamma) = (27.3 \pm 1.6)\%$ [48], and $\mathcal{B}(\chi_{c2} \to J/\psi\gamma) = (13.5 \pm 1.1)\%$ [48]. In the calculation of $\mathcal{B}[B \to \chi_{c1,2}(\text{direct})X]$, we also assume the following values: $\mathcal{B}(B \to \psi(2S)X) = (3.5 \pm 0.5) \times 10^{-3}$ [48], $\mathcal{B}(\psi(2S) \to \chi_{c1}\gamma) = (8.7 \pm 0.8)\%$ [48], and $\mathcal{B}(\psi(2S) \to \chi_{c2}\gamma) = (7.8 \pm 0.8)\%$ [48].

3.3.3 Analysis of $B \to \chi_{c1,2}X_s$ with X_s reconstruction

So far we have studied inclusive $B \to \chi_{c1,2}X$ decays by reconstructing only J/ψ and γ. Thus obtained branching fraction measurements are model-independent. The lack of knowledge about the X system composition and about the polarization of the $\chi_{c1,2}$ mesons very mildly affects the results and is reflected in the systematic uncertainty.

B-reconstruction technique

In the second part of this work, called the B-reconstruction analysis, we employ the B-reconstruction technique similar to the one developed for the $b \to s\gamma$ rate measurement [51]. This technique has also been successfully applied to the $B \to \eta' X_s$ analysis [52]. We still extract χ_{c1} and χ_{c2} signal yields from a fit to $M(J/\psi\gamma) - M(J/\psi)$ distribution, but we select only those $J/\psi\gamma$ combinations that reconstruct to a $B \to J/\psi\gamma X_s$ decay. This B-reconstruction technique is used to suppress backgrounds and allows us to probe the composition of the X_s system accompanying $\chi_{c1,2}$ mesons. The reconstruction efficiency,

Table 3.2: Systematic uncertainties on $\mathcal{B}(B \to \chi_{c1,2}X)$. The uncertainties from $\mathcal{B}(B \to \psi(2S)X)$ and $\mathcal{B}(\psi(2S) \to \chi_{c1,2}\gamma)$ are given relative to $\mathcal{B}[B \to \chi_{c1,2}(\text{direct})X]$.

Source of	relative uncertainty in %	
systematic uncertainty	$\mathcal{B}(B \to \chi_{c1}X)$	$\mathcal{B}(B \to \chi_{c2}X)$
Fit procedure		
γ energy scale	0.4	5.6
γ energy resolution	2.8	6.9
Background shape	1.8	6.8
Bin size	0.0	1.9
Efficiency calculation		
$N(B\overline{B})$	2.0	2.0
Tracking efficiency	2.0	2.0
Lepton identification	4.2	4.2
Photon finding	2.5	2.5
Monte Carlo statistics	0.7	0.7
Model for X in $B \to \chi_{c1,2}X$	3.3	3.3
Polarization of $\chi_{c1,2}$	1.0	1.0
Assumed branching fractions		
$\mathcal{B}(\chi_{c1,2} \to J/\psi\gamma)$	5.9	8.1
$\mathcal{B}(J/\psi \to \ell^+\ell^-)$	1.5	1.5
$\mathcal{B}(B \to \psi(2S)X)$	1.1	5.5
$\mathcal{B}(\psi(2S) \to \chi_{c1,2}\gamma)$	0.7	4.0

however, becomes strongly model-dependent. We therefore measure the branching ratio $\Gamma(B \to \chi_{c2}[\text{direct}]X_s)/\Gamma(B \to \chi_{c1}[\text{direct}]X_s)$ with an explicit assumption that the X_s system is the same for χ_{c1} and χ_{c2} production. This assumption is crucial. If, for example, χ_{c1} is preferentially accompanied by a single K or K^* and χ_{c2} is accompanied by a kaon with 5 pions, then our χ_{c1} and χ_{c2} reconstruction efficiencies will be very different.

We extract the branching ratio $\mathcal{R}(\chi_{c2}/\chi_{c1}) \equiv \Gamma[B \to \chi_{c2}(\text{direct})X_s]/\Gamma[B \to \chi_{c1}(\text{direct})X_s]$ for the following three X_s configurations:

1. *Sample A.*— X_s is reconstructed as a kaon (K^+ or $K^0_S \to \pi^+\pi^-$) with 0 to 4 pions, one of which can be a π^0. We consider 21 possible X_s modes (Table 3.3) as well as the charge conjugates of these modes.

2. *Sample B.*— X_s is reconstructed as a single kaon or $K^*(892)$. A $K\pi$ combination is a K^* candidate if $|M(K\pi) - M_{K^*}| < 75$ MeV/c^2, where M_{K^*} is the world average $K^*(892)$ mass.

3. *Sample C.*— X_s is reconstructed as a kaon with 1 to 4 pions, but not as a $K^*(892)$ candidate ($|M(K\pi) - M_{K^*}| > 200$ MeV/c^2).

Thus samples B and C are subsets of A. To an excellent approximation, sample A is a sum of B and C. With sample A we try to reconstruct as many $B \to J/\psi\gamma X_s$ decays as possible. Dividing sample A into subsamples B and C, we also probe the dynamics of the $B \to \chi_{c1,2}X_s$ decays. If the dominant production mechanisms for χ_{c1} and χ_{c2} are

Table 3.3: The X_s modes for $B \to J/\psi\gamma X_s$ reconstruction. The charge-conjugated modes are also used.

Number of pions	X_s reconstruction modes	
	with K^+	with K^0_S
0	K^+	K^0_S
1	$K^+\pi^0$	$K^0_S\pi^0$
	$K^+\pi^-$	$K^0_S\pi^-$
2	$K^+\pi^+\pi^-$	$K^0_S\pi^+\pi^-$
	$K^+\pi^-\pi^0$	$K^0_S\pi^-\pi^0$
	$K^+\pi^-\pi^-$	
3	$K^+\pi^+\pi^-\pi^0$	$K^0_S\pi^+\pi^-\pi^0$
	$K^+\pi^+\pi^-\pi^-$	$K^0_S\pi^+\pi^-\pi^-$
	$K^+\pi^-\pi^-\pi^0$	
4	$K^+\pi^+\pi^-\pi^+\pi^-$	$K^0_S\pi^+\pi^-\pi^+\pi^-$
	$K^+\pi^+\pi^-\pi^-\pi^0$	$K^0_S\pi^+\pi^-\pi^-\pi^0$
	$K^+\pi^+\pi^-\pi^-\pi^-$	

different — color-singlet mechanism for χ_{c1} and color-octet for χ_{c2} — then it is natural to expect that χ_{c2}, in comparison with χ_{c1}, is more often accompanied by multi-body X_s states rather than a single K or K^*. Thus the measured χ_{c2}-to-χ_{c1} production ratio might be quite different for samples B and C.

We require that the charged kaon and pion candidates have, if available, dE/dx and time-of-flight measurements that lie within 3σ of the expected values. The dE/dx measurement is required for kaons, but used only if available for pions. The time-of-flight measurement is used only if available. The $K^0_S \to \pi^+\pi^-$ candidates are selected from pairs of tracks forming displaced vertices. We require the absolute value of the normalized $K^0_S \to \pi^+\pi^-$ mass to be less than 4 and perform a fit [107] constraining the mass of each K^0_S candidate to the world average value. Photon candidates for $\pi^0 \to \gamma\gamma$ decays are required to have an energy of at least 30 MeV in the barrel and at least 50 MeV in the endcap region ($0.71 < |\cos\theta_\gamma| < 0.95$) of the calorimeter. We require the absolute value of the normalized $\pi^0 \to \gamma\gamma$ mass to be less than 3 and perform a fit constraining the mass of each π^0 candidate to the world average value. The J/ψ four-momentum used in $B \to J/\psi\gamma X_s$ reconstruction is obtained by performing a fit constraining the J/ψ candidate mass to the world average value.

To select B candidates, we require $|\Delta E|/\sigma(\Delta E) < 3$ and $|M(B) - M_B|/\sigma(M) < 3$. The average ΔE resolution varies from 12 to 17 MeV depending on the B-reconstruction mode. The average $M(B)$ resolution is 2.7 MeV/c^2 and is dominated by the beam energy spread.

A check of the B-reconstruction technique, with simulated events, is described in Section 3.5.1.

Measurement of $\Gamma(B \to \chi_{c2}[\text{direct}]X_s)/\Gamma(B \to \chi_{c1}[\text{direct}]X_s)$

The fit to $M(J/\psi\gamma) - M(J/\psi)$ distribution is then performed in the same manner as in the inclusive analysis. We still use a 5th order Chebyshev polynomial to fit the background for samples A and C, but we reduce the order of the polynomial to 3 for the low-statistics sample B. The fits are shown in Figure 3.1 and the χ_{c1} and χ_{c2} signal yields are listed in Table 3.4. When we compare the inclusive analysis (Section 3.3.1) to the B-reconstruction analysis, we obtain that for Sample A the B-reconstruction technique reduces background by a factor of 5.2 for the price of reducing the signal efficiency by a factor of 2.3 (compare plots (a) and (b) in Figure 3.1). Goodness-of-fit tests are discussed in Section 3.5.2. The B-reconstruction technique renders negligible the contribution from non-$B\overline{B}$ continuum events (Section 3.5.3). We finally subtract the $\psi(2S) \to \chi_{c1,2}\gamma$ feeddown to obtain the rates for direct $\chi_{c1,2}$ production in B decays. For all three X_s configurations, we observe a strong χ_{c1} signal yet no statistically significant signal for direct χ_{c2} production (see Table 3.4 and Section 3.5.4 for more details). To calculate the branching ratio $\mathcal{R}(\chi_{c2}/\chi_{c1})$, we multiply the ratio of the feeddown-corrected $\chi_{c1,2}$ yields by the reconstruction efficiency ratio $\mathcal{E}(\chi_{c1})/\mathcal{E}(\chi_{c2})$ and by the branching ratio $\mathcal{B}(\chi_{c1} \to J/\psi\gamma)/\mathcal{B}(\chi_{c2} \to J/\psi\gamma)$. The efficiency of the B-reconstruction depends on the composition of the X_s system. We assume that the X_s system composition is the same for χ_{c1} and χ_{c2} production. From our simulation we determine $\mathcal{E}(\chi_{c1})/\mathcal{E}(\chi_{c2}) \simeq 0.93$ for all three X_s configurations. The resulting χ_{c2}-to-χ_{c1} production ratios are listed in Table 3.4. The production ratio calculations are discussed in more detail in Section 3.5.5.

Table 3.4: Results for each of the three X_s configurations used in reconstruction of the $B \to J/\psi\gamma X_s$. The χ_{c1} and χ_{c2} event yields with associated statistical uncertainties are listed in lines 1 and 2. Line 3 contains the significance of the $B \to \chi_{c2}(\text{direct})X_s$ signal with statistical and systematic uncertainties taken into account. Lines 4 and 5 contain the measured value and 95% confidence interval for the branching ratio $\mathcal{R}(\chi_{c2}/\chi_{c1}) \equiv \Gamma[B \to \chi_{c2}(\text{direct})X_s]/\Gamma[B \to \chi_{c1}(\text{direct})X_s]$, determined with an assumption that the X_s system composition is the same for χ_{c1} and χ_{c2} production.

	Sample A	Sample B	Sample C
$N(B \to \chi_{c1}X_s)$	279 ± 25	96 ± 12	183 ± 22
$N(B \to \chi_{c2}X_s)$	31^{+18}_{-17}	$13.9^{+7.0}_{-6.2}$	18 ± 16
Signif. of $B \to \chi_{c2}(\text{direct})X_s$	1.2σ	2.0σ	0.6σ
$\mathcal{R}(\chi_{c2}/\chi_{c1})$	$0.18 \pm 0.12 \pm 0.09$	$0.27^{+0.15}_{-0.13} \pm 0.05$	$0.14 \pm 0.18 \pm 0.14$
$\mathcal{R}(\chi_{c2}/\chi_{c1})$ 95% C.L. interval	$[0.00, 0.48]$	$[0.04, 0.58]$	$[0.00, 0.59]$

3.3.4 Systematic uncertainties in the B-reconstruction analysis

The systematic uncertainties for the B-reconstruction analysis are listed in Table 3.5. Many uncertainties are correlated; we therefore use Monte Carlo methods to properly take into account such correlations when we estimate the uncertainty on the ratio $\Gamma(B \to \chi_{c2}[\text{direct}]X_s)/\Gamma(B \to \chi_{c1}[\text{direct}]X_s)$. The sources of uncertainty can be grouped into the following four categories:

Fit procedure.— As in the inclusive analysis, we estimate the uncertainties in the signal and background shapes. We shift the $\chi_{c1,2}$ templates by ± 0.6 MeV/c^2 and vary their widths by $\pm 4\%$. The requirement on ΔE in $B \to J/\psi\gamma X_s$ reconstruction truncates the low-side tail of the $\chi_{c1,2}$ shapes. We estimate the uncertainty due to this effect by using the $\chi_{c1,2}$ templates obtained from the simulation with a requirement that the measured χ_c energy is within 3σ of the generated value. The uncertainty in the background shape dominates the fit procedure uncertainty. To probe this uncertainty, we fit the background with different templates, allowing only the template normalization, not its shape, to float in the fit. One template is extracted from simulation separately for each of the samples A, B, and C. Another template — the same for all three X_s configurations — is the background shape from the inclusive analysis (Figure 3.1a). The systematic uncertainties associated with the fit procedure are discussed in more detail in Sections 3.5.6 and 3.5.7.

$\psi(2S)$ subtraction.— The sources of the systematic uncertainty associated with the $\psi(2S)$-feeddown subtraction include $\mathcal{B}(B \to \psi(2S)X)$, $\mathcal{B}(\psi(2S) \to \chi_{c1,2}\gamma)$, the size of our $B \to \psi(2S)X$ simulation sample, and the composition of X in $B \to \psi(2S)X$ decays. To estimate the uncertainty due to our model of the X system composition in the $B \to \psi(2S)X$ simulation, we check whether the data and the simulation agree on the ratio of $\psi(2S) \to \ell^+\ell^-$ event yields obtained in the inclusive reconstruction and after the $B \to \psi(2S)X_s$ reconstruction (Section 3.5.8). This systematics category also includes the uncertainties that would have canceled for the ratio $\mathcal{R}(\chi_{c2}/\chi_{c1})$ were it not for the $\psi(2S)$-feeddown subtraction. These sources of uncertainty are $\mathcal{B}(J/\psi \to \ell^+\ell^-)$, $N(B\overline{B})$, tracking, photon finding, and lepton identification.

$\mathcal{E}(\chi_{c2})/\mathcal{E}(\chi_{c1})$.— We assume that the X_s system in $B \to \chi_{c1,2}X_s$ is the same for χ_{c1} and χ_{c2}. We do not assign any uncertainty for this assumption. The remaining sources of uncertainty are the $\chi_{c1,2}$ polarization and the statistics of the $B \to \chi_{c1,2}X_s$ simulation samples.

$\mathcal{B}(\chi_{c1,2} \to J/\psi\gamma)$.— Our measurement depends on the ratio $\mathcal{B}(\chi_{c1} \to J/\psi\gamma)/\mathcal{B}(\chi_{c2} \to J/\psi\gamma)$ and its uncertainty.

Table 3.5: The absolute systematic uncertainties on the branching ratio $\mathcal{R}(\chi_{c2}/\chi_{c1})$ for each of the three X_s configurations used in $B \to J/\psi\gamma X_s$ reconstruction.

	uncertainty on $\mathcal{R}(\chi_{c2}/\chi_{c1})$		
Source of uncertainty	Sample A	Sample B	Sample C
Fit procedure	0.084	0.039	0.142
$\psi(2S)$ subtraction	0.007	0.001	0.006
$\mathcal{E}(\chi_{c1})/\mathcal{E}(\chi_{c2})$	0.003	0.006	0.003
$\mathcal{B}(\chi_{c1,2} \to J/\psi\gamma)$	0.022	0.026	0.019
Added in quadrature	0.09	0.05	0.14

3.3.5 Discussion of results

In conclusion, we have measured the branching fractions for inclusive B decays to the χ_{c1} and χ_{c2} charmonium states. The resulting branching fractions are listed in Table 3.1. We have also studied $B \to \chi_{c1,2} X_s$ decays, reconstructing X_s as a kaon and up to four pions. In this way, we have measured the branching ratio $\Gamma[B \to \chi_{c2}(\text{direct}) X_s]/\Gamma[B \to \chi_{c1}(\text{direct}) X_s]$ for three X_s configurations. The branching ratios measured in this study are listed in Table 3.4. In all the cases, we observe strong χ_{c1} signal yet no statistically significant signal for χ_{c2} production. We will briefly discuss the implications of our measurement of the χ_{c2}-to-χ_{c1} production ratio for the theoretical frameworks described in Section 3.2.

Color-singlet model (CSM).— CSM predicts the χ_{c2}-to-χ_{c1} production ratio to be $0:1$ [40], which agrees well with our measurement. CSM, however, fails to explain high-P_T charmonium production rate at the Tevatron [34] and underestimates the $B \to J/\psi X$ decay rate by a factor of $5-10$ [41].

Color-evaporation model (CEM).— CEM accommodates high-P_T charmonium production rate [34, 45] and polarization [44] measurements at the Tevatron. It predicts the χ_{c2}-to-χ_{c1} production ratio in B decays of $5:3$ [46]. Such a high rate of χ_{c2} production is confidently ruled out by our measurement.

NRQCD formalism.— The high-P_T charmonium production rate at the Tevatron is now well understood in the NRQCD formalism. The recent CDF measurement of charmonium polarization [44], however, appears to disagree with the NRQCD prediction. More theoretical work is needed to calculate the short-distance coefficient for color-singlet contribution to $B \to \chi_{c1} X$ decay [41]. If the color-octet mechanism dominates in $B \to \chi_{cJ} X$ decays, then the χ_{c2}-to-χ_{c1} production ratio should be 5:3 because the color-octet contribution is proportional to $2J+1$. In contrast, if the color-singlet contribution dominates, then χ_{c2} production should be strongly suppressed relative to χ_{c1} production. Our measurement suggests that the color-octet mechanism does not dominate in $B \to \chi_c X$ decays.

3.4 More details on the analysis of inclusive $B \to \chi_{c1,2} X$ decays

3.4.1 π^0 veto

A photon from the decay $\chi_{c1} \to J/\psi\gamma$ has an energy between 250 and 600 MeV (Figure 3.9). Most of the photons in B meson decays come from π^0's. In order to reduce background, we therefore do not use a photon if it can be paired with another photon to produce an invariant mass in the π^0 region ($-3 < [M(\gamma\gamma) - M_{\pi^0}]/\sigma(M) < 2$). Figure 3.2 shows the π^0 candidates we veto. Figure 3.3 shows the $M(J/\psi\gamma) - M(J/\psi)$ distribution for all the candidates in $\Upsilon(4S)$ data with no π^0 veto applied and for the vetoed candidates.

3.4.2 χ_{c1} and χ_{c2} signal shapes

We generated the samples of the simulated $B \to \chi_{c1} X_s$ and $B \to \chi_{c2} X_s$ decays with 285,000 events in each sample. We forced $\chi_{c1,2} \to J/\psi\gamma$, $J/\psi \to \ell^+\ell^-(\gamma)$ decay

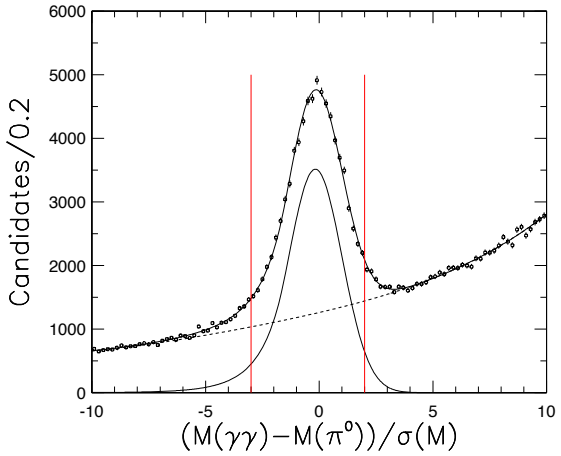

Figure 3.2: Normalized π^0 mass distribution for the π^0's that we veto in our selection of isolated photons used in $\chi_{c1,2} \to J/\psi\gamma$ reconstruction. To produce this plot, we require that at least one photon in a pair is detected in the good barrel region and has an energy between 300 and 600 MeV. Veto region $(-3; +2)$ is marked by vertical lines. A fit to a polynomial and a Crystal Ball lineshape (Appendix A.2) is shown by the solid line.

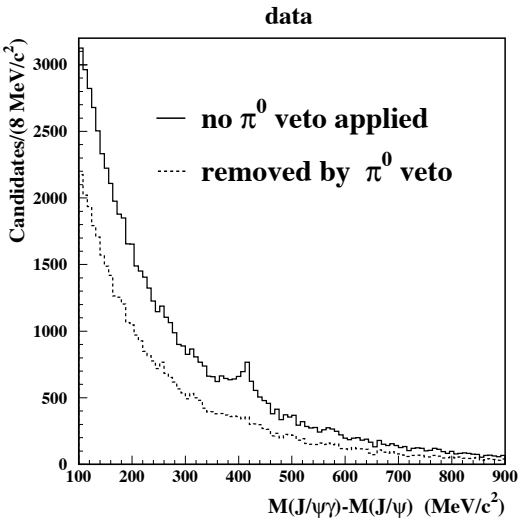

Figure 3.3: The $M(J/\psi\gamma) - M(J/\psi)$ distribution for all the candidates with no π^0 veto applied (solid line) and for the candidates removed by π^0 veto (dashed line).

sequence, whereas all the other particles in the event were forced to decay into neutrinos. The $M(J/\psi\gamma) - M(J/\psi)$ distributions for the χ_{c1} and χ_{c2} candidates reconstructed in these Monte Carlo samples are shown in Figure 3.4. Both χ_{c1} and χ_{c2} peaks were shifted by -0.6 MeV/c^2 to correct for the calorimeter energy scale difference between the data and the Monte Carlo simulation, which was observed in our π^0 study (Appendix A). Thus obtained χ_{c1} and χ_{c2} histograms are smoothed and used as templates to fit the data and the Monte Carlo samples. In fits to the Monte Carlo samples the -0.6 MeV correction to the peak positions is not applied.

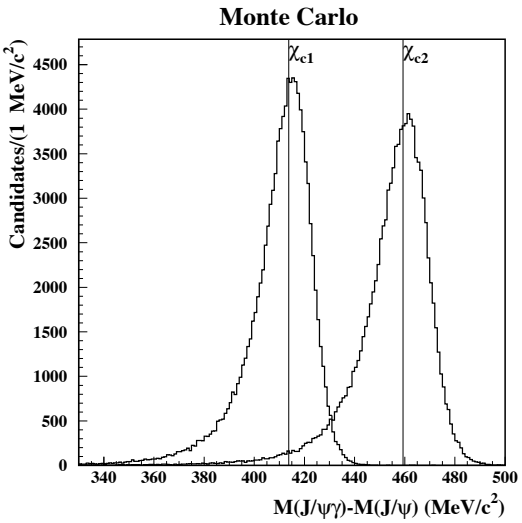

Figure 3.4: The $M(J/\psi\gamma) - M(J/\psi)$ distributions for $\chi_{c1,2}$ candidates reconstructed from the simulated event samples. Input $M(\chi_{c1,2}) - M(J/\psi)$ mass difference values are shown by vertical lines.

3.4.3 Fit to $\Upsilon(4S)$ data

There are 8 free parameters in the fit:

- the 6 coefficients of the 5th order Chebyshev polynomial,
- the normalization of the χ_{c1} template,
- the normalization of the χ_{c2} template.

The $\chi_{c1,2}$ mass resolution is approximately 8 MeV/c^2 (Figure 3.4). We fit a binned $M(J/\psi\gamma)-M(J/\psi)$ distribution from 100 to 900 MeV/c^2 with a bin size of 1 MeV/c^2. We plot the data using 4 MeV/c^2 bins (Figure 3.1a). The maximum likelihood fit is performed in `MN_FIT` [53]. The likelihood function to maximize is defined by

$$\mathcal{L} = \prod_i \frac{\mu_i^{r_i} e^{-\mu_i}}{r_i!},$$

where $r \equiv N^{\rm obs}$ is the observed number of events in a particular bin, and $\mu \equiv N^{\rm th}$ is the number of events predicted by the model ("theory") to be in this bin. In practice, the fit is performed by minimizing the following expression:

$$-2\ln\left(\prod_i \frac{\mu_i^{r_i}e^{-\mu_i}}{r_i!}\times\frac{r_i!}{r_i^{r_i}e^{-r_i}}\right) = \sum_i \left[2(N_i^{\rm th}-N_i^{\rm obs}) + 2N_i^{\rm obs}\ln(N_i^{\rm obs}/N_i^{\rm th})\right].$$

The fitting function is integrated across a bin.

The χ_{c1} and χ_{c2} signal yields in the $\Upsilon(4S)$ data are

$$N^{\rm ON}(\chi_{c1}) = 672 \pm 47 \text{ and } N^{\rm ON}(\chi_{c2}) = 83 \pm 37.$$

The fit determines the correlation coefficient between $N(\chi_{c1})$ and $N(\chi_{c2})$ to be $+0.14$.

3.4.4 Goodness of fit

We estimate goodness of the fit using a bin width of 4 MeV/c^2 (Figure 3.1a), which equals to about a half of the experimental resolution. There are 200 bins in the histogram (Figure 3.1a), and 8 fitting function parameters were determined in the fit.

We perform several goodness-of-fit tests and conclude that the fit quality is acceptable.

Pearson's χ^2

Pearson's χ^2 is defined by

$$\chi^2_P = \sum_i (N_i^{\rm obs}-N_i^{\rm th})^2/N_i^{\rm th}.$$

The number of events in a typical bin is still high enough for this statistic to give accurate goodness-of-fit estimation (Figure 3.1a).
We obtain $\chi^2_P/\text{d.o.f.} = 196.9/(200-8)$, C.L. $= 39\%$.
To a good approximation, χ^2_P should follow a Gaussian distribution with a mean of $200-8 = 192$ and $\sigma = \sqrt{2\cdot(200-8)} = 19.6$. Therefore the χ^2_P value we obtained is 0.25σ above the expected average.

Baker-Cousins's χ^2

When the number of events per bin in not large, the statistic proposed by Baker and Cousins [54, 48] is preferable to χ^2_P for goodness-of-fit estimation:

$$\chi^2_{BC} = \sum_i \left[2(N_i^{\rm th}-N_i^{\rm obs}) + 2N_i^{\rm obs}\ln(N_i^{\rm obs}/N_i^{\rm th})\right],$$

We obtain $\chi^2_{BC}/\text{d.o.f.} = 198.8/(200-8)$ d.o.f., C.L. $= 35\%$.
The χ^2_{BC} value we obtained is 0.35σ above the expected average.

Nelson's method

The goodness of the fit is also estimated using a method described in [55].
Poisson log-likelihood is calculated as

$$-2\ln\mathcal{L} = -2\sum_i \ln f(r_i,\mu_i) = -2\sum_i \ln(\frac{\mu_i^{r_i}e^{-\mu_i}}{r_i!}),$$

where $\mu \equiv N^{\rm th}$ and $r \equiv N^{\rm obs}$. In Nelson's method, one then evaluates the expected mean and variance of the above expression. The mean for one bin is given by

$$\langle -2\ln f(r,\mu)\rangle = -2\sum_{r=0}^{\infty} f(r,\mu)\ln f(r,\mu) = -2\sum_{r=0}^{\infty}\frac{\mu^r e^{-\mu}}{r!}\ln(\frac{\mu^r e^{-\mu}}{r!}),$$

whereas variance for one bin is given by

$$\langle[-2\ln f(r,\mu)]^2\rangle - \langle -2\ln f(r,\mu)\rangle^2 = \sum_{r=0}^{\infty} f(r,\mu)[-2\ln f(r,\mu) - \langle -2\ln f(r,\mu)\rangle]^2.$$

After summing the calculated means and variances for all the bins, we subtract number of fit parameters $m = 8$ from the mean and $2m = 16$ from the variance. The $-2\ln\mathcal{L}$ is expected to follow a Gaussian distribution with a mean of 1421.2 and $\sigma = 19.6$. We obtained $-2\ln\mathcal{L} = 1426.5$, which is 0.27σ above the expected average.

The runs test

The runs test [56] is a supplement to the χ^2 test. In the χ^2 test the signs of the deviations are not used. The runs test uses this information under the hypothesis that all patterns of signs are equally probable. A *run* is a sequence of deviations of the same sign. Suppose a histogram has 8 bins, and we mark a bin with a + or − sign depending on whether the number of events in a bin is above or below the number predicted by the fitted curve. Then, for example, a sequence $++---+-+$ has 5 runs. If there are M positive and N negative deviations, the distribution of number of runs R has mean and variance given by

$$E(R) = 1 + \frac{2MN}{M+N}, \quad V(R) = \frac{2MN(2MN-M-N)}{(M+N)^2(M+N+1)}.$$

In our fit, we obtain $M = 96$, $N = 104$, and $R = 90$. To a good approximation, R should follow a Gaussian distribution with a mean of 100.8 and $\sigma = 7.0$. Therefore the R value we obtained is 1.5σ below the expected average.

3.4.5 Fit to off-$\Upsilon(4S)$ data

The contribution from non-$B\overline{B}$ events to signal or background is very small (Figure 3.5-left). We perform the same fit as for $\Upsilon(4S)$ data, but we fix the background shape from a fit to continuum Monte Carlo sample. The statistics of the generic continuum Monte Carlo sample correspond to "10 times the off-$\Upsilon(4S)$ data". Signal and background template normalizations are determined in the fit (Figure 3.5). The χ_{c1} and χ_{c2} signal yields are consistent with zero: $N^{\rm OFF}(\chi_{c1}) = 4.1 \pm 7.1$ and $N^{\rm OFF}(\chi_{c2}) = 1.1 \pm 6.5$ events.

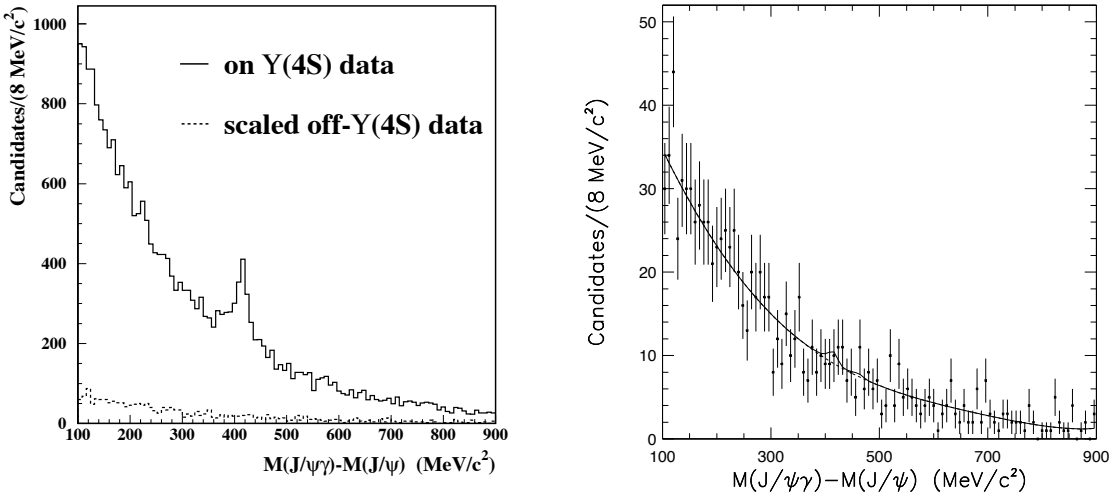

Figure 3.5: The left plot shows $M(J/\psi\gamma) - M(J/\psi)$ distribution in $\Upsilon(4S)$ data (solid line) and luminosity-scaled off-$\Upsilon(4S)$ data (dashed line). The right plot shows the fit to $M(J/\psi\gamma) - M(J/\psi)$ distribution in off-$\Upsilon(4S)$ data.

3.4.6 Reconstruction efficiency

The reconstruction efficiency is determined from the samples of simulated $B \to \chi_{c1} X_s$ and $B \to \chi_{c2} X_s$ events by fitting $M(J/\psi\gamma) - M(J/\psi)$ distribution with a polynomial and $\chi_{c1,2}$ templates (Figure 3.6). The $\chi_{c1,2} \to J/\psi\gamma$ helicity angle distribution is assumed to be flat in $\cos\theta_h$. The X_s system is a mixture of K, K^*, and higher K resonances (24% K, 24% $K^*(892)$, 14% $K_1(1270)$, 14% $K_1(1400)$, 13% $K_0^*(1430)$, and 11% $K_2^*(1430)$). We also include $B \to \psi(2S) X_s$, $\psi(2S) \to \chi_{c1,2}\gamma$ decay chain [48]. In Figure 3.7 the resulting χ_{c1} momentum spectrum is compared with the χ_{c1} spectrum from $B \to \chi_{c1} K$ decays. The reconstruction efficiencies are determined to be $\mathcal{E}(\chi_{c1}) = (25.72 \pm 0.19)\%$ and $\mathcal{E}(\chi_{c2}) = (26.64 \pm 0.18)\%$, with the quoted uncertainty arising from finite statistics of the Monte Carlo samples.

3.4.7 Calculation of $\mathcal{B}(B \to \chi_{c1} X)$

Event yields in on- and off-$\Upsilon(4S)$ data are

$$N^{\rm ON}(\chi_{c1}) = 672 \pm 47[\text{stat}] \text{ and } N^{\rm OFF}(\chi_{c1}) = 4.1 \pm 7.1[\text{stat}].$$

The $B \to \chi_{c1} X$ event yield is

$$N(B \to \chi_{c1} X) = N^{\rm ON} - 1.99 \times N^{\rm OFF} = 664 \pm 49[\text{stat}].$$

The resulting branching fraction is

$$\mathcal{B}(B \to \chi_{c1} X) = (4.14 \pm 0.31[\text{stat}] \pm 0.40[\text{syst}]) \times 10^{-3}.$$

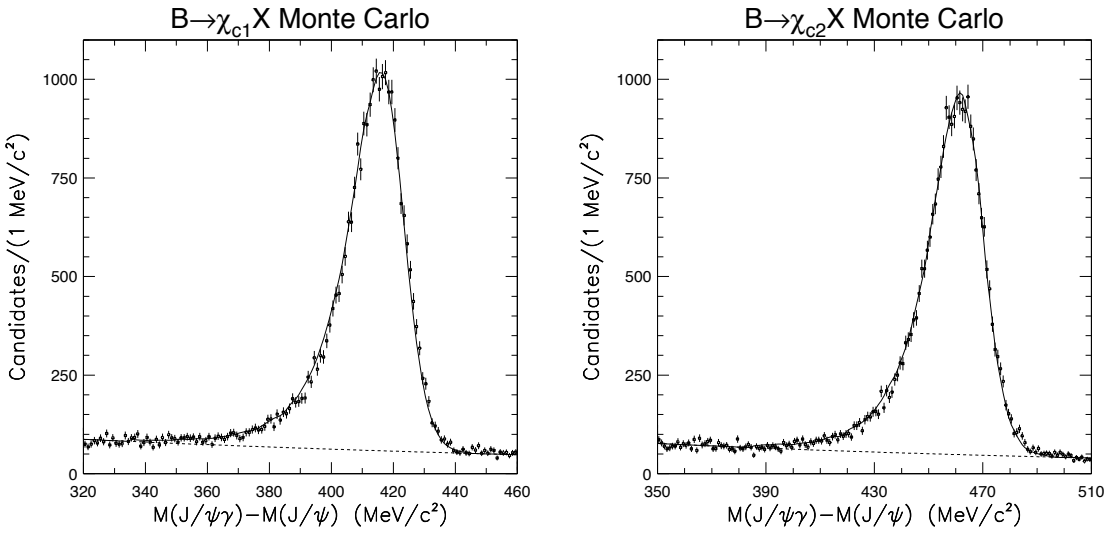

Figure 3.6: The fit to the $M(J/\psi\gamma) - M(J/\psi)$ distribution for (left) $B \to \chi_{c1}X$ and (right) $B \to \chi_{c2}X$ signal Monte Carlo samples.

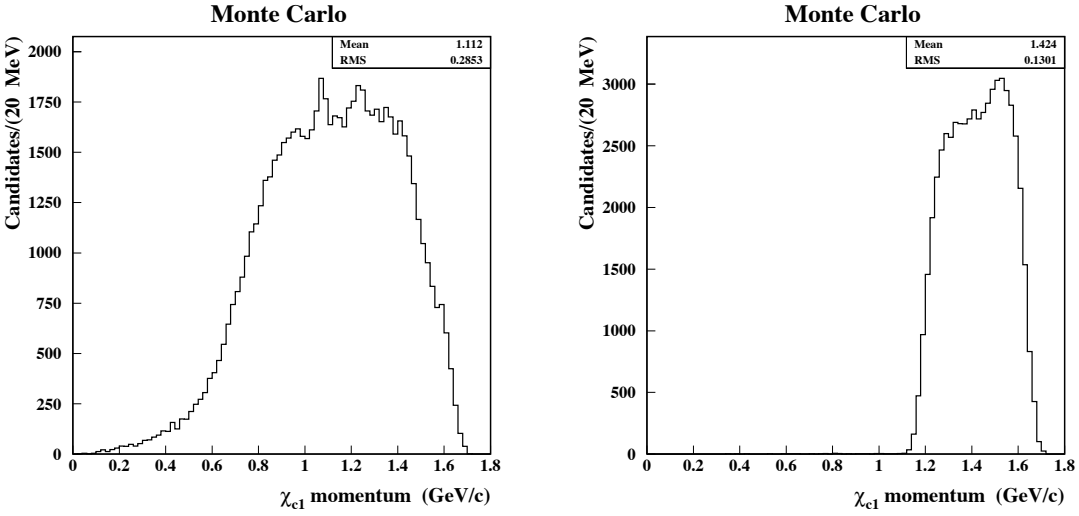

Figure 3.7: The χ_{c1} momentum in $B \to \chi_{c1}X_s$ (left) and in $B \to \chi_{c1}K$ (right) Monte Carlo samples. Generator-level information is shown.

The comparison with the previous CLEO measurements is given in Table 3.6.

Table 3.6: Our measurement of $\mathcal{B}(B \to \chi_{c1}X)$ compared with previous CLEO results. Note that we use $\mathcal{B}(J/\psi \to \ell^+\ell^-) = 5.89\%$, whereas $\mathcal{B}(J/\psi \to \ell^+\ell^-) = 6.02\%$ was used in [28, 58].

Reference	Luminosity (fb^{-1})	$N^{ON}(\chi_{c1})$	$\mathcal{B}(B \to \chi_{c1}X)$ ($\times 10^{-3}$)
[28]	2.0	112 ± 17	$4.0 \pm 0.6 \pm 0.4$
[58]	3.1	145 ± 21	$3.7 \pm 0.5 \pm 0.4$
This measurement	9.2	672 ± 47	$4.14 \pm 0.31 \pm 0.40$

Next, we calculate the branching fraction for direct χ_{c1} production in B decays. We assume that the only feeddown from higher charmonium states comes from $B \to \psi(2S)X$, $\psi(2S) \to \chi_{c1}\gamma$ decay chain. We obtain

$$\begin{aligned}\mathcal{B}(B \to \chi_{c1}[\text{direct}]X) &= \mathcal{B}(B \to \chi_{c1}X) - \mathcal{B}(B \to \psi(2S)X) \times \mathcal{B}(\psi(2S) \to \chi_{c1}\gamma) = \\ &= (4.14 \pm 0.31 \pm 0.40) \times 10^{-3} - (0.31 \pm 0.05) \times 10^{-3} = \\ &= (3.83 \pm 0.31[\text{stat}] \pm 0.40[\text{syst}]) \times 10^{-3}.\end{aligned}$$

3.4.8 Calculation of $\mathcal{B}(B \to \chi_{c2}X)$

The $B \to \chi_{c2}X$ event yield is

$$N(B \to \chi_{c2}X) = N^{\text{ON}} - 1.99 \times N^{\text{OFF}} = 81 \pm 39[\text{stat}] \pm 9[\text{syst}],$$

where we quote the systematic uncertainty associated with the fit. The $B \to \chi_{c2}X$ signal yield significance is 2.0σ.

Subtracting the feeddown from $B \to \psi(2S)X$, $\psi(2S) \to \chi_{c1}\gamma$ decay chain, we obtain

$$N(B \to \chi_{c2}[\text{direct}]X) = 58 \pm 41.$$

The significance of the evidence for the decay $B \to \chi_{c2}[\text{direct}]X$ is 1.4σ.

Total inclusive $B \to \chi_{c2}X$ branching fraction is

$$\mathcal{B}(B \to \chi_{c2}X) = (0.98 \pm 0.48[\text{stat}] \pm 0.15[\text{syst}]) \times 10^{-3}.$$

We add in quadrature the statistical and systematic uncertainties, use Gaussian approximation for the measured branching fraction, and follow the Feldman-Cousins approach [49] to calculate the confidence interval for the mean of a Gaussian constrained to be non-negative given the measured mean. We obtain

$$\mathcal{B}(B \to \chi_{c2}X) \in [0.2; 2.0] \times 10^{-3} \ @ \ 95\% \text{ C.L.}$$

The comparison with the previous CLEO measurements is given in Table 3.7.

Table 3.7: Our measurement of $\mathcal{B}(B \to \chi_{c2}X)$ compared with previous CLEO results.

Reference	Luminosity (fb^{-1})	$N^{ON}(\chi_{c2})$	$\mathcal{B}(B \to \chi_{c2}X)$ ($\times 10^{-3}$)
[28]	2.0	35 ± 13	$2.5 \pm 1.0 \pm 0.3$
[58]	3.1	27 ± 16	$1.8 \pm 0.9 \pm 0.2$
This measurement	9.2	83 ± 37	$0.98 \pm 0.48 \pm 0.15$

Assuming that the only feeddown from higher charmonium states comes from $B \to \psi(2S)X$, $\psi(2S) \to \chi_{c2}\gamma$ decay chain, we calculate the branching fraction for direct χ_{c2} production in B decays

$$\mathcal{B}(B \to \chi_{c2}[\text{direct}]X) = (0.98 \pm 0.48 \pm 0.15) \times 10^{-3} - (0.27 \pm 0.05) \times 10^{-3} = \\ = (0.71 \pm 0.48[\text{stat}] \pm 0.16[\text{syst}]) \times 10^{-3}$$

The Feldman-Cousins confidence interval is

$$\mathcal{B}(B \to \chi_{c2}[\text{direct}]X) \in [0.0; 1.7] \times 10^{-3} \ @\ 95\%\ \text{C.L.}$$

3.4.9 Calculation of $\Gamma(B \to \chi_{c2}[\text{direct}]X)/\Gamma(B \to \chi_{c1}[\text{direct}]X)$

Taking into account correlations between the uncertainties, we calculate the branching ratio for direct χ_{c1} and χ_{c2} production in B meson decays. Common systematic uncertainties do not cancel exactly in the ratio because of the $\psi(2S) \to \chi_{c1,2}\gamma$ feeddown subtraction. For example, tracking efficiency uncertainty of 2%, which is the same for $\mathcal{B}(B \to \chi_{c2}X)$ and $\mathcal{B}(B \to \chi_{c1}X)$, is translated into a 0.7% uncertainty on the ratio $\Gamma(B \to \chi_{c2}[\text{direct}]X)/\Gamma(B \to \chi_{c1}[\text{direct}]X)$.

We obtain

$$\frac{\Gamma(B \to \chi_{c2}[\text{direct}]X)}{\Gamma(B \to \chi_{c1}[\text{direct}]X)} = 0.18 \pm 0.13[\text{stat}] \pm 0.04[\text{syst}].$$

The Feldman-Cousins confidence interval is

$$\frac{\Gamma(B \to \chi_{c2}[\text{direct}]X)}{\Gamma(B \to \chi_{c1}[\text{direct}]X)} \in [0.00; 0.44] \ @\ 95\%\ \text{C.L.}$$

3.4.10 Assumed value for $\mathcal{B}(\chi_{c1} \to J/\psi\gamma)/\mathcal{B}(\chi_{c2} \to J/\psi\gamma)$

We need the branching ratio $\mathcal{B}(\chi_{c1} \to J/\psi\gamma)/\mathcal{B}(\chi_{c2} \to J/\psi\gamma)$ in order to calculate the ratio $\mathcal{B}(B \to \chi_{c2}X)/\mathcal{B}(B \to \chi_{c1}X)$. Taking PDG values [48] and assuming the uncertainties to be independent, we obtain

$$\frac{\mathcal{B}(\chi_{c1} \to J/\psi\gamma)}{\mathcal{B}(\chi_{c2} \to J/\psi\gamma)} = \frac{(27.3 \pm 1.6)\%}{(13.5 \pm 1.1)\%} = 2.02 \pm 0.20. \tag{3.2}$$

We have also checked the original Crystal Ball paper [57] for possible cancelations of systematic uncertainties which would yield a more precise value of this ratio. From [57] we extract $\mathcal{B}(\chi_{c1} \to J/\psi\gamma)/\mathcal{B}(\chi_{c2} \to J/\psi\gamma) = 2.30 \pm 0.32$. We therefore use the slightly more precise value from Equation 3.2.

3.4.11 Systematic uncertainty associated with signal shape

Calorimeter energy scale

Differences between the data and the Monte Carlo simulation in the calibration of the calorimeter energy scale will result in an offset of the $\chi_{c1,2}$ peak positions in the data with respect to the simulation. The $\chi_{c2} - \chi_{c1}$ mass difference is only 46 MeV/c^2, therefore we can consider the offset to be the same for χ_{c2} and χ_{c1} peaks. The possible discrepancies between data and the simulation are investigated in our π^0 study (Appendix A). For the signal photons from $\chi_{c1,2} \to J/\psi\gamma$ decays, the energy scale of the calorimeter differs by -0.6 MeV/c^2 between data and the simulation. We therefore have introduced a -0.6 MeV/c^2 correction to the χ_{c1} and χ_{c2} template positions. In addition we observe the energy scale variation over the individual datasets (Figure A.3-left).
We perform 3 tests:

1. The χ_{c1} and χ_{c2} templates extracted from simulation are shifted by ± 0.6 MeV/c^2 in the fit.

2. Dataset-dependent shifts for the measured photon energies are introduced. The corrections are taken from Figure A.3-right. For example, the π^0 peak in `4SB` data is shifted by $+2.0$ MeV/c^2 with respect to the average π^0 peak position for all the datasets combined. The $+2.0$ MeV/c^2 shift in π^0 peak position can be translated into $+6.0$ MeV overestimation of the measured photon energies. We therefore apply a -6.0 MeV/c^2 correction to $M(J/\psi\gamma) - M(J/\psi)$ for `4SB` data.

3. We allow the position of the χ_{c1} to float in the fit, while keeping the relative $\chi_{c2} - \chi_{c1}$ offset fixed. The fit wants to move the χ_{c1} peak by $+1.4 \pm 0.9$ MeV/c^2, which is consistent with zero.

The resulting yield variations and the assigned systematic uncertainties are listed in Table 3.8.

Table 3.8: Variations of the χ_{c1} and χ_{c2} yields in the tests probing the systematic uncertainty due to calorimeter energy scale calibration.

Test	change in		
	$N(\chi_{c1})$ events/%	$N(\chi_{c2})$ events/%	$\frac{N(\chi_{c2})}{N(\chi_{c1})}$ %
(1) shift of $\chi_{c1,2}$ templates			
-0.6 MeV/c^2	$-2.7/-0.4\%$	$+4.7/+5.6\%$	$+6.0\%$
$+0.6$ MeV/c^2	$+1.6/+0.2\%$	$-4.5/-5.4\%$	-5.6%
(2) dataset-dependent energy corrections	$+1.5/+0.2\%$	$-0.2/-0.2\%$	-0.4%
Systematic uncertainty	$\pm 0.4\%$	$\pm 5.6\%$	$\pm 6.0\%$

Calorimeter energy resolution

The experimental width of the $\chi_{c1,2}$ peaks in the distribution of $M(J/\psi\gamma) - M(J/\psi)$ is dominated by the photon energy resolution. Differences between the data and the Monte Carlo simulation in the photon energy resolution will result in the $\chi_{c1,2}$ templates with which we fit the data that too wide or too narrow. The possible discrepancies between the data and the simulation are investigated in our π^0 study (Appendix A). We have found that the π^0 peak is 1% narrower in the data than in the simulation. Assuming that this discrepancy results only from the different energy resolutions in the data and the simulation, we infer that the signal photon energy resolution is 4% better in the data compared to the simulation. To estimate the systematic uncertainty, we use Crystal Ball function (see Appendix A.2) to fit χ_{c1} and χ_{c2} signal shapes and vary the width of the χ_{c1} and χ_{c2} Crystal Ball templates by $\pm 4\%$. The resulting yield variations and the assigned systematic uncertainties are listed in Table 3.9.

Table 3.9: Variations of the χ_{c1} and χ_{c2} yields in the tests probing the systematic uncertainty due to photon energy resolution.

Change in width of $\chi_{c1,2}$ templates	change in		
	$N(\chi_{c1})$ events/%	$N(\chi_{c2})$ events/%	$\frac{N(\chi_{c2})}{N(\chi_{c1})}$ %
4% decrease	$-18.6/-2.8\%$	$-5.9/-6.9\%$	$+4.3\%$
4% increase	$+18.0/+2.7\%$	$+5.6/+6.6\%$	$+3.8\%$
Systematic uncertainty	$\pm 2.8\%$	$\pm 6.9\%$	$\pm 4.3\%$

3.4.12 Systematic uncertainty associated with background shape

To fit the background, we use a 5th order Chebyshev polynomial with all the coefficients floating. We check the $\chi_{c1,2}$ yield stability with respect to the following variations in background shape:

1. We fit the background to a 6th order Chebyshev polynomial with all the coefficients floating.

2. We fit the background to a "rigid" background template extracted from the Monte Carlo simulation. We use a "35 times the data" sample of simulated generic $B\overline{B}$ events and a "5 times the on-$\Upsilon(4S)$ data" sample of simulated generic continuum events. We fit the histograms extracted from $B\overline{B}$ and continuum Monte Carlo samples separately with a 6th order Chebyshev polynomial. Then we add the 2 curves with continuum-to-$B\overline{B}$ weights of 7:1, reflecting difference in statistics of the Monte Carlo samples. We use thus obtained shape with floating normalization to fit the data. The resulting background shape is shown in Figure 3.8. We also vary the continuum-to-$B\overline{B}$ ratio by $\pm 20\%$.

The resulting yield variations and the assigned systematic uncertainties are listed in Table 3.10.

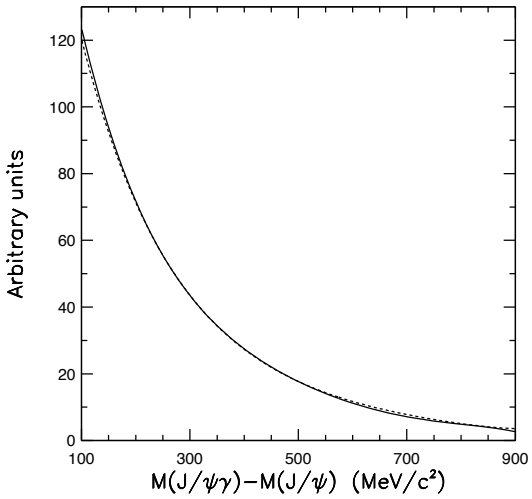

Figure 3.8: The $M(J/\psi\gamma) - M(J/\psi)$ background shapes. Solid line represents a fit to a 5th-order Chebyshev polynomial with all the coefficients floating (Figure 3.1a). Dashed line represents a fit to a "rigid" background shape extracted from the Monte Carlo simulation.

3.4.13 Systematic uncertainty associated with bin width

The fit is performed to the $M(J/\psi\gamma) - M(J/\psi)$ histogram with 1 MeV/c^2-wide bins, whereas the $\chi_{c1,2}$ peak width is 8 MeV/c^2. We repeat the fit to the histogram with 0.1 MeV/c^2-wide bins. The resulting yield variations and the assigned systematic uncertainties are listed in Table 3.11.

3.4.14 Systematic uncertainty associated with helicity angle distribution for $\chi_{c1,2} \to J/\psi\gamma$ decays

The angular distribution of the $\chi_{c1,2} \to J/\psi\gamma$ decays affects the photon energy spectrum. We define the helicity angle θ_h to be the angle between the γ direction in χ_c frame and the χ_c direction in the B frame. We assume flat $\cos\theta_h$ distribution in the Monte Carlo simulation used for the evaluation of the reconstruction efficiency (Section 3.4.6). The $\chi_{c1} \to J/\psi\gamma$ photon energy distribution in this Monte Carlo sample is shown in Figure 3.9(left). To estimate the systematic uncertainty due to $\chi_{c1,2} \to J/\psi\gamma$ angular distributions, we have generated two additional samples of simulated $B \to \chi_{c1}X_s$ events with $I(\theta_h) \propto \cos^2\theta_h$ and $I(\theta_h) \propto \sin^2\theta_h$. The photon energy distributions in these Monte Carlo samples are shown

Table 3.10: Variations of the χ_{c1} and χ_{c2} yields in the tests probing the systematic uncertainty due to background shape. The χ_{c1} and χ_{c2} signal yields in $\Upsilon(4S)$ data are $N^{\rm ON}(\chi_{c1}) = 672 \pm 47$[stat] and $N^{\rm ON}(\chi_{c2}) = 83 \pm 37$[stat].

Background shape	change in		
	$N(\chi_{c1})$ events/%	$N(\chi_{c2})$ events/%	$\frac{N(\chi_{c2})}{N(\chi_{c1})}$ %
6th order Chebyshev polynomial	$-11.9/-1.8\%$	$-2.9/-3.5\%$	-1.8%
Monte Carlo background template	$+5.4/+0.8\%$	$+4.1/+5.0\%$	$+4.2\%$
20% less continuum	$+7.8/+1.1\%$	$+5.7/+6.8\%$	$+5.7\%$
20% more continuum	$+3.0/+0.4\%$	$+1.8/+2.2\%$	$+1.7\%$
Systematic uncertainty	$\pm 1.8\%$	$\pm 6.8\%$	$\pm 5.7\%$

Table 3.11: Variations of the χ_{c1} and χ_{c2} yields in the tests probing the systematic uncertainty due to bin width of the $M(J/\psi\gamma) - M(J/\psi)$ histogram.

Bin width	change in		
	$N(\chi_{c1})$ events/%	$N(\chi_{c2})$ events/%	$\frac{N(\chi_{c2})}{N(\chi_{c1})}$ %
0.1 MeV/c^2	$-0.3/-0.05\%$	$+1.6/+1.9\%$	$+2.0\%$
Systematic uncertainty	0.0%	$\pm 1.9\%$	$\pm 2.0\%$

in Figure 3.10. The resulting efficiency ratio for these two samples is

$$\frac{\mathcal{E}[I(\theta_h) \propto \sin^2\theta_h]}{\mathcal{E}[I(\theta_h) \propto \cos^2\theta_h]} - 1 = (+1.3 \pm 1.5[\text{MC stat}])\%.$$

We assign 1% systematic uncertainty on the $\chi_{c1,2}$ reconstruction efficiencies and their ratio.

3.4.15 Systematic uncertainty associated with the composition of X system in $B \to \chi_{c1,2}X$ decays

The X_s system in the samples of simulated $B \to \chi_{c1,2}X_s$ events is described in Section 3.4.6. The reconstruction efficiency will depend on the assumptions about X_s system composition. First, the photon energy spectrum is affected (Figure 3.9). Second, the efficiency and purity of the π^0 veto depends on the π^0 multiplicity. To estimate the systematic uncertainty, we compare the $\chi_c \to J/\psi\gamma$ detection efficiency extracted using this sample with the efficiency in the sample where we assume that X is either a $K^\pm$ or $K^0_S \to \pi^+\pi^-$. In $B \to \chi_{c1}K$ sample, K is either a K^+ or $K^0_S \to \pi^+\pi^-$. In $B \to \chi_{c1}X_s$ sample, the average π^0 multiplicity of the X_s system is 0.56, with 61%, 28%, 8%, and 3% of events having, respectively, 0, 1, 2, and 3 π^0's in the final state (including the π^0's from

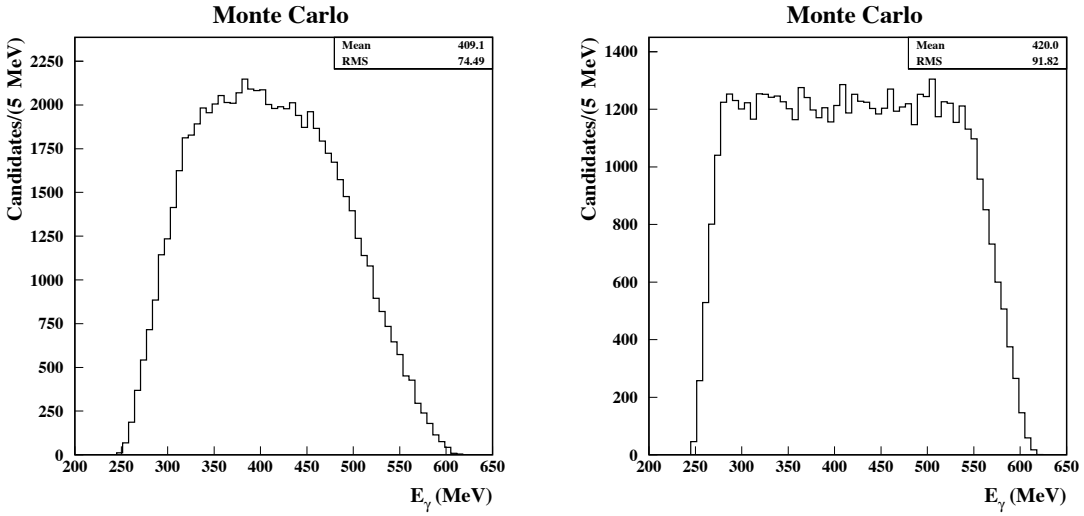

Figure 3.9: The photon energy distribution for $\chi_{c1} \to J/\psi\gamma$ decays in $B \to \chi_{c1} X_s$ (left) and in $B \to \chi_{c1} K$ (right) Monte Carlo samples. The $\chi_{c1} \to J/\psi\gamma$ helicity angle distribution is flat in $\cos\theta_h$. Generator-level information is shown.

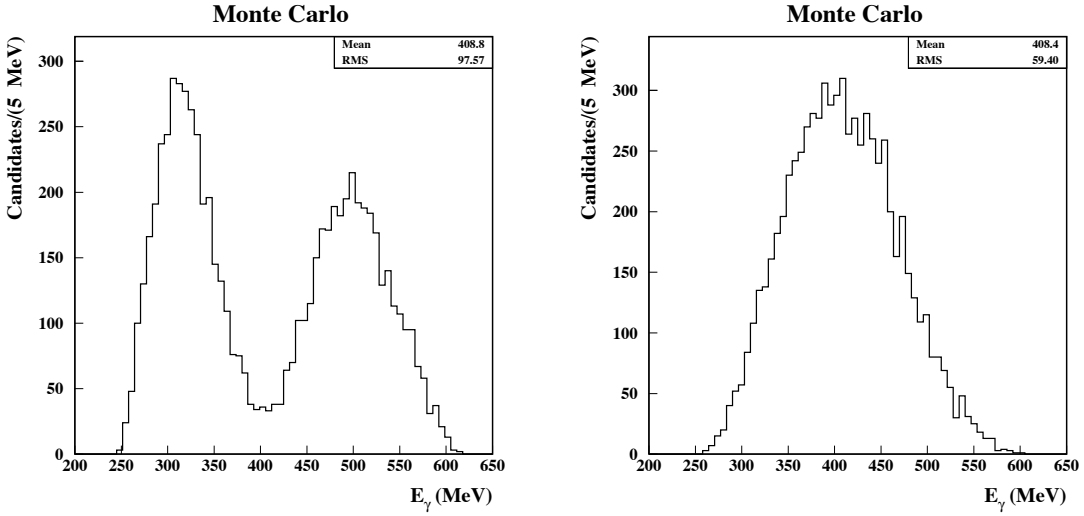

Figure 3.10: The photon energy distribution for $\chi_{c1} \to J/\psi\gamma$ decays in $B \to \chi_{c1} X_s$ Monte Carlo sample. The $\chi_{c1} \to J/\psi\gamma$ helicity angle distribution is assumed to be $I(\theta_h) \propto \cos^2\theta_h$ (left) and $I(\theta_h) \propto \sin^2\theta_h$ (right). Generator-level information is shown.

$K^0_S \to \pi^0\pi^0$ decays). The resulting efficiency ratio is:

$$\frac{\mathcal{E}(B \to \chi_{c1}K)}{\mathcal{E}(B \to \chi_{c1}X_s)} - 1 = (+3.3 \pm 0.8[\text{MC stat}])\%.$$

We assign 3.3% systematic uncertainties for the $\chi_{c1,2}$ reconstruction efficiencies and their ratio.

3.4.16 π^0 veto check

The π^0 veto uncertainty is taken into account in Section 3.4.15, where we varied the π^0 multiplicity. In this section, we explore the stability of our results with respect to variations of the π^0 veto window (Figure 3.2). Nominally, we do not use a photon shower if it can be paired with another shower to form a π^0 candidate with the normalized mass between -3 and $+2$. We vary the window boundaries by $\pm 0.5\sigma$. We also remove the π^0 veto altogether. The resulting yield variations are listed in Table 3.12. All the variations are consistent with statistical fluctuations. We do not assign any additional systematic uncertainty due to π^0 veto.

Table 3.12: The raw $\chi_{c1,2}$ yield and change in efficiency-corrected yield with respect to a variation in the π^0 veto window. The quoted uncertainties are statistical.

π^0 veto window	$N(\chi_{c1})$	$N(\chi_{c2})$	change in $N(\chi_{c1})/\mathcal{E}(\chi_{c1})$	change in $N(\chi_{c2})/\mathcal{E}(\chi_{c2})$
$[-3.0; +2.0]$	672	83	0	0
$[-3.5; +2.5]$	643	72	-14 ± 39	-28 ± 41
$[-2.5; +1.5]$	695	97	-23 ± 50	$+38 \pm 35$
no π^0 veto	886	89	$+45 \pm 147$	-41 ± 128

3.5 More details on the analysis of $B \to \chi_{c1,2}X_s$ with X_s reconstruction

3.5.1 Check of the B-reconstruction technique with Monte Carlo simulation

We want our $B \to \chi_{c1,2}X_s$ reconstruction to be as inclusive as possible. However, the energy release in $B \to \chi_{c1,2}X_s$ is much smaller than in $B \to \gamma X_s$, and in our case it might turn out that going after high-multiplicity states is *a priori* unreasonable because of prohibitively low efficiency and high combinatorial background. For example, if for $B \to \chi_c K 4\pi$ mode the reconstruction efficiency is 10 times lower and the combinatorial background is 10 times higher than for $B \to \chi_c K 3\pi$, then we might want to limit the X_s composition to a kaon and up to 3 — not 4 — pions.

To probe the efficiency of our B-reconstruction technique, we have generated several samples of simulated $B \to \chi_{c1}K^+n\pi$ events. The $B \to \chi_{c1}K^+n\pi$ decay is assumed to

proceed according to phase space, with no resonant substructure in the $K^+n\pi$ system. The other B meson in the event decays generically. Then we determine the $\chi_{c1} \to J/\psi\gamma$ yield by applying the same B-reconstruction procedure as used for data. We use all the X_s reconstruction modes listed in Table 3.3 and extract χ_{c1} yield from the fit to $M(J/\psi\gamma) - M(J/\psi)$ distribution. Thus defined reconstruction efficiencies are listed in Table 3.13. We see that our B-reconstruction procedure is quite efficient even for high-multiplicity $B \to \chi_{c1}Kn\pi$ decays.

What about background? We use a sample of simulated generic $B\overline{B}$ events to study the dependence of background rate on the allowed pion multiplicity in the X_s reconstruction. This dependence is shown in Figure 3.11 and Table 3.14.

We conclude that *a priori* there are no compelling reasons to restrict the allowed number of pions in the X_s reconstruction to 3 or 2. We therefore use all the modes listed in Table 3.3 in the analysis of the data.

Table 3.13: The efficiency of the $B \to J/\psi\gamma X_s$ reconstruction technique for several samples of simulated $B \to \chi_{c1}K^+n\pi$ events. The quoted uncertainties reflect only the finite statistics of the Monte Carlo samples.

Generated B decay mode	Efficiency of B-reconstruction
$\chi_{c1}K^+\pi^-$	$(19.6 \pm 0.4)\%$
$\chi_{c1}K^+\pi^0$	$(12.5 \pm 0.4)\%$
$\chi_{c1}K^+\pi^+\pi^-$	$(17.0 \pm 0.4)\%$
$\chi_{c1}K^+\pi^-\pi^0$	$(12.8 \pm 0.4)\%$
$\chi_{c1}K^+\pi^+\pi^-\pi^-$	$(13.4 \pm 0.3)\%$
$\chi_{c1}K^+\pi^+\pi^-\pi^0$	$(11.2 \pm 0.3)\%$
$\chi_{c1}K^+\pi^+\pi^-\pi^+\pi^-$	$(11.2 \pm 0.2)\%$
$\chi_{c1}K^+\pi^+\pi^-\pi^-\pi^0$	$(10.3 \pm 0.3)\%$

Table 3.14: Dependence of the $B \to J/\psi\gamma X_s$ background level in the sample of simulated generic $B\overline{B}$ events on the allowed pion multiplicity in the X_s reconstruction (Figure 3.11).

pion multiplicity	Background (relative to $n \leq 4$)
≤ 4	100%
≤ 3	89%
≤ 2	57%
≤ 1	22%
$= 0$	3%

3.5.2 Goodness of fit

We estimate goodness of fits using a bin width of 8 MeV/c^2 (Figure 3.1b,c,d), which approximately equals to the experimental resolution. There are 100 bins in each

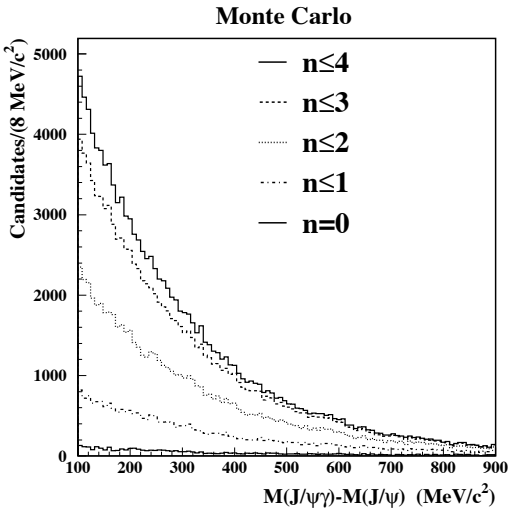

Figure 3.11: The $B \to J/\psi\gamma X_s$ background in the sample of simulated generic $B\overline{B}$ events. The X_s is reconstructed as a kaon and up to n pions (Table 3.3). Different histograms are obtained by limiting the allowed pion multiplicity in the X_s reconstruction.

histogram. See Section 3.4.4 for the details on the goodness-of-fit tests.

Sample A

There are 8 fitting parameters: 6 Chebyshev polynomial coefficients and 2 signal template normalizations.

- *Pearson's* χ^2

$$\chi^2_P/\text{d.o.f.} = 110.0/(100-8),\ \text{C.L.} = 10\%.$$

- *Baker-Cousins's* χ^2

$$\chi^2_{BC}/\text{d.o.f.} = 110.7/(100-8),\ \text{C.L.} = 9\%.$$

  The χ^2_{BC} value we obtained is 1.4σ above the expected average.

- *Nelson's method*
  The $-2\ln\mathcal{L}$ should follow a Gaussian distribution with a mean of 608.7 and $\sigma = 13.5$. We obtain $-2\ln\mathcal{L} = 625.7$, which is 1.3σ above the expected average.

- *The runs test*
  We obtain $M(+) = 48$, $N(-) = 52$, and $R = 54$. Number of runs R should follow a Gaussian distribution with a mean of 50.9 and $\sigma = 4.9$. Therefore the R value we obtained is 0.6σ above the expected average.

Sample B

There are 6 fitting parameters: 4 Chebyshev polynomial coefficients and 2 signal template normalizations.

- *Pearson's* χ^2

$$\chi^2_P/\text{d.o.f.} = 107.2/(100-6),\ \text{C.L.} = 17\%.$$

- *Baker-Cousins's* χ^2

$$\chi^2_{BC}/\text{d.o.f.} = 108.9/(100-6),\ \text{C.L.} = 14\%.$$

  The χ^2_{BC} value we obtained is 1.1σ above the expected average.

- *Nelson's method*
  The $-2\ln\mathcal{L}$ should follow a Gaussian distribution with a mean of 408.7 and $\sigma = 13.0$. We obtain $-2\ln\mathcal{L} = 419.4$, which is 0.9σ above the expected average.

- *The runs test*
  We obtain $M(+) = 48$, $N(-) = 52$, and $R = 57$. Number of runs R should follow a Gaussian distribution with a mean of 50.9 and $\sigma = 4.9$. Therefore the R value we obtained is 1.2σ above the expected average.

Sample C

There are 8 fitting parameters: 6 Chebyshev polynomial coefficients and 2 signal template normalizations.

- *Pearson's* χ^2

$$\chi^2_P/\text{d.o.f.} = 106.0/(100-8),\ \text{C.L.} = 15\%.$$

- *Baker-Cousins's* χ^2

$$\chi^2_{BC}/\text{d.o.f.} = 109.2/(100-8),\ \text{C.L.} = 11\%.$$

  The χ^2_{BC} value we obtained is 1.3σ above the expected average.

- *Nelson's method*
  The $-2\ln\mathcal{L}$ should follow a Gaussian distribution with a mean of 591.2 and $\sigma = 13.4$. We obtain $-2\ln\mathcal{L} = 605.1$, which is 1.0σ above the expected average.

- *The runs test*
  We obtain $M(+) = 46$, $N(-) = 54$, and $R = 46$. Number of runs R should follow a Gaussian distribution with a mean of 50.7 and $\sigma = 4.9$. Therefore the R value we obtained is 1.0σ below the expected average.

We conclude that the fit quality is acceptable for all the three fits.

3.5.3 Non-$B\overline{B}$ event contribution

The χ_{c1} and χ_{c2} signal yields in non-$B\overline{B}$ events are consistent with zero in the inclusive analysis (Section 3.4.5). Our B-reconstruction method further reduces the continuum background (compare Figures 3.5 and 3.12). We therefore neglect the contribution from non-$B\overline{B}$ events.

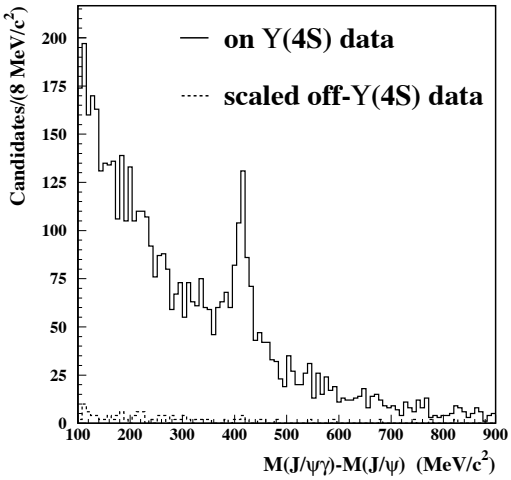

Figure 3.12: The $M(J/\psi\gamma) - M(J/\psi)$ distribution for the $B \to J/\psi\gamma X_s$ candidates. The X_s is reconstructed as a kaon and 0 to 4 pions (Sample A). The solid line represents $\Upsilon(4S)$ data, whereas the dashed line shows luminosity-scaled off-$\Upsilon(4S)$ data.

3.5.4 χ_{c2} signal significance

The systematic uncertainties on the χ_{c2} yield are summarized in Table 3.15. The $B \to \chi_{c2}[\text{direct}]X_s$ signal yield is obtained by subtracting the $\psi(2S)$ feeddown. The expected contributions from the $B \to \psi(2S)X$, $\psi(2S)\chi_{c2}\gamma$ decay chain are listed in Table 3.16. The derivation of the $B \to \chi_{c2}[\text{direct}]X_s$ signal yield significance can be inferred from Table 3.16.

Table 3.15: The systematic uncertainties on the χ_{c2} signal yield.

Source of uncertainty	uncertainty on $N(\chi_{c2})$ (events)		
	Sample A	Sample B	Sample C
Signal shape	± 5.5	± 1.6	± 3.5
Background shape	± 13.2	± 1.8	± 13.6
Total	± 14.3	± 2.4	± 14.0

Table 3.16: Signal yield for $B \to \chi_{c2} X_s$ with statistical and systematic uncertainties (Line 1); contribution to $B \to \chi_{c2} X_s$ from $B \to \psi(2S)X$, $\psi(2S) \to \chi_{c2}\gamma$ decay chain (Line 2); signal yield and statistical significance for $B \to \chi_{c2}[\text{direct}]X_s$ (Lines 3 and 4).

Mode	χ_{c2} signal yield (events)		
	Sample A	Sample B	Sample C
$B \to \chi_{c2} X_s$	$31.2^{+17.7}_{-16.9} \pm 14.3$	$13.9^{+7.0}_{-6.2} \pm 2.4$	$17.7^{+16.2}_{-15.5} \pm 14.0$
$\psi(2S) \to \chi_{c2}\gamma$	$5.7 \quad \pm 1.2$	$0.5 \quad \pm 0.1$	$5.1 \quad \pm 1.1$
$B \to \chi_{c2}[\text{direct}]X_s$	$25.6^{+17.7}_{-16.9} \pm 14.4$	$13.4^{+7.0}_{-6.2} \pm 2.4$	$12.6^{+16.2}_{-15.5} \pm 14.1$
$B \to \chi_{c2}[\text{direct}]X_s$ signal significance	1.2σ	2.0σ	0.6σ

3.5.5 Calculation of $\Gamma(B \to \chi_{c2}[\text{direct}]X_s)/\Gamma(B \to \chi_{c1}[\text{direct}]X_s)$

The branching ratio is calculated as

$$\frac{\Gamma(B \to \chi_{c2}[\text{direct}]X_s)}{\Gamma(B \to \chi_{c1}[\text{direct}]X_s)} = \frac{N(\chi_{c2}) - N(\psi(2S) \to \chi_{c2}\gamma)}{N(\chi_{c1}) - N(\psi(2S) \to \chi_{c1}\gamma)} \times \frac{\mathcal{E}(\chi_{c1})}{\mathcal{E}(\chi_{c2})} \times \frac{\mathcal{B}(\chi_{c1} \to J/\psi\gamma)}{\mathcal{B}(\chi_{c2} \to J/\psi\gamma)}.$$

The ingredients going into the calculation are listed in Table 3.17. The signal yields $N(\chi_{c1,2})$ are extracted from the fits to the $M(J/\psi\gamma) - M(J/\psi)$ distributions. The $\psi(2S)$ feeddown contributions are calculated as $N(\psi(2S) \to \chi_{c1,2}\gamma) = 2 \times N(B\overline{B}) \times \mathcal{B}(B \to \psi(2S)X) \times \mathcal{B}(\psi(2S) \to \chi_{c1,2}\gamma) \times \mathcal{E}(\psi(2S) \to \chi_{c1,2}\gamma)$, where the feeddown reconstruction efficiency $\mathcal{E}(\psi(2S) \to \chi_{c1,2}\gamma)$ is determined from the Monte Carlo simulation.

To extract the relative χ_{c2}-to-χ_{c1} reconstruction efficiency $\mathcal{E}(\chi_{c2})/\mathcal{E}(\chi_{c1})$, we use the samples of simulated $B \to \chi_{c1,2} X_s$ events described in Section 3.4.6. The events containing the $B \to \psi(2S)X$, $\psi(2S) \to \chi_{c1,2}\gamma$ decay chain have been removed from the simulated event samples. The X_s composition is the same for χ_{c1} and χ_{c2}. The resulting efficiency ratios are given in Table 3.17; the quoted uncertainties reflect only the finite statistics of the Monte Carlo simulation.

Table 3.17: The $\chi_{c1,2}$ signal yields, calculated $\psi(2S)$ feeddown contributions, efficiency ratio, ratio of $\mathcal{B}(\chi_{c1,2} \to J/\psi\gamma)$, and the calculated χ_{c2}-to-χ_{c1} production ratio.

	Sample A	Sample B	Sample C
$N(\chi_{c2})$	31^{+18}_{-17}[stat]	$13.9^{+7.0}_{-6.2}$[stat]	18 ± 16[stat]
$N(\psi(2S) \to \chi_{c2}\gamma)$	5.7	0.5	5.1
$N(\chi_{c1})$	279 ± 25[stat]	96 ± 12[stat]	183 ± 22[stat]
$N(\psi(2S) \to \chi_{c1}\gamma)$	13.7	1.2	12.5
$\mathcal{E}(\chi_{c2})/\mathcal{E}(\chi_{c1})$	1.067 ± 0.017	1.074 ± 0.024	1.061 ± 0.022
$\mathcal{B}(\chi_{c1} \to J/\psi\gamma)/\mathcal{B}(\chi_{c2} \to J/\psi\gamma)$	2.02	2.02	2.02
$\frac{\Gamma(B \to \chi_{c2}[\text{direct}]X_s)}{\Gamma(B \to \chi_{c1}[\text{direct}]X_s)}$	0.18 ± 0.12[stat]	$0.27^{+0.15}_{-0.13}$[stat]	0.14 ± 0.18[stat]

3.5.6 Systematic uncertainty associated with signal shape

Calorimeter energy scale

As described in Section 3.4.11, we shift the $\chi_{c1,2}$ templates by ± 0.6 MeV/c^2 in the fit in order to estimate the uncertainty due to the calorimeter energy scale. The resulting changes in the signal yields are listed in Table 3.18.

Table 3.18: Changes of χ_{c1} and χ_{c2} yields resulting from ± 0.6 MeV/c^2 shifts of the $\chi_{c1,2}$ templates.

X_s composition/ $\chi_{c1,2}$ template shift	change in	
	$N(\chi_{c1})$ events/%	$N(\chi_{c2})$ events/%
Sample A		
-0.6 MeV/c^2	$-0.8/-0.3\%$	$+1.45/+4.6\%$
$+0.6$ MeV/c^2	$+0.5/+0.2\%$	$-1.50/-4.8\%$
Sample B		
-0.6 MeV/c^2	$-0.9/-0.9\%$	$+0.63/+4.5\%$
$+0.6$ MeV/c^2	$+0.9/+0.9\%$	$-0.59/-4.2\%$
Sample C		
-0.6 MeV/c^2	$-0.5/-0.3\%$	$+1.06/+4.8\%$
$+0.6$ MeV/c^2	$+0.1/0.0\%$	$-1.07/-4.9\%$

Calorimeter energy resolution

As described in Section 3.4.11, we vary the width of the $\chi_{c1,2}$ templates by $\pm 4\%$ in the fit in order to estimate the uncertainty due to the calorimeter energy resolution. The resulting changes in the signal yields are listed in Table 3.19.

Tail truncation

The B-reconstruction technique involves cutting on the energy and the beam-constrained mass of the $B \to J/\psi\gamma X_s$ candidate. This will lead to a change of the $\chi_{c1,2}$ lineshapes. Such a change should not significantly affect the measurement of the branching ratio $\Gamma(B \to \chi_{c2}[\text{direct}]X_s)/\Gamma(B \to \chi_{c1}[\text{direct}]X_s)$ because it affects both χ_{c1} and χ_{c2} and because we correct the data for the detection efficiencies extracted from the Monte Carlo simulation, for which the identical fitting procedure is applied. We probe the systematic uncertainty by using the $\chi_{c1,2}$ templates with the truncated tails to fit the distributions extracted from the data and the Monte Carlo simulation. The truncated $\chi_{c1,2}$ shapes are obtained from the Monte Carlo sample described in Section 3.4.2. We select only those $\chi_{c1,2} \to J/\psi\gamma$ candidates, for which the reconstructed energy is within 3σ from the generated value ($|E(\text{meas}) - E(\text{gen})|/\sigma(E) < 3$). The resulting change in the templates is shown in Figure 3.13. Such a truncation could only overestimate the change of the $\chi_{c1,2}$

Table 3.19: Changes of χ_{c1} and χ_{c2} yields resulting from the $\pm 4\%$ variations of the $\chi_{c1,2}$ template widths.

X_s composition/ change in $\chi_{c1,2}$ template widths	change in	
	$N(\chi_{c1})$ events/%	$N(\chi_{c2})$ events/%
Sample A		
-4%	$-7.0/-2.5\%$	$+1.06/+4.8\%$
$+4\%$	$+6.8/+2.4\%$	$-1.07/-4.9\%$
Sample B		
-4%	$-2.1/-2.1\%$	$-0.32/-2.3\%$
$+4\%$	$+1.9/+2.0\%$	$+0.26/+1.9\%$
Sample C		
-4%	$-4.6/-2.5\%$	$-1.23/-6.9\%$
$+4\%$	$+4.4/+2.4\%$	$+1.16/+6.4\%$

lineshapes in $B \to J/\psi\gamma X_s$ reconstruction. If the B candidate energy resolution is not dominated by the energy resolution of $J/\psi\gamma$ combination, then the effect of the ΔE cut on the low-side tail of the $\chi_{c1,2}$ lineshapes will be less pronounced. The changes in the $\chi_{c1,2}$ yields and the ratio of the yields in the data and the simulation are listed in Table 3.20.

Table 3.20: Changes in $\chi_{c1,2}$ yields and the ratio of the yields in the data and the simulation resulting from the change of the $\chi_{c1,2}$ template shapes as shown in Figure 3.13.

X_s composition	change in			
	$N_{\rm data}(\chi_{c1})$ events	$N_{\rm data}(\chi_{c1})/N_{\rm MC}(\chi_{c1})$ %	$N(\chi_{c2})$ events	$N_{\rm data}(\chi_{c2})/N_{\rm MC}(\chi_{c2})$ %
Sample A	-19.2	-1.7%	-4.9	-12.1%
Sample B	-4.0	0.0%	-1.5	-7.4%
Sample C	-13.6	-1.7%	-3.1	-13.6%

3.5.7 Systematic uncertainty associated with background shape

We check the $\chi_{c1,2}$ yield stability with respect to variations in background shape. In either test the background shape is fixed in the fit, only its normalization is allowed to float.

1. We fit the background to a "rigid" background template extracted from the simulation. The shapes are individually derived for each of the samples A, B, and C. We checked that the change of the continuum-to-$B\overline{B}$ ratio by $\pm 20\%$ does not affect the results of this test.

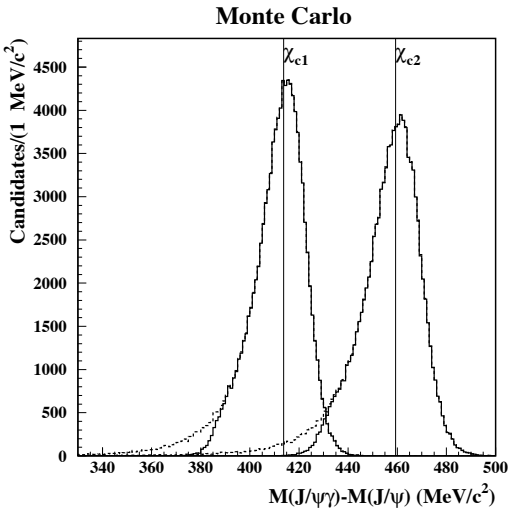

Figure 3.13: The $M(J/\psi\gamma) - M(J/\psi)$ distribution for $\chi_{c1,2}$ candidates reconstructed from the Monte Carlo sample. The solid line represents the candidates for which the reconstructed energy is within 3σ from the generated value. No energy restriction is imposed on the candidates represented by the dashed line. Input $M(\chi_{c1,2}) - M(J/\psi)$ mass difference values are shown by vertical lines.

2. We take the background shape obtained in the inclusive analysis (Figure 3.1a). The same "rigid" background template is used for the samples A, B, and C.

The variations in the background shapes are shown in Figure 3.14. The resulting yield variations are listed in Table 3.21.

3.5.8 Systematic uncertainty associated with composition of X in $B \to \psi(2S)X$ decays

In order to calculate the branching ratio for direct $B \to \chi_{c1,2}X_s$ decays, we need to subtract the feeddown from the $B \to \psi(2S)X$, $\psi(2S) \to \chi_{c1,2}\gamma$ decay chain. If the reconstruction of the $B \to \chi_{c1,2}X_s$ decays were perfect, there would be no $\psi(2S)$ feeddown because of the missing transition photon from the $\psi(2S) \to \chi_{c1,2}\gamma$ decay. The B-reconstruction technique is not perfect, however, and some $\psi(2S)$ feeddown remains. We rely on the Monte Carlo simulation of $B \to \psi(2S)X_s$ decays for the feeddown subtraction. We model the X_s system in $B \to \psi(2S)X_s$ as a mixture of K, K^*, and higher K resonances (20% K, 25% $K^*(892)$, 14% $K_1(1270)$, 14% $K_1(1400)$, 14% $K_0^*(1430)$, and 13% $K_2^*(1430)$). The branching fractions for $B \to \psi(2S)K$ and $B \to \psi(2S)K^*(892)$ decays are taken from [59], they account for approximately half of the $B \to \psi(2S)X$ inclusive rate [48]. To test our $B \to \psi(2S)X_s$ decay model, we reconstruct $\psi(2S) \to \ell^+\ell^-$ decays in the data and in our samples of simulated $B \to \psi(2S)X_s$ events. We compare the $\psi(2S) \to \ell^+\ell^-$ event yields in inclusive reconstruction and after the $B \to \psi(2S)X_s$ reconstruction (Fig-

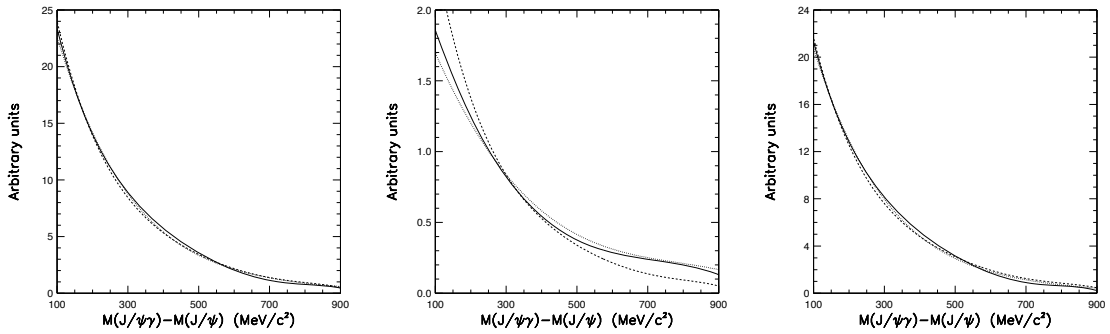

Figure 3.14: The variation of the $M(J/\psi\gamma) - M(J/\psi)$ background shape in the systematic uncertainty study. We show the background shapes in the fits to the samples A (left), B (middle), and C (right). Three background shapes are overlaid in each plot. Solid line represents the fit to a Chebyshev polynomial with all the coefficients floating (Figures 3.1b,c,d). Dashed line shows a fit to a "rigid" background shape extracted from the Monte Carlo simulation. Dotted line represents a fit to "rigid" shape obtained in the inclusive analysis (Figure 3.1a). The relative normalization of the background shapes is obtained from the fits to data.

ure 3.15). The ratio of the yields differs by $0 \pm 8\%$ between the data and the simulation, where 8% is the statistical uncertainty. We therefore assign an 8% uncertainty due to our modeling of the $B \to \psi(2S)X_s$ decays.

Table 3.21: Variations of the χ_{c1} and χ_{c2} yields arising from the changes in background shape.

X_s composition/ background shape	change in	
	$N(\chi_{c1})$ events/%	$N(\chi_{c2})$ events/%
Sample A		
Monte Carlo shape	$+15.2/+5.4\%$	$+13.2/+42.1\%$
shape from inclusive analysis	$+17.5/+6.3\%$	$+11.1/+35.6\%$
Sample B		
Monte Carlo shape	$-2.2/-2.2\%$	$-1.8/-13.2\%$
shape from inclusive analysis	$+0.9/+0.9\%$	$+1.2/+8.4\%$
Sample C		
Monte Carlo shape	$+16.3/+8.9\%$	$+13.6/+76.9\%$
shape from inclusive analysis	$+17.0/+9.3\%$	$+9.3/+52.5\%$

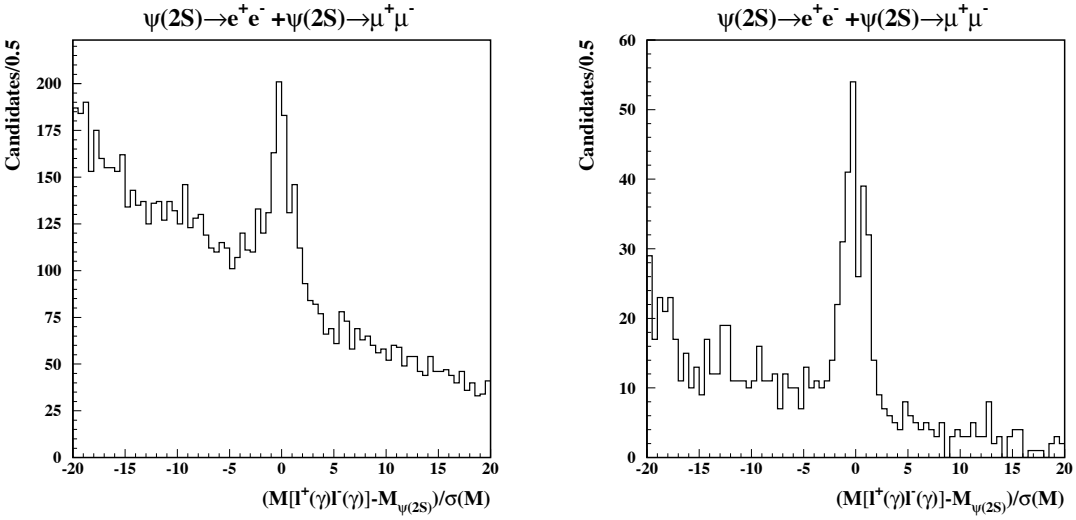

Figure 3.15: Normalized invariant mass for $\psi(2S) \to \ell^+\ell^-$ candidates in data. The left plot shows the inclusive $\psi(2S) \to \ell^+\ell^-$ candidates, whereas the right plot shows only the candidates passing the $B \to \psi(2S)X_s$ reconstruction.

Chapter 4

First observation of the decay $B \to J/\psi\,\phi\,K$

4.1 Abstract

We present the first observation of the decay $B \to J/\psi\,\phi\,K$. Using a sample of 9.6×10^6 $B\overline{B}$ meson pairs, we have observed 10 fully reconstructed $B \to J/\psi\,\phi\,K$ candidates, whereas the estimated background is 0.5 ± 0.2 events. We obtain a branching fraction of $\mathcal{B}(B \to J/\psi\,\phi\,K) = (8.8^{+3.5}_{-3.0}[\text{stat}] \pm 1.3[\text{syst}]) \times 10^{-5}$. This is the first observed B meson decay requiring a creation of an additional $s\overline{s}$ quark pair.

4.2 Introduction

An observation of a B meson decay requiring a creation of an additional $s\overline{s}$ quark pair in the final state would enhance our understanding of strong interactions in the final states of B decays. Previous studies of such processes involved searches for the "lower vertex" $B \to D_s^- X$ transitions (Figure 4.1). ARGUS [60] and CLEO [61] searched for the "lower-vertex" D_s production through the exclusive $B^+ \to D_s^{(*)-} K^+\pi^+$ decays and through D_s–lepton charge correlations. No statistically significant signal has been observed in either search.

The decay $B \to J/\psi\,\phi\,K$ can occur only if an additional $s\overline{s}$ quark pair is created in the decay chain besides the quarks produced in the weak $b \to c\bar{c}s$ transition. The $B \to J/\psi\,\phi\,K$ transition most likely proceeds as a three-body decay (Figure 4.2). Another possibility is that the $B \to J/\psi\,\phi\,K$ decay proceeds as a quasi-two-body decay in which the J/ψ and ϕ mesons are daughters of a hybrid charmonium state [62].

4.3 Analysis summary and results

4.3.1 Reconstruction of $B \to J/\psi\phi K$

We searched for $B^+ \to J/\psi\,\phi\,K^+$ and $B^0 \to J/\psi\,\phi\,K^0_S$ decays, reconstructing $J/\psi \to \ell^+\ell^-$, $\phi \to K^+K^-$, and $K^0_S \to \pi^+\pi^-$. Both e^+e^- and $\mu^+\mu^-$ modes were used for

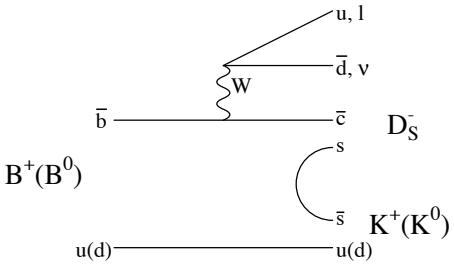

Figure 4.1: A diagram for the lower-vertex D_s production in B decays.

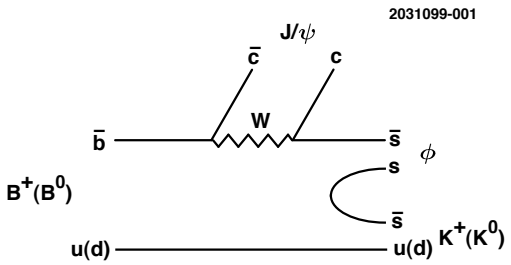

Figure 4.2: The most likely $B \to J/\psi\,\phi\,K$ decay mechanism.

the J/ψ reconstruction. The results of this search are based upon an integrated luminosity of 9.1 fb^{-1} of e^+e^- data taken at the $\Upsilon(4S)$ energy and 4.4 fb^{-1} recorded 60 MeV below the $\Upsilon(4S)$ energy.

The normalized invariant mass distributions for the $J/\psi \to \ell^+\ell^-$ signal in data are shown in Figure 2.16. We required the normalized invariant mass to be from -10 to $+3$ (from -4 to $+3$) for the $J/\psi \to e^+e^-(J/\psi \to \mu^+\mu^-)$ candidates. To improve the energy and momentum resolution of a J/ψ candidate, we performed a fit constraining the mass of each J/ψ candidate to the world average value.

We required that the charged kaon candidates have dE/dx and, if available, time-of-flight measurements that lie within 3 standard deviations of the expected values. Good electron and muon candidates are vetoed in $K^\pm$ selection. If for the $B \to J/\psi\,\phi\,K$ decays we assume a uniform Dalitz distribution and isotropic decays of J/ψ and ϕ mesons, then the expected efficiency of the combined dE/dx and time-of-flight selection is approximately 90% per kaon candidate. The dE/dx measurements alone provide the K/π separation of more than 4 standard deviations for 92% of the ϕ daughter kaons and for 64% of the "bachelor" kaons from B decay. We selected $\phi \to K^+K^-$ candidates by requiring the K^+K^- invariant mass to be within 10 MeV/c^2 of the ϕ mass. We did not use the normalized K^+K^- invariant mass because the mass resolution (1.2 MeV/c^2) is smaller than the ϕ width (4.4 MeV).

The K^0_S candidates were selected from pairs of tracks forming well-measured displaced vertices. The resolution in $\pi^+\pi^-$ invariant mass is about 4 MeV/c^2. We required the absolute value of the normalized $\pi^+\pi^-$ invariant mass to be less than 4, then we performed a fit constraining the mass of each K^0_S candidate to the world average value.

To select $B \to J/\psi\,\phi\,K$ candidates, we required $|\Delta E|/\sigma(\Delta E) < 3$ and $|M(B) - M_B|/\sigma(M) < 3$. The resolution in ΔE for the $B \to J/\psi\,\phi\,K$ candidates is approximately 6 MeV. The resolution in $M(B)$ for the $B \to J/\psi\,\phi\,K$ candidates is about 2.7 MeV/c^2. The distributions of the ΔE vs $M(B)$ for $B^+ \to J/\psi\,\phi\,K^+$ and $B^0 \to J/\psi\,\phi\,K^0_S$ are shown in Figure 4.3. We observed 8(2) events in the signal region for the $B^+ \to J/\psi\,\phi\,K^+$ ($B^0 \to J/\psi\,\phi\,K^0_S$) mode. Considering that K^0 can decay as K^0_S or as K^0_L, and also taking into account $\mathcal{B}(K^0_S \to \pi^+\pi^-)$ and the difference in reconstruction efficiencies, we expect to observe on average 4.3 $B^+ \to J/\psi\,\phi\,K^+$ candidates for every $B^0 \to J/\psi\,\phi\,K^0_S$ candidate. More details on the signal candidate selection can be found in Section 4.4.1.

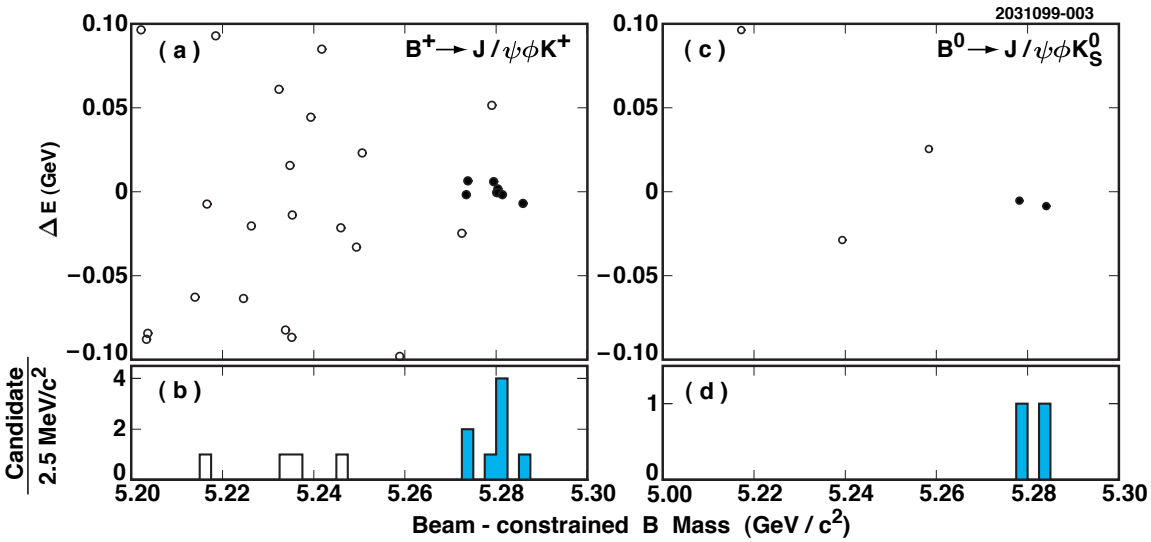

Figure 4.3: The ΔE vs $M(B)$ distribution for (a) $B^+ \to J/\psi\,\phi\,K^+$ and (c) $B^0 \to J/\psi\,\phi\,K^0_S$ candidates in data. The signal candidates, selected using normalized ΔE and $M(B)$ variables, are shown by filled circles. The $M(B)$ distribution for (b) $B^+ \to J/\psi\,\phi\,K^+$ and (d) $B^0 \to J/\psi\,\phi\,K^0_S$ candidates satisfying $|\Delta E|/\sigma(\Delta E) < 3$; the shaded parts of the histograms represent signal candidates.

4.3.2 J/ψ and ϕ polarization in $B \to J/\psi\phi K$ decay

The cosine of helicity angle distributions for the 10 $B \to J/\psi\,\phi\,K$ signal candidates is shown in Figure 4.4. The helicity angle for $J/\psi \to \ell^+\ell^-$ decay is defined as the angle between a lepton momentum in the J/ψ rest frame and the J/ψ momentum in the B rest frame. An analogous definition is used for the $\phi \to K^+K^-$ decay. We expect $I(\cos\theta_{\rm h}) \propto 1 + \cos^2\theta_{\rm h}$ distribution for the transversely polarized J/ψ's ($\lambda_{J/\psi} = \pm 1$); $I(\cos\theta_{\rm h}) \propto 1 - \cos^2\theta_{\rm h}$ for the longitudinal polarization ($\lambda_{J/\psi} = 0$); $I(\cos\theta_{\rm h}) \propto 1 - \cos^2\theta_{\rm h}$ for $\lambda_\phi = \pm 1$; $I(\cos^2\theta_{\rm h}) \propto \cos^2\theta_{\rm h}$ for $\lambda_\phi = 0$. With so few signal events, no conclusion can be drawn yet about the J/ψ and the ϕ polarizations in $B \to J/\psi\,\phi\,K$ decay.

4.3.3 Check for resonant substructure in $B \to J/\psi\phi K$ decay

The Dalitz plot as well as the $M(J/\psi\phi)$, $M(\phi K)$, and $M(J/\psi K)$ distributions for the 10 $B \to J/\psi\,\phi\,K$ signal candidates are shown in Figure 4.5. The Dalitz distribution for the 10 $B \to J/\psi\phi K$ signal candidates is consistent with that of a three-body decay. There are no known $J/\psi\phi$ and $J/\psi K$ resonances. Decays of only 2 particles into ϕK final state have been firmly established [48]:

1. The Particle Data Group lists $K_2(1770) \to \phi K$ decay as "seen" with the $K_2(1770) \to K_2^*(1430)\pi$ mode listed as "dominant";

2. The weak $D^0 \to \phi\overline{K}^0$ decay has been observed with $\mathcal{B}(D^0 \to \phi\overline{K}^0) = (0.86 \pm 0.10)\%$.

If the J/ψ and ϕ mesons are the products of the hybrid charmonium ψ_g decay, then the $J/\psi\,\phi$ invariant mass is expected to be below the DD^{**} threshold (4.3 GeV/c^2) because $\psi_g \to DD^{**}$ decay is likely to dominate above the threshold [62]. The $J/\psi\,\phi$ invariant mass is above 4.3 GeV/c^2 for all 10 $B \to J/\psi\,\phi\,K$ candidates thus disfavoring the hybrid charmonium dominance scenario.

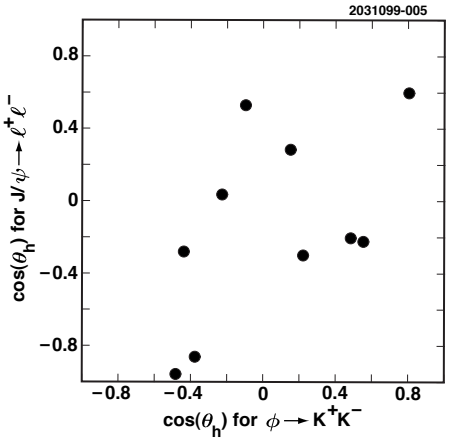

Figure 4.4: The distribution of the cosine of helicity angle for $J/\psi \to \ell^+\ell^-$ vs the cosine of helicity angle for $\phi \to K^+K^-$ for the 10 $B \to J/\psi\,\phi\,K$ candidates.

4.3.4 Background estimation

The background can be divided into two categories. First category is the combinatorial background from $\Upsilon(4S) \to B\overline{B}$ and continuum non-$B\overline{B}$ events. Second category is the background from non-resonant $B \to J/\psi\,K^+\,K^-\,K$ decays.

Combinatorial background. — The combinatorial background from $\Upsilon(4S) \to B\overline{B}$ events was estimated using a sample of simulated events approximately 32 times the data sample; events containing a $B \to J/\psi\,K^+\,K^-\,K$ decay were excluded. We estimated the background from $\Upsilon(4S) \to B\overline{B}$ decays to be $0.25^{+0.10}_{-0.08}$ events. In addition, we specifically considered $B \to J/\psi\,K^*\,\pi^+$ with $K^* \to K\pi^-$ and $B \to J/\psi\,\rho^0\,K$ decays because the B-candidate momentum and therefore the $M(B)$ distribution for these modes is the same as for the $B \to J/\psi\,\phi\,K$ decays. Using data and simulated events, we verified that these backgrounds are rendered negligible by the kaon identification, ϕ mass, and ΔE requirements. The combinatorial background from the continuum non-$B\overline{B}$ events was estimated using simulated events and the data collected below $B\overline{B}$ threshold. We found the continuum background to be negligible.

Non-resonant $B \to J/\psi\,K^+\,K^-\,K$ events. — To estimate the background contribution from the non-resonant $B \to J/\psi\,K^+\,K^-\,K$ decays, we reconstructed $B^+ \to J/\psi\,K^+\,K^-\,K^+$ and $B^0 \to J/\psi\,K^+\,K^-\,K^0_S$ candidates in data requiring $|M(K^+K^-) - M_\phi| > 20$ MeV/c^2 to exclude $B \to J/\psi\,\phi\,K$ events. We observed 7 $B \to J/\psi\,K^+\,K^-\,K$ candidates with the estimated $B\overline{B}$ combinatorial background of 2.8 events. We estimated

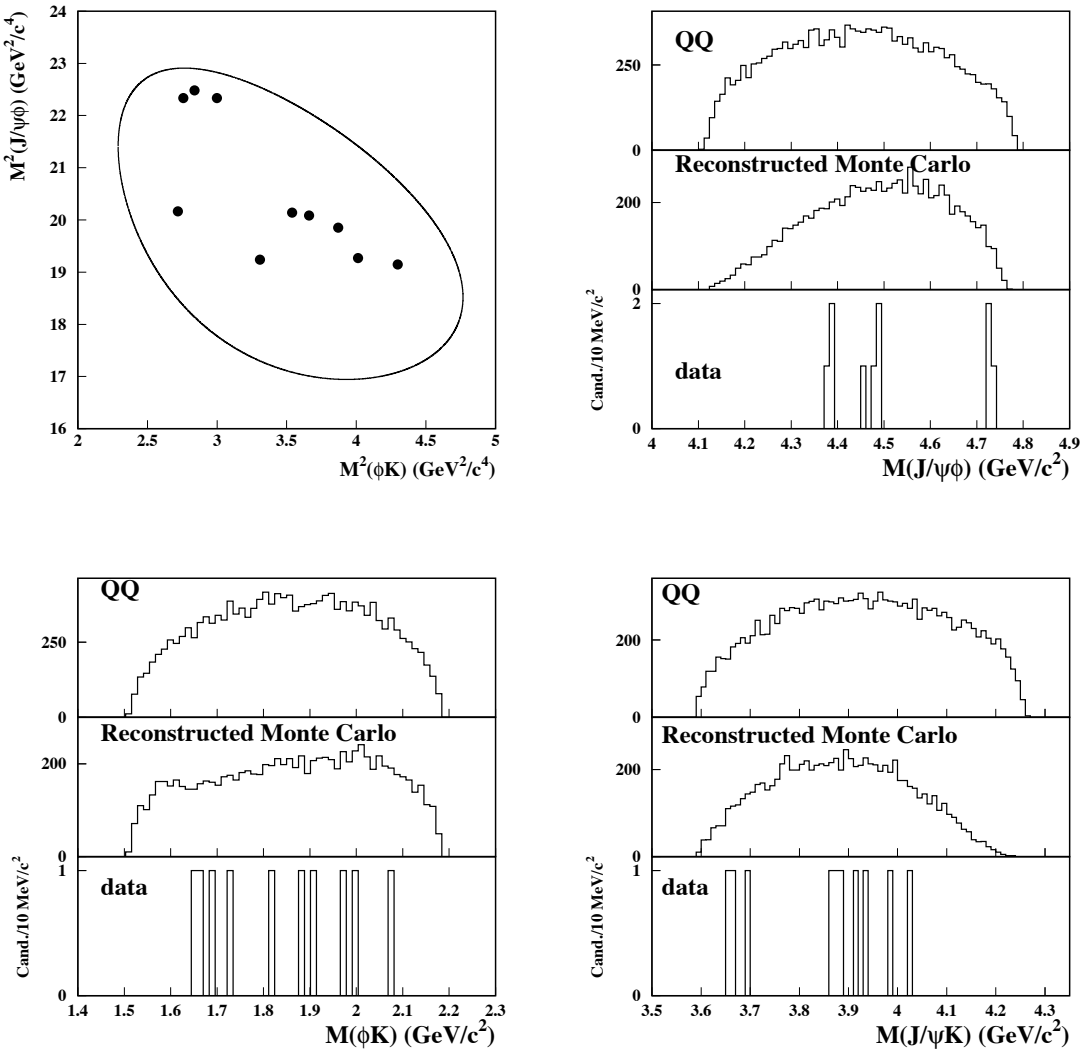

Figure 4.5: Dalitz plot for the 10 $B \to J/\psi\phi K$ candidates (top left); the kinematic boundary is represented by solid line. Invariant mass of the $J/\psi\phi$ (top right), ϕK (bottom left), and $J/\psi K$ (bottom right) system for the 10 signal candidates. We also show the invariant mass distributions obtained from the samples of simulated phase-space $B \to J/\psi\phi K$ decays.

the mean background from $B \to J/\psi\,K^+\,K^-\,K$ decays for the $B \to J/\psi\,\phi\,K$ signal to be $0.27^{+0.21}_{-0.17}$ events; we assumed that $B \to J/\psi\,K^+\,K^-\,K$ decay proceeds according to phase space.

In summary, the estimated total background for the combined $B \to J/\psi\,\phi\,K$ signal is 0.5 ± 0.2 events. The expected background is almost equally split between the $B\overline{B}$ combinatorial background and contribution from non-resonant $B \to J/\psi\,K^+\,K^-\,K$ decays. More details on the background estimation can be found in Section 4.4.2. The Poisson probability of finding 10 or more events when 0.5 is expected is 2×10^{-10}; the corresponding probability of finding 10 or more events when $0.5 + 0.2 = 0.7$ are expected is 4×10^{-9}. The Poisson probability of the background fluctuation to 10 or more events is smaller than 0.27% when the expected background mean is less than 3.4 events.

4.3.5 Reconstruction efficiency

We evaluated the reconstruction efficiency using a sample of simulated $B \to J/\psi\,\phi\,K$ decays. We assumed a uniform Dalitz distribution and isotropic decays of J/ψ and ϕ mesons; these assumptions are consistent with data (Figures 4.4 and 4.5). The reconstruction efficiency, which does not include branching fractions of daughter particle decays, is $(15.5 \pm 0.2)\%$ for the $B^+ \to J/\psi\,\phi\,K^+$ mode and $(10.3 \pm 0.2)\%$ for the $B^0 \to J/\psi\,\phi\,K^0_S$ mode. The reconstruction efficiency is close to zero at the edges of phase space where either ϕ or K meson is produced nearly at rest in the laboratory frame. Thus, the overall detection efficiency would be much smaller than the above values if the $B \to J/\psi\,\phi\,K$ decay is dominated by either a $J/\psi\,K$ resonance with a mass around 4.3 GeV/c^2 or a $J/\psi\,\phi$ resonance with a mass around 4.8 GeV/c^2. No such resonances are expected. To assign the systematic uncertainty due to the decay model dependence of the reconstruction efficiency, we generated two additional samples of simulated $B \to J/\psi\,\phi\,K$ events. One sample was generated with a uniform Dalitz distribution for $B \to J/\psi\,\phi\,K$ and 100% transverse polarization for J/ψ and ϕ. The other sample was generated assuming the ϕ and K mesons to be daughters of a hypothetical spin-0 resonance with mass 1.7 GeV/c^2 and width 100 MeV. We estimated the relative systematic uncertainty due to the decay model dependence of the reconstruction efficiency extraction to be 7%. More details on the reconstruction efficiency estimation can be found in Section 4.4.3.

4.3.6 Branching fraction calculation

For the branching fraction calculation we assumed equal production of B^+B^- and $B^0\overline{B}^0$ pairs at the $\Upsilon(4S)$ resonance [4] and $\mathcal{B}(B^+ \to J/\psi\,\phi\,K^+) = \mathcal{B}(B^0 \to J/\psi\,\phi\,K^0) = \mathcal{B}(B \to J/\psi\,\phi\,K)$. We did not assign any systematic uncertainty due to these two assumptions. We used the world average values of $\mathcal{B}(J/\psi \to \ell^+\ell^-)$, $\mathcal{B}(\phi \to K^+K^-)$, and $\mathcal{B}(K^0_S \to \pi^+\pi^-)$ [47]. We used the Feldman-Cousins method [49] to assign the 68% C.L. intervals for the Poisson signal mean. The resulting branching fraction is $\mathcal{B}(B \to J/\psi\,\phi\,K) = (8.8^{+3.5}_{-3.0}[\text{stat}] \pm 1.3[\text{syst}]) \times 10^{-5}$.

4.3.7 Systematic uncertainties

The systematic error includes the uncertainty in the reconstruction efficiency due to decay modeling plus the uncertainties in track finding, track fitting, lepton and charged-kaon identification, K^0_S finding, background subtraction, uncertainty in the number of $B\overline{B}$ pairs used for this measurement, statistics of the simulated event samples, and the uncertainties on the daughter branching fractions $\mathcal{B}(J/\psi \to \ell^+\ell^-)$ and $\mathcal{B}(\phi \to K^+K^-)$ [47]. We estimated the total relative systematic uncertainty of the $\mathcal{B}(B \to J/\psi\,\phi\,K)$ measurement to be 15%. More details on the systematic uncertainty estimation can be found in Section 4.4.4.

4.3.8 Conclusion

In conclusion, we have fully reconstructed 10 $B \to J/\psi\,\phi\,K$ candidates with a total estimated background of 0.5 events. Assuming equal production of B^+B^- and $B^0\overline{B}^0$ pairs at the $\Upsilon(4S)$ resonance and $\mathcal{B}(B^+ \to J/\psi\,\phi\,K^+) = \mathcal{B}(B^0 \to J/\psi\,\phi\,K^0) = \mathcal{B}(B \to J/\psi\,\phi\,K)$, we have measured $\mathcal{B}(B \to J/\psi\,\phi\,K) = (8.8^{+3.5}_{-3.0}[\text{stat}] \pm 1.3(\text{syst})) \times 10^{-5}$. This is the first observed B meson decay requiring a creation of an additional $s\overline{s}$ quark pair.

4.4 More details on the analysis

4.4.1 Reconstruction of $B \to J/\psi\phi K$

The momentum spectrum of the kaons produced in $B \to J/\psi\phi K$ decay is shown in Figure 4.6. Note that the kaons from the signal decay chain usually have high enough momentum to be reliably reconstructed by the tracking system, and at the same time they are sufficiently soft for good particle identification (Figure 1.10). The momentum spectrum of ϕ mesons produced in $B \to J/\psi\phi K$ decay is shown in Figure 4.7. The $\phi \to K^+K^-$ mass peak is shown in Figure 4.8.

The distributions of the normalized ΔE vs normalized $M(B)$ for $B^+ \to J/\psi\phi K^+$ and $B^0 \to J/\psi\phi K^0_S$ modes are shown in Figure 4.9. We multiplied the reported ΔE uncertainties by a scale factor of 1.2 to make the normalized ΔE distribution look more like a unit Gaussian in the simulation of signal events. All signal candidates come from different events, even though we did not attempt to select a single candidate in a given event.

4.4.2 Background estimation

Combinatorial background from $B\overline{B}$ events

The combinatorial background from $\Upsilon(4S) \to B\overline{B}$ events was estimated using a sample of simulated events approximately 32 times the data sample; events containing a $B \to J/\psi\,K^+\,K^-\,K$ decay were excluded. The distributions of the normalized ΔE vs normalized $M(B)$ obtained with this Monte Carlo sample are shown in Figure 4.10. We estimated the background from generic $B\overline{B}$ decays for the combined $B \to J/\psi\phi K$ signal to be $0.25^{+0.10}_{-0.08}$ events.

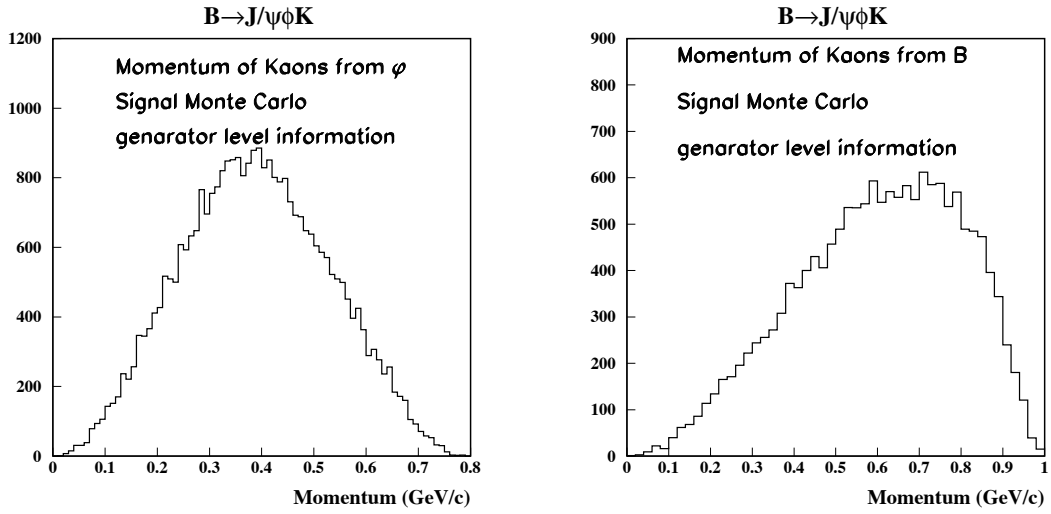

Figure 4.6: Momentum of kaons produced in $B \to J/\psi\phi K$ decay. Left plot is for the kaons from $\phi \to K^+K^-$ decay; right plot is for the bachelor kaons from B decay. The Monte Carlo sample was generated assuming uniform Dalitz plot distribution and non-polarized J/ψ and ϕ.

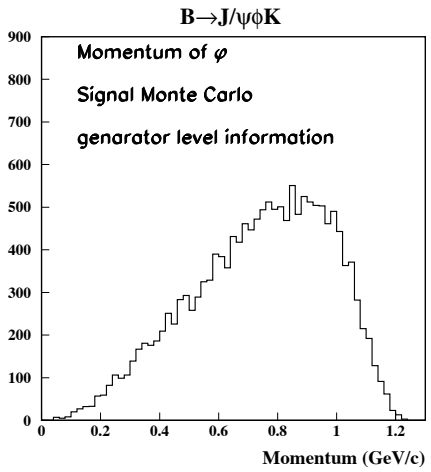

Figure 4.7: Momentum of ϕ mesons produced in $B \to J/\psi\phi K$ decay as determined from the simulated phase-space $B \to J/\psi\phi K$ decays.

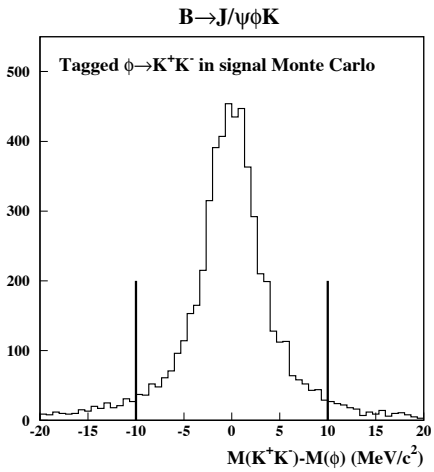

Figure 4.8: Invariant mass peak for tagged $\phi \to K^+K^-$ decays reconstructed from the simulated events. Vertical lines denote the signal region.

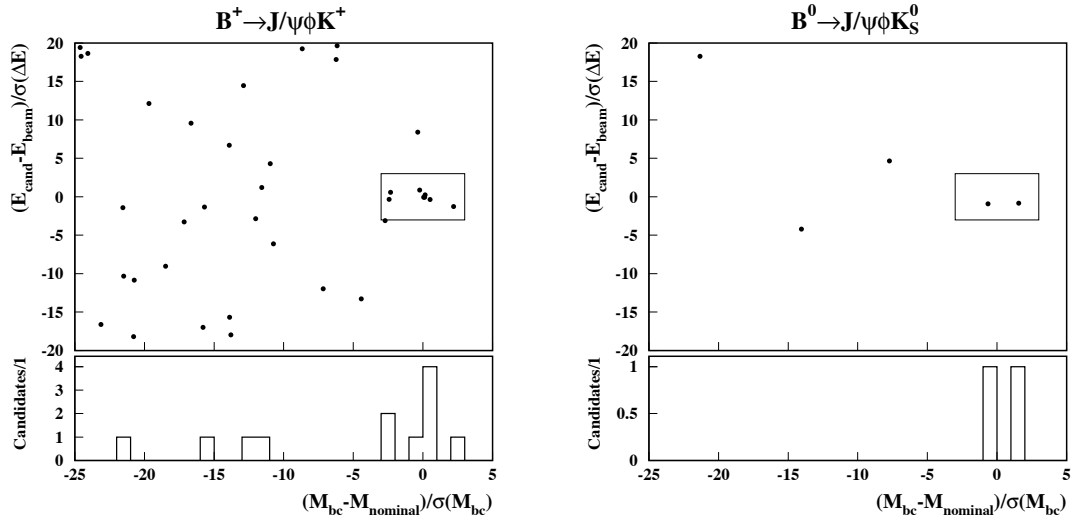

Figure 4.9: Normalized ΔE vs normalized $M(B)$ for $B^+ \to J/\psi\,\phi\,K^+$ (left) and $B^0 \to J/\psi\,\phi\,K^0_S$ (right) candidates in data. The signal box is defined by $|\Delta E|/\sigma(\Delta E) < 3$ and $|M(B) - M_B|/\sigma(M) < 3$. Bottom parts of the plots show the normalized $M(B)$ distribution for the candidates satisfying $|\Delta E|/\sigma(\Delta E) < 3$. There are 8 (2) candidates in the 3σ signal box for the $B^+ \to J/\psi\phi K^+$ ($B^0 \to J/\psi\phi K^0_S$) mode.

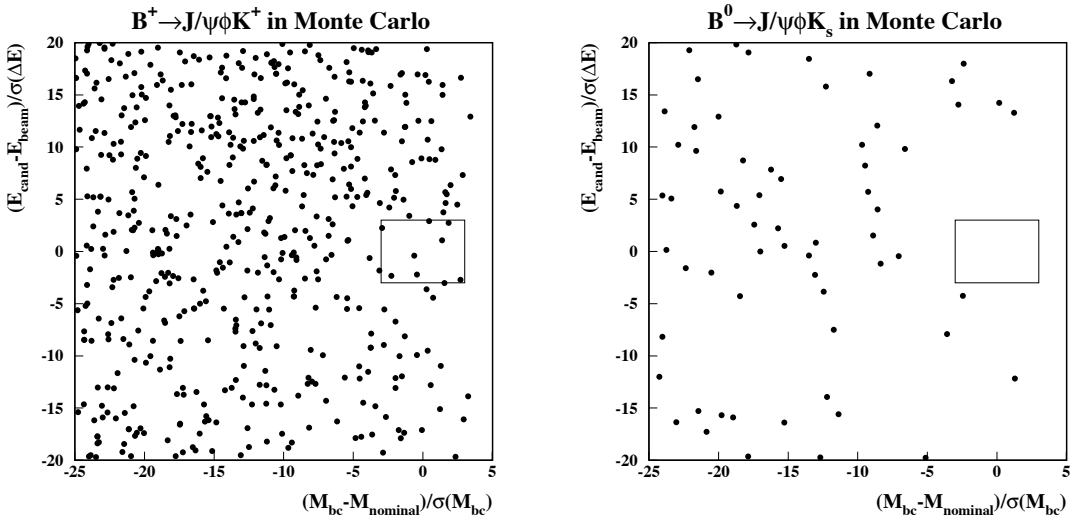

Figure 4.10: Normalized ΔE vs normalized $M(B)$ for $B^+ \to J/\psi\,\phi\,K^+$ (left) and $B^0 \to J/\psi\,\phi\,K^0_S$ (right) candidates in "32 times the data" sample of simulated generic $B\overline{B}$ events.

Background from non-$B\overline{B}$ continuum events

No events from off-$\Upsilon(4S)$ data passed the requirements $-50 < (M(B)-M_B)/\sigma(M) < 5$ and $|\Delta E|/\sigma(\Delta E) < 50$ for either $B^+ \to J/\psi\phi K^+$ or $B^0 \to J/\psi\phi K^0_S$ modes. Only 5 (1) events from the "3.4 times the on-$\Upsilon(4S)$ data" sample of simulated continuum events entered the $-25 < (M(B)-M_B)/\sigma(M) < 5$ and $|\Delta E|/\sigma(\Delta E) < 20$ plane for $B^+ \to J/\psi\phi K^+$ ($B^0 \to J/\psi\phi K^0_S$) mode; no events entered the signal box. We neglect the background from continuum events.

Consistency check for background estimation procedure

Using the samples of simulated $B\overline{B}$ and continuum events as well as off-resonance data, we can estimate the number of events outside the signal box in Figure 4.9.

We learn from the samples of simulated $B^+ \to J/\psi\phi K^+$ events that for every candidate entering signal box we should expect 0.4 events outside the signal box in the same plot. We expect to see, on average, 22 ± 2 events outside the signal box in Figure 4.9(left). We observed 29 events.

The same procedure applied to the $B^0 \to J/\psi\phi K^0_S$ decay yields $2.9^{+0.9}_{-0.5}$ expected events outside the signal box in Figure 4.9(right). We observed 3 events.

Background from $B^+ \to J/\psi K^{*0}\pi^+$, $K^{*0} \to K^+\pi^-$ and $B^+ \to J/\psi\rho^0 K^+$ decays

These decays do not require $s\overline{s}$ popping and could possibly fake the signal because the beam-constrained B mass distribution for these modes is the same as for $B \to J/\psi\,\phi\,K$ decays. The $K^{*0} \to K^+\pi^-$ background for $\phi \to K^+K^-$ was studied in [63].

The branching fraction $\mathcal{B}(B^+ \to J/\psi K^{*0}\pi^+)$ has not yet been measured. We also did not attempt to carefully measure it. In the full data set we observed 240 $B^0 \to J/\psi K^{*0}$, $K^{*0} \to K^+\pi^-$ candidates. In the same data sample we observed 140 $B^+ \to J/\psi K^{*0}\pi^+$, $K^{*0} \to K^+\pi^-$ candidates with about 4 times higher background. Assuming the efficiency penalty for reconstructing an extra pion to be 80%, we obtained $\frac{\mathcal{B}(B^+ \to J/\psi K^{*0}\pi^+)}{\mathcal{B}(B^0 \to J/\psi K^{*0})} < \frac{140}{240 \cdot 0.8} = 0.7$. Then we generated 29,000 simulated events containing $B^+ \to J/\psi K^{*0}\pi^+$; the size of the sample corresponds to "38 times the data" assuming $\mathcal{B}(B^+ \to J/\psi K^{*0}\pi^+) = 0.7 \cdot \mathcal{B}(B^0 \to J/\psi K^{*0})$. Not a single candidate from this Monte Carlo sample entered the signal box in $B^+ \to J/\psi\phi K^+$ analysis. As an independent check, we thought that if we suspect $B^+ \to J/\psi K^{*0}\pi^+$, $K^{*0} \to K^+\pi^-$ to fake $B^+ \to J/\psi\phi K^+$, then the huge $B^0 \to J/\psi K^{*0}$, $K^{*0} \to K^+\pi^-$ signal should produce some fake signal in $B^0 \to J/\psi\phi$ mode. We observed no signal candidates for the $B^0 \to J/\psi\phi$ decay in data. We conclude that the background from $B^+ \to J/\psi K^{*0}\pi^+$ decays can be neglected.

We also generated 15,000 simulated events containing $B^+ \to J/\psi\rho^0 K^+$; the size of the sample corresponds to "20 times the data" assuming $\mathcal{B}(B^+ \to J/\psi\rho^0 K^+) = 0.7 \cdot \mathcal{B}(B^0 \to J/\psi K^{*0})$. Not a single candidate entered the signal box in $B^+ \to J/\psi\phi K^+$ analysis. We conclude that the background from $B^+ \to J/\psi\rho^0 K^+$ decays is negligible.

Background from non-resonant $B \to J/\psi K^+K^-K$ decays

This mode is not yet a signal but already a background. The only cut which discriminates $B \to J/\psi\phi K$ from $B \to J/\psi K^+K^-K$ is the cut on ϕ mass. To estimate the background from $B \to J/\psi K^+K^-K$ decays, we first reconstructed $B \to J/\psi K^+K^-K$ events in data imposing the requirement $|M(K^+K^-) - M_\phi| > 20$ MeV (Figure 4.11). Then, using the simulation of the phase-space $B \to J/\psi K^+K^-K$ decays, we estimated the number of $B \to J/\psi K^+K^-K$ events expected to pass $|M(K^+K^-) - M_\phi| < 10$ MeV cut, given the number of events reconstructed with $|M(K^+K^-) - M_\phi| > 20$ MeV cut. There are 6 events in the signal box for $B^+ \to J/\psi K^+K^-K^+$ mode and 1 event in the signal box for $B^0 \to J/\psi K^+K^-K^0_S$ mode. The estimated $B\overline{B}$ background from the "32 times the data" sample is 2.8 events. The Poisson probability for 2.8 events to fluctuate to 7 or more is 2.5%, therefore we do not claim an observation of the non-resonant $B \to J/\psi K^+K^-K$ decay. the non-resonant $B \to J/\psi K^+K^-K$ decay. Using the Feldman-Cousins tables [49], we determined the 68% C.L. interval for the $B \to J/\psi K^+K^-K$ signal to be $4.2^{+3.3}_{-2.6}$. The simulation of the $B \to J/\psi K^+K^-K$ signal events tells us that for every event observed with $|M(K^+K^-) - M_\phi| > 20$ MeV cut, we should see $6.4 \cdot 10^{-2}$ signal events reconstructed with the cut $|M(K^+K^-) - M_\phi| < 10$ MeV. Total background from $B \to J/\psi K^+K^-K$ decays is estimated to be $0.27^{+0.21}_{-0.17}$ events.

Top two plots in Figure 4.12 display the distribution of the K^+K^- invariant mass for all $B \to J/\psi K^+K^-K$ candidates in data entering signal box in $M(B)$ vs ΔE plane; the ϕ mass cut was not applied. There are 15 $B^+ \to J/\psi K^+K^-K^+$ candidates (top left plot in Figure 4.12), 8 of which were classified as $B^+ \to J/\psi\phi K^+$ candidates ($|M(K^+K^-) - M_\phi| <$ 10 MeV/c^2). There are 4 $B^0 \to J/\psi K^+K^-K^0_S$ candidates (top right plot in Figure 4.12), 2 of which were classified as $B^0 \to J/\psi\phi K^0_S$ candidates. Two plots in the middle row of Figure 4.12 display the distribution of the K^+K^- invariant mass for all $B \to J/\psi K^+K^-K$ candidates in the sample of simulated phase-space $B \to J/\psi K^+K^-K$ events. Two bottom plots were obtained using "32 times the data" sample of simulated generic $B\overline{B}$ events; the events containing a $B \to J/\psi\,K^+\,K^-\,K$ decay were excluded.

4.4.3 Reconstruction efficiency

The Dalitz plot structure and the polarization of J/ψ and ϕ are not known for the $B \to J/\psi\phi K$ decay. We estimated the reconstruction efficiency using the Monte Carlo simulation of the $B \to J/\psi\phi K$ events, where we assumed uniform Dalitz plot distribution and non-polarized J/ψ and ϕ (Figure 4.13-left column). To study the decay model dependence of the reconstruction efficiency, we generated two additional samples of simulated signal events. One sample was generated with uniform Dalitz plot distribution and 100% transverse polarization of J/ψ and ϕ (Figure 4.13-middle column). The other sample was generated assuming ϕ and K are daughters of a hypothetical spin-0 resonance with the mass of 1.7 GeV and the width of 100 MeV (Figure 4.13-right column). Note that we defined the helicity angle for $\phi \to K^+K^-$ decay as the angle between K^+ direction in ϕ rest frame and ϕ direction in B rest frame. If we take ϕ direction in ϕK^+ resonance rest frame, we will obtain $\cos^2\theta_{\rm helicity}$ distribution, as expected for $\lambda_\phi = 0$ state.

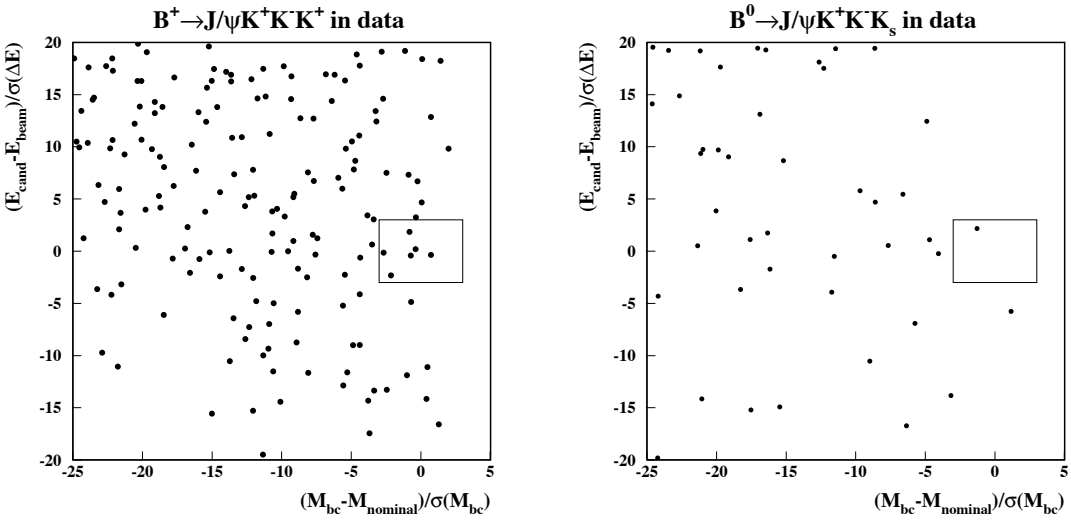

Figure 4.11: Normalized ΔE vs normalized $M(B)$ for $B^+ \to J/\psi K^+K^-K^+$ (left) and $B^0 \to J/\psi K^+K^-K^0_S$ (right) candidates in data. We required $|M(K^+K^-) - M_\phi| > 20$ MeV (for both K^+K^- pairs in $B^+ \to J/\psi K^+K^-K^+$) to exclude contribution from $B \to J/\psi\phi K$ decays. There are 6 (1) candidates in the 3σ signal box for the $B^+ \to J/\psi K^+K^-K^+$ ($B^0 \to J/\psi K^+K^-K^0_S$) mode.

The Dalitz plots for the $B^+ \to J/\psi\phi K^+$ candidates reconstructed from the simulated signal events are shown in Figure 4.14. One can clearly see two depleted regions. In the first region the mass of the $J/\psi\phi$ system is high, therefore bachelor kaons are soft for the depleted region in upper part of the plots. In the second region the mass of the $J/\psi K^+$ system is high, therefore ϕ's are soft for the depleted region in lower part of the plots.

The reconstruction efficiencies obtained for different samples of simulated signal events are listed in Table 4.1.

4.4.4 Systematic uncertainties

We estimated the total relative systematic uncertainty on the $\mathcal{B}(B \to J/\psi\phi K)$ measurement to be 15%. The systematic uncertainty includes contributions from the uncertainty in the number of $B\overline{B}$ pairs (2%), tracking efficiency (1% per charged track), lepton detection efficiency (3% per lepton), $K^0_S \to \pi^+\pi^-$ finding efficiency (3%), 3σ dE/dx cut for kaons (3% per track), 3σ time-of-flight cut for kaons (4% per track), $K^0_S \to \pi^+\pi^-$ finding efficiency (3%), background subtraction (5%), and statistics of the simulated event sample (1%). We also included the uncertainties on the branching fractions of secondary decays [47]: $\mathcal{B}(J/\psi \to \ell^+\ell^-)$ (3%), $\mathcal{B}(\phi \to K^+K^-)$ (2%), and $\mathcal{B}(K^0_S \to \pi^+\pi^-)$ (0.4%). At the time of the measurement Monte Carlo simulation was tuned for only one of ten CLEO II.V datasets (`4SP`). We assigned 4% uncertainty for this shortcoming, which is half of the difference in efficiency between CLEO II and CLEO II.V detector configurations (Table 4.1). From the study described in Section 4.4.3, we assigned 7% uncertainty for the decay model depen-

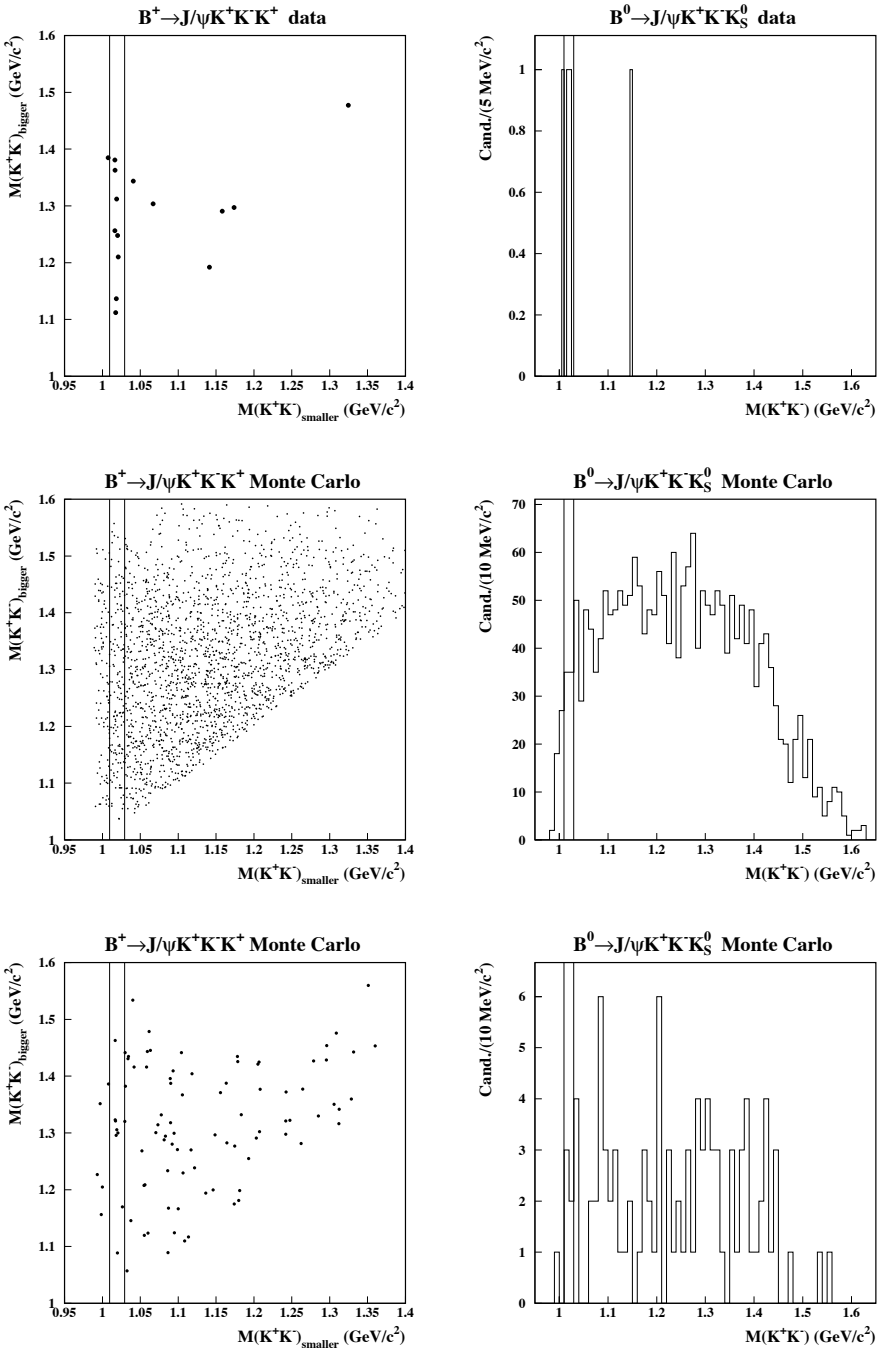

Figure 4.12: $M(K^+K^-)$ for $B \to J/\psi K^+K^-K$ candidates passing $M(B)$ and ΔE cuts. Top row – data, middle row – simulation of phase-space signal $B \to J/\psi K^+K^-K$ decays, bottom row – "32 times the data" sample of simulated generic $B\overline{B}$ events. Note that one can assemble two K^+K^- pairs for $B^+ \to J/\psi K^+K^-K^+$ mode. Vertical lines represent ± 10 MeV/c^2 window around the ϕ mass.

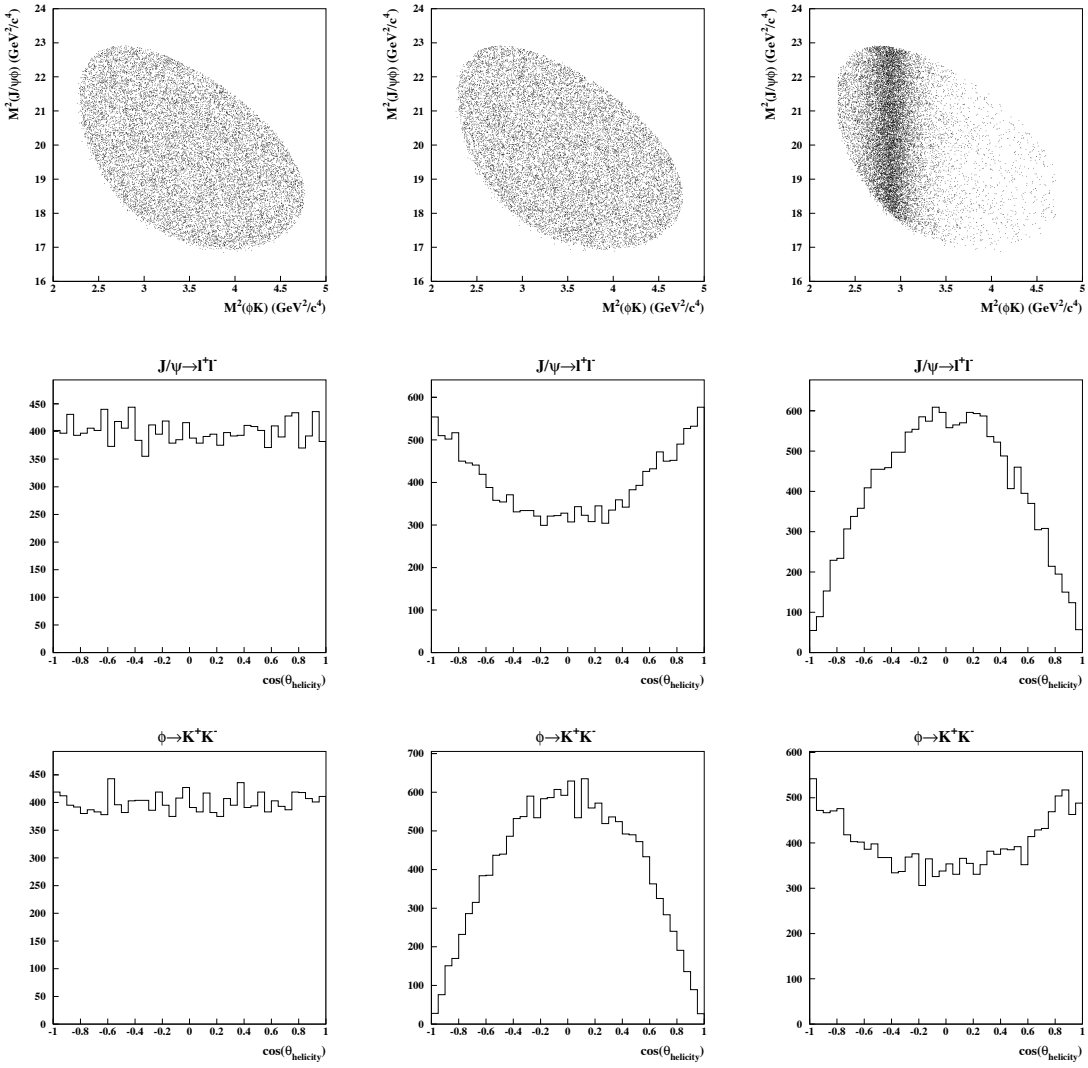

Figure 4.13: Various distributions for the three signal Monte Carlo samples. Generator-level information was used. Top row — Dalitz plots; middle row — cosine of helicity angle for $J/\psi \to \ell^+\ell^-$; bottom row — cosine of helicity angle for $\phi \to K^+K^-$. Left column — phase-space, no polarization Monte Carlo sample; middle column — phase-space, J/ψ and ϕ are produced in helicity ± 1 state; right column — ϕ and K are daughters of a hypothetical spin-0 resonance with the mass of 1.7 GeV and the width of 100 MeV.

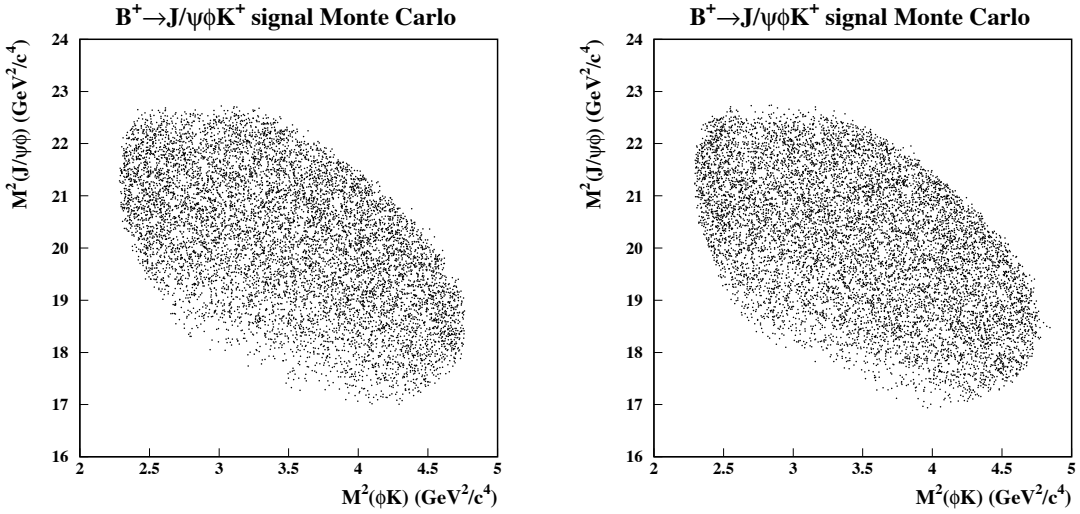

Figure 4.14: Dalitz plot for the $B^+ \to J/\psi\phi K^+$ candidates reconstructed from the simulated signal events. To obtain the left plot, we used phase-space simulated decays with flat angular distribution for the $J/\psi \to \ell^+\ell^-$ and $\phi \to K^+K^-$ decays (Figure 4.13-left column); for the right plot we used phase-space simulated decays with J/ψ's and ϕ's produced in helicity ± 1 state (Figure 4.13-middle column).

Table 4.1: Reconstruction efficiency for different samples of simulated $B \to J/\psi\,\phi\,K$ events.

Monte Carlo Sample	Data set	Efficiency	
		$B^+ \to J/\psi\phi K^+$	$B^\to J/\psi\phi K^0_S$
Phase space	CLEO II+II.V	$(15.50 \pm 0.16)\%$	$(10.33 \pm 0.17)\%$
no polarization	CLEO II	$(14.58 \pm 0.27)\%$	$(10.52 \pm 0.24)\%$
(Figure 4.13-left column)	CLEO II.V	$(15.98 \pm 0.21)\%$	$(10.38 \pm 0.17)\%$
Phase space	CLEO II+II.V	$(16.58 \pm 0.17)\%$	
polarized J/ψ and ϕ	CLEO II	$(15.74 \pm 0.28)\%$	
(Figure 4.13-middle column)	CLEO II.V	$(17.02 \pm 0.21)\%$	
ϕK^+ resonance	CLEO II+II.V	$(14.37 \pm 0.16)\%$	
	CLEO II	$(13.63 \pm 0.26)\%$	
(Figure 4.13-right column)	CLEO II.V	$(14.67 \pm 0.20)\%$	

dence of the reconstruction efficiency (Table 4.1). We assumed equal production of B^+B^- and $B^0\overline{B}^0$ pairs at the $\Upsilon(4S)$ resonance and $\mathcal{B}(B^+ \to J/\psi\phi K^+) = \mathcal{B}(B^0 \to J/\psi\phi K^0) = \mathcal{B}(B \to J/\psi\phi K)$; we did not assign any systematic error for these two assumptions.

Chapter 5

Measurement of the B^0 and B^+ meson masses from $B \to \psi^{(\prime)} K$ decays

5.1 Abstract

Using a sample of 9.6×10^6 $B\overline{B}$ meson pairs, we have fully reconstructed 135 $B^0 \to \psi^{(\prime)} K^0_S$ and 526 $B^+ \to \psi^{(\prime)} K^+$ candidates with very low background. We fitted the $\psi^{(\prime)} K$ invariant mass distributions of these B meson candidates and measured the masses of the neutral and charged B mesons to be $M(B^0) = 5279.1 \pm 0.7[\text{stat}] \pm 0.3[\text{syst}]$ MeV/c^2 and $M(B^+) = 5279.1 \pm 0.4[\text{stat}] \pm 0.4[\text{syst}]$ MeV/c^2. The precision is a significant improvement over previous measurements.

5.2 Introduction

The previous measurements of the B meson masses at e^+e^- colliders operating at $\Upsilon(4S)$ energy [64, 65] were obtained from fits to the distributions of the beam-constrained B mass $M_{\rm bc} \equiv \sqrt{E^2_{\rm beam} - p^2(B)}$ [1] for the copious $B \to D^{(*)}\pi$, $D^{(*)}\rho$, $J/\psi K^{(*)}$ decay modes. Substitution of the beam energy for the measured energy of the B meson candidate results in a significant improvement of the mass resolution, therefore the beam-constrained mass method is the technique of choice for the $M(B^0) - M(B^+)$ mass difference measurement. However, the precision of the measurement of the absolute B^0 and B^+ meson masses is limited by the systematic uncertainties in the absolute beam energy scale (± 2 MeV) and in the correction for initial state radiation (± 0.5 MeV). The absolute value of the CESR beam energy in the $\Upsilon(4S)$ region was determined by the extrapolation from $\Upsilon(1S)$ energy which is known from the resonant beam depolarization studies [66]. The extrapolation uncertainty was estimated by making small perturbations in the magnetic field strengths assumed in the algorithm used to compute the beam energy at the $\Upsilon(4S)$ [67].

[1] In this chapter we use $M_{\rm bc}$ notation for beam-constrained B mass. The B^0 and B^+ masses are denoted by $M(B^0)$ and $M(B^+)$.

For this measurement we selected $B^0 \to \psi^{(\prime)} K^0_S$ and $B^+ \to \psi^{(\prime)} K^+$ candidates[2], reconstructing $\psi^{(\prime)} \to \ell^+\ell^-$ and $K^0_S \to \pi^+\pi^-$ decays. We used both e^+e^- and $\mu^+\mu^-$ modes for the $\psi^{(\prime)}$ reconstruction. We then determined the B^0 and B^+ meson masses by fitting the $\psi^{(\prime)} K^0_S$ and $\psi^{(\prime)} K^+$ invariant mass distributions. The main reasons to use the $\psi^{(\prime)}K$ rather than more copious $D^{(*)}n\pi$ final states are, first, that the background is very low; second, that the J/ψ and $\psi(2S)$ mesons are heavy, and their masses are very well measured. As discussed below, constraining the reconstructed J/ψ and $\psi(2S)$ masses to their world average values makes our B mass measurement insensitive to imperfections in the lepton momentum reconstruction. By comparing the beam-constrained B mass to the B^0 and B^+ mass values obtained in our measurement, one could set the absolute beam energy scale at the e^+e^- colliders operating in the $\Upsilon(4S)$ energy region.

5.3 Analysis summary and results

5.3.1 B^0 and B^+ candidate selection

For this measurement we used 9.1 fb^{-1} of e^+e^- data taken at the $\Upsilon(4S)$ energy and 4.4 fb^{-1} recorded 60 MeV below the $\Upsilon(4S)$ energy. The J/ψ selection criteria were modified slightly from those used in our other analyses and described in Chapter 2. First, we do not use the shallow-angle muon candidates pointing to the detector region not instrumented by the muon chambers ($|\cos\theta| > 0.85$); these tracks are poorly measured and result in higher background. Second, the J/ψ mass cut was made symmetric in order to reduce backgrounds and limit the B mass measurement bias caused by bremsstrahlung. The $\psi(2S) \to \ell^+\ell^-$ candidates were selected using the same cuts as used for the J/ψ selection. The $e^+(\gamma)e^-(\gamma)$ and $\mu^+\mu^-$ invariant mass distributions for the $\psi^{(\prime)} \to \ell^+\ell^-$ candidates in data are shown in Figure 5.1. We selected the $\psi^{(\prime)} \to \ell^+\ell^-$ signal candidates requiring the absolute value of the normalized invariant mass to be less than 3. For each $\psi^{(\prime)}$ candidate we performed a fit constraining its mass to the world average value. This mass-constraint fit improves the J/ψ energy resolution almost by a factor of 4 and the absolute momentum resolution by 30%.

The K^0_S candidates were selected from pairs of tracks forming well-measured displaced vertices. The daughter pion tracks were re-fitted taking into account the position of the displaced vertex and were constrained to originate from the same spatial point. The resolution in $\pi^+\pi^-$ invariant mass is approximately 4 MeV/c^2. After requiring the absolute value of the normalized $\pi^+\pi^-$ invariant mass to be less than 3, we performed a fit constraining the mass of each K^0_S candidate to the world average value. We required that the charged kaon candidates have dE/dx measurement that lie within 3 standard deviations of the expected value. Good electron and muon candidates were vetoed in $K^\pm$ selection.

The $B \to \psi^{(\prime)} K$ candidates were selected by means of two observables. The first observable is the beam-constrained B mass $M_{\rm bc} \equiv \sqrt{E^2_{\rm beam} - p^2(B)}$. The resolution in $M_{\rm bc}$ for the $B \to \psi^{(\prime)} K$ candidates is approximately 2.7 MeV/c^2 and is dominated by the beam energy spread. We required $|M_{\rm bc} - 5280\ {\rm MeV}/c^2|/\sigma(M_{\rm bc}) < 3$. The requirement on $M_{\rm bc}$, equivalent to a requirement on the absolute value of the B candidate

[2] $\psi^{(\prime)}$ stands for J/ψ and $\psi(2S)$.

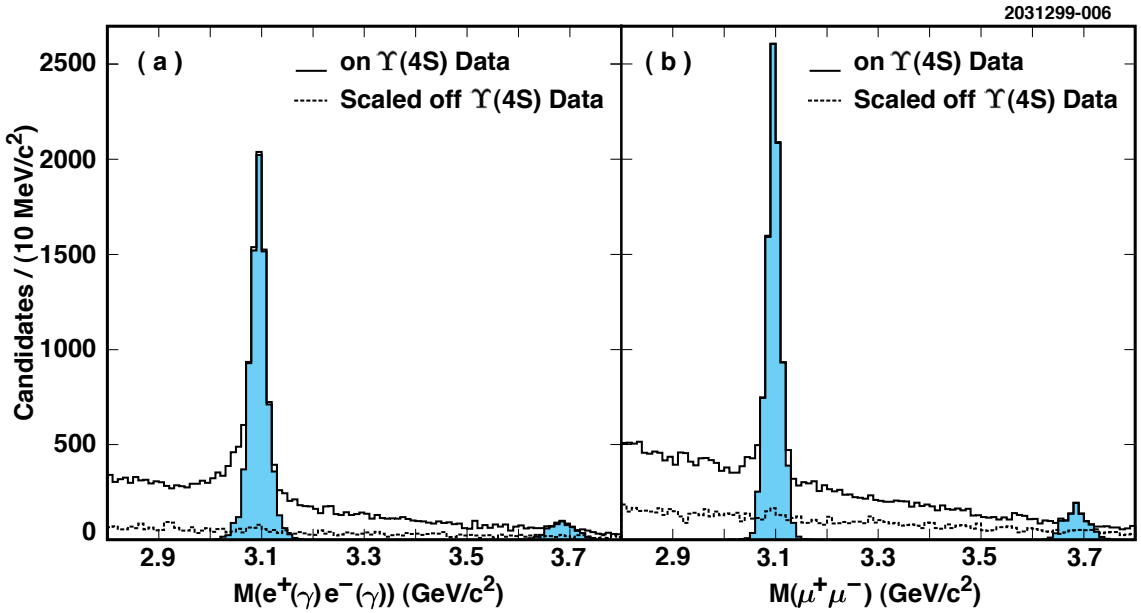

Figure 5.1: (a) $\psi^{(\prime)} \to e^+e^-$ and (b) $\psi^{(\prime)} \to \mu^+\mu^-$ candidates in data. The solid line represents the $\Upsilon(4S)$ data; the dashed line represents the scaled off-resonance data showing the level of background from non-$B\overline{B}$ events. The shaded parts of the histograms represent the $\psi^{(\prime)}$ candidates with the absolute value of the normalized invariant mass less than 3.

momentum, is used only for background suppression and does not bias the B mass measurement. The second observable is the invariant mass of the $\psi^{(\prime)} K$ system. The average resolutions in $M(\psi^{(\prime)} K^0_S)$ and $M(\psi^{(\prime)} K^+)$ are, respectively, 8 MeV/c^2 and 11 MeV/c^2. The $M(\psi^{(\prime)} K)$ distributions for the candidates passing the $M_{\rm bc}$ requirement are shown in Figure 5.2. More plots pertaining to the selection of the B candidates can be found Section 5.4.1. To select signal candidates, we required $|M(\psi^{(\prime)} K^0_S) - 5280 \text{ MeV}/c^2|/\sigma(M) < 4$ and $|M(\psi^{(\prime)} K^+) - 5280 \text{ MeV}/c^2|/\sigma(M) < 3$; the allowed invariant mass intervals are sufficiently wide not to introduce bias in the B mass measurement. This selection yielded 135 $B^0 \to \psi^{(\prime)} K^0_S$ candidates: 125 in the $B^0 \to J/\psi\, K^0_S$ mode and 10 in the $B^0 \to \psi(2S)\, K^0_S$ mode. We estimated the background to be $0.13^{+0.09}_{-0.05}$ events. The selection yielded 526 $B^+ \to \psi^{(\prime)} K^+$ candidates: 468 in $B^+ \to J/\psi\, K^+$ mode and 58 in $B^+ \to \psi(2S)\, K^+$ mode. The background from $B^+ \to \psi^{(\prime)} \pi^+$ decays was estimated to be 0.9 ± 0.3 events, whereas all other background sources were estimated to contribute $2.3^{+1.0}_{-0.5}$ events. The backgrounds were evaluated with simulated events and the data recorded at the energy below the $B\overline{B}$ production threshold. The background estimation for B^0 and B^+ candidates is described in more detail in Sections 5.4.2 and 5.4.3. We discuss the systematics associated with background in Section 5.3.3, together with other systematic uncertainties.

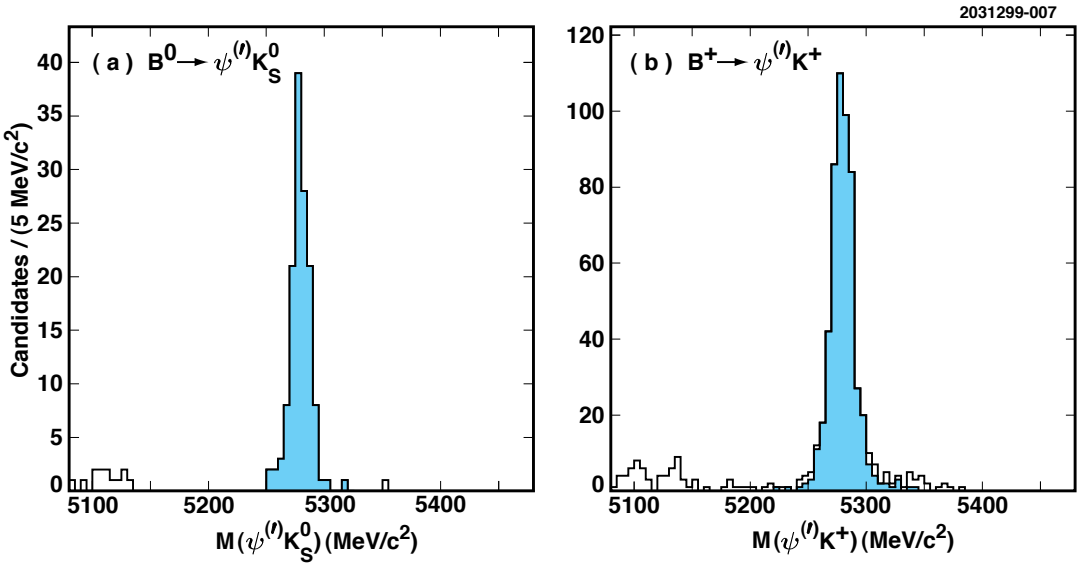

Figure 5.2: The invariant mass distributions for (a) $B^0 \to \psi^{(\prime)} K^0_S$ and (b) $B^+ \to \psi^{(\prime)} K^+$ candidates passing the beam-constrained B mass requirement. The shaded parts of the histograms represent the candidates selected for the B mass measurement fits by requiring that the absolute value of the normalized invariant mass to be less than 4 in (a) and 3 in (b).

5.3.2 B-mass likelihood fit

The B^0 and B^+ meson masses were extracted from the $\psi^{(\prime)} K^0_S$ and $\psi^{(\prime)} K^+$ invariant mass distributions with an unbinned likelihood fit. The likelihood function is

$$\mathcal{L}(M(B), S) = \prod_i \frac{G(M_i - M(B)|S\sigma_i)}{\int G(M - M(B)|S\sigma_i) dM} \quad , \tag{5.1}$$

where M_i is the invariant mass of a $\psi^{(\prime)} K$ combination, σ_i is the calculated invariant mass uncertainty for that $\psi^{(\prime)} K$ combination, and $G(x|\sigma) \equiv 1/(\sqrt{2\pi}\sigma) \exp(-x^2/2\sigma^2)$. The product is over the B^0 or B^+ meson candidates. The parameters of the fit are the B meson mass $M(B)$ and a global scale factor S that modifies the calculated invariant-mass uncertainties σ_i. The integration limits of the normalization integral in the denominator correspond to the signal regions defined for the $\psi^{(\prime)} K$ invariant mass distributions: [5280 MeV/$c^2 \pm 4\sigma(M)$] for B^0 and [5280 MeV/$c^2 \pm 3\sigma(M)$] for B^+ candidates. From the fits to the $\psi^{(\prime)} K^0_S$ invariant-mass distribution, we obtained $M(B^0) = 5278.97 \pm 0.67$ MeV/c^2, $S = 1.24 \pm 0.08$, and the correlation coefficient $\rho(M(B^0), S) = -0.013$. For $\psi^{(\prime)} K^+$ we obtained $M(B^+) = 5279.50 \pm 0.41$ MeV/c^2, $S = 1.09 \pm 0.04$, and $\rho(M(B^+), S) = -0.015$. The values of the scale factor S and uncertainty in $M(B)$ returned by the fits are in good agreement with the values obtained from simulated events (Section 5.4.4).

5.3.3 Bias corrections and systematic uncertainties

Table 5.1 lists the bias corrections together with associated systematic uncertainties, which we will discuss below.

Table 5.1: Bias corrections and associated systematic uncertainties. The total systematic uncertainty was obtained by adding in quadrature all the uncertainties listed in the table.

	Source of bias	Correction and uncertainty (MeV/c^2)	
		$M(B^0)$	$M(B^+)$
(i)	Bias observed for simulated events	$+0.08 \pm 0.08$	-0.13 ± 0.13
(ii)	Background	± 0.05	± 0.17
(iii)	B mass likelihood fit	± 0.14	± 0.09
(iv)	$\psi^{(\prime)}$ four-momentum measurement	± 0.05	± 0.06
(v)	K^0_S four-momentum measurement	± 0.28	—
(vi)	K^+ momentum measurement	—	-0.32 ± 0.34
(vii)	Detector misalignment	± 0.04	± 0.05
Total correction and systematic uncertainty		$+0.08 \pm 0.33$	-0.45 ± 0.42

(i) *Measuring B masses using simulated events.* — Applying the same procedure as in the data analysis, we measured the B^0 and B^+ mass using 30286 $B^0 \to \psi^{(\prime)} K^0_S$ and 34519 $B^+ \to \psi^{(\prime)} K^+$ candidates reconstructed from a sample of simulated events (Section 5.4.4). We obtained $M(B^0) - M^{\rm input}_{B^0} = -0.08 \pm 0.04$ MeV/c^2 and $M(B^+) - M^{\rm input}_{B^+} = +0.13 \pm 0.05$ MeV/c^2. We applied $+0.08$ MeV/c^2 and -0.13 MeV/c^2 corrections to the B^0 and B^+ mass values and assigned 100% of those corrections as systematic uncertainties.

(ii) *Background.* — The estimated mean background for the B^0 candidates is $0.13^{+0.09}_{-0.05}$ events, we therefore conservatively assumed the probability of finding a single background event in our B^0 sample to be 22%. The B^0 background candidates are expected to be uniformly distributed across the B^0 mass signal region. We performed the B^0 mass fits excluding the one candidate with the highest or the lowest normalized $\psi^{(\prime)} K^0_S$ invariant mass; the largest observed B^0 mass shift was 0.25 MeV/c^2. We multiplied this 0.25 MeV/c^2 shift by the 22% probability of having a background event in our sample and assigned 0.05 MeV/c^2 as the systematic uncertainty in B^0 mass due to background. For the B^+ signal, the background from $B^+ \to \psi^{(\prime)} \pi^+$ decays was estimated to be 0.9 ± 0.3 events, all other background sources were estimated to contribute $2.3^{+1.0}_{-0.5}$ events. The B^+ background candidates, with the exception of $B^+ \to \psi^{(\prime)} \pi^+$ events, are expected to be uniformly distributed across the B mass signal region. The $B^+ \to \psi^{(\prime)} \pi^+$ events reconstructed as $B^+ \to \psi^{(\prime)} K^+$ produce high $\psi^{(\prime)} K^+$ invariant mass. We performed the B^+ mass fits excluding 4 candidates with the highest or the lowest normalized $\psi^{(\prime)} K^+$ invariant mass and assigned the largest shift of the measured B^+ mass (0.17 MeV/c^2) as the systematic uncertainty in B^+ mass due to background. More details can be found in Section 5.4.5.

(iii) *B mass likelihood fit.* — We studied the systematics associated with the unbinned likelihood fit procedure by changing the fit function from a Gaussian to sum of two Gaussians. We also allowed the fit to determine different scale factors S for the candidates coming from CLEO II and CLEO II.V data, or for the candidates with $\psi^{(\prime)} \to e^+e^-$ and

$\psi^{(\prime)} \to \mu^+\mu^-$. We assigned the largest shift of the measured B mass as the systematic uncertainty. More details can be found in Section 5.4.6.

(iv) *$\psi^{(\prime)}$ four-momentum measurement.* — Even if the B mass measurements using the simulated events show negligible bias, a bias in the measurement is still in principle possible because of the uncertainty in the absolute magnetic field scale, an imperfect description of the detector material used by the Billoir fitter, or a detector misalignment. For the $\psi^{(\prime)}$ four-momentum measurement, these systematic effects along with the systematics associated with bremsstrahlung are rendered negligible by the the $\psi^{(\prime)}$ mass-constraint fit. The measured position of the J/ψ mass peak allows a reliable evaluation of the possible bias in the lepton momentum measurement. We measured the positions of the $J/\psi \to \mu^+\mu^-$ and $J/\psi \to e^+e^-$ peaks by fitting the inclusive $\mu^+\mu^-$ and $e^+(\gamma)e^-(\gamma)$ invariant mass distributions (Appendix B). In these fits we used the signal shapes derived from a high-statistics sample of simulated $J/\psi \to \ell^+\ell^-$ events generated with the J/ψ mass of 3096.88 MeV/c^2 [47]. In simulated $J/\psi \to \mu^+\mu^-$ events, the reconstruction procedure introduces a bias of less than 0.03 MeV/c^2 in the measured J/ψ mass. We found that the $J/\psi \to \mu^+\mu^-$ peak was shifted by $+0.5 \pm 0.2$ MeV/c^2 in data compared to simulated events; the corresponding value of the $J/\psi \to e^+e^-$ peak shift was $+0.7 \pm 0.2$ MeV/c^2. A $+0.5$ MeV/c^2 shift corresponds to an overestimation of the lepton absolute momenta by approximately 0.02%. A variation of the lepton absolute momenta by 0.1% produced a shift of less than 0.02 MeV/c^2 in the measured B mass. We therefore neglected the systematic uncertainty associated with the lepton momentum measurement. In addition, we varied the world average J/ψ and $\psi(2S)$ mass values used in the mass-constraint fits by one standard deviation [47]; the resulting 0.05 MeV/c^2 and 0.06 MeV/c^2 shifts of the measured B^0 and B^+ masses were assigned as systematic uncertainties. More details can be found in Section 5.4.7.

(v) *K^0_S four-momentum measurement* — The systematic uncertainty of our B mass measurement is dominated by a possible bias in the kaon four-momentum measurement. The measured position of the K^0_S mass peak allows a reliable evaluation of the possible bias in the K^0_S four-momentum measurement. We selected inclusive K^0_S candidates satisfying the same K^0_S selection criteria as in the $B^0 \to \psi^{(\prime)} K^0_S$ analysis; the momenta of the selected inclusive K^0_S candidates were further restricted to be from 1.55 to 1.85 GeV/c, which corresponds to the momentum range of the K^0_S mesons from $B^0 \to J/\psi K^0_S$ decays. Using this sample, we measured the mean reconstructed K^0 mass to be within 10 keV/c^2 of the world average value of 497.672 ± 0.031 MeV/c^2 [47]. However, we also observed a ± 40 keV/c^2 variation of the measured mean K^0 mass depending on the radial position of the K^0_S decay vertex. To assign the systematic uncertainty, we conservatively took the K^0 mass shift to be 40 keV/c^2 and added in quadrature the 30 keV/c^2 uncertainty in the world average K^0 mass to obtain a total shift of 50 keV/c^2. This 50 keV/c^2 variation in the measured K^0_S mass could be obtained by varying each daughter pion's momentum by 0.018%; the resulting variation of the measured B^0 mass was 0.26 MeV/c^2, which we assigned as a systematic uncertainty due to the K^0_S four-momentum measurement. This uncertainty in $M(B^0)$ has a contribution from the uncertainty in the world average value of the K^0 mass, which partially limited the precision of our K^0_S mass peak position measurement. In addition, we varied by one standard deviation the world average K^0 mass value used for

the K^0_S mass-constraint fit; the resulting 0.04 MeV/c^2 variation of the measured B^0 mass was added to the systematic uncertainty. More details can be found in Section 5.4.8.

(vi) K^+ *momentum measurement.* — Comparing the momentum spectra of the muons from inclusive J/ψ decays and the kaons from $B^+ \to \psi^{(\prime)} K^+$ decays, we concluded that $J/\psi \to \mu^+\mu^-$ decays provide excellent calibration sample for the study of the systematic uncertainty associated with the K^+ momentum measurement. As discussed above, the observed $+0.5 \pm 0.2$ MeV/c^2 shift of the $J/\psi \to \mu^+\mu^-$ mass peak corresponds to a systematic overestimation of the muon momenta by 0.02%. We decreased the measured K^+ momenta by 0.02%, which resulted in a -0.32 MeV/c^2 shift of the measured B^+ mass. We applied a -0.32 MeV/c^2 correction to our final result and assigned 100% of the correction value as the systematic uncertainty. The ionization energy loss for muons from inclusive J/ψ's differs slightly from the loss for kaons from $B^+ \to \psi^{(\prime)} K^+$ decays. To account for the systematic uncertainty due to this difference, we measured the B^+ mass using the pion Billoir fit hypothesis for kaon tracks. The resulting shift (0.08 MeV/c^2) was added in quadrature to the systematic uncertainty. Because of acceptance of the muon chambers, the muons pointing to the end-cap region of the detector are under-represented in comparison with the kaons from the $B^+ \to \psi^{(\prime)} K^+$ decays. The tracks with low transverse momentum are more likely to be affected by the magnetic field inhomogeneity, thus providing an additional source of systematic bias, which will not be taken into account by studying $J/\psi \to \mu^+\mu^-$ decays. However, if a K^+ track has low transverse momentum, then its track parameters are poorly measured, and the mass fit naturally assigns a low weight to this B^+ candidate. We studied the possible systematic bias both by varying the measured K^+ momentum by 0.1% for the K^+ tracks with $|\cos\theta| > 0.8$, where θ is the angle between a track and the beam direction, and by excluding these low angle tracks altogether. The largest shift (0.08 MeV/c^2) was added in quadrature to the systematic uncertainty. More details can be found in Section 5.4.9.

(vii) *Detector misalignment.* — The detector misalignment effects were studied with high-momentum muon tracks from $e^+e^- \to \mu^+\mu^-$ events (Appendix C). We measured the mean of the transverse momentum difference between the μ^+ and μ^- tracks. We also studied the dependence of the sum of the μ^+ and μ^- momenta on azimuthal angle ϕ and polar angle θ of the μ^+ track. We parametrized our findings in terms of an average as well as ϕ- and θ-dependent false curvature. We varied the measured curvature of the $K^\pm$ and K^0_S daughter tracks according to these parametrizations and assigned the largest B mass variation as a systematic uncertainty. More details can be found in Section 5.4.11.

5.3.4 Results

In conclusion, we have determined the masses of neutral and charged B mesons with significantly better precision than any previously published result [47]. We obtained $M(B^0) = 5279.1 \pm 0.7[\text{stat}] \pm 0.3[\text{syst}]$ MeV/c^2 and $M(B^+) = 5279.1 \pm 0.4[\text{stat}] \pm 0.4[\text{syst}]$ MeV/c^2. The systematic uncertainties for the $M(B^0)$ and $M(B^+)$ measurements can be considered independent except for the small common uncertainties due to the imperfect knowledge of the J/ψ and $\psi(2S)$ masses (item (iv) in Table I). Combining our $M(B^0)$ and $M(B^+)$ measurements with the world average value of the mass difference $M(B^0) - M(B^+) = 0.34 \pm 0.32$ MeV/c^2 [47], we obtained $M(B^0) = 5279.2 \pm 0.5$ MeV/c^2

and $M(B^+) = 5278.9 \pm 0.5$ MeV/c^2. Although these $M(B^0)$ and $M(B^+)$ values are more precise than the results given above, obviously they are strongly correlated: the correlation coefficient is $\rho(M(B^0), M(B^+)) = 0.81$.

5.4 More details on the analysis

5.4.1 B^0 and B^+ candidate selection

The distributions of the normalized $M(\psi^{(\prime)}K)$ vs normalized M_{bc} for $B^0 \to J/\psi K^0_S$, $B^0 \to \psi(2S)K^0_S$, $B^+ \to J/\psi K^+$, and $B^+ \to \psi(2S)K^+$ candidates are shown in Figure 5.3. In Figure 5.4 we show the distribution of the normalized $M(\psi^{(\prime)}K)$ for the $B^0 \to \psi^{(\prime)}K^0_S$ and $B^+ \to \psi^{(\prime)}K^+$ candidates passing the 3σ cut on $M_{\rm bc}$. Figure 5.5 shows the event-by-event reported uncertainties of the $\psi^{(\prime)}K$ invariant mass measurements for the signal candidates; $\sigma[M(\psi^{(\prime)}K^+)] < 30$ MeV/c^2 was required for $B^+ \to \psi^{(\prime)}K^+$ candidates.

5.4.2 Background estimation for $B^0 \to \psi^{(\prime)}K^0_S$

Background from non-$B\overline{B}$ continuum events

Using off-$\Upsilon(4S)$ data and "4 times the on-$\Upsilon(4S)$ data" sample of simulated generic continuum events, we found the continuum background to be negligible.

Background from $B\overline{B}$ events

To study the background from generic $B\overline{B}$ decays, we used the "31 times the data" sample of simulated generic $B\overline{B}$ events. The $B\overline{B}$ background for the combined $B^0 \to \psi^{(\prime)}K^0_S$ signal was estimated to be $0.13^{+0.09}_{-0.05}$ events.

Consistency checks for background estimation procedure

We estimate the number of events we expect to observe outside the signal box in Figure 5.3 (top left) to be: $37.1(\mathrm{B\overline{B}}) + 4.3(\text{continuum}) + 0.3(B^0 \to \psi^{(\prime)}K^0_S \text{ spillover}) = 42$. We observe 36 events.

The same procedure applied to the $B^0 \to \psi(2S)K^0_S$ decay yields 14 expected events outside the signal box in Figure 5.3 (top right). We observe 8 events.

5.4.3 Background estimation for $B^+ \to \psi^{(\prime)}K^+$

Background from non-$B\overline{B}$ continuum events

Using off-$\Upsilon(4S)$ data and "4 times the on-$\Upsilon(4S)$ data" sample of simulated generic continuum events, we estimated the continuum background to be $0.3^{+0.4}_{-0.2}$ events for $B^+ \to J/\psi K^+$ and $0.8^{+0.6}_{-0.5}$ events for $B^+ \to \psi(2S)K^+$.

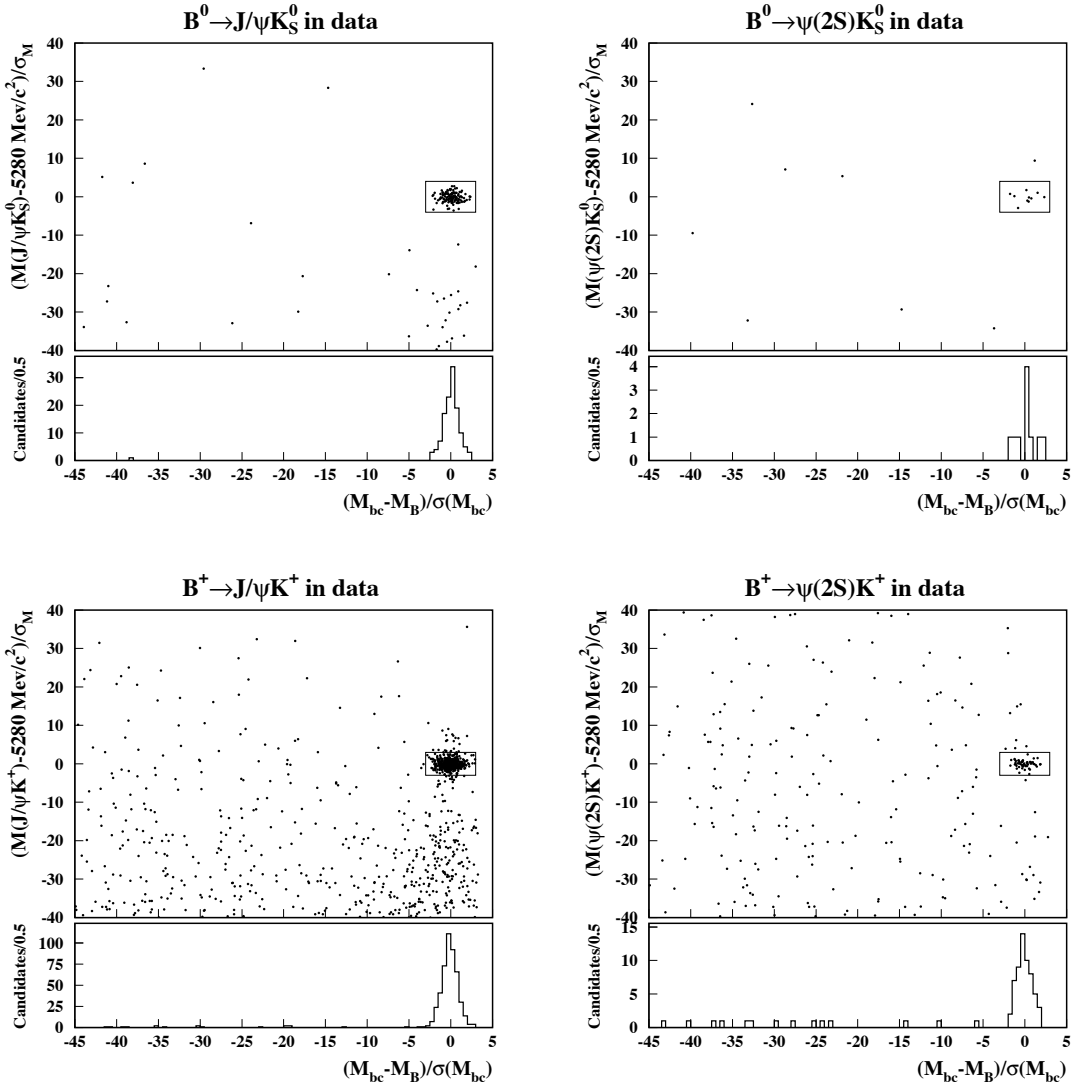

Figure 5.3: $B^0 \to J/\psi K^0_S$ (top left), $B^0 \to \psi(2S)K^0_S$ (top right), $B^+ \to J/\psi K^+$ (bottom left), and $B^+ \to \psi(2S)K^+$ (bottom right) candidates in data. There are 125 $B^0 \to J/\psi K^0_S$, 10 $B^0 \to \psi(2S)K^0_S$, 468 $B^+ \to J/\psi K^+$, and 58 $B^+ \to \psi(2S)K^+$ candidates in the signal boxes. The lower parts of the plots show the normalized beam-constrained mass distributions for the candidates passing the 4σ (3σ) cut on normalized $\psi^{(\prime)}K^0_S$ ($\psi^{(\prime)}K^+$) invariant mass.

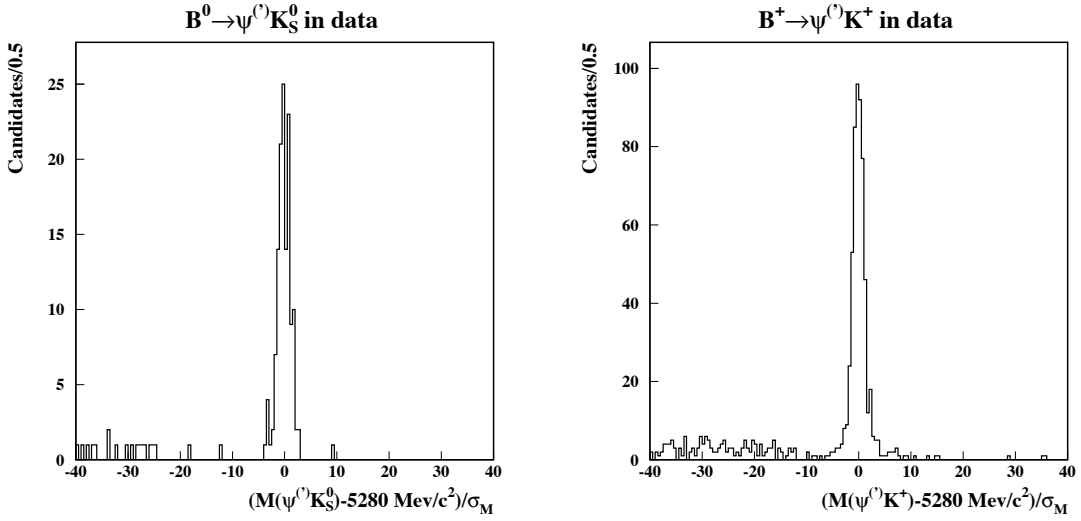

Figure 5.4: Normalized $M(\psi^{(\prime)}K)$ for the $B^0 \to \psi^{(\prime)}K^0_S$ (left) and $B^+ \to \psi^{(\prime)}K^+$ (right) candidates passing the 3σ cut on $M_{\rm bc}$.

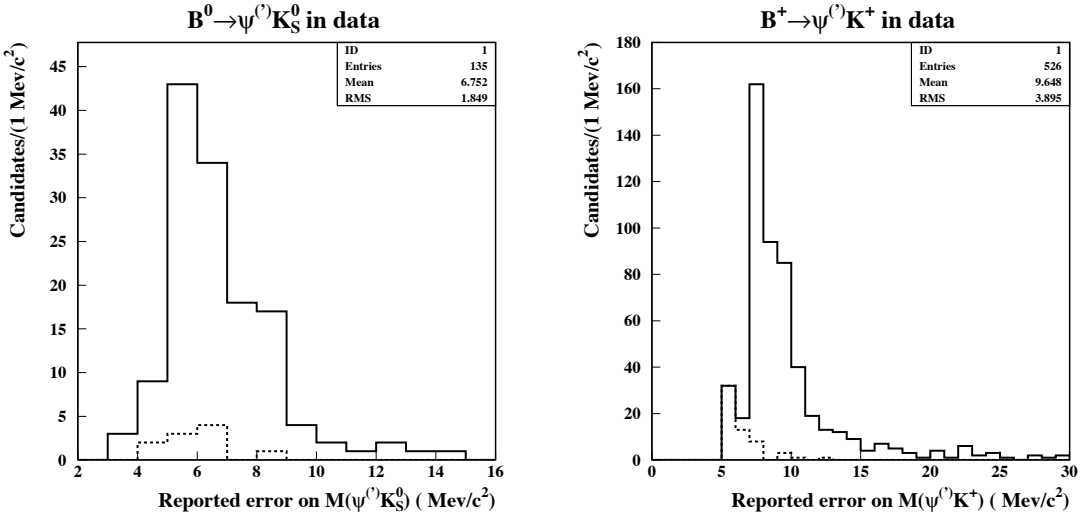

Figure 5.5: Event-by-event reported uncertainty of the $\psi^{(\prime)}K$ invariant mass measurement for the 135 $B^0 \to \psi^{(\prime)}K^0_S$ (left) and 526 $B^+ \to \psi^{(\prime)}K^+$ (right) signal candidates in data. The dashed-line histograms represent the contributions from $B^0 \to \psi(2S)K^0_S$ and $B^+ \to \psi(2S)K^+$ events.

Background from generic $B\overline{B}$ events

To study the background from generic $B\overline{B}$ decays, we used the "31 times the data" sample of simulated generic $B\overline{B}$ events. The events containing $B^+ \to \psi^{(\prime)}\pi^+$ were excluded from the sample. The $B\overline{B}$ background was estimated to be 0.4 ± 0.1 events for $B^+ \to J/\psi K^+$ and $0.6^{+0.6}_{-0.2}$ events for $B^+ \to \psi(2S)K^+$.

$B^+ \to \psi^{(\prime)}\pi^+$ background

This is the most pernicious background because it is likely to bias the measured B^+ mass towards higher values. The distributions of the normalized $M(J/\psi K^+)$ and $M(\psi(2S)K^+)$ for the simulated $B^+ \to \psi^{(\prime)}K^+/\pi^+$ events are shown in Figure 5.6. With high-statistics sample of simulated $B^+ \to J/\psi\pi^+$ events and using the branching ratio $\mathcal{B}(B^+ \to J/\psi\pi^+)/\mathcal{B}(B^+ \to J/\psi K^+) = (5.1 \pm 1.4)\%$ [47], we estimated the $B^+ \to J/\psi\pi^+$ mean background to be 0.9 ± 0.3 events. Using high-statistics sample of simulated $B^+ \to \psi(2S)\pi^+$ events and assuming $\frac{\mathcal{B}(B^+\to\psi(2S)\pi^+)}{\mathcal{B}(B^+\to\psi(2S)K^+)} = \frac{\mathcal{B}(B^+\to J/\psi\pi^+)}{\mathcal{B}(B^+\to J/\psi K^+)}$, we found $B^+ \to \psi(2S)\pi^+$ background to be 0.03 events. We therefore neglected this background.

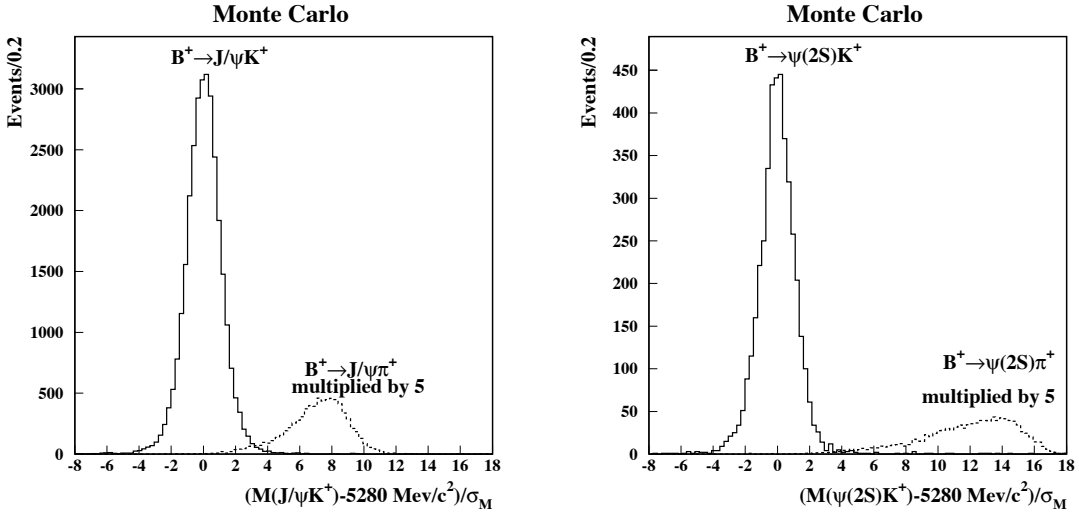

Figure 5.6: Normalized $J/\psi K^+$ invariant mass for $B^+ \to J/\psi K^+/\pi^+$ (left) and normalized $\psi(2S)K^+$ invariant mass for $B^+ \to \psi(2S)K^+/\pi^+$ (right). We assumed $\frac{\mathcal{B}(B^+\to\psi(2S)\pi^+)}{\mathcal{B}(B^+\to\psi(2S)K^+)} = \frac{\mathcal{B}(B^+\to J/\psi\pi^+)}{\mathcal{B}(B^+\to J/\psi K^+)} = 5\%$.

$B \to J/\psi\rho$ background

The Cabibbo-suppressed $B \to J/\psi\rho$ decays are not included into our simulation generic $B\overline{B}$ events. We used combination of data and simulated $B \to J/\psi\rho$ events to estimate the background from $B \to J/\psi\rho$ decays. We attempted the reconstruction of

$B^0 \to J/\psi\rho^0$ candidates in data and observed 17 $B^0 \to J/\psi\rho^0$ candidates entering 2σ signal box in normalized M_{bc} vs normalized ΔE plane. No background subtraction was performed, which could only lead to an overestimation of $\mathcal{B}(B^0 \to J/\psi\rho^0)$. Using a high-statistics sample of simulated $B^0 \to J/\psi\rho^0$ events (Figure 5.7) and normalizing this sample to data, we estimated the $B^0 \to J/\psi\rho^0$ background to be less than 0.04 events; this background can therefore be neglected. To be conservative, we assumed 100% longitudinal polarization (helicity 0) for ρ^0. In this case we underestimate the efficiency of $B^0 \to J/\psi\rho^0$ reconstruction, at the same time overestimating the probability for $B^0 \to J/\psi\rho^0$ event to be reconstructed as $B^+ \to J/\psi K^+$. Therefore we could only overestimate the background for $B^+ \to J/\psi K^+$.

Isospin symmetry leads to $\mathcal{B}(B^+ \to J/\psi\rho^+) \approx 2 \cdot \mathcal{B}(B^0 \to J/\psi\rho^0)$. Note, however, that longitudinally polarized ρ^0 will always produce an energetic charged pion capable of faking the charged kaon from $B^+ \to J/\psi K^+$; on the other hand, ρ^+ will produce an energetic charged pion only half of the time. Therefore we conclude that the background from $B^+ \to J/\psi\rho^+$ decays could also be neglected.

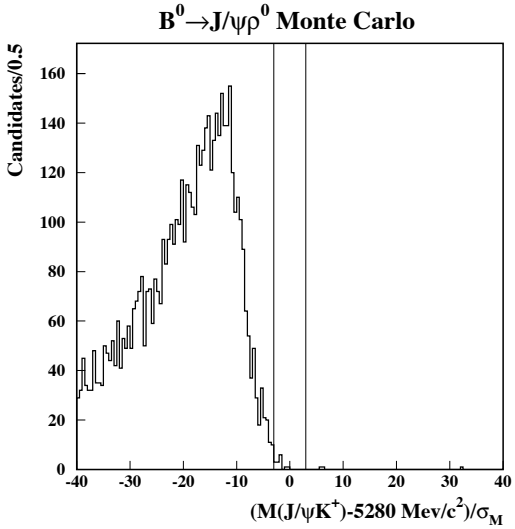

Figure 5.7: Normalized $J/\psi K^+$ invariant mass for simulated $B^0 \to J/\psi\rho^0$ events. We assumed 100% longitudinal polarization for ρ^0. A 3σ cut on normalized $M_{\rm bc}$ was applied. Vertical lines show $\pm 3\sigma$ signal region for normalized $J/\psi K^+$ invariant mass.

$B^+ \to J/\psi K^+$ reconstructed as $B^+ \to \psi(2S)K^+$

Very rarely, when μ^+ and K^+ tracks are swapped, we reconstruct $B^+ \to J/\psi K^+$, $J/\psi \to \mu^+\mu^-$ as $B^+ \to \psi(2S)K^+$. We therefore veto a $B^+ \to \psi(2S)K^+$ candidate if it is reconstructed from the same physical tracks as a $B^+ \to J/\psi K^+$ candidate. This veto decreases the expected background from this cross-feed from 0.7 to 0.3 events; the veto removes 1 $B^+ \to \psi(2S)K^+$ candidate in data.

Consistency checks for background estimation procedure

We estimate the number of events we expect to observe outside the signal box for $B^+ \to J/\psi K^+$ in Figure 5.3(bottom left) to be: 405(generic $B\overline{B}$) + 75(continuum) + $25(B^+ \to J/\psi K^+) + 23(B^+ \to J/\psi \pi^+) = 528$. We observe 553 events.

We estimate the number of events we expect to observe outside the signal box for $B^+ \to \psi(2S)K^+$ in Figure 5.3(bottom right) to be: 90(generic $B\overline{B}$) + 100(continuum) + $12(B^+ \to \psi^{(\prime)}K^+ + B^+ \to \psi(2S)\pi^+) = 202$. We observe 204 events.

5.4.4 B mass measurement with simulated events

Before the fit to data was performed, the fitting procedure was checked with high-statistics samples of simulated signal events. We reconstructed 30286 signal candidates in our sample of simulated $B^0 \to J/\psi K^0_S$ events. Our sample of simulated B^+ signal decays includes events with $B^+ \to J/\psi K^+$, $B^+ \to J/\psi \pi^+$, $B^+ \to \psi(2S)K^+$, and $B^+ \to \psi(2S)\pi^+$ decays. We assumed $\frac{\mathcal{B}(B^+ \to \psi(2S)\pi^+)}{\mathcal{B}(B^+ \to \psi(2S)K^+)} = \frac{\mathcal{B}(B^+ \to J/\psi\pi^+)}{\mathcal{B}(B^+ \to J/\psi K^+)} = 5\%$ [47]. The results of the B mass fits performed using signal Monte Carlo samples are listed in Table 5.2. At least in the simulation we get back what we put in. Based on this study, we applied a $+0.08$ MeV/c^2 correction to the measured B^0 mass and a -0.13 MeV/c^2 correction to the B^+ mass value and assigned 100% of the correction as a systematic uncertainty.

Table 5.2: Results of the B^0 and B^+ mass fits for the samples of simulated signal events.

Sample composition	Number of events	$M(B) - M_B^{\rm input}$ (MeV/c^2)	S
$B^0 \to J/\psi K^0_S$			
$B^0 \to J/\psi K^0_S$	30286	-0.078 ± 0.042	1.1579 ± 0.0048
$B^+ \to \psi^{(\prime)} K^+$			
True signal only	34519	$+0.134 \pm 0.048$	1.0542 ± 0.0044
$B^+ \to \psi^{(\prime)}\pi^+$ allowed	34519+56	$+0.145 \pm 0.048$	1.0577 ± 0.0045
$B^+ \to \psi^{(\prime)}\pi^+$ and and $J/\psi K^+ \Rightarrow \psi(2S)K^+$ cross-feed allowed	34519+75	$+0.147 \pm 0.048$	1.0581 ± 0.0045

We would like to show that the values of the scale factors S and the uncertainties on the B^0 and B^+ mass measurements are plausible for the simulated event samples of the same size as the data samples. From 30286 candidates reconstructed in $B^0 \to J/\psi K^0_S$ signal Monte Carlo samples, we have randomly drawn 224 samples each containing 135 candidates. Then we performed the B^0 mass fit separately for each of those 224 samples. The scatter plot of the scale factor S vs the uncertainty on the B^0 mass measurement returned by `MINUIT` [109] for each of 224 Monte Carlo samples is shown in Figure 5.8 (left). The variation of the scale factor values returned by the fits is natural if we note that the typical uncertainty on S reported by a fit is 0.08. Obviously, the values of the scale factor S and the uncertainty on the B^0 mass measurement returned by `MINUIT` are strongly correlated.

From 34594 candidates reconstructed in the sample of simulated signal B^+ decays ($B^+ \to \psi^{(\prime)}\pi^+$ events and $B^+ \to J/\psi K^+ \Longrightarrow B^+ \to \psi(2S)K^+$ cross-feed included), we have randomly drawn 65 samples each containing 526 candidates. Then we performed the B^+ mass fit separately for each of those 65 samples. The scatter plot of the scale factor S vs the uncertainty on the B^+ mass measurement returned by `MINUIT` for each of the 65 simulated event samples is shown in Figure 5.8 (right).

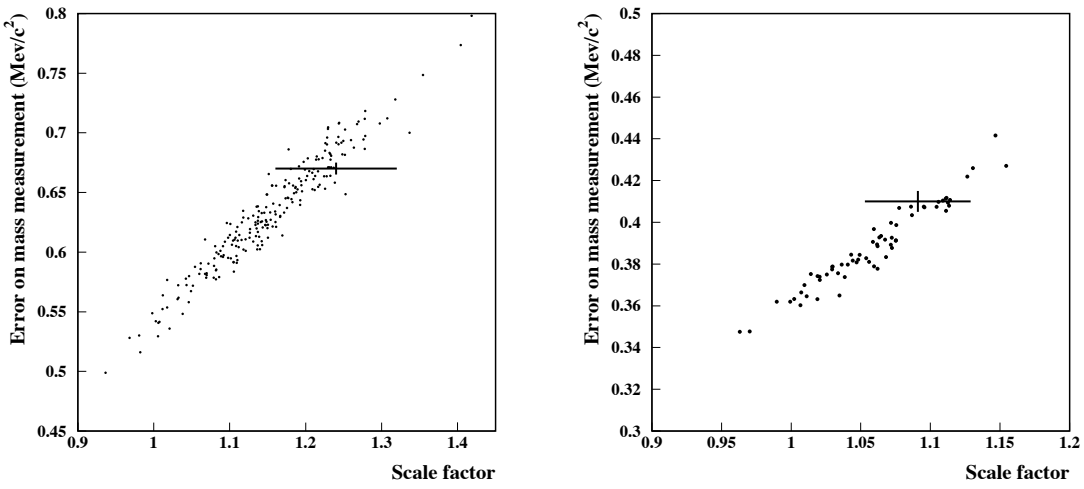

Figure 5.8: Scale factor S vs the uncertainty in the B mass measurement returned by `MINUIT` for each of the signal Monte Carlo subsamples. The signal Monte Carlo sample was divided into 224 data-sized independent subsamples for $B^0 \to J/\psi K^0_S$ and into 65 subsamples for $B^+ \to \psi^{(\prime)}K^+$. Also shown are the values for the data fit: $S(B^0) = 1.240 \pm 0.079$, $\sigma(M(B^0)) = 0.67$ MeV/c^2 (left plot) and $S(B^+) = 1.089 \pm 0.038$, $\sigma(M(B^+)) = 0.41$ MeV/c^2 (right plot).

5.4.5 Possible bias in $M(B^+)$ measurement caused by background events

We estimated $B^+ \to J/\psi\pi^+$ background mean to be 0.9 ± 0.3 events; the sum of combinatorial background and $B^+ \to J/\psi K^+ \Longrightarrow B^+ \to \psi(2S)K^+$ cross-feed was found to be $2.3^{+1.0}_{-0.5}$ events. The $B^+ \to J/\psi\pi^+$ events produce high $M(J/\psi K^+)$ (Figure 5.6(left)), whereas the other background events are expected to be uniformly distributed across the signal region. In Section 5.4.4 we showed that for the high-statistics Monte Carlo sample the bias in the B^+ mass measurement caused by allowing $B^+ \to \psi^{(\prime)}\pi^+$ events and $B^+ \to J/\psi K^+ \Longrightarrow B^+ \to \psi(2S)K^+$ cross-feed events is very small (+0.013 MeV/c^2). We also studied the systematic uncertainty due to the presence of background events by excluding from 526 signal candidates 1 to 4 candidates with the extreme values of $M(\psi^{(\prime)}K^+)$ or normalized $M(\psi^{(\prime)}K^+)$. The resulting shifts of the measured B^+ mass are listed in Table 5.3. We assigned the largest shift (0.17 MeV/c^2) as a systematic uncertainty due to the presence of background events.

Table 5.3: Results of the B^+ mass measurements obtained by excluding 1 to 4 candidates with the extreme values of $M(\psi^{(\prime)}K^+)$ or normalized $M(\psi^{(\prime)}K^+)$.

Number of events excluded	Shift in measured $M(B^+)$ (MeV/c^2)			
	$M(\psi^{(\prime)}K^+)$		normalized $M(\psi^{(\prime)}K^+)$	
	lowest	highest	lowest	highest
1	$+0.024$	-0.011	$+0.024$	-0.056
2	$+0.037$	-0.022	$+0.077$	-0.080
3	$+0.063$	-0.046	$+0.12$	-0.11
4	$+0.073$	-0.062	$+0.17$	-0.16

5.4.6 Systematic uncertainty associated with a choice of fit function

To determine the B masses in the real analysis, we fit the $\psi^{(\prime)}K$ invariant mass to a single Gaussian, allowing the reported event-by-event errors on $M(\psi^{(\prime)}K)$ to be multiplied by a global scale factor S (Equation 5.1). As a check for a systematic bias, we tried other likelihood functions:

1. We performed a fit to a double Gaussian, allowing for two global scale factors $S_{\rm narrow}$ and $S_{\rm wide}$. The the likelihood function is described by

$$\mathcal{L}(M(B)) = \prod_i \{(1 - f_{\rm wide}) \cdot \frac{G(M_i - M(B)|S_{\rm narrow}\sigma_i)}{\int G(M - M(B)|S_{\rm narrow}\sigma_i)dM} + \\ + f_{\rm wide} \cdot \frac{G(M_i - M(B)|S_{\rm wide}\sigma_i)}{\int G(M - M(B)|S_{\rm wide}\sigma_i)dM}\}. \quad (5.2)$$

   `MINUIT` had a hard time floating all the parameters for B^+ mass fit; we therefore fixed $S_{\rm wide} = 2.0$.

2. We performed a fit to a single Gaussian, allowing for different global scale factors for events with $\psi^{(\prime)} \to e^+e^-$ (S_{ee}) and $\psi^{(\prime)} \to \mu^+\mu^-$ ($S_{\mu\mu}$).

3. We performed a fit to a single Gaussian, allowing for different global scale factors for CLEO II and CLEO II.V events.

The parameter values returned by these 3 fits are listed in Table 5.4. We assigned the largest shift of the measured B mass as the systematic uncertainty.

5.4.7 Systematic uncertainty associated with $\psi^{(\prime)}$ four-momentum measurement

Kalman hypothesis used for lepton track fits

The information from the Kalman fits performed using muon and electron hypotheses is not stored in the data skim we used in this analysis; the parameters returned by the pion-hypothesis fit are used instead. We show that this peculiarity of the data skim is not a problem for our analysis.

Table 5.4: Results of the B mass likelihood fits with the 3 different fit functions.

	B^0		B^+	
	Data	Monte Carlo	Data	Monte Carlo
Number of events	135	30286	526	34594
	1. Double Gaussian			
$M(B)$ shift (MeV/c^2)	$+0.11$	$+0.02$	-0.09	$+0.02$
$S_{\rm narrow}$	0.90 ± 0.26	0.963 ± 0.028	0.877 ± 0.070	0.9289 ± 0.0097
$S_{\rm wide}$	1.60 ± 0.57	1.65 ± 0.11	2.0(fixed)	2.0(fixed)
$f_{\rm wide}$	0.47 ± 0.42	0.269 ± 0.065	0.250 ± 0.073	0.167 ± 0.011
	2. Different scale factors S_{ee} and $S_{\mu\mu}$			
$M(B)$ shift (MeV/c^2)	$+0.14$	-0.0015	0.0	0.0
S_{ee}	1.14 ± 0.10	1.1905 ± 0.0071	1.080 ± 0.052	1.0759 ± 0.0065
$S_{\mu\mu}$	1.34 ± 0.12	1.1253 ± 0.0066	1.102 ± 0.056	1.0428 ± 0.0061
	3. Different scale factors $S_{\rm CLEOII}$ and $S_{\rm CLEOII.V}$			
$M(B)$ shift (MeV/c^2)	-0.013	0.0	$+0.03$	0.00
$S_{\rm CLEOII}$	1.21 ± 0.13	1.1601 ± 0.0083	1.153 ± 0.071	1.0655 ± 0.0077
$S_{\rm CLEOII.V}$	1.25 ± 0.10	1.1572 ± 0.0059	1.058 ± 0.045	1.0556 ± 0.0055

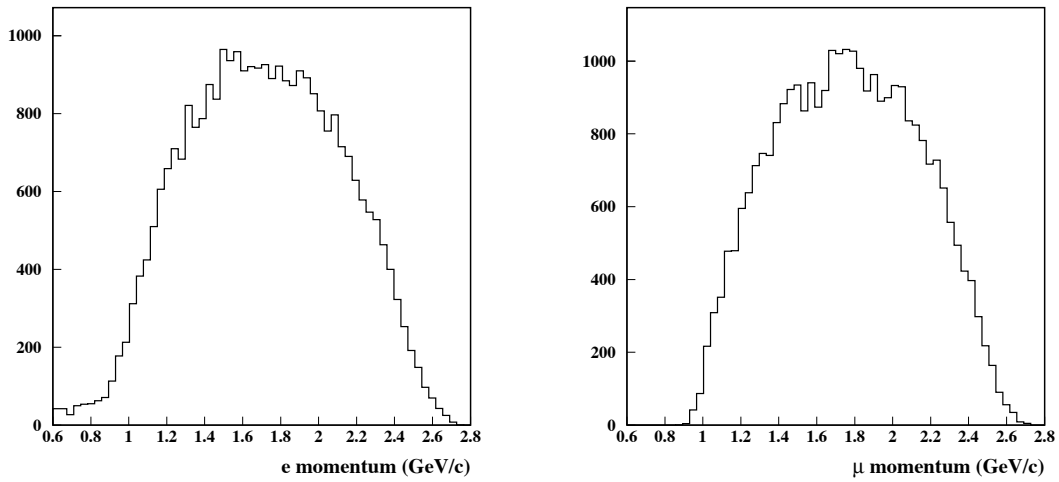

Figure 5.9: Reconstructed momentum of the J/ψ daughter electrons (left plot) and muons (right plot) for the simulated $B \to J/\psi K$ events.

The momentum spectrum of the reconstructed leptons from $B \to J/\psi K$, $J/\psi \to \ell^+\ell^-$ decay chain is shown in Figure 5.9. In Figure 5.10 we show the momentum dependence of the mean ionization energy loss for hadrons and muons. To obtain these energy loss curves, we used Billoir fitter material transport routine to estimate the energy loss in the detector material inside the main drift chamber (radius= 20 cm). For each momentum value, we obtained the energy loss corrections by averaging the imaginary tracks over charge, $|\cos\theta|$ (from 0.05 to 0.8), and ϕ. From these plots we can see that the pion hypothesis fit

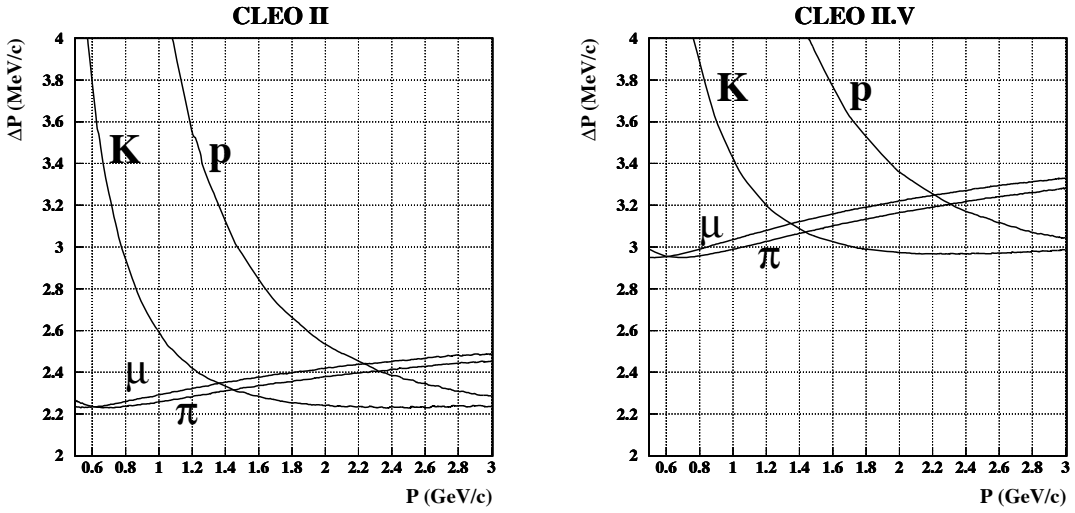

Figure 5.10: Momentum dependence of the mean ionization energy loss for muons and hadrons. Left plot is for CLEO II, right plot is for CLEO II.V.

will probably work well for muons. However, neither the pion nor the electron hypothesis fit will properly account for the electron energy loss in material because electrons lose energy mainly through bremsstrahlung, not through ionization[3]. Our only hope is that the $\psi^{(\prime)}$ mass-constraint fit will cure all these problems... And it does! We repeated the B mass measurement with the data and the simulation, using lepton (for Monte Carlo samples only), kaon, and proton Kalman fit hypotheses for lepton tracks. The resulting B mass shifts are listed in Table 5.5. The B mass shifts resulting from substituting lepton for pion hypotheses are only 0.02 MeV/c^2. We neglected this systematic uncertainty.

Effects of uncertain magnetic field scale and imperfect detector material description on $\psi^{(\prime)}$ four-momentum measurement

Is it possible to measure the correct B mass with the simulated event samples and still get it wrong in the data? Sure, it is possible:

[3]The electron critical energy for, say, Beryllium is about 100 MeV; for comparison, the pion or muon critical energy for the same material is around 1 TeV.

Table 5.5: Shifts of the measured B mass resulting from use of different Kalman hypotheses for lepton tracks, varying the measured lepton momenta, and varying the J/ψ and $\psi(2S)$ mass values used in the mass-constraint fit.

	B^0		B^+	
	Data	Monte Carlo	Data	Monte Carlo
Number of events	135	30286	526	34594
	shift in $M(B^0)$ (MeV/c^2)		shift in $M(B^+)$ (MeV/c^2)	
π for e and μ	0	0	0	0
e for e, μ for μ	Not available	-0.023	Not available	-0.024
K for e and μ	-0.049	-0.057	-0.053	-0.060
p for e and μ	-0.241	-0.270	-0.261	-0.275
ℓ momentum increased by 0.1%	$+0.017$	$+0.020$	$+0.004$	$+0.012$
$M_{J/\psi}$ and $M_{\psi(2S)}$ increased by 1σ	$+0.050$	$+0.050$	$+0.060$	$+0.058$

1. The Monte Carlo simulation uses the same magnetic field value for generation and reconstruction. This may not be the true for data.

2. To account for energy losses in the detector material, the Billoir track fitter uses the same detector material description for the data and the simulation. Unfortunately, Nature, as opposed to the simulation, does not use our GEANT-based description of the CLEO detector to generate events.

The miscalculation of the absolute magnetic field scale and imperfect description of the detector material will bias the lepton momentum measurement in the data compared to the simulation. The ionization energy loss non-trivially depends on particle momentum. Therefore, for example, even if the mean of the $K^0_S \to \pi^+\pi^-$ mass peak for inclusive K^0_S's is exactly at the nominal value, we cannot conclude that the momentum measurement of high-momentum leptons is unbiased.

Fortunately, the measurement of the relative position of the J/ψ mass peak in the data with respect to the simulation allows a reliable evaluation of the possible bias in the lepton momentum measurement. In Appendix B we showed that both $J/\psi \to \mu^+\mu^-$ and $J/\psi \to e^+e^-$ mass peaks in data are shifted by approximately $+0.5$ MeV/c^2 with respect to the simulation. The $+0.5$ MeV/c^2 shift can be interpreted as an overestimation of the magnetic field scale by $0.5/3097 \approx 2 \cdot 10^{-4}$. As a check for a possible systematic bias, we multiplied the measured momentum of each lepton by $1+1\cdot10^{-3}$ (this would result in a big $10^{-3} \times 3097 = 3$ MeV/c^2 shift of the J/ψ mass peak); the observed shifts of the measured B mass are very small both for the data and the simulation (Table 5.5). Again, the $\psi^{(\prime)}$ mass-constraint fit saves the day. We did not assign any systematic uncertainty.

Uncertainty in the J/ψ and $\psi(2S)$ mass values used in the mass-constraint fit

In the mass-constraint fit we used the PDG'98 world average values $M_{J/\psi} = 3096.88 \pm 0.04$ MeV/c^2 and $M_{\psi(2S)} = 3686.00 \pm 0.09$ MeV/c^2 [47]. We simultaneously increased by 1σ the J/ψ and $\psi(2S)$ mass values; the resulting shifts of the measured B^0 and B^+ masses (Table 5.5) were assigned as systematic uncertainties.

Beating $\psi^{(\prime)} \to \mu^+\mu^-$ against $\psi^{(\prime)} \to e^+e^-$

We would like to disperse any remaining concerns that using the $\psi^{(\prime)} \to e^+e^-$ mode with its nasty radiative tail might significantly bias the B mass measurement.

- The final state radiation in the $\psi^{(\prime)} \to \ell^+\ell^-$ decays is well understood theoretically and is simulated by `QQ` event generator. GEANT [24] simulates bremsstrahlung in the detector material.

- Figure B.3 shows that $J/\psi \to \ell^+\ell^-$ lineshapes in the data and the simulation agree remarkably well.

- In Section 5.4.4 we showed that the B mass values measured in the samples of simulated events are very close to the input values.

- As a check, in our sample of simulated $B^0 \to J/\psi K^0_S$ events we separated candidates with $J/\psi \to e^+e^-$ from the candidates with $J/\psi \to \mu^+\mu^-$ and measured B^0 mass for each of the two subsamples. The results are listed in Table 5.6.

Table 5.6: Results of the B^0 mass measurement for the sample of simulated $B^0 \to J/\psi K^0_S$ events when we separate the candidates with $J/\psi \to \mu^+\mu^-$ from the ones with $J/\psi \to e^+e^-$.

	$M(B^0) - M^{\rm input}_{B^0}$ (MeV/c^2)
$J/\psi \to \mu^+\mu^-$ and $J/\psi \to e^+e^-$ (30286 events)	-0.078 ± 0.042
$J/\psi \to \mu^+\mu^-$ (15234 events)	-0.102 ± 0.057
$J/\psi \to e^+e^-$ (15052 events)	-0.051 ± 0.062

- We accepted more of the radiative tail by extending the lower boundary of the normalized J/ψ mass cut from -3 to -6 for both $J/\psi \to \mu^+\mu^-$ and $J/\psi \to e^+e^-$ (Figure 2.16). In our sample of simulated $B^0 \to J/\psi K^0_S$ events the number of reconstructed B^0 candidates increased by 2166 (from 30286 to 32452). The measured B^0 mass shifted by -0.058 MeV/c^2.

- Combining the following decay modes:
  - $B^+ \to \psi^{(\prime)} K^+$,
  - $B^+ \to \psi^{(\prime)} K^{*+}$, $K^{*+} \to K^0_S \pi^+$,
  - $B^0 \to \psi^{(\prime)} K^0_S$,
  - $B^0 \to \psi^{(\prime)} K^{*0}$, $K^{*0} \to K^+ \pi^-$,

we reconstructed 958 signal candidates in data. We fed those candidates into our B mass fitter, allowing to float $M(B^0)$, $M(B^0) - M(B^+)$, and global scale factor S. Then we separated the events with $\psi^{(\prime)} \to e^+e^-$ and $\psi^{(\prime)} \to \mu^+\mu^-$ and repeated the fits fixing $M(B^0) - M(B^+)$. Note that we are interested only in the difference between the B mass values measured with ee and $\mu\mu$ samples. The results are:

- $M_B(ee \text{ sample}) - M_B(ee + \mu\mu \text{ sample}) = -0.20 \pm 0.40 \text{ MeV}/c^2$,
- $M_B(\mu\mu \text{ sample}) - M_B(ee + \mu\mu \text{ sample}) = +0.18 \pm 0.41 \text{ MeV}/c^2$,
- $\chi^2/dof = \left[\left(\frac{0.20}{0.40}\right)^2 + \left(\frac{0.18}{0.41}\right)^2\right]/2 = 0.44/2.$

We conclude that we do not need to worry about differences in $\psi^{(\prime)}$ reconstruction using dielectron or dimuon channel. We did not assign any systematic uncertainty.

5.4.8 Systematic uncertainty associated K^0_S four-momentum measurement

Position of $K^0_S \to \pi^+\pi^-$ mass peak

Again, we are worried that the miscalculation of the absolute magnetic field scale and imperfect description of the detector material will bias the K^0_S four-momentum measurement. The measured position of the K^0_S mass peak allows a reliable evaluation of the possible bias in the K^0_S four-momentum measurement. We selected inclusive K^0_S candidates satisfying the same K^0_S selection criteria as in the $B^0 \to \psi^{(\prime)} K^0_S$ analysis; the momenta of the selected inclusive K^0_S candidates were further restricted to be from 1.55 to 1.85 GeV/c, which corresponds to the momentum range of the K^0_S mesons from $B^0 \to J/\psi\, K^0_S$ decays (Figure 5.11). The K^0_S mass distribution is shown in Figure 5.12. We fitted the distribution

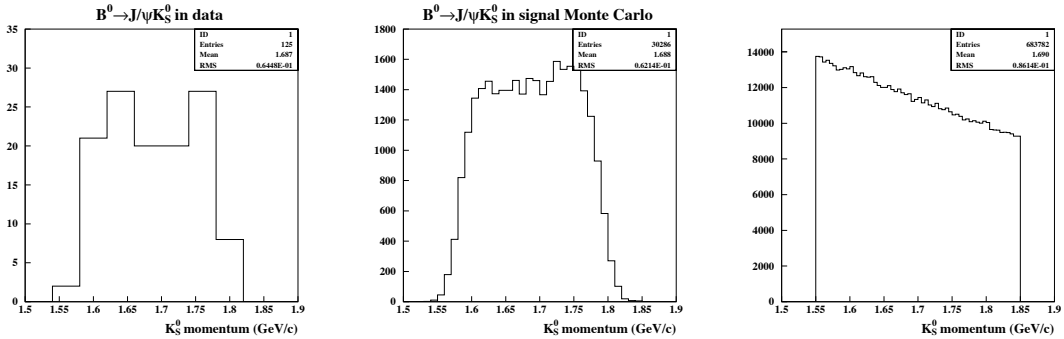

Figure 5.11: Left (middle) plot shows the momentum distribution for K^0_S's from $B^0 \to J/\psi K^0_S$ decays in data (signal Monte Carlo sample). Right plot shows the momentum distribution of the inclusive K^0_S candidates selected in all CLEO II and CLEO II.V data for our study of the K^0_S reconstruction systematics.

in Figure 5.12 using double Gaussian to represent a signal shape and 0th or 1st order polynomial as a background shape. As a check, we performed a single-Gaussian fit of the same distribution restricting the fit only to the peak region (± 3 MeV/c^2). We also performed

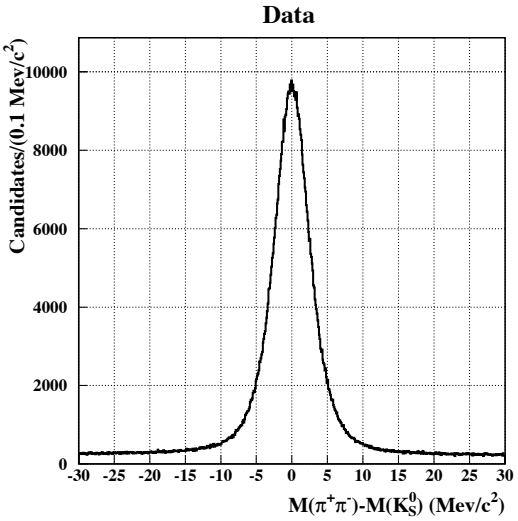

Figure 5.12: K^0_S candidates with momentum between 1.55 GeV/c and 1.85 GeV/c in all CLEO II and CLEO II.V data.

the fits dividing the sample according to K^0_S momentum as well as the radius of the decay vertex. The results are listed in Table 5.7. Dividing the sample according to the radius of the decay vertex and weighting by the number of events in each sub-sample (Table 5.7), we found RMS spread of the measured mean K^0_S mass values to be 40 keV/c^2.

Table 5.7: Shifts of the measured K^0_S mass peak position from the nominal value for all the K^0_S candidates with momentum between 1.55 GeV/c and 1.85 GeV/c in all CLEO II and CLEO II.V data.

K^0_S's used	Events in peak	$M(\pi^+\pi^-) - M_{K^0}$ (keV/c^2) $P0$ bkg	$P1$ bkg	± 3 MeV
ALL	646890 ± 935	-9 ± 4	-3 ± 4	$+3 \pm 6$
1.55< $\lvert P(K^0_S)\rvert$ <1.85 GeV	(100%)			
1.55< $\lvert P(K^0_S)\rvert$ <1.70 GeV	55%	-14 ± 6	-8 ± 6	0 ± 8
1.70< $\lvert P(K^0_S)\rvert$ <1.85 GeV	45%	-3 ± 6	$+8 \pm 6$	8 ± 9
decayed inside beam pipe	26%	-54 ± 9	-55 ± 9	-45 ± 15
decayed in `SVX` or `PTL`	38%	-34 ± 7	-26 ± 7	-7 ± 11
decayed in `VD`	26%	$+52 \pm 7$	$+59 \pm 7$	$+46 \pm 9$
decayed in `DR`	10%	-1 ± 10	$+1 \pm 10$	-2 ± 11

Effects of uncertain magnetic field scale and imperfect detector material description on K^0_S four-momentum measurement

The world average value of the K^0 mass is 497.672 ± 0.031 MeV/c^2 [47]. Let us assume for a moment that the K^0 mass is perfectly known. In our study of the K^0_S

mass peak position (Table 5.7) we measured the mean reconstructed K^0 mass to be within 10 keV/c^2 of the world average value. However, we also observed a ± 40 keV/c^2 variation of the measured mean K^0 mass depending on the radial position of the K^0_S decay vertex. To assign the systematic uncertainty, we conservatively took the K^0 mass shift to be 40 keV/c^2. However, the K^0 mass is known only with the precision of 30 keV/c^2 [47]. Adding in quadrature 40 and 30 keV/c^2, we obtain 50 keV/c^2 — the variation of the measured mean K^0_S mass we will use to assign a systematic uncertainty. For the K^0_S's from $B^0 \to J/\psi K^0_S$, the 50 keV/c^2 shift in the measured K^0_S mass could result from either multiplying each daughter pion's measured momentum by $1 + 1.8 \cdot 10^{-4}$ or by adding 150 keV/c to each pion's momentum. In either case, the resulting variation in the measured B^0 mass was 0.26 MeV/c^2 for the data and the simulation. This 0.26 MeV/c^2 variation could be represented as $0.16 \oplus 0.20$ MeV/c^2, where the 0.16 MeV/c^2 variation is due to the uncertainty in the world average value of the K^0_S mass. This 0.16 MeV/c^2 should be added linearly with the 0.04 MeV/c^2 uncertainty associated with the K^0_S mass value used in the mass-constraint fit (see below).

Uncertainty in the K^0_S mass value used in the mass-constraint fit

In the mass-constraint fit we used the PDG'98 [47] world average value $M(K^0) = 497.672 \pm 0.031$ MeV/c^2. We varied the K^0 mass used in the mass-constraint fit by 1σ; the observed variation of the measured B^0 mass is 0.041 MeV/c^2 for the data and 0.039 MeV/c^2 for the simulation. We assigned 0.04 MeV/c^2 as a systematic uncertainty.

5.4.9 Systematic uncertainty associated with K^+ momentum measurement

We need to find a way of probing a relative $\mathcal{O}(10^{-4})$ bias in the K^+ momentum measurement. Comparing the momentum spectrum of the muons from inclusive J/ψ's (Figure B.1) with the spectrum of the kaons from $B^+ \to \psi^{(\prime)} K^+$ decays (Figure 5.13) and looking at the ionization energy loss curves (Figure 5.10), we concluded that $J/\psi \to \mu^+\mu^-$ decays provide an excellent calibration sample for the study of the systematic uncertainty associated with the K^+ momentum measurement. In Appendix B we determined that the $J/\psi \to \mu^+\mu^-$ mass peak appears to be shifted by $+0.5 \pm 0.2$ MeV/c^2 in the data with respect to the Monte Carlo simulation; this conclusion is also supported by the $J/\psi \to e^+e^-$ data. This shift corresponds to systematic overestimating of the muon momenta by $0.5/3097 \approx 2 \cdot 10^{-4}$. We multiplied the measured K^+ momenta by $(1 - 2 \cdot 10^{-4})$; the observed shift of the measured B^+ mass is -0.32 MeV/c^2 for data and -0.32 MeV/c^2 for the simulation. We applied this -0.32 MeV/c^2 correction to our final result and assigned 100% of the correction value as a systematic uncertainty. The kaons from $B^+ \to \psi^{(\prime)} K^+$ decay typically lose around 3 MeV of energy before entering the main drift chamber (Figure 5.10). Therefore variation of the K^+ momentum by $2 \cdot 10^{-4}$ corresponds to varying the energy loss correction by about 10%.

The ionization energy loss by muons from inclusive J/ψ's is not exactly the same as for kaons from $B^+ \to \psi^{(\prime)} K^+$ decays, although typical discrepancy is less than 5% of the energy loss value (see Figures 5.10, B.1, and 5.13). To account for systematics due to

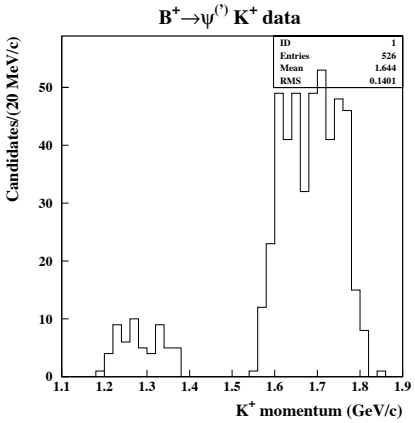

Figure 5.13: Momenta of the kaons from $B^+ \to \psi^{(\prime)} K^+$ decays for 526 signal candidates in data. The left bump corresponds to $B^+ \to \psi(2S) K^+$ events.

this difference, we measured the B^+ mass using pion Kalman hypothesis for kaon tracks. The observed shift of the measured B^+ mass is $+0.083$ MeV/c^2 for the data and $+0.074$ MeV/c^2 for the simulation. We assigned 0.08 MeV/c^2 as a systematic uncertainty.

5.4.10 High-$|\cos\theta|$ K^+ tracks

We used inclusive $J/\psi \to \mu^+\mu^-$ events to probe possible systematic bias in K^+ momentum reconstruction. Because of acceptance of the muon chambers, the muons with high $|\cos\theta|$ are underrepresented in comparison with the kaons from $B^+ \to \psi^{(\prime)} K^+$ decays (Figure 5.14). The tracks with low transverse momentum are more likely to be affected by the magnetic field inhomogeneity, thus providing an additional source of systematic bias, which will not be taken into account by studying $J/\psi \to \mu^+\mu^-$ decays. Note, however, that the reported uncertainty in $M(\psi^{(\prime)} K^+)$ is large if $|\cos\theta|$ of the K^+ track is large (Figure 5.15). Therefore the $B^+ \to \psi^{(\prime)} K^+$ candidates with high-$|\cos\theta|$ K^+ tracks are naturally given low weight in the B^+ mass measurement. If we exclude $B^+ \to \psi^{(\prime)} K^+$ candidates with K^+ tracks having $|\cos\theta| > 0.8$, then we lose 74 out of 526 signal candidates and the measured B^+ mass shifts by -0.06 MeV/c^2. We also varied the measured K^+ momentum by 0.1% for the K^+ tracks with $|\cos\theta| > 0.8$; the resulting shift of the measured B^+ mass is 0.08 MeV/c^2. We assigned 0.08 MeV/c^2 as a systematic uncertainty.

5.4.11 Effects of detector misalignment on kaon four-momentum measurement

Because of detector misalignments, the measured curvature of a track can have an offset $CU_{\rm meas.} = CU_{\rm true} + \delta$. Due to this effect, a non-zero false curvature will be assigned to an infinite-momentum track, and measured momenta will be different for positive and negative tracks of the same true momenta. Also, there could be an azimuthal and polar-angle-dependent bias in the momentum measurement. One can think of this bias as of false

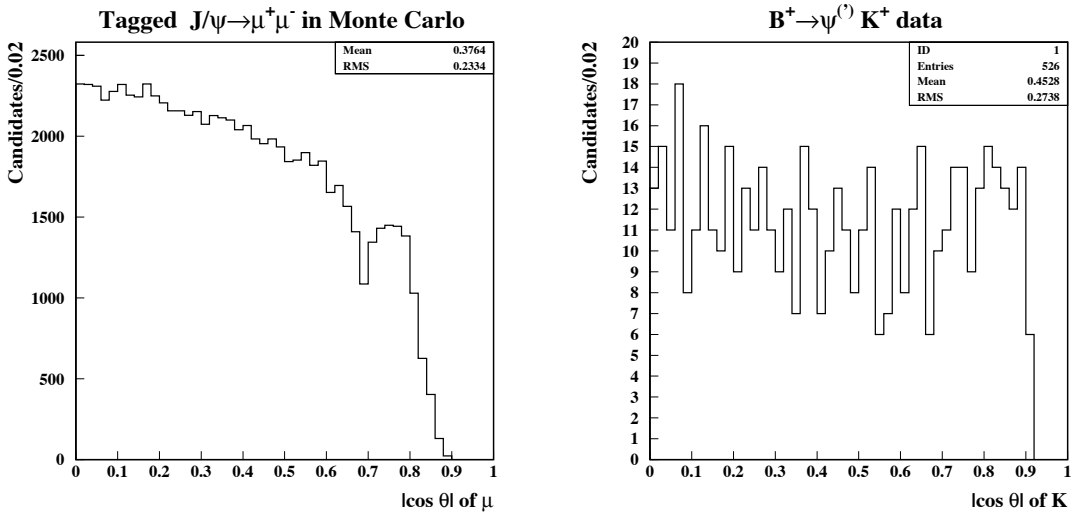

Figure 5.14: The $|\cos\theta|$ distribution for muons from inclusive $J/\psi \to \mu^+\mu^-$ decays (left) and for kaons from $B^+ \to \psi^{(\prime)} K^+$ candidates (right).

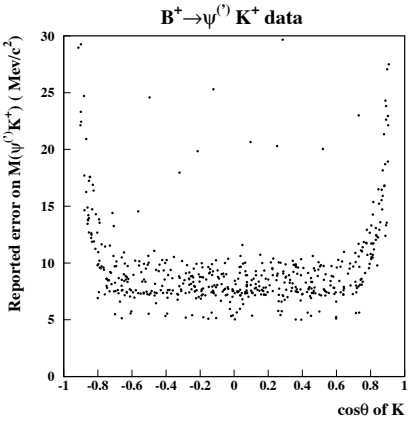

Figure 5.15: The reported uncertainty in $M(\psi^{(\prime)} K^+)$ vs $\cos\theta$ of the kaon track for $B^+ \to \psi^{(\prime)} K^+$ candidates in data.

curvature which depends on ϕ and θ of the track. In the limit of infinite statistics, false curvature effect will not cause a systematic bias in the B mass measurement. These biases are studied in Appendix C with high-momentum muon tracks from $e^+e^- \to \mu^+\mu^-$ events.

To correct the measured momenta of the kaons from $B^\pm \to \psi^{(\prime)}K^\pm$ and charged pions from $B^0 \to \psi^{(\prime)}K^0_S$, $K^0_S \to \pi^+\pi^-$ decays for the false curvature inferred from $e^+e^- \to \mu^+\mu^-$ data, we used the following formula:

$$p^\pm_{new} = p^\pm_{old} \cdot (1 \mp p^\pm_{t,old} < \frac{\delta}{p^\mu_t \cdot CU(\mu)} >). \tag{5.3}$$

The correction has opposite signs for positive and negative tracks. The false curvature divided by the average curvature of the muon tracks is calculated as $< \frac{\delta}{CU(\mu)} > = < \frac{p^+_t - p^-_t}{p^+_t + p^-_t} >$. To obtain the value of $< \frac{\delta}{p^\mu_t \cdot CU(\mu)} >$ from $e^+e^- \to \mu^+\mu^-$ data, we fitted the distribution of $\frac{1}{(p^+_t + p^-_t)/2} \cdot \frac{(p^+_t - p^-_t)}{(p^+_t + p^-_t)}$; the results of the fits are listed in the last column of Table C.1. The 526 $B^\pm \to \psi^{(\prime)}K^\pm$ candidates in data are divided as follows: 230 $B^+ \to J/\psi K^+$ vs 238 $B^- \to J/\psi K^-$ and 29 $B^+ \to \psi(2S)K^+$ vs 29 $B^- \to \psi(2S)K^-$ events. From Table C.1, we used $14 \cdot 10^{-5}$ $(\mathrm{GeV}/c)^{-1}$ as a representative value of $< \frac{\delta}{p^\mu_t \cdot CU(\mu)} >$. We then recalculated the measured kaon momenta for $B^\pm \to \psi^{(\prime)}K^\pm$ candidates in data using Equation 5.3. The average transverse momentum of the kaons is about 1.4 GeV/c, therefore the false curvature effect changes the measured $K^\pm$ momentum by $1 \pm 1.4 \cdot 14 \cdot 10^{-5} = 1 \pm 2 \cdot 10^{-4}$. The resulting shifts of the measured B^0 and B^+ mass are listed in Table 5.4.

Table 5.8: Shifts of the measured B masses resulting from varying the measured momenta of $K^\pm$ and $\pi^\pm$ tracks according to the parametrization $p^\pm_{new} = p^\pm_{old} \times (1 \mp C)$. The form of the correction coefficient C for different tests is given in the first column.

correction coefficient C	$M(B^0)$ shift (MeV/c^2)	$M(B^+)$ shift (MeV/c^2)
False curvature correction		
$A_1 \cdot p^\pm_{t,old}$	0.02	0.02
ϕ-dependent correction		
$A_2 \cdot \sin\phi \cdot p^\pm_{old}$	0.04	0.02
$A_2 \cdot \cos\phi \cdot p^\pm_{old}$	0.04	0.05
θ-dependent correction		
$A_3 \cdot \cos\theta \cdot p^\pm_{old}$	0.02	0.01

To estimate possible systematic bias due to ϕ dependence of a track reconstruction, we took an amplitude of the $|p(\mu^+)| + |p(\mu^-)|$ peak position variation to be 0.03 GeV/c (Figure C.2) and varied the measured $K^\pm$ and $\pi^\pm$ momenta according to the following formula:

$$p^\pm_{new} = p^\pm_{old} \cdot (1 \mp \frac{p^\pm_{old}}{5.3\ \mathrm{GeV}} \cdot \frac{0.03\ \mathrm{GeV}}{10.6\ \mathrm{GeV}} \cdot \sin\phi). \tag{5.4}$$

We also replaced $\sin\phi$ by $\cos\phi$ in Equation 5.4. To estimate possible systematic bias due to θ dependence of a track reconstruction, we took an amplitude of the $|p(\mu^+)| + |p(\mu^-)|$ peak

position variation to be 0.015 GeV/c at $\cos\theta = \pm 0.8$ (Figure C.2) and varied the measured $K^\pm$ momenta according to the following formula:

$$p^{\pm}_{new} = p^{\pm}_{old} \cdot (1 \pm \frac{p^{K^\pm}_{old}}{5.3\ \text{GeV}} \cdot \frac{0.015\ \text{GeV}}{10.6\ \text{GeV}} \cdot \frac{\cos\theta}{0.8}). \tag{5.5}$$

The resulting shifts of the measured B^0 and B^+ mass are listed in Table 5.4. We assigned the largest shift of the measured B mass as a systematic uncertainty.

Chapter 6

Study of exclusive two-body B^0 meson decays to charmonium

6.1 Abstract

We present a study of three B^0 decay modes that should be useful for measurement of time-dependent CP asymmetries. From a sample of 9.7×10^6 $B\overline{B}$ meson pairs, we have reconstructed the decays $B^0 \to J/\psi\, K^0_S$, $B^0 \to \chi_{c1}\, K^0_S$, and $B^0 \to J/\psi\, \pi^0$. The latter two decay modes were observed for the first time. We describe a $K^0_S \to \pi^0\pi^0$ detection technique and its application to the reconstruction of the decay $B^0 \to J/\psi\, K^0_S$. Combining the results obtained using $K^0_S \to \pi^+\pi^-$ and $K^0_S \to \pi^0\pi^0$ decays, we determine $\mathcal{B}(B^0 \to J/\psi\, K^0) = (9.5 \pm 0.8 \pm 0.6) \times 10^{-4}$, where the first uncertainty is statistical and the second one is systematic. We also obtain $\mathcal{B}(B^0 \to \chi_{c1}\, K^0) = (3.9^{+1.9}_{-1.3} \pm 0.4) \times 10^{-4}$ and $\mathcal{B}(B^0 \to J/\psi\, \pi^0) = (2.5^{+1.1}_{-0.9} \pm 0.2) \times 10^{-5}$.

6.2 Introduction

In this Chapter we present a study of the decays $B^0 \to J/\psi\, K^0_S$, $B^0 \to \chi_{c1}\, K^0_S$, and $B^0 \to J/\psi\, \pi^0$. The latter two decay modes were observed for the first time. We describe a $K^0_S \to \pi^0\pi^0$ detection technique and its application to the reconstruction of the decay $B^0 \to J/\psi\, K^0_S$.

CP violation arises naturally in the Standard Model which has three quark generations [68]; however, it still remains one of the least experimentally constrained sectors of the Standard Model. Measurements of time-dependent rate asymmetries in the decays of neutral B mesons will provide an important test of the Standard Model mechanism for CP violation [69, 70, 71]. The time-dependent asymmetry in neutral B decays into a final CP eigenstate f is given by

$$a_f(t) = \frac{\Gamma[B^0(t)] - \Gamma[\overline{B}^0(t)]}{\Gamma[B^0(t)] + \Gamma[\overline{B}^0(t)]} = a_f^{\cos}\cos(\Delta m t) + a_f^{\sin}\sin(\Delta m t) \tag{6.1}$$

with

$$a_f^{\cos} = \frac{1-|\lambda|^2}{1+|\lambda|^2}, \quad a_f^{\sin} = \frac{-2\mathrm{Im}\lambda}{1+|\lambda|^2}, \quad \lambda = \frac{q}{p}\frac{\overline{A}_f}{A_f}, \tag{6.2}$$

where $A_f = \langle f|H\,|B^0\rangle$, $\overline{A}_f = \langle f|H\,\left|\overline{B}^0\right\rangle$, and the coefficients p and q ($p^2+q^2=1$) express the mass eigenstates $B_{1,2}$ through the flavor eigenstates $|B_{1,2}\rangle = p\,|B^0\rangle \pm q\,\left|\overline{B}^0\right\rangle$.

$B^0 \to J/\psi\, K_S^0$ and $B^0 \to \chi_{c1}\, K_S^0$

For the $b \to c\bar{c}s$ transition that governs $B \to J/\psi K$ decays, the penguin amplitude (Figure 6.1) is expected to be small, and the relative tree–penguin weak phase is guaranteed to be small in the Standard Model (Section 8.2). A measurement of the CP asymmetry

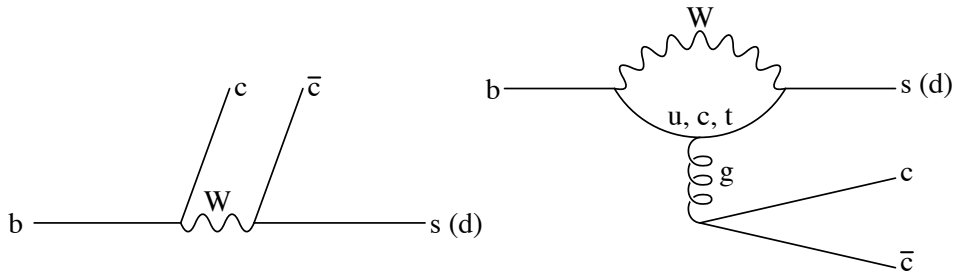

Figure 6.1: Standard Model tree and penguin diagrams for $b \to c\bar{c}s$ and $b \to c\bar{c}d$ transitions.

in $B^0(\overline{B}^0) \to J/\psi\, K_S^0$ decays probes the relative weak phase between the $B^0 - \overline{B}^0$ mixing amplitude and the $b \to c\bar{c}s$ decay amplitude [72, 73, 74, 75, 76, 77]. In the Standard Model this measurement determines $\sin 2\beta$, where $\beta \equiv \mathrm{Arg}\,(-V_{cd}V_{cb}^*/V_{td}V_{tb}^*)$:

$$a_{\psi K_S}^{\cos} = 0, \quad a_{\psi K_S}^{\sin} = -\sin 2\beta, \tag{6.3}$$

where $a^{\cos}$ and $a^{\sin}$ are defined in Equations 6.1 and 6.2. The same argument holds for $B^0(\overline{B}^0) \to \chi_{c1}\, K_S^0$ decays. Therefore a measurement of $\sin 2\beta$ with this decay mode is as theoretically clean as the one with $B^0(\overline{B}^0) \to J/\psi\, K_S^0$. The rate prediction and references to the previous searches for $B^0 \to \chi_{c1}\, K_S^0$ decay can be found in Section 6.5.1.

$B^0 \to J/\psi\, \pi^0$

For the purposes of CP violation measurements, the $B^0 \to J/\psi\, \pi^0$ decay is similar to $B^0 \to D^+ D^-$: both decays are governed by the $b \to c\bar{c}d$ quark transition (Figure 6.1), and both final states are CP eigenstates of the same CP sign. A search for the decay $B^0 \to D^+D^-$ has been attempted at CLEO, but no statistically significant signal has been observed in the full CLEO II and CLEO II.V data set [78]. The rate prediction and references to the previous searches for the $B^0 \to J/\psi\, \pi^0$ decay can be found in Section 6.6.1.

We can write the amplitude of the $b \to c\bar{c}d$ transition as a sum of tree ($T_{c\bar{c}d}$) and penguin ($P_{\{u,c,t\}}$) contributions (Figure 6.1): $A(c\bar{c}d) = V_{cb}V_{cd}^*(T_{c\bar{c}d} + P_c) + V_{ub}V_{ud}^* P_u +$

$V_{tb}V_{td}^*P_t$. Using the constraint provided by the unitarity of the Cabibbo-Kobayashi-Maskawa matrix, $V_{cb}V_{cd}^*+V_{ub}V_{ud}^*+V_{tb}V_{td}^*=0$, we can recast the expression for the $A(c\bar{c}d)$ as $A(c\bar{c}d) = V_{cb}V_{cd}^*(T_{c\bar{c}d}+P_c-P_u)+V_{tb}V_{td}^*(P_t-P_u)$. The relative weak phase between the two terms is $\mathrm{Arg}\,(V_{cb}V_{cd}^*/V_{tb}V_{td}^*) = \pi-\beta$.

The penguin contribution to $B^0 \to J/\psi\pi^0$ decay is possibly significant, and the relative weak phase between the tree and penguin amplitudes is big (β). Therefore the expressions for the time-dependent CP asymmetry for $J/\psi\pi^0$ are more complicated than for $J/\psi K_S^0$ mode (Equations 6.3):

$$a_{\psi\pi^0}^{\cos} = 2r\sin\beta\sin\delta+\mathcal{O}(r^2),\quad a_{\psi\pi^0}^{\sin} = +\sin 2\beta - 2r\cos\delta\cos 2\beta\sin\beta+\mathcal{O}(r^2), \tag{6.4}$$

where $a^{\cos}$ and $a^{\sin}$ are defined in Equations 6.1 and 6.2, δ is the strong phase difference between penguin and tree amplitudes, and $r = A_P/A_T$ is the signed ratio of their magnitudes [80].

If the penguin amplitude is negligible compared to the tree amplitude, then $|r| = 0$ and the Equations 6.4 yield $a_{\psi\pi^0}^{\cos} = 0$ and $a_{\psi\pi^0}^{\sin} = +\sin 2\beta$. Therefore the measurement of the time-dependent CP asymmetry in $B^0(\overline{B}^0) \to J/\psi\pi^0$ decay allows a theoretically clean extraction of $\sin 2\beta$, the relative phase between the $B^0-\overline{B}^0$ mixing amplitude and the $b \to c\bar{c}d$ tree amplitude. In this case the $B^0 \to J/\psi\pi^0$ mode could be added to the "gold-plated" $B^0 \to J/\psi K_S^0$ mode to augment statistics in the $\sin 2\beta$ measurement. The asymmetries measured with $J/\psi K_S^0$ and $J/\psi\pi^0$ modes should have exactly the same absolute values but opposite signs, because $CP(K_S^0) \simeq +$ and $CP(\pi^0) = -$. Therefore, a comparison of the asymmetries measured with these two modes provides a useful check for a charge-correlated systematic bias in B flavor tagging.

Another useful application of the $B^0 \to J/\psi\pi^0$ decay arises if penguin and tree amplitudes are comparable. Ciuchini *et al.* [79] estimated that the penguin to tree amplitude ratio $|r|$ could be as large as 30%. It might be possible to use the tree–penguin interference in $B^0 \to J/\psi\pi^0$ decays to measure the sign of $\sin\beta$, thus removing one of the two discrete ambiguities ($\beta \to \beta+\pi$) remaining after the $\sin 2\beta$ measurement with $B^0(\overline{B}^0) \to J/\psi K_S^0$ decays [80]. Comparing the asymmetries observed in $B^0(\overline{B}^0) \to J/\psi K_S^0$ and $B^0(\overline{B}^0) \to J/\psi\pi^0$ decays (Equations 6.3 and 6.4), we obtain

$$a_{\psi K_S}^{\sin} + a_{\psi\pi^0}^{\sin} = -2r\cos\delta\cos 2\beta\sin\beta.$$

We can fix the sign of $\sin\beta$ if we know the signs of $\cos 2\beta$ and $r\cos\delta$. The sign of $\cos 2\beta$ can be determined using one of the methods described, for example, in [80] or [81]. One has to rely on models to predict the sign of $(r\cos\delta)$. For example, if the final state interactions in $B^0 \to J/\psi\pi^0$ decay are small, then $\delta \approx 0 \Rightarrow \cos\delta > 0$ and $sign(r\cos\delta) = sign(r)$. It has been pointed out, however, that this method of resolving discrete ambiguities becomes unreliable in the presence of New Physics [80, 82] because the angle "β" measured in $B^0(\overline{B}^0) \to J/\psi K_S^0$ may not be the same as the relative phase between penguin and tree amplitudes in $b \to c\bar{c}d$ transition.

The work presented in this Chapter would have been an input to CLEO's own measurement of $\sin 2\beta$. However, the sensitivity study described in Chapter 7 discouraged this undertaking.

6.3 Analysis summary and results

We use 9.2 fb^{-1} of e^+e^- data taken at the $\Upsilon(4S)$ resonance and 4.6 fb^{-1} taken 60 MeV below the $\Upsilon(4S)$ resonance.

6.3.1 J/ψ selection

The normalized mass distributions for the $J/\psi \to \ell^+\ell^-$ candidates are shown in Figure 2.16. We require the normalized mass to be from -10 to $+3$ for the $J/\psi \to e^+e^-$ and from -4 to $+3$ for the $J/\psi \to \mu^+\mu^-$ candidates. For each J/ψ candidate, we perform a fit constraining its mass to the world average value.

6.3.2 γ and π^0 selection

Photon candidates for $\chi_{c1} \to J/\psi\,\gamma$ and $\pi^0 \to \gamma\gamma$ decays are required to have an energy of at least 30 MeV in the barrel region ($|\cos\theta_\gamma| < 0.71$) and at least 50 MeV in the endcap region ($0.71 < |\cos\theta_\gamma| < 0.95$), where θ_γ is the angle between the beam axis and the candidate photon. To select the π^0 candidates for $B^0 \to J/\psi\,\pi^0$ reconstruction, we require the normalized $\pi^0 \to \gamma\gamma$ mass to be between -5 and $+4$ (Appendix D). The average $\gamma\gamma$ invariant mass resolution for these π^0 candidates is 7 MeV/c^2. We perform a fit constraining the mass of each π^0 candidate to the world average value.

6.3.3 χ_{c1} selection

We reconstruct χ_{c1} in the $\chi_{c1} \to J/\psi\,\gamma$ decay mode. Most of the photons in $\Upsilon(4S) \to B\overline{B}$ events come from π^0 decays. We therefore do not use a photon if it can be paired with another photon to produce a π^0 candidate with the normalized $\pi^0 \to \gamma\gamma$ mass between -4 and $+3$. The resolution in the $J/\psi\,\gamma$ invariant mass is 8 MeV/c^2. We select the χ_{c1} candidates with the normalized $\chi_{c1} \to J/\psi\,\gamma$ mass between -4 and $+3$ and perform a fit constraining the mass of each χ_{c1} candidate to the world average value.

6.3.4 $K^0_S \to \pi^+\pi^-$ selection

The $K^0_S \to \pi^+\pi^-$ candidates are selected from pairs of tracks forming well-measured displaced vertices. The resolution in the $\pi^+\pi^-$ invariant mass is 4 MeV/c^2. We select the $K^0_S \to \pi^+\pi^-$ candidates with the normalized $K^0_S \to \pi^+\pi^-$ mass between -4 and $+4$ and perform a fit constraining the mass of each K^0_S candidate to the world average value.

6.3.5 $K^0_S \to \pi^0\pi^0$ reconstruction

In order to increase our $B^0 \to J/\psi\,K^0_S$ sample, we also reconstruct $K^0_S \to \pi^0\pi^0$ decays (Appendix E). The average flight distance for the K^0_S from $B^0 \to J/\psi\,K^0_S$ decay is 9 cm. We find the K^0_S decay vertex using only the calorimeter information and the known position of the e^+e^- interaction point. The K^0_S flight direction is calculated as the line passing through the e^+e^- interaction point and the center of energy of the four photon

showers in the calorimeter. The K^0_S decay vertex is defined as the point along the K^0_S flight direction for which the product $f[M(\gamma_1\gamma_2)] \times f[M(\gamma_3\gamma_4)]$ is maximal. In the above expression, $M(\gamma_1\gamma_2)$ and $M(\gamma_3\gamma_4)$ are the diphoton invariant masses recalculated assuming a particular K^0_S decay point, and $f(M)$ is the π^0 mass lineshape obtained from the simulation where we use the known K^0_S decay vertex. This π^0 lineshape is asymmetric, with its low-side tail arising from the energy leakage in the calorimeter. For simulated events, the K^0_S flight distance is found without bias with a resolution of 5 cm. The uncertainty in the K^0_S decay vertex position arising from the K^0_S direction approximation is much smaller than the resolution of the flight distance. We select the K^0_S candidates by requiring the reconstructed K^0_S decay length to be in the range from -10 to $+60$ cm. After the K^0_S decay vertex is found, we select the $K^0_S \to \pi^0\pi^0$ candidates by requiring $-15 < M(\gamma\gamma) - M_{\pi^0} < 10$ MeV/c^2 for both photon pairs. Then we perform a kinematic fit simultaneously constraining $M(\gamma_1\gamma_2)$ and $M(\gamma_3\gamma_4)$ to the world average value of the π^0 mass. The resulting K^0_S mass resolution is 12 MeV/c^2. We select the $K^0_S \to \pi^0\pi^0$ candidates with the normalized $K^0_S \to \pi^0\pi^0$ mass between -3 and $+3$ and perform a fit constraining the mass of each K^0_S candidate to the world average value. The $K^0_S \to \pi^0\pi^0$ detection efficiency is determined from simulation. The systematic uncertainty associated with this determination can be reliably estimated by comparing the $K^0_S \to \pi^0\pi^0$ and $K^0_S \to \pi^+\pi^-$ yields for inclusive K^0_S candidates in data and in simulated events.

6.3.6 B^0 selection

The B^0 candidates are selected by means of two observables: ΔE and $M(B)$ (Section 1.7). The average ΔE resolution for each decay mode is listed in Table 6.1. We use the normalized ΔE for candidate selection and require $|\Delta E|/\sigma(\Delta E) < 3$ for $B^0 \to J/\psi\, K^0_S$ and $B^0 \to \chi_{c1}\, K^0_S$ candidates with $K^0_S \to \pi^+\pi^-$. To account for a low-side ΔE tail arising from the energy leakage in the calorimeter, we require $-5 < \Delta E/\sigma(\Delta E) < 3$ for $B^0 \to J/\psi\, K^0_S$ with $K^0_S \to \pi^0\pi^0$ and $-4 < \Delta E/\sigma(\Delta E) < 3$ for $B^0 \to J/\psi\, \pi^0$ candidates. The second observable is the beam-constrained B mass, $M(B) \equiv \sqrt{E^2_{\rm beam} - p^2(B)}$, where $p(B)$ is the magnitude of the B^0 candidate momentum. The resolution in $M(B)$ is dominated by the beam energy spread for all the decay modes under study and varies from 2.7 to 3.0 MeV/c^2 depending on the mode. We use the normalized $M(B)$ for candidate selection and require $|M(B) - M_B|/\sigma(M) < 3$, where M_B is the nominal B^0 meson mass. The ΔE vs. $M(B)$ distributions together with the projections on the $M(B)$ axis are shown in Figure 6.2. The number of B^0 candidates selected in each decay mode is listed in Table 6.1. More details on the selection of the B^0 candidates can be found in Sections 6.4.1, 6.5.2, and 6.6.2.

6.3.7 Backgrounds

Backgrounds can be divided into two categories. The first category is the background from those exclusive B decays that tend to produce a peak in the signal region of the $M(B)$ distribution. We identify these exclusive B decays and estimate their contributions to background using simulated events with the normalizations determined from the known branching fractions or from our data. The second category is the combinatorial background from $B\overline{B}$ and continuum non-$B\overline{B}$ events. To estimate the combinatorial background, we

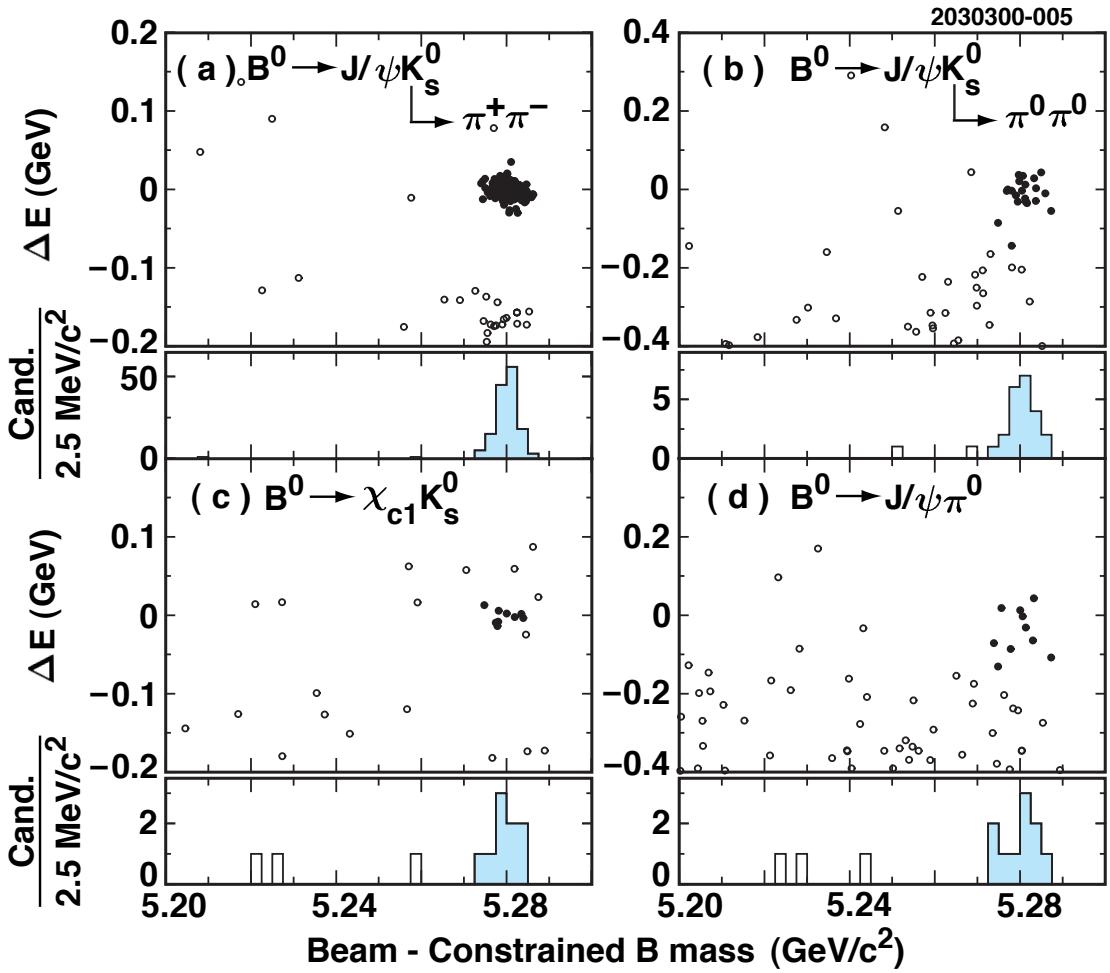

Figure 6.2: The ΔE vs. $M(B)$ distribution for (a) $B^0 \to J/\psi\, K^0_S$ with $K^0_S \to \pi^+\pi^-$, (b) $B^0 \to J/\psi\, K^0_S$ with $K^0_S \to \pi^0\pi^0$, (c) $B^0 \to \chi_{c1}\, K^0_S$, and (d) $B^0 \to J/\psi\, \pi^0$ candidates. The signal candidates, selected using normalized ΔE and $M(B)$ variables, are shown by filled circles. Below each ΔE vs. $M(B)$ plot, we show the projection on the $M(B)$ axis with the ΔE requirement applied. The shaded parts of the histograms represent the candidates that pass the $|M(B) - M_B|/\sigma(M) < 3$ requirement.

Table 6.1: Number of signal candidates (N_{signal}), estimated background (N_{bckgr}), average ΔE resolution, product of secondary branching fractions ($\mathcal{B}_s$), detection efficiency, and measured branching fraction. Line 1 contains the combined value of $\mathcal{B}(B^0 \to J/\psi\, K^0)$, lines 2 and 3 contain the individual results for the two K^0_S decay modes. For $B^0 \to J/\psi\, \pi^0$ and $B^0 \to J/\psi\, K^0_S$ with $K^0_S \to \pi^0\pi^0$ the ΔE distribution has a low-side tail due to the energy leakage in the calorimeter, and the quoted efficiency value includes the loss of efficiency due to Dalitz decay $\pi^0 \to e^+e^-\gamma$.

Decay mode	N_{signal}	N_{bckgr}	$\sigma(\Delta E)$ (MeV)	$\mathcal{B}_s$ (%)	Efficiency (%)	Branching fraction ($\times 10^{-4}$)
$J/\psi\, K^0$						$9.5 \pm 0.8 \pm 0.6$
$K^0_S \to \pi^+\pi^-$	142	0.3 ± 0.2	11	4.04 ± 0.06	37.0 ± 2.3	$9.8 \pm 0.8 \pm 0.7$
$K^0_S \to \pi^0\pi^0$	22	1.1 ± 0.3	25	1.85 ± 0.03	13.9 ± 1.1	$8.4^{+2.1}_{-1.9} \pm 0.7$
$\chi_{c1}\, K^0$	9	0.9 ± 0.3	10	1.10 ± 0.07	19.2 ± 1.3	$3.9^{+1.9}_{-1.3} \pm 0.4$
$J/\psi\, \pi^0$	10	1.0 ± 0.5	28	11.8 ± 0.2	31.4 ± 2.2	$0.25^{+0.11}_{-0.09} \pm 0.02$

fit the $M(B)$ distribution in the region from 5.1 to 5.3 GeV/c^2. As a consistency check, we also estimate the combinatorial background using high-statistics samples of simulated $\Upsilon(4S) \to B\overline{B}$ and non-$B\overline{B}$ continuum events together with the data collected below the $B\overline{B}$ production threshold. The total estimated backgrounds are listed in Table 6.1. Below we describe the background estimation for each decay channel under study. More details on the background estimation can be found in Sections 6.4, 6.5, and 6.6.

Background for $B^0 \to J/\psi\, K^0_S$ with $K^0_S \to \pi^+\pi^-$. Only combinatorial background contributes, with the total background estimated to be 0.3±0.2 events (Sections 6.4.4–6.4.6).

Background for $B^0 \to J/\psi\, K^0_S$ with $K^0_S \to \pi^0\pi^0$. The combinatorial background is estimated to be 0.5 ± 0.2 events (Sections 6.4.4–6.4.6). The other background source is $B \to J/\psi\, K^*$, with $K^* \to K\pi^0$ or $K^* \to K^0_S\pi$ with $K^0_S \to \pi^0\pi^0$ (Section 6.4.7). The background from these decays is estimated to be 0.6 ± 0.2 events.

Background for $B^0 \to \chi_{c1}\, K^0_S$. The combinatorial background is estimated to be 0.5 ± 0.3 events (Sections 6.5.6 and 6.5.8). We estimate the $B \to J/\psi\, K^0_S\pi$ background from the samples of simulated events, with the normalizations obtained from the fits to the $M(K\pi)$ distributions for $B^+ \to J/\psi\, K^0_S\pi^+$ and $B^0 \to J/\psi\, K^-\pi^+$ candidates in data (Section 6.5.4). The background from $B \to J/\psi\, K^0_S\pi$ is estimated to be 0.41 ± 0.07 events and is dominated by $B \to J/\psi\, K^*$ decays with $K^* \to K^0_S\pi$. We find no evidence for $B \to \chi_{c2}\, K$ production and estimate the background from $B^0 \to \chi_{c2}\, K^0_S$ to be 0.01 ± 0.01 events (Section 6.5.5).

Background for $B^0 \to J/\psi\, \pi^0$. The combinatorial background is estimated to be $0.4^{+0.5}_{-0.3}$ events (Sections 6.6.7–6.6.9). The ΔE resolution is good enough to render negligible the background from any of the Cabibbo-allowed $B \to J/\psi K\pi^0(X)$ decays, where at least a kaon mass is missing from the energy sum. The background from $B^0 \to J/\psi\, K^0_S$ decays with $K^0_S \to \pi^0\pi^0$ is estimated to be 0.38±0.05 events (Section 6.6.4). We estimate the background from B decays to the $J/\psi\,\pi\pi^0$ final state from the samples of simulated events, with the normalizations obtained from the fits to the $M(\pi\pi)$ distributions for $B^+ \to J/\psi\, \pi^+\pi^0$ and $B^0 \to J/\psi\, \pi^0\pi^0$ candidates in data (Sections 6.6.5 and 6.6.6). The background from

$B \to J/\psi\,\pi^0\pi$ is estimated to be 0.2 ± 0.2 events, and is dominated by $B^+ \to J/\psi\,\rho^+$ decays.

6.3.8 Calculation of branching fractions

The statistical significance of the signal in the $B^0 \to \chi_{c1}\,K^0_S$ and $B^0 \to J/\psi\,\pi^0$ decay modes is discussed in Sections 6.5.10 and 6.6.10. We use the Feldman-Cousins approach [49] to assign the 68% C.L. intervals for the signal mean for the three low-statistics decay modes ($B^0 \to \chi_{c1}\,K^0_S$, $B^0 \to J/\psi\,\pi^0$, and $B^0 \to J/\psi\,K^0_S$ with $K^0_S \to \pi^0\pi^0$). We assume $\mathcal{B}(\Upsilon(4S) \to B^0\overline{B}^0) = \mathcal{B}(\Upsilon(4S) \to B^+B^-)$ for all branching fractions in this Chapter. We use the following branching fractions for the secondary decays: $\mathcal{B}(J/\psi \to \ell^+\ell^-) = (5.894 \pm 0.086)\%$ [50], $\mathcal{B}(\chi_{c1} \to J/\psi\gamma) = (27.3 \pm 1.6)\%$ [47], $\mathcal{B}(K^0_S \to \pi^+\pi^-) = (68.61 \pm 0.28)\%$ [47], and $\mathcal{B}(K^0_S \to \pi^0\pi^0) = (31.39 \pm 0.28)\%$ [47]. The reconstruction efficiencies are determined from simulation. The angular distribution assumed in the simulation of the decay chain $B^0 \to \chi_{c1}\,K^0_S$ with $\chi_{c1} \to J/\psi\gamma$ is discussed in Section 6.5.9. The resulting branching fractions are listed in Table 6.1. Combining the results for the two K^0_S modes used in $B^0 \to J/\psi\,K^0_S$ reconstruction and taking into account correlated systematic uncertainties, we obtain $\mathcal{B}(B^0 \to J/\psi\,K^0) = (9.5 \pm 0.8 \pm 0.6) \times 10^{-4}$. This measurement of $\mathcal{B}(B^0 \to J/\psi\,K^0)$ is consistent with and improves upon the previous CLEO measurement [30]; it is also consistent with the world average value [47]. The measurements of $\mathcal{B}(B^0 \to J/\psi\,K^0)$, $\mathcal{B}(B^0 \to \chi_{c1}\,K^0)$, and $\mathcal{B}(B^0 \to J/\psi\,\pi^0)$ presented in this Chapter improve upon and supersede the previous CLEO results [30, 65, 84]. A cross-check for the $\mathcal{B}(B^0 \to \chi_{c1}\,K^0)$ measurement is described in Section 6.5.11.

6.3.9 Systematic uncertainties

The systematic uncertainties in the branching fraction measurements include contributions from the uncertainty in the number of $B\overline{B}$ pairs (2%), tracking efficiencies (1% per charged track), photon detection efficiency (2.5%), lepton detection efficiency (3% per lepton), $K^0_S \to \pi^+\pi^-$ finding efficiency (2%), $K^0_S \to \pi^0\pi^0$ finding efficiency (5%), background subtraction ($0.01 - 5.5\%$, see Table 6.1), statistics of the simulated event samples ($0.6 - 1.0\%$), and the uncertainties on the branching fractions of secondary decays (see Table 6.1). More details on the systematic uncertainties can be found in Section 6.7.

6.3.10 Conclusion

In summary, we have studied three B^0 decay modes useful for the measurement of $\sin 2\beta$. We report the first observation and measure branching fractions of the $B^0 \to \chi_{c1}\,K^0$ and $B^0 \to J/\psi\,\pi^0$ decays. We describe a $K^0_S \to \pi^0\pi^0$ detection technique and its application to the reconstruction of the decay $B^0 \to J/\psi\,K^0_S$. We measure the branching fraction for $B^0 \to J/\psi\,K^0$ decays with K^0_S mesons reconstructed in both $\pi^+\pi^-$ and $\pi^0\pi^0$ decay modes.

6.4 More details on the $B^0 \to J/\psi K^0_S$ analysis

6.4.1 Selection of signal candidates

The $K^0_S \to \pi^0\pi^0$ reconstruction technique is described in Appendix E. Figure 6.3 shows the normalized $M(B)$ and ΔE distributions for the $B^0 \to J/\psi K^0_S$, $K^0_S \to \pi^0\pi^0$ candidates reconstructed from the sample of the simulated signal events. The distributions

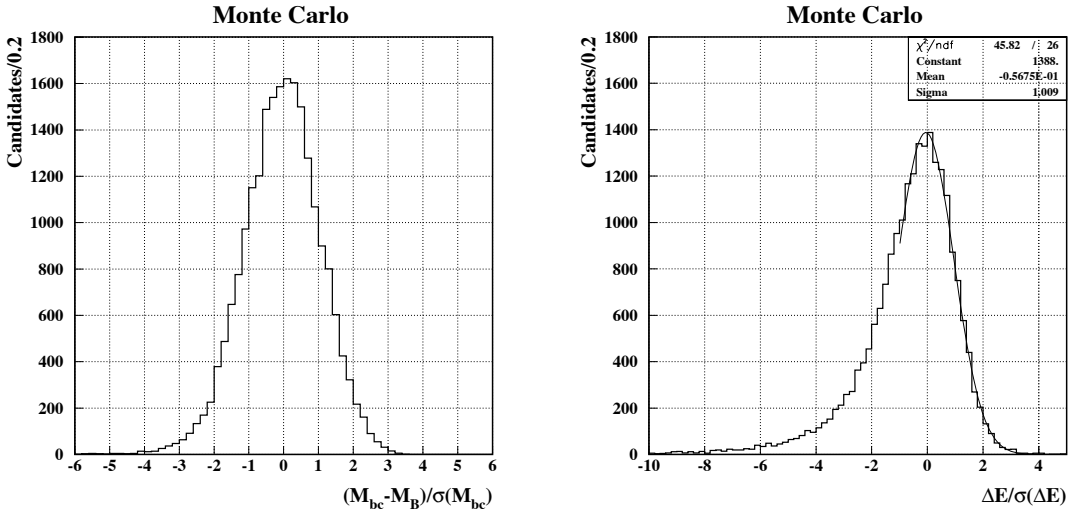

Figure 6.3: Normalized $M(B)$ (left) and ΔE (right) distributions for $B^0 \to J/\psi K^0_S$, $K^0_S \to \pi^0\pi^0$ candidates reconstructed from the sample of the simulated signal events.

of the normalized ΔE vs. normalized $M(B)$ for $B^0 \to J/\psi K^0_S$ candidates in data are shown in Figure 6.4. For $K^0_S \to \pi^+\pi^-$ we multiplied the reported ΔE uncertainties by a scale factor of 1.2 to make the normalized ΔE distribution for the simulated signal events look more like a unit Gaussian. The signal box is defined as $|M(B) - M_B|/\sigma(M) < 3$ for both modes and $-5 < \Delta E/\sigma(\Delta E) < 3$ ($|\Delta E|/\sigma(\Delta E) < 3$) for $K^0_S \to \pi^0\pi^0$ ($K^0_S \to \pi^+\pi^-$). There are 22 (142) candidates in the signal box for $K^0_S \to \pi^0\pi^0$ ($K^0_S \to \pi^+\pi^-$) mode. All $B^0 \to J/\psi K^0_S$ signal candidates come from different events, even though we did not attempt to select a single candidate in a given event. The distribution of the found K^0_S flight distances for 22 $B^0 \to J/\psi K^0_S$, $K^0_S \to \pi^0\pi^0$ candidates is shown in Figure 6.5. Figure 6.6 shows an event display for one of the $B^0 \to J/\psi K^0_S$, $J/\psi \to \mu^+\mu^-$, $K^0_S \to \pi^0\pi^0$ candidates.

6.4.2 Summary of background estimation

$B^0 \to J/\psi K^0_S$, $K^0_S \to \pi^0\pi^0$

In data we selected 22 $B^0 \to J/\psi K^0_S$, $K^0_S \to \pi^0\pi^0$ candidates. The total background is estimated to be 1.1 ± 0.3 events.

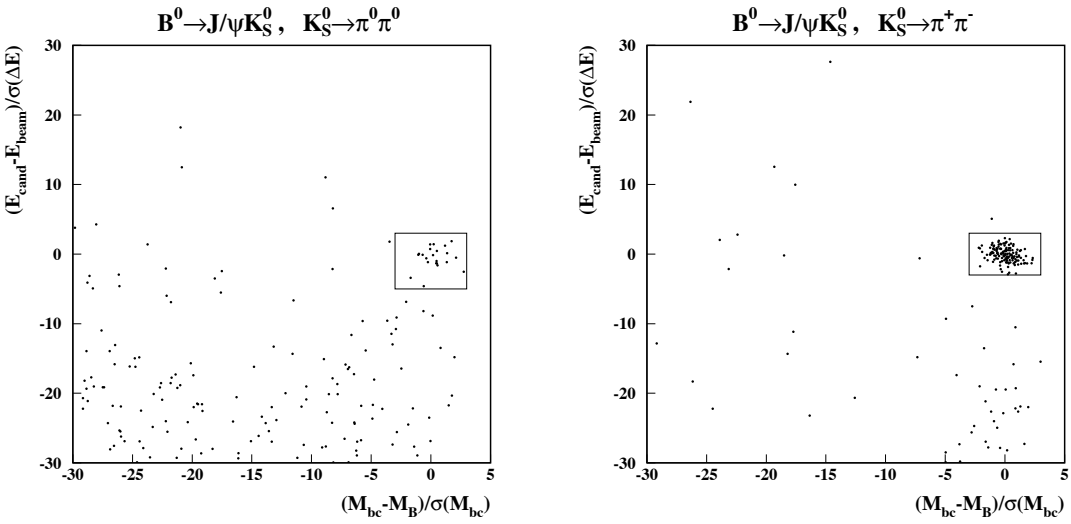

Figure 6.4: Normalized ΔE vs. normalized $M(B)$ for $B^0 \to J/\psi K_S^0$ candidates in data. Left plot represents the candidates with $K_S^0 \to \pi^0\pi^0$, whereas right plot is for $K_S^0 \to \pi^+\pi^-$. There are 22 (142) candidates in the signal box for the $K_S^0 \to \pi^0\pi^0$ ($K_S^0 \to \pi^+\pi^-$) mode.

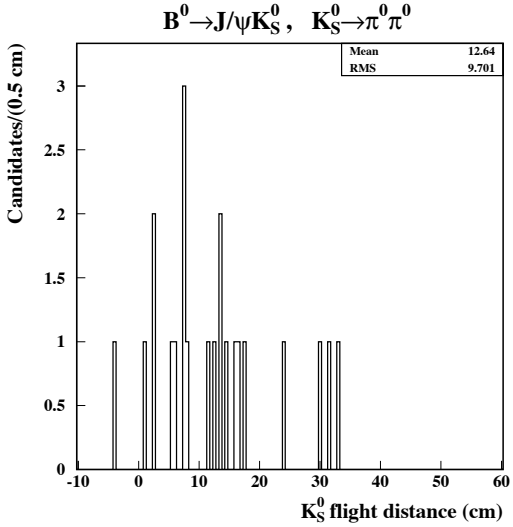

Figure 6.5: Found K_S^0 flight distance for 22 $B^0 \to J/\psi K_S^0$, $K_S^0 \to \pi^0\pi^0$ candidates in data.

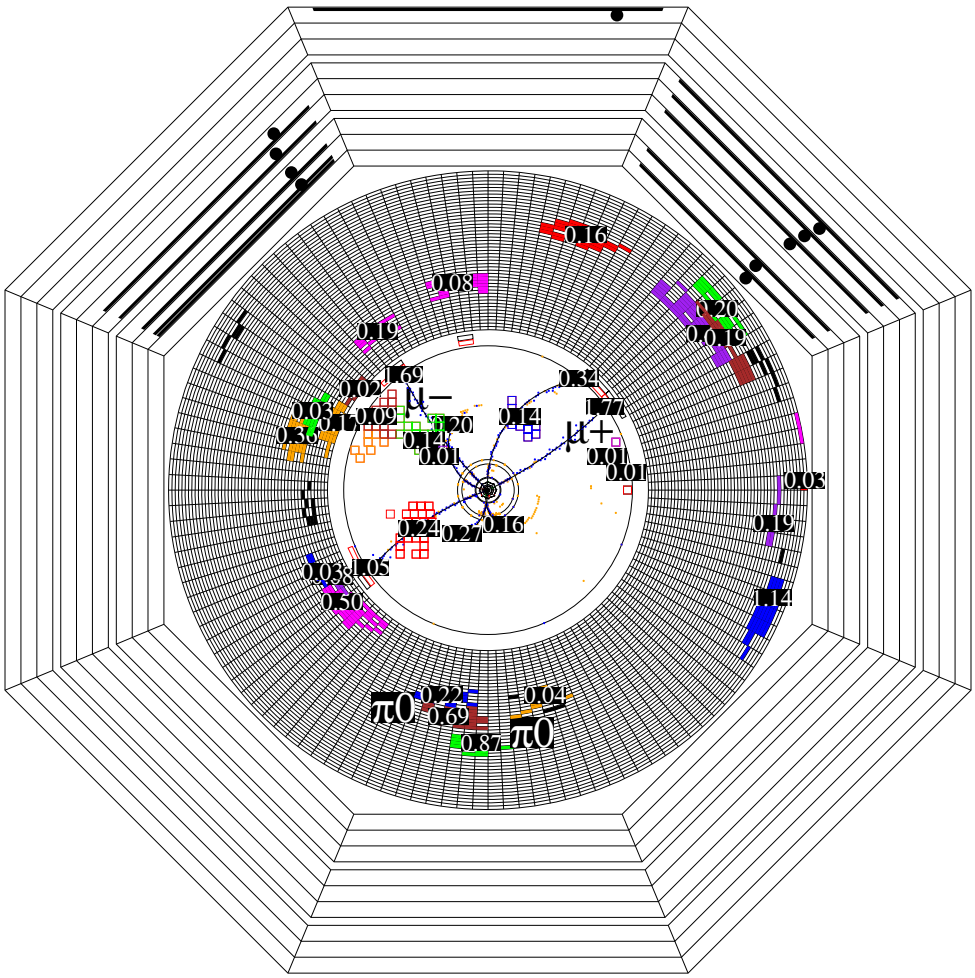

Figure 6.6: One of the $B^0 \to J/\psi K^0_S$, $J/\psi \to \mu^+\mu^-$, $K^0_S \to \pi^0\pi^0$ events reconstructed from data. The four showers at 6 o'clock come from K^0_S. The K^0_S direction of flight is almost perpendicular to the beam direction; we found the radius of K^0_S decay vertex to be 24 cm, which corresponds to the 4th layer of the main drift chamber (DR).

- Using off-$\Upsilon(4S)$ data together with the samples of simulated generic continuum and $B\overline{B}$ events, we estimated the total background to be 1.3 ± 0.2 events.

- From fits to $M(B)$ distribution, we estimated the combinatorial background to be 0.5 ± 0.2 events.

- The events from the following two decay chains $B \to J/\psi(K\pi^0)^*$[1] and $B \to J/\psi(K^0_S\pi)^*$, $K^0_S \to \pi^0\pi^0$ produce a broad peak in the signal region of the $M(B)$ distribution. The contribution from these decays can be reliably estimated from the Monte Carlo simulation, as the branching fraction $\mathcal{B}(B \to J/\psi K^*)$ is well measured. The background from these two decay chains is estimated to be 0.57 ± 0.15 events.

- Adding background from $B \to J/\psi(K\pi^0)^*$ and $B \to J/\psi(K^0_S\pi)^*$, $K^0_S \to \pi^0\pi^0$ to the combinatorial background estimated from fits to $M(B)$ distribution, we obtain the total background of 1.1 ± 0.3.

$B^0 \to J/\psi K^0_S, \;\; K^0_S \to \pi^+\pi^-$

In data we selected 142 $B^0 \to J/\psi K^0_S$, $K^0_S \to \pi^+\pi^-$ candidates. The total background for this mode is estimated to be 0.3 ± 0.2 events.

- Using off-$\Upsilon(4S)$ data together with the simulated generic continuum and $B\overline{B}$ events, we estimated the total background to be 0.2 ± 0.1 events.

- The resolution in ΔE for this mode is good enough to render negligible the background from J/ψ K^0_S combinations originating from the same B meson, for example, $B \to J/\psi(K^0_S\pi)^*$. Therefore all backgrounds can be considered as combinatorial. From fits to beam constrained mass distribution, we estimated the background to be 0.3 ± 0.2 events.

6.4.3 Continuum background estimation from Monte Carlo simulation and off-$\Upsilon(4S)$ data

Continuum background was estimated from off-$\Upsilon(4S)$ data and "5 times the on-$\Upsilon(4S)$ data" sample of simulated generic continuum events. In our analysis the background from continuum events is strongly suppressed by J/ψ selection requirements (Figure 2.16). There are very few real J/ψ's produced in the continuum and virtually all of them have a momentum greater than 2 GeV/c, which is the upper kinematic limit for a J/ψ produced in a B decay. To get more statistics for continuum background evaluation, we relaxed the $J/\psi \to \ell^+\ell^-$ mass cut and required the absolute value of the normalized J/ψ mass to be less than 30 both for $J/\psi \to e^+e^-$ and for $J/\psi \to \mu^+\mu^-$ modes (Figure 2.16). Combining off-$\Upsilon(4S)$ data and the simulated continuum event sample, we estimated the continuum background to be $0.13^{+0.09}_{-0.05}$ events for $K^0_S \to \pi^0\pi^0$ mode and $0.06^{+0.07}_{-0.04}$ events for $K^0_S \to \pi^+\pi^-$ mode.

[1] The $B \to J/\psi(K\pi^0)^*$ notation stands for the decay chain $B \to J/\psi K^*$ with $K^* \to K\pi^0$

6.4.4 $B\overline{B}$ background estimation from Monte Carlo simulation

To study the background from generic $B\overline{B}$ decays, we used a high-statistics sample of simulated $B\overline{B}$ events corresponding to "35 times the data". The distributions of the normalized ΔE vs. normalized $M(B)$ for $B^0 \to J/\psi K^0_S$ candidates reconstructed from this Monte Carlo sample are shown in Figure 6.7. We estimated the $B\overline{B}$ background to be 1.2 ± 0.2 events for $B^0 \to J/\psi K^0_S$, $K^0_S \to \pi^0\pi^0$ and $0.14^{+0.08}_{-0.06}$ events for $K^0_S \to \pi^+\pi^+$.

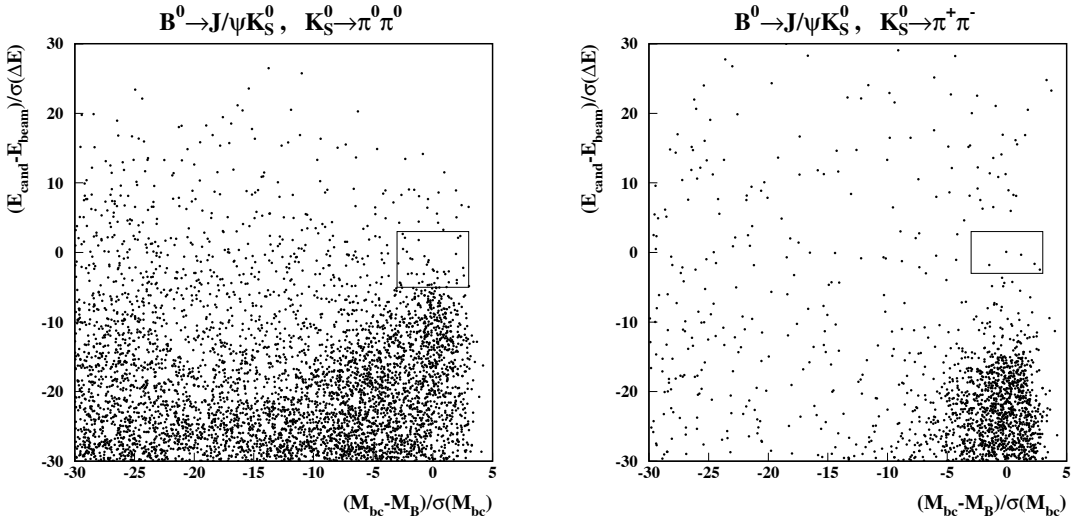

Figure 6.7: $B^0 \to J/\psi K^0_S$ background from generic $B\overline{B}$ decays. Left plot represents the candidates with $K^0_S \to \pi^0\pi^0$, whereas right plot is for $K^0_S \to \pi^+\pi^-$. The plot was obtained using "35 times the data" sample of simulated generic $B\overline{B}$ events. There are 41 (5) candidates in the signal box for the $K^0_S \to \pi^0\pi^0$ ($K^0_S \to \pi^+\pi^-$) mode.

6.4.5 Consistency checks for background estimation procedure

We estimated the background from $B\overline{B}$ and continuum Monte Carlo samples together with off-$\Upsilon(4S)$ data. We verified the quality of our background estimation procedure by predicting the number of events in 3 control regions of the ΔE vs. $M(B)$ plots shown in Figure 6.4. The 3 control regions are defined as follows (signal box is excluded from all 3 regions):

1. Region 1: $|\Delta E|/\sigma(\Delta E) < 30$, $-30 < [M(B) - M_B]/\sigma(M) < +5$
2. Region 2: $|\Delta E|/\sigma(\Delta E) < 30$, $-30 < [M(B) - M_B]/\sigma(M) < -3$
3. Region 3: $|\Delta E|/\sigma(\Delta E) < 30$, $-3 < [M(B) - M_B]/\sigma(M) < +3$.

The results for are listed in Table 6.2. The agreement is satisfactory everywhere, except for the region below the signal box for $K^0_S \to \pi^0\pi^0$ (Region 3). The discrepancy most likely

arises because the multi-body $B \to J/\psi K n\pi$ decays in QQ do not respect isospin symmetry, with the bias towards producing more neutral pions than is justified by isospin. For example, $\mathcal{B}(B \to J/\psi K\pi^+) = \mathcal{B}(B \to J/\psi K\pi^0)$ is assumed, whereas $\mathcal{B}(B \to J/\psi K\pi^+) = 2 \cdot \mathcal{B}(B \to J/\psi K\pi^0)$ is expected from isospin symmetry. This feature of QQ may lead to a slight overestimation of the combinatorial $B\overline{B}$ background. Note that the combinatorial background will be estimated from a fit to $M(B)$ distribution in data.

Table 6.2: Quality control of the background estimation procedure for $B^0 \to J/\psi K^0_S$. We predict and compare with data the number of events in 3 control regions of the ΔE vs. $M(B)$ plots shown in Figure 6.4.

Source	Region 1	Region 2	Region 3
	$B^0 \to J/\psi K^0_S,\ K^0_S \to \pi^0\pi^0$		
Continuum	26.2 ± 0.9	24.7 ± 0.9	1.4 ± 0.2
$B\overline{B}$	135.7 ± 2.0	107.5 ± 1.8	27.6 ± 0.9
$B^0 \to J/\psi K^0_S,\ K^0_S \to \pi^0\pi^0$	4.9 ± 1.1	2.8 ± 0.6	2.1 ± 0.4
Total predicted $N^{\rm pred}$	167 ± 2	135 ± 2	31 ± 1
Observed $N^{\rm obs}$	150	133	17
$N^{\rm obs}/N^{\rm pred} - 1$	$(-10 \pm 7)\%$	$(-1 \pm 9)\%$	$(-45 \pm 13)\%$
	$B^0 \to J/\psi K^0_S,\ K^0_S \to \pi^+\pi^-$		
Continuum	9.0 ± 0.5	8.4 ± 0.5	0.6 ± 0.1
$B\overline{B}$	46.3 ± 1.2	16.0 ± 0.7	29.8 ± 0.9
$B^0 \to J/\psi K^0_S,\ K^0_S \to \pi^+\pi^-$	4.9 ± 0.4	1.1 ± 0.1	3.6 ± 0.3
Total predicted $N^{\rm pred}$	60 ± 1	26 ± 1	34 ± 1
Observed $N^{\rm obs}$	49	23	26
$N^{\rm obs}/N^{\rm pred} - 1$	$(-18 \pm 12)\%$	$(-12 \pm 19)\%$	$(-24 \pm 15)\%$

6.4.6 Combinatorial background estimation from fits to $M(B)$ distribution

Figure 6.8 shows fits to $M(B)$ distributions for $B^0 \to J/\psi K^0_S$ candidates in data. The ΔE requirements have been applied to obtain these $M(B)$ distributions. Signal is fit with a Gaussian shape determined from simulation. In Figure 6.8 the background is fit with the ARGUS shape [83] $f(x) \propto x \cdot \sqrt{1-x^2} \cdot e^{\lambda(1-x^2)}$, where $x = M(B)/E_{beam}$; the parameter λ is fixed to the value extracted from a fit to the combinatorial background histograms obtained from a sample of simulated $B\overline{B}$ and continuum events as well as the off-$\Upsilon(4S)$ data.

We also fitted the background using "flat with roll-off" function [4]:

$$f(M(B)) \propto 1, \quad M(B) < M_0 \qquad (6.5)$$
$$f(M(B)) \propto \sqrt{1 - \left(\frac{M(B) - M_0}{E_{beam} - M_0}\right)^2}, \quad M(B) > M_0,$$

where we fix $M_0 = 5.27$ GeV/c^2.

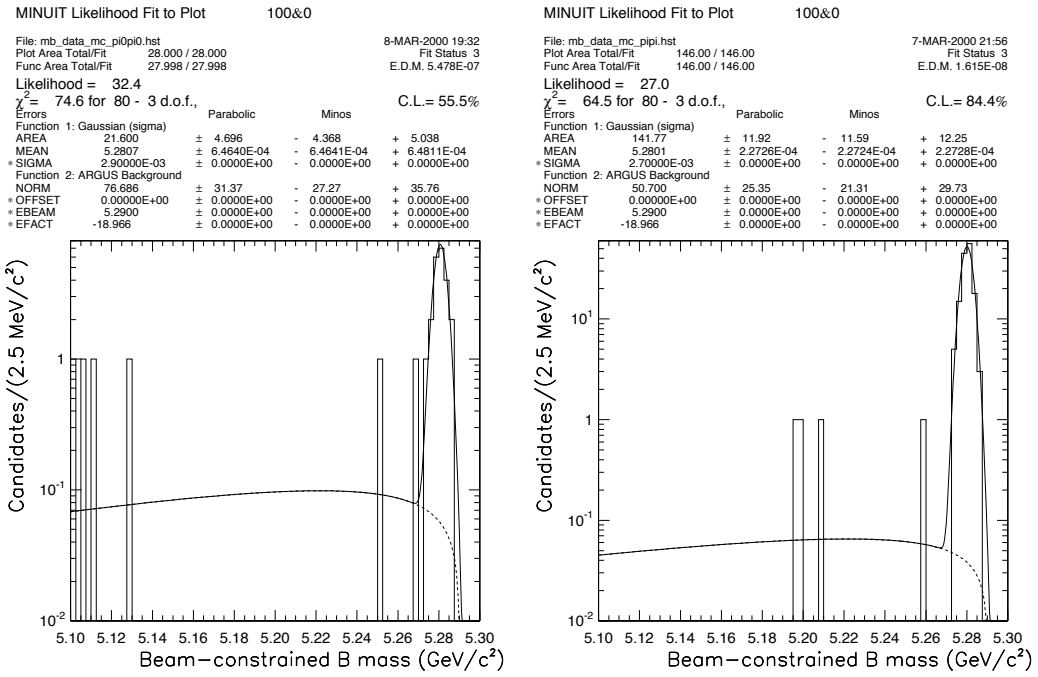

Figure 6.8: Fits to $M(B)$ distribution for $B^0 \to J/\psi K^0_S$ candidates in data. Left (right) plot is for $K^0_S \to \pi^0\pi^0$ ($K^0_S \to \pi^+\pi^-$). We fit the background with the ARGUS function; the background shape is fixed from a fit to a sample of simulated $B\overline{B}$ and continuum events as well as the off-$\Upsilon(4S)$ data.

The background for $B^0 \to J/\psi K^0_S$, $K^0_S \to \pi^0\pi^0$ obtained from the fit to the ARGUS shape is $0.38^{+0.18}_{-0.14}$ events. If we use "flat with roll-off" shape, then the background is $0.49^{+0.23}_{-0.18}$ events. We take 0.5 ± 0.2 events as our estimate of combinatorial background for $B^0 \to J/\psi K^0_S$, $K^0_S \to \pi^0\pi^0$.

The background for $B^0 \to J/\psi K^0_S$, $K^0_S \to \pi^+\pi^-$ obtained from the fit to the ARGUS shape is $0.24^{+0.14}_{-0.10}$ events. If we use a "flat with roll-off" shape, then the background is $0.30^{+0.18}_{-0.13}$ events. We take 0.3 ± 0.2 events as our background estimate for $B^0 \to J/\psi K^0_S$, $K^0_S \to \pi^+\pi^-$.

6.4.7 Background from $B \to J/\psi(K\pi^0)^*$ and $B \to J/\psi(K^0_S\pi)^*$, $K^0_S \to \pi^0\pi^0$

We can consider all the backgrounds for the $B^0 \to J/\psi K^0_S$, $K^0_S \to \pi^+\pi^-$ mode to be combinatorial because the excellent ΔE resolution renders negligible the background from $J/\psi\ K^0_S$ combinations originating from the same B meson, for example, $B \to J/\psi(K^0_S\pi)^*$.

The ΔE resolution for $B^0 \to J/\psi K^0_S$, $K^0_S \to \pi^0\pi^0$ mode is not so good, and according to simulation about half of the $B\overline{B}$ background comes from these two decay chains: $B \to J/\psi(K\pi^0)^*$ and $B \to J/\psi(K^0_S\pi)^*$, $K^0_S \to \pi^0\pi^0$. The events from these decays produce a broad peak in the signal region of the $M(B)$ distribution. We therefore should add these backgrounds to the background value obtained from a fit to $M(B)$ distribution. The contribution from these decays can be reliably estimated from the simulation, as the $\mathcal{B}(B \to J/\psi K^*)$ is measured. The background from these two decay chains is estimated to be 0.57 ± 0.15 events.

6.4.8 Check for background from uncorrelated $J/\psi\ K^0_S$ combinations

If the J/ψ and K^0_S candidates are not correlated (for example, they come from different B mesons), then this background should not care about reversing the J/ψ momentum direction. If we reverse the J/ψ momentum direction, we observe no candidates in the signal boxes for either K^0_S decay mode.

6.5 More details on the first observation of the decay $B^0 \to \chi_{c1}K^0_S$

6.5.1 Rate prediction and previous searches

The first evidence for $B^+ \to \chi_{c1}K^+$ decay came from the ARGUS [85]; later this decay was observed with certainty at CLEO [65]. The latest study of $B \to \chi_{c1}K$ decays is presented in [27]. With 2 fb^{-1} of $\Upsilon(4S)$ data, CLEO observed 13 $B^+ \to \chi_{c1}K^+$ candidates with 0.3 events background and measured $\mathcal{B}(B^+ \to \chi_{c1}K^+) = (8.7 \pm 2.5 \pm 0.9) \times 10^{-4}$ [27]. No $B^0 \to \chi_{c1}K^0_S$ candidates were observed in that search and a 90% C.L. upper limit $\mathcal{B}(B^0 \to \chi_{c1}K^0) < 7 \times 10^{-4}$ was obtained [27].

6.5.2 Selection of signal candidates

We reconstruct χ_{c1} in the $\chi_{c1} \to J/\psi\,\gamma$ decay mode. A photon from $\chi_{c1} \to J/\psi\gamma$ has an energy between 250 and 600 MeV (Figure 6.17). Most of the photons in B meson decays come from π^0's. We therefore do not use a photon if it can be paired with another photon to produce an invariant mass in the π^0 region ($-4 < (M(\gamma\gamma) - M_{\pi^0})/\sigma(M) < 3$). Figure 6.9 shows the π^0 candidates whose photon daughters we veto. The χ_{c1} normalized mass distribution for the simulated signal events is shown in Figure 6.10. The distribution

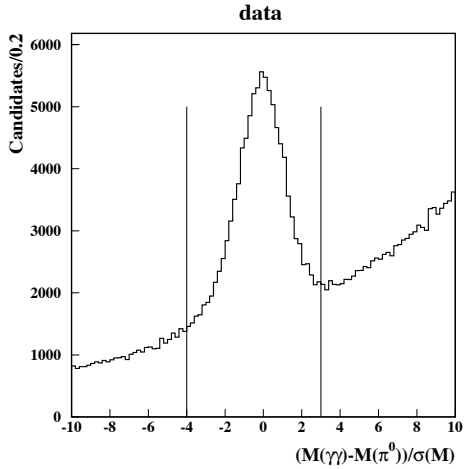

Figure 6.9: Normalized $\pi^0 \to \gamma\gamma$ mass for the π^0 candidates we veto in our photon selection. The energy of one of the daughter photons is required to be between 250 and 600 MeV. Vertical lines show the veto region.

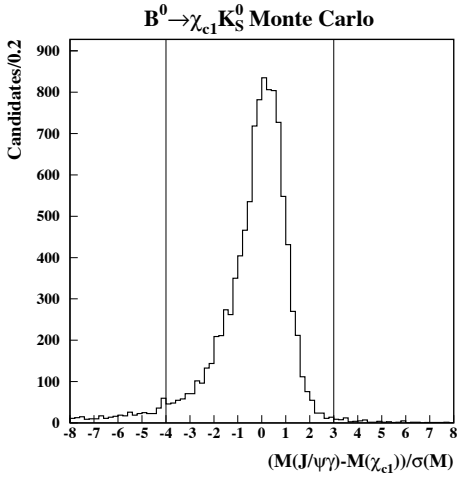

Figure 6.10: Normalized χ_{c1} mass for tagged χ_{c1} candidates in a sample of simulated $B^0 \to \chi_{c1}K^0_S$ events. Vertical lines show the chosen signal region.

of the normalized ΔE vs. normalized $M(B)$ for $B^0 \to \chi_{c1}K^0_S$ candidates is shown in Figure 6.11. We multiplied the reported ΔE uncertainties by a scale factor of 1.2 to make the normalized ΔE distribution look more like a unit Gaussian for the simulated signal events. The signal box is defined as $|M(B) - M_B|/\sigma(M) < 3$ and $|\Delta E|/\sigma(\Delta E) < 3$. There are 9 $B^0 \to \chi_{c1}K^0_S$ candidates in the signal box. All signal candidates come from different events, even though we did not attempt to select a single candidate in a given event.

6.5.3 Summary of background estimation

Backgrounds can be divided into the following categories:

1. *Background from* $B \to J/\psi(K^0_S\pi)^{(*)}$. — We estimated these backgrounds using high-statistics Monte Carlo samples normalized in the fit to $M(K\pi)$ distribution for $B \to J/\psi K\pi$ candidates in data. The total $B \to J/\psi(K^0_S\pi)^{(*)}$ background is estimated to be 0.41 ± 0.07 events.

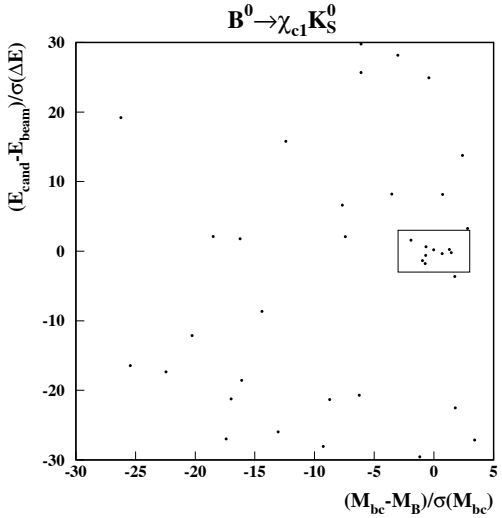

Figure 6.11: The distribution of normalized ΔE vs. normalized $M(B)$ for $B^0 \to \chi_{c1} K^0_S$ candidates in data. There are 9 candidates in the signal box.

2. *Background from $B^0 \to \chi_{c2} K^0_S$.* — We estimated this background using high-statistics Monte Carlo sample normalized in the fit to $M(J/\psi\gamma)$ distribution for $B \to J/\psi\gamma K$ candidates in data. We have not seen any evidence for $B \to \chi_{c2} K$ decays. The background from $B^0 \to \chi_{c2} K^0_S$ is estimated to be 0.01 ± 0.01 events.

3. *Combinatorial background from continuum and $B\overline{B}$ events.* —

   - From a fit to the $M(B)$ distribution, we estimated this background to be 0.5 ± 0.3 events.
   - Using off-$\Upsilon(4S)$ data together with a sample of simulated generic continuum and $B\overline{B}$ events, we estimated this background to be 0.1 ± 0.1 events.

   We estimate the combinatorial background to be 0.5 ± 0.3 events.

The total background is estimated to be (0.5 ± 0.3)[combinatorial] + $(0.41 \pm 0.07)[B \to J/\psi(K^0_S\pi)^{(*)}] + (0.01 \pm 0.01)[B^0 \to \chi_{c2} K^0_S] = 0.9 \pm 0.3$ events.

6.5.4 Background from $B \to J/\psi(K^0_S\pi)^{(*)}$

The most serious background comes from $B \to J/\psi K^*$, $K^* \to K^0_S\pi$ decays because the $J/\psi K^0_S$ combinations with random photons tend to concentrate around the signal region of $M(B)$ distribution (Figure 6.12). We estimated these backgrounds as well as the backgrounds from other $B \to J/\psi K^0_S\pi$ final states, using simulated event samples normalized to data. The branching fraction $\mathcal{B}(B \to J/\psi K^*)$ is well measured; however, there are also other B decays to $J/\psi K^0_S\pi$ final state which must be taken into account in this background study. We therefore studied $B \to J/\psi K\pi$ decays in data. We reconstructed

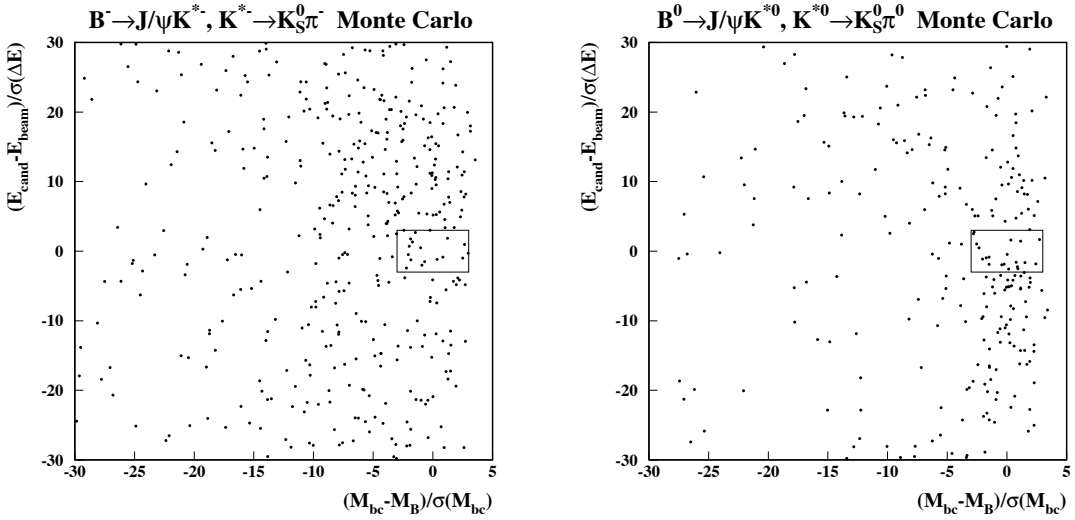

Figure 6.12: The distributions of normalized ΔE vs. normalized $M(B)$ for $B \to J/\psi(K^0_S\pi)^*$ decays reconstructed as $B^0 \to \chi_{c1}K^0_S$. Left plot is for $K^{*-} \to K^0_S\pi^-$, right one is for $K^{*0} \to K^0_S\pi^0$.

$B^0 \to J/\psi K^+\pi^-$ and $B^- \to J/\psi K^0_S\pi^-$ candidates, requiring the normalized $M(B)$ and ΔE to be between -3 and $+3$. We selected a single $B \to J/\psi K\pi$ candidate per event based on the χ^2 composed of $M(B)$ and ΔE variables. Figure 6.13 shows the $M(K\pi)$ distribution for $B^0 \to J/\psi K^+\pi^-$ and $B^- \to J/\psi K^0_S\pi^-$ candidates reconstructed from data. As noted in [30], the $M(K\pi)$ distribution cannot be described just by K^* and phase space contributions. The accumulation of events in the region $1.0 < M(K\pi) < 1.6$ GeV/c^2 most likely comes from several higher K^*_J resonances. The cosine of the $K\pi$ helicity angle distribution for the candidates with $1.05 < M(K\pi) < 1.65$ GeV/c^2 is consistent with being flat.

In this background study we make an approximation that there are two contributions to $B \to J/\psi K\pi$ decays: $B \to J/\psi K^*(892)$ and isotropic $B \to J/\psi K\pi$ phase-space decays with $M(K\pi)$ mass truncated to be between 1.05 and 1.65 GeV/c^2. We fit the $M(K\pi)$ distributions in Figure 6.13 with two histograms: K^* lineshape obtained from a sample of simulated $B \to J/\psi K^*$ events and a truncated $K\pi$ mass distribution ($1.05 < M(K\pi) < 1.65$ GeV/c^2) obtained from a sample of simulated $B \to J/\psi K\pi^-$ events.

We estimated the background from $B \to J/\psi K^0_S\pi$ decays with simulated events, using the normalizations from the fits to data. We checked that the branching fractions $\mathcal{B}(B \to J/\psi K^*)$ we obtain from the fits are consistent with the PDG [47] values. The background from $B \to J/\psi K^*$, $K^* \to K^0_S\pi$ decays is estimated to be 0.32 ± 0.06 events, with almost equal contributions from $K^{*-} \to K^0_S\pi^-$ and $K^{*0} \to K^0_S\pi^0$ modes. The background from other $B \to J/\psi K^0_S\pi$ decays is estimated to be 0.09 ± 0.04 events

The total $B \to J/\psi(K^0_S\pi)^{(*)}$ background is estimated to be 0.41 ± 0.07 events.

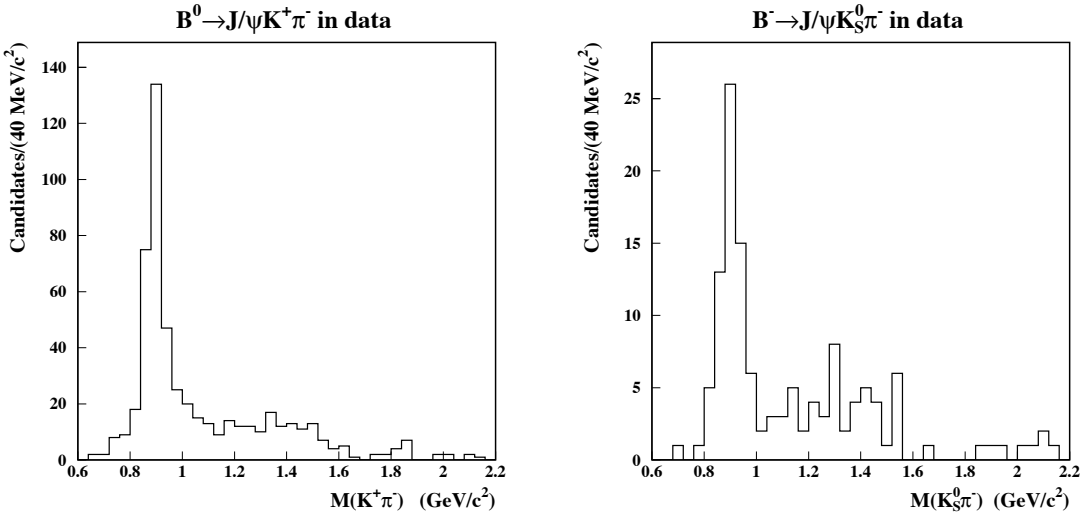

Figure 6.13: Invariant mass of $K\pi^-$ system for $B^0 \to J/\psi K^+\pi^-$ (left) and $B^- \to J/\psi K^0_S\pi^-$ (right) candidates in data. Prominent K^* peaks are seen in both distributions. Backgrounds were not subtracted and no efficiency correction was done.

6.5.5 Background from $B^0 \to \chi_{c2}K^0_S$

The decay $B \to \chi_{c2}K$ has not been observed; in fact, there is still no evidence for χ_{c2} production in B decays (Chapter 3). The final states $\chi_{c1}K^0_S$ and$\chi_{c2}K^0_S$ have opposite signs of CP, therefore it is important to distinguish $B^0 \to \chi_{c1,2}K^0_S$ decays in CP violation measurements.

According to the Monte Carlo simulation, the efficiency of $B^0 \to \chi_{c2}K^0_S$, $\chi_{c2} \to J/\psi\gamma$ to be reconstructed as $B^0 \to \chi_{c1}K^0_S$ is a factor of 63 lower than the efficiency of $B^0 \to \chi_{c1}K^0_S$ reconstruction. We compared the $B \to \chi_{c1,2}K$ yields in data, combining $B^+ \to \chi_c K^+$ and $B^0 \to \chi_c K^0_S$ modes. Figure 6.14 shows $M(J/\psi\gamma)$ distribution $B \to J/\psi\gamma K$ candidates reconstructed from data and from a sample of simulated $B^0 \to \chi_{c1,2}K^0_S$ events. We fit the $M(J/\psi\gamma)$ distribution with the χ_{c1} and χ_{c2} lineshapes obtained from simulation and a straight line to approximate background. From this fit we extracted the ratio of the $B \to \chi_{c2}K$ to $B \to \chi_{c1}K$ yields to be 0.073 ± 0.056. The background from $B^0 \to \chi_{c2}K^0_S$ is therefore estimated to be 0.01 ± 0.01 events.

6.5.6 Combinatorial background estimation from Monte Carlo simulation and off-$\Upsilon(4S)$ data

Background from continuum events

Continuum background was estimated from off-$\Upsilon(4S)$ data and "5 times the on-$\Upsilon(4S)$ data" sample of simulated generic continuum events. To get more statistics for continuum background evaluation, we relaxed the $J/\psi \to \ell^+\ell^-$ mass cut and required the

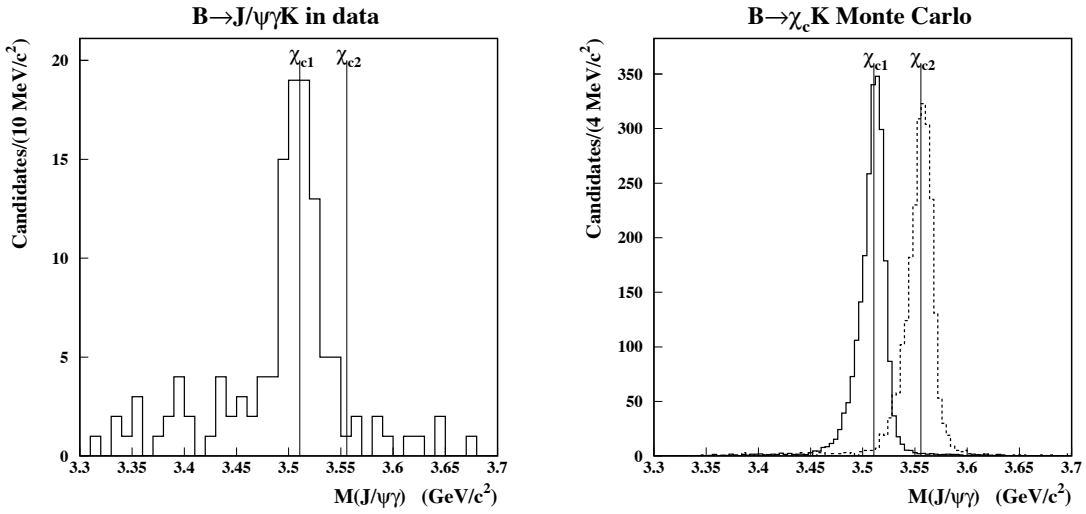

Figure 6.14: Invariant mass of the $J/\psi\gamma$ system for $B \to J/\psi\gamma K$ candidates. We used both K^+ and K^0_S. Left plot is for data, right plot was obtained from a sample of simulated $B^0 \to \chi_{c1,2}K^0_S$ events. The χ_{c1} peak is apparent in data, while no evidence for χ_{c2} is seen.

absolute value of the normalized J/ψ mass to be less than 30 both for $J/\psi \to e^+e^-$ and for $J/\psi \to \mu^+\mu^-$ modes. The continuum background is estimated to be $0.03^{+0.06}_{-0.02}$ events.

Combinatorial background from $B\overline{B}$ events

The backgrounds from $B \to J/\psi(K^0_S\pi)^{(*)}$ and $B^0 \to \chi_{c2}K^0_S$ decays were discussed above; we therefore excluded these decays from our samples of simulated $B\overline{B}$ events. To study the background from generic $B\overline{B}$ decays, we used "35 times the data" sample of simulated generic $B\overline{B}$ events. The distribution of the normalized ΔE vs. normalized $M(B)$ for $B^0 \to \chi_{c1}K^0_S$ candidates reconstructed from a sample of generic $B\overline{B}$ events is shown in Figure 6.15. The $B\overline{B}$ combinatorial background is estimated to be $0.09^{+0.07}_{-0.05}$ events.

6.5.7 Consistency check for background estimation procedure

Combinatorial background estimation from the Monte Carlo simulation depends on QQ physics model. We therefore performed a consistency check by predicting the number of events in 3 control regions of the ΔE vs. $M(B)$ plot shown in Figure 6.11. The 3 control regions are defined in Section 6.4.5. The results are listed in Table 6.3. There is a good agreement between data and our prediction from the Monte Carlo simulation.

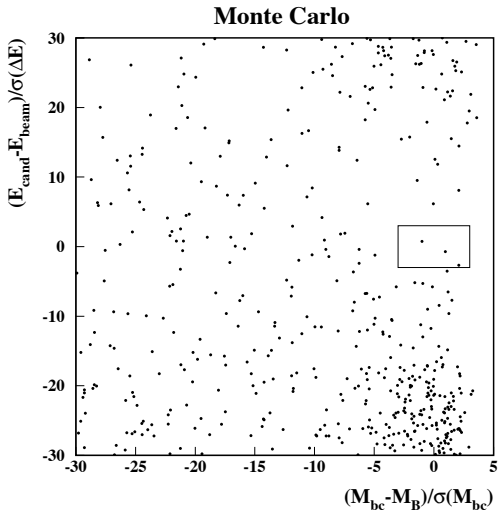

Figure 6.15: Combinatorial background from $B\overline{B}$ decays for $B^0 \to \chi_{c1}K^0_S$. The plot was obtained from a sample of simulated generic $B\overline{B}$ events with "35 times the data" statistics. We excluded the following decay chains: $B^0 \to \chi_{c1}K^0_S$, $B \to \chi_{c2}X$, and $B \to J/\psi(K^0_S\pi)^{(*)}$. There are 3 events in the signal box.

Table 6.3: Quality control of the background estimation procedure. We predict and compare with data the number of events in 3 control regions of the ΔE vs. $M(B)$ plots shown in Figure 6.11.

Source	Region 1	Region 2	Region 3
Continuum	2.5 ± 0.3	2.2 ± 0.3	0.2 ± 0.1
$B \to J/\psi(K^0_S\pi)^{(*)}$	7.1 ± 0.5	4.6 ± 0.4	2.4 ± 0.2
$B^0 \to \chi_{c2}K^0_S$	0.8 ± 0.8	0.2 ± 0.2	0.6 ± 0.6
$B^0 \to \chi_{c1}K^0_S$	1.5 ± 0.5	1.0 ± 0.3	0.5 ± 0.2
the rest of $B\overline{B}$	13.7 ± 0.6	8.4 ± 0.5	5.1 ± 0.4
Total predicted $N^{\rm pred}$	25.6 ± 1.3	16.4 ± 0.8	8.8 ± 0.8
Observed $N^{\rm obs}$	29	21	7

6.5.8 Combinatorial background estimation from fits to $M(B)$ distribution

In this section we fit $M(B)$ distribution to estimate combinatorial background. Figure 6.16 shows fits to $M(B)$ distributions for $B^0 \to \chi_{c1} K^0_S$ candidates in data. The ΔE requirements have been applied to obtain these $M(B)$ distributions. Signal is fit with a

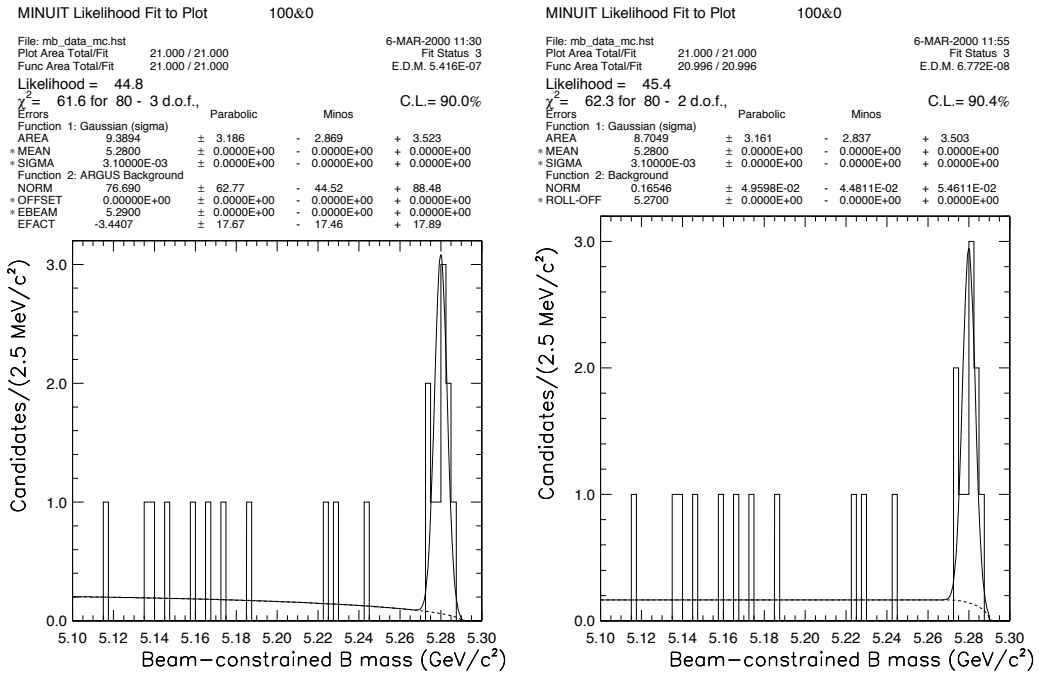

Figure 6.16: Fits to $M(B)$ distribution for $B^0 \to \chi_{c1} K^0_S$ candidates in data. In the left plot we fit the background with the ARGUS function; the background shape is fixed from a fit to simulated $B\overline{B}$ and continuum events as well as off-$\Upsilon(4S)$ data. In the right plot we use "flat with roll-off" shape for background.

Gaussian shape determined from simulation.

In Figure 6.16(left) the background is fit with the ARGUS shape $f(x) \propto x \cdot \sqrt{1-x^2} \cdot e^{\lambda(1-x^2)}$, where $x = M(B)/E_{beam}$; the parameter λ is fixed to the value extracted from a fit to the combinatorial background histograms obtained from samples of simulated $B\overline{B}$ and continuum events and off-$\Upsilon(4S)$ data. The background under the peak is $0.51^{+0.26}_{-0.19}$ events. In Figure 6.16(right) the background is fit using a "flat with roll-off" function described in Section 6.4.6. The background under the peak is $0.40^{+0.20}_{-0.15}$ events. We take 0.5 ± 0.3 events as our estimation of the combinatorial background.

6.5.9 Reconstruction efficiency

In $B^0 \to \chi_{c1} K^0_S$ decay, the χ_{c1} is produced in a helicity-0 state. We calculated the angular distribution for the $\chi_{c1} \to J/\psi\gamma$ decay using the note by Rob Kutschke [86]. We define θ to be the angle between the photon direction in the χ_{c1} frame and the χ_{c1} direction

in the B frame: if $\theta = 0$, then the photon has the maximal possible energy. Because the photon is always transversely polarized, there are 4 allowed helicity amplitudes $\mathcal{A}_{\lambda(\psi)\lambda(\gamma)}$: $\mathcal{A}_{11}$, $\mathcal{A}_{-1-1}$, $\mathcal{A}_{01}$, and $\mathcal{A}_{0-1}$. For example, $\mathcal{A}_{11}$ describes the configuration, in which both J/ψ and γ are transversely polarized, and their spins point in opposite directions. Out of the 4 allowed amplitudes, only 2 are independent because of the parity conservation in the radiative $\chi_{c1} \to J/\psi\gamma$ transition: $\mathcal{A}_{11} = -\mathcal{A}_{-1-1}$ and $\mathcal{A}_{01} = -\mathcal{A}_{0-1}$. The angular distribution is described by $I(\theta) \propto 2\cos^2\theta \cdot |\mathcal{A}_{11}|^2 + \sin^2\theta \cdot |\mathcal{A}_{01}|^2$. The amplitudes $\mathcal{A}_{01}$ and $\mathcal{A}_{11}$ may be expressed as linear combinations of the multipole transition amplitudes a_1 and a_2 which correspond to electric dipole ($E1$) and magnetic quadrupole ($M2$) transitions [87, 88]. Note that the authors of [87, 88] use a different notation for the helicity amplitudes $A_{|\lambda(\psi)\lambda(\gamma)|}$; the correspondence with our notation is $A_0 = \mathcal{A}_{11}$ and $A_1 = \mathcal{A}_{01}$. Theoretically, the $E1$ transition is expected to dominate: $a_1 >> a_2$. Indeed, the decay $\chi_{c1} \to J/\psi\gamma$ has been found to be an essentially pure $E1$ transition. Adopting the conventions $a_1 > 0$ and $|a_1|^2 + |a_2|^2 = 1$, Crystal Ball has measured $a_2 = -(0.002^{+0.020}_{-0.008})$ [89] and the R704 Collaboration has measured $a_2 = -0.13 \pm 0.19$ [90]. In addition, using the relation $a_2(\chi_{c2})/a_2(\chi_{c1}) = 3/\sqrt{5}$ derived in [91], a value of $a_2(\chi_{c1}) = -0.09 \pm 0.04$ can be inferred from the measurement of $a_2(\chi_{c2})$ amplitude performed by E760 Collaboration [92].

For pure $E1$ transition $|\mathcal{A}_{01}| = |\mathcal{A}_{11}|$. Figure 6.17 shows the photon energy distributions for 3 different ratios of the helicity amplitudes. Figure 6.18 shows the distributions of the measured photon energy for the fully reconstructed $B \to \chi_{c1}K$ candidates in data and in a sample of simulated signal events.

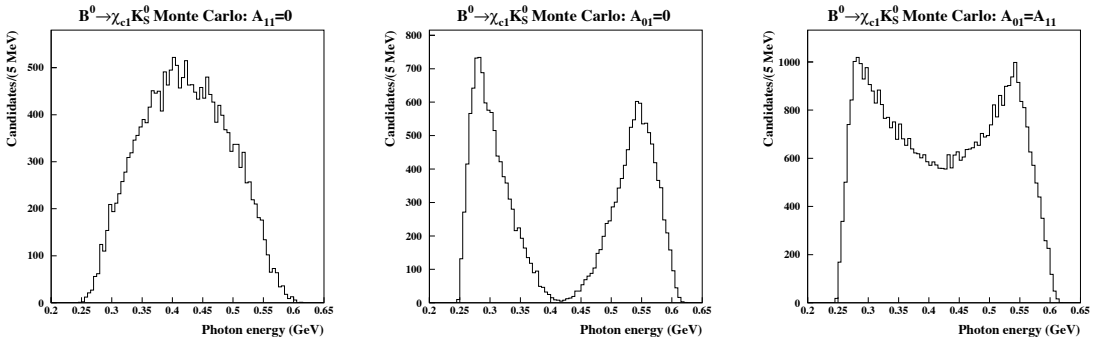

Figure 6.17: Laboratory frame energy of the photon from $B \to \chi_{c1}K$, $\chi_{c1} \to J/\psi\gamma$ decays. Three plots correspond to different values of the 2 independent helicity amplitudes in $\chi_{c1} \to J/\psi\gamma$ decay: $\mathcal{A}_{11} = 0$ (left), $\mathcal{A}_{01} = 0$ (middle), and $|\mathcal{A}_{01}| = |\mathcal{A}_{11}|$ (right). The configuration $|\mathcal{A}_{01}| = |\mathcal{A}_{11}|$ corresponds to pure electric dipole ($E1$) transition. The generator-level information is shown.

The reconstruction efficiencies were determined from the Monte Carlo simulation. Assuming $|\mathcal{A}_{01}| = |\mathcal{A}_{11}|$ (Figure 6.17-right), we obtained the reconstruction efficiency of $(19.16 \pm 0.19)\%$; this value does not include daughter branching fractions. If $|\mathcal{A}_{11}| = 0$ (Figure 6.17-left) is assumed, then the resulting relative change in efficiency is $(-0.9 \pm 2.0)\%$. The corresponding change for $|\mathcal{A}_{01}| = 0$ (Figure 6.17-center) is $(-2.9 \pm 2.0)\%$. We did not assign any systematic uncertainty.

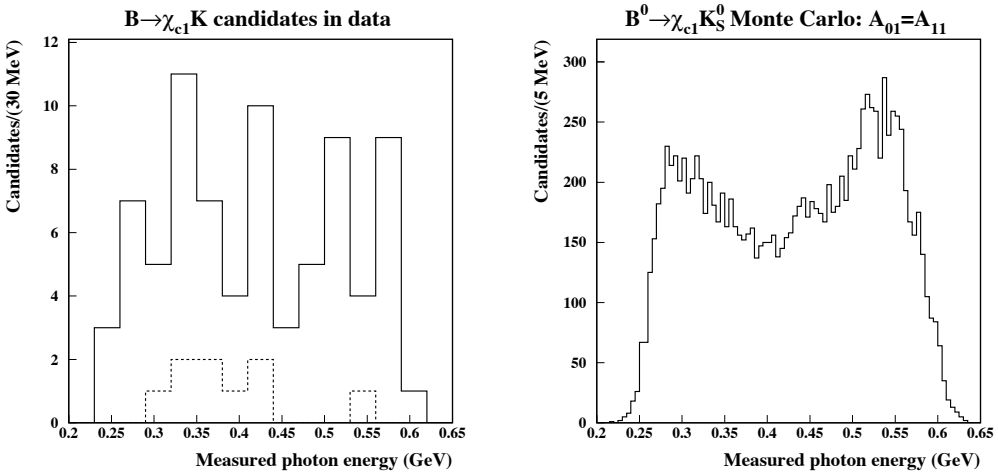

Figure 6.18: Measured energy of the photon for the fully reconstructed $B \to \chi_{c1}K$, $\chi_{c1} \to J/\psi\gamma$ candidates. The π^0 veto has been applied. Left plot is for data; the solid line represents a sum of 69 $B^+ \to \chi_{c1}K^+$ and 9 $B^0 \to \chi_{c1}K^0_S$ candidates, whereas the dashed line shows the contribution from $B^0 \to \chi_{c1}K^0_S$. Right plot was obtained from a sample of $B^0 \to \chi_{c1}K^0_S$ events simulated with $|\mathcal{A}_{01}| = |\mathcal{A}_{11}|$ (see Figure 6.17-right).

6.5.10 Statistical significance of the signal

We observed 9 $B^0 \to \chi_{c1}K^0_S$ candidates with the estimated background of 0.9 ± 0.3 events. The Poisson probability of finding 9 or more events when 0.9 is expected is 5×10^{-7}; the corresponding probability of finding 9 or more events when $0.9 + 0.3 = 1.2$ are expected is 5×10^{-6}. The Poisson probability of the background fluctuation to 9 or more events is smaller than 0.27% when the expected background mean is less than 2.9 events. The 68% C.L. interval for the signal mean [49] is $8.1^{+3.8}_{-2.7}$ events.

6.5.11 Consistency checks for $\mathcal{B}(B^0 \to \chi_{c1}K^0)$ measurement

The central value of the measured branching fraction $\mathcal{B}(B^0 \to \chi_{c1}K^0) = (3.9^{+1.9}_{-1.3} \pm 0.4) \times 10^{-4}$ looks a little low compared to $\mathcal{B}(B^+ \to \chi_{c1}K^+) = (8.7 \pm 2.5 \pm 0.9) \times 10^{-4}$ [27]. We performed several consistency checks to make sure that we did not make a mistake.

- *Reconstruction of* $B^0 \to J/\psi K^0_S$. — The J/ψ and K^0_S selection criteria in this analysis are the same as in $B^0 \to J/\psi K^0_S$ analysis. We once again verified it by reconstructing $B^0 \to J/\psi K^0_S$ candidates in data. We observed 142 $B^0 \to J/\psi K^0_S$ candidates — exactly the number expected.

- *Reconstruction of* $B^+ \to \chi_{c1}K^+$. — Using the same χ_{c1} cuts as in $B^0 \to \chi_{c1}K^0_S$ analysis, we reconstructed $B^+ \to \chi_{c1}K^+$ decay mode. Figure 6.19 shows $B^+ \to \chi_{c1}K^+$ signal in data. We observed 69 $B^+ \to \chi_{c1}K^+$ signal candidates. The reconstruction efficiency, determined from the Monte Carlo simulation, is (24.1±0.3)%. Neglecting backgrounds, we obtained a branching fraction $\mathcal{B}(B^+ \to \chi_{c1}K^+) = (9.1 \pm 1.1[\text{stat}]) \times 10^{-4}$,

which is in good agreement with the value $\mathcal{B}(B^+ \to \chi_{c1}K^+) = (8.7 \pm 2.5 \pm 0.9) \times 10^{-4}$ from [27].

We conclude that fluctuations happen.

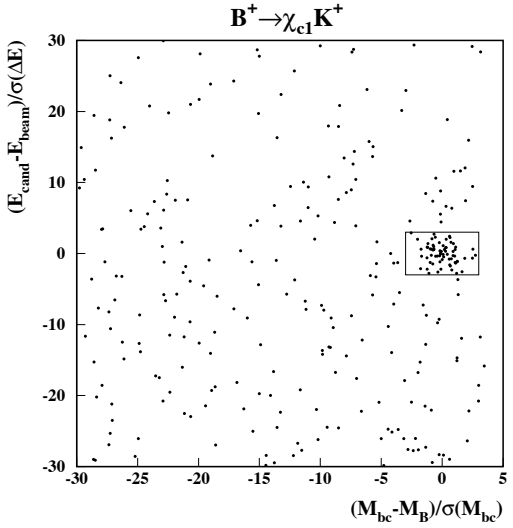

Figure 6.19: The distribution of normalized ΔE vs. normalized $M(B)$ for $B^+ \to \chi_{c1}K^+$ candidates in data; there are 69 candidates in the signal box.

6.6 More details on the first observation of the decay $B^0 \to J/\psi\pi^0$

6.6.1 Rate prediction and previous searches

The isospin counterpart $B^+ \to J/\psi\pi^+$ decay was observed by CLEO [94, 84] and later confirmed by CDF [95]. The branching fraction is $\mathcal{B}(B^+ \to J/\psi\pi^+) = (5.0 \pm 1.5) \times 10^{-5}$ [47]. We expect $\Gamma(B^0 \to J/\psi\pi^0) = 1/2 \cdot \Gamma(B^+ \to J/\psi\pi^+)$ because $\pi^0 = (u\overline{u} - d\overline{d})/\sqrt{2}$, whereas only $d\overline{d}$ pairs are produced in the decay $b\overline{d} \to c\overline{c}d\overline{d}$. A single $B^0 \to J/\psi\pi^0$ candidate was observed in the previous CLEO search [84] and a 90% C.L. upper limit of 5.8×10^{-5} was obtained for $\mathcal{B}(B^0 \to J/\psi\pi^0)$.

6.6.2 Selection of signal candidates

A study of high-momentum π^0's used for $B^0 \to J/\psi\pi^0$ reconstruction is presented in Appendix D. Figure 6.20 shows normalized $M(B)$ and ΔE distributions for $B^0 \to J/\psi\pi^0$ candidates reconstructed from a sample of simulated signal events. To select $B^0 \to J/\psi\pi^0$ candidates we required the normalized $M(B)$ to be between -3 and $+3$ and normalized ΔE to be between -4 and $+3$. The asymmetric cut on ΔE was motivated by the desire to include

some of the low-side tail (Figure 6.20-right), while still not letting in too much background from $B^0 \to J/\psi K^0_S$, $K^0_S \to \pi^0\pi^0$ and $B^+ \to J/\psi\rho^+$ decays (see Figures 6.22 and 6.24). Figure 6.21 shows $B^0 \to J/\psi\pi^0$ signal in data. We observe 10 $B^0 \to J/\psi\pi^0$ signal candi-

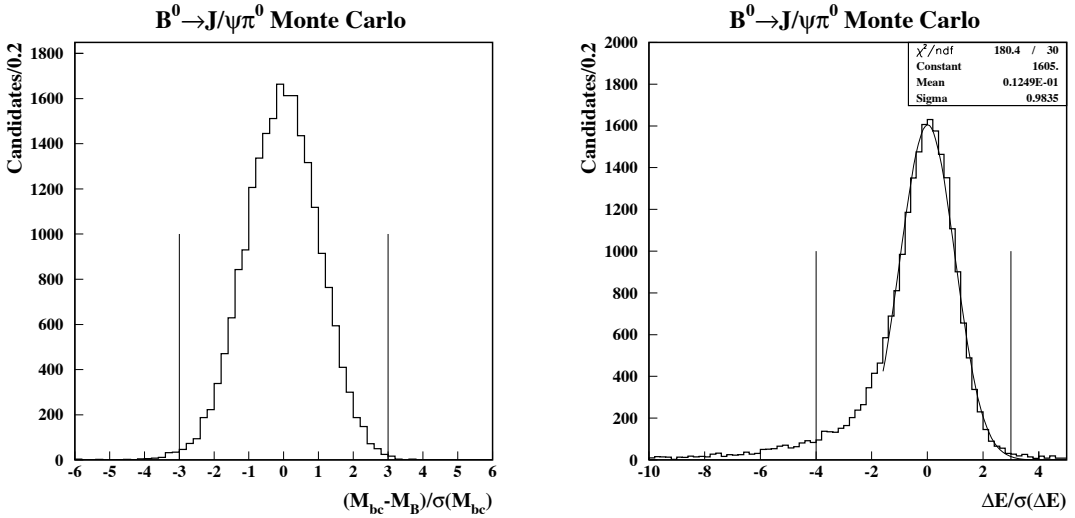

Figure 6.20: Normalized $M(B)$ (left) and normalized ΔE (right) distributions for $B^0 \to J/\psi\pi^0$ candidates in a sample of simulated signal events. Vertical lines depict the chosen signal regions.

dates. All the $B^0 \to J/\psi\pi^0$ signal candidates come from different events, even though we did not attempt to select a single candidate in a given event.

6.6.3 Summary of background estimation

Let us first consider which $B \to J/\psi X$ decays are most likely to fake $B^0 \to J/\psi\pi^0$. The ΔE resolution is good enough to render negligible the background from any of the Cabibbo-allowed $B \to J/\psi K\pi^0 X$ decays, where at least a kaon mass is missing from the energy sum. Not a single signal candidate was observed in a "70 times the data" sample of simulated $B \to J/\psi K^*$, $K^* \to K\pi^0$ events. Of all the Cabibbo-allowed decays, the most serious background process is $B^0 \to J/\psi K^0_S$, $K^0_S \to \pi^0\pi^0$, for which the ΔE peak is shifted by at least a π^0 mass (Figure 6.22). Of the Cabibbo-suppressed decays, the most serious background process is $B^+ \to J/\psi\rho^+$; again, however, the ΔE peak is shifted by at least a π^0 mass (Figure 6.24).

Backgrounds can be divided into the following categories:

1. *Background from* $B^0 \to J/\psi K^0_S$, $K^0_S \to \pi^0\pi^0$. — The $B^0 \to J/\psi K^0_S$ branching fraction is well measured. Using a high-statistics sample of simulated $B^0 \to J/\psi K^0_S$, $K^0_S \to \pi^0\pi^0$ events, we estimated this background to be 0.38 ± 0.05 events.

2. *Background from* $B^+ \to J/\psi\rho^+$. — This decay has yet to be observed, therefore we rely on our own data to estimate the rate for this decay. We estimate the background

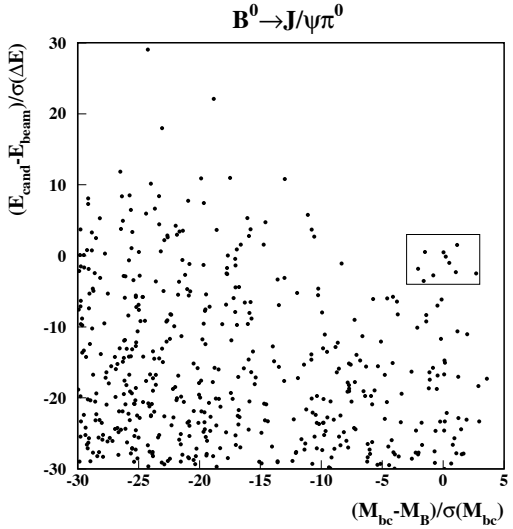

Figure 6.21: The distribution of normalized ΔE vs. normalized $M(B)$ for $B^0 \to J/\psi\pi^0$ candidates in data; there are 10 candidates in the signal box.

from $B^+ \to J/\psi\rho^+$ to be $0.15 \pm 0.06 \pm 0.13$ events, where first quoted error comes from the uncertainty in $\mathcal{B}(B^+ \to J/\psi\rho^+)$ and the second one is from the uncertainty in ρ^+ polarization.

3. *Background from non-resonant $B \to J/\psi\pi\pi^0$ decays.* — In addition to the background from $B^+ \to J/\psi\rho^+$, we estimated background from non-resonant $B^+ \to J/\psi\pi^+\pi^0$ and $B^0 \to J/\psi\pi^0\pi^0$ decays. We assumed that the decays $B \to J/\psi\pi\pi$ are isotropic and uniformly distributed across Dalitz plot. We used data to estimate the decay rates. We estimate the background from $B^+ \to J/\psi\pi^+\pi^0$ ($B^0 \to J/\psi\pi^0\pi^0$) decays to be 0.03 ± 0.03 (0.03 ± 0.02) events.

4. *Combinatorial background from continuum and $B\overline{B}$ events.* —

   - From a fit to $M(B)$ distribution, we estimated this background to be $0.4^{+0.5}_{-0.3}$ events.
   - Using off-$\Upsilon(4S)$ data together with samples of simulated generic continuum and $B\overline{B}$ events, we estimated this background to be 1.0 ± 0.2 events.
   - As a check for combinatorial background, we tried to reconstruct $B^0 \to J/\psi\pi^0$ candidates in data with the reversed J/ψ momentum direction. No candidates were observed in the signal box.

   We estimate the combinatorial background to be $0.4^{+0.5}_{-0.3}$ events.

The total background is estimated to be $(0.4^{+0.5}_{-0.3})$[combinatorial]$+(0.38\pm0.04)[B^0 \to J/\psi K^0_S] + (0.15 \pm 0.14)[B^+ \to J/\psi\rho^+] + (0.06 \pm 0.04)[B \to J/\psi(\pi\pi^0)_{\rm non-res.}] = 1.0 \pm 0.5$ events.

6.6.4 Background from $B^0 \to J/\psi K^0_S$, $K^0_S \to \pi^0\pi^0$

This is the only Cabibbo-allowed decay, for which $E(J/\psi) + E(\pi^0)$ can be a pion mass short of the beam energy. We used our own measured value of the branching fraction $\mathcal{B}(B^0 \to J/\psi K^0) = (9.5 \pm 1.0) \times 10^{-4}$, which is in good agreement with the PDG world average value $\mathcal{B}(B^0 \to J/\psi K^0) = (8.9 \pm 1.2) \times 10^{-4}$ [47]. We used a sample of simulated $B^0 \to J/\psi K^0_S$, $K^0_S \to \pi^0\pi^0$ events with "586 ± 62 times the data" statistics. Figure 6.22 shows the distribution of normalized ΔE vs. normalized $M(B)$ and normalized ΔE projection for $B^0 \to J/\psi K^0_S$, $K^0_S \to \pi^0\pi^0$ events reconstructed as $B^0 \to J/\psi\pi^0$. We estimate the background from this decay chain to be 0.38 ± 0.05 events.

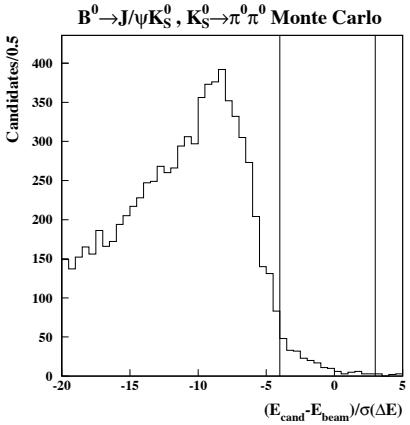

Figure 6.22: $B^0 \to J/\psi K^0_S$, $K^0_S \to \pi^0\pi^0$ reconstructed as $B^0 \to J/\psi\pi^0$. The plot shows the normalized ΔE projection for the candidates with normalized $M(B)$ between -3 and $+3$. The plot was obtained from a sample of $B^0 \to J/\psi K^0_S$, $K^0_S \to \pi^0\pi^0$ simulated events with "586 ± 62 times the data" statistics.

6.6.5 Background from $B^+ \to J/\psi\pi^+\pi^0$

$E(J/\psi) + E(\pi^0)$ can be only a pion mass short of the beam energy for this decay. We assumed that only $B^+ \to J/\psi\rho^+$ and non-resonant $B^+ \to J/\psi\pi^+\pi^0$ decays produce $B^+ \to J/\psi\pi^+\pi^0$ final state. These decays have not yet been observed, therefore we rely on our own data to estimate the decay rates.

In $B^+ \to J/\psi\pi^+\pi^0$ reconstruction, we applied a decay angle cut $\cos\theta_d > 0$, where θ_d is the angle between π^0 momentum in the $\pi^+\pi^0$ rest frame and the $\pi^+\pi^0$ system momentum in the laboratory frame. This cut selects hard π^0's and soft π^+'s, thus reducing background from random photon combinations and from misidentified charged kaons. Figure 6.23 shows the $M(\pi^+\pi^0)$ distribution for $B^+ \to J/\psi\pi^+\pi^0$ candidates reconstructed from data as well as from samples of $B^+ \to J/\psi\rho^+$ and $B^+ \to J/\psi\pi^+\pi^0$ simulated events. We conservatively assumed that there is no background. We fitted the data distribution in Figure 6.23(left) with the histograms obtained from the simulation, which are shown in Figure 6.23(middle, right), and determined the decay rates for $B^+ \to J/\psi\rho^+$ and

$B^+ \to J/\psi(\pi^+\pi^0)_{\rm non-res}$. Figure 6.24 shows the projections on the normalized ΔE for

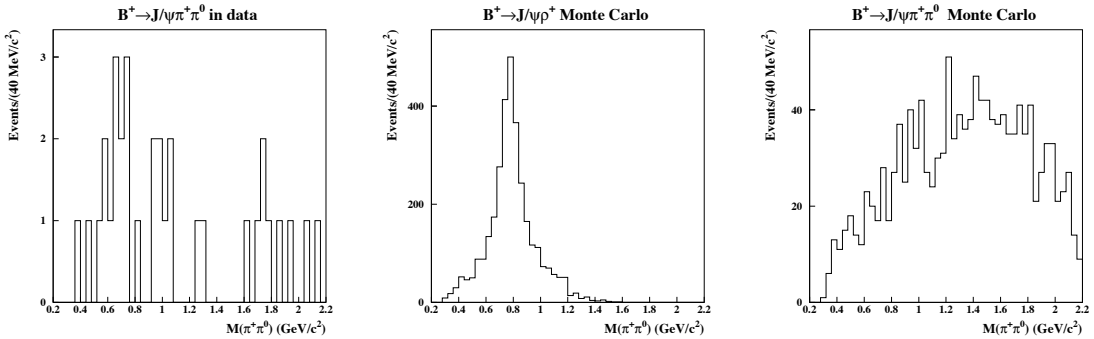

Figure 6.23: Invariant mass of $\pi^+\pi^0$ system for $B^+ \to J/\psi\pi^+\pi^0$ candidates reconstructed from data (left), a sample of simulated $B^+ \to J/\psi\rho^+$ events (middle), and a sample of simulated $B^+ \to J/\psi\pi^+\pi^0$ events (right).

simulated $B^+ \to J/\psi\rho^+$ and $B^+ \to J/\psi\pi^+\pi^0$ decays reconstructed as $B^0 \to J/\psi\pi^0$. With

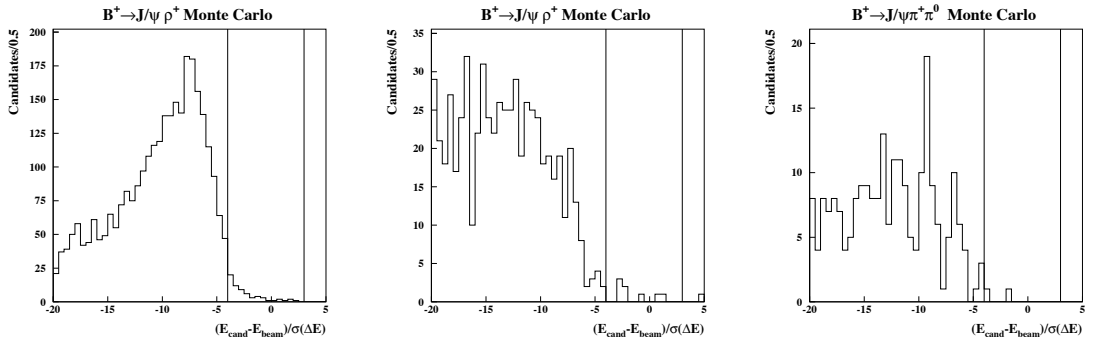

Figure 6.24: $B^+ \to J/\psi\pi^+\pi^0$ reconstructed as $B^0 \to J/\psi\pi^0$. The plots show the normalized ΔE projections for the candidates with normalized $M(B)$ between -3 and $+3$. Left (middle) plot is for a sample of $B^+ \to J/\psi\rho^+$ simulated events with longitudinally (transversely) polarized ρ^+. Right plot was obtained from a sample of $B^+ \to J/\psi\pi^+\pi^0$ simulated events.

high-statistics samples of simulated $B^+ \to J/\psi\rho^+$ events, we estimated the background from these decays to be 0.15 ± 0.06 events. In this calculation we assumed non-polarized ρ^+ ($\Gamma_L/\Gamma = 0.5$). This assumption is consistent with the measurements of K^* polarization in $B \to J/\psi K^*$ decays. CLEO has measured $\Gamma_L/\Gamma = 0.52 \pm 0.07 \pm 0.04$ [30]; the latest result from CDF is $\Gamma_L/\Gamma = 0.59 \pm 0.06 \pm 0.01$ [93]. If 100% longitudinal (transverse) polarization for ρ^+ is assumed, then the background mean is estimated to be 0.28 (0.03) events. We therefore assigned a systematic error of 0.13 events on the background mean due to uncertainty in ρ polarization. We estimate the background to be $0.15 \pm 0.06 \pm 0.13$ events from $B^+ \to J/\psi\rho^+$, and 0.03 ± 0.03 events from non-resonant $B^+ \to J/\psi\pi^+\pi^0$.

6.6.6 Background from $B^0 \to J/\psi\pi^0\pi^0$

The $B^0 \to J/\psi\pi^0\pi^0$ decay rate has to be estimated from data. We followed the same procedure as for $B^+ \to J/\psi\pi^+\pi^0$ reconstruction. We did not, however, impose any decay angle requirement on $\pi^0\pi^0$ pairs. The resulting $M(\pi^0\pi^0)$ distributions for $B^0 \to J/\psi\pi^0\pi^0$ candidates in data and in a sample of simulated $B^0 \to J/\psi\pi^0\pi^0$ events are shown in Figure 6.25. The prominent peak at $M(\pi^0\pi^0) \approx 0.5$ GeV/c^2 in data is produced by $B^0 \to J/\psi K^0_S$, $K^0_S \to \pi^0\pi^0$ decays. We assumed that $B^0 \to J/\psi\pi^0\pi^0$ decays are isotropic and uniformly distributed across Dalitz plot. Figure 6.26 shows the normalized ΔE projections plots for simulated $B^0 \to J/\psi\pi^0\pi^0$ decays reconstructed as $B^0 \to J/\psi\pi^0$. We estimate the background from non-resonant $B^0 \to J/\psi\pi^0\pi^0$ decays to be 0.03 ± 0.02 events.

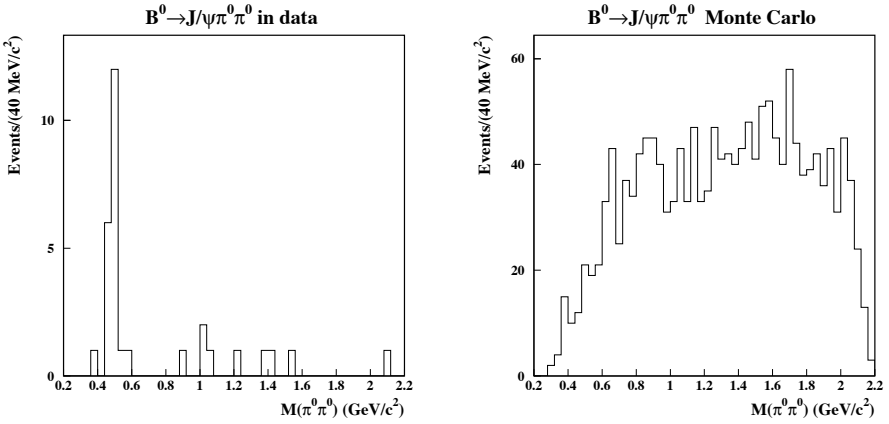

Figure 6.25: Invariant mass of $\pi^0\pi^0$ system for $B^0 \to J/\psi\pi^0\pi^0$ candidates reconstructed from data (left) and a sample of $B^0 \to J/\psi\pi^0\pi^0$ simulated events (right). The peak at $M(\pi^0\pi^0) \approx 0.5$ GeV/c^2 in data is from $B^0 \to J/\psi K^0_S$, $K^0_S \to \pi^0\pi^0$ decays.

6.6.7 Combinatorial background estimation from Monte Carlo simulation and off-$\Upsilon(4S)$ data

Background from continuum events

Continuum background was estimated from off-$\Upsilon(4S)$ data and "5 times the on-$\Upsilon(4S)$ data" sample of simulated generic continuum events. To get more statistics for continuum background evaluation, we relaxed the $J/\psi \to \ell^+\ell^-$ mass cut and required the absolute value of the normalized J/ψ mass to be less than 30 both for $J/\psi \to e^+e^-$ and for $J/\psi \to \mu^+\mu^-$ modes. The continuum background is estimated to be 0.51 ± 0.12 events.

Combinatorial background from $B\overline{B}$ events

The backgrounds from $B^0 \to J/\psi K^0_S$, $K^0_S \to \pi^0\pi^0$ and $B^+ \to J/\psi\rho^+$ decays were discussed above; we therefore excluded these decays from our samples of simulated $B\overline{B}$ events. To study the background from generic $B\overline{B}$ decays, we used "35 times the

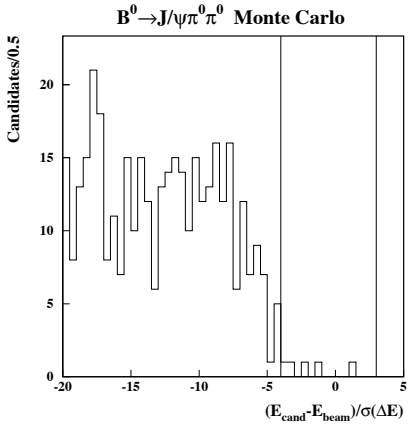

Figure 6.26: Non-resonant $B^0 \to J/\psi\pi^0\pi^0$ reconstructed as $B^0 \to J/\psi\pi^0$. The plot shows the normalized ΔE projections for the candidates with normalized $M(B)$ between -3 and $+3$. The distribution was obtained from a sample of simulated $B^0 \to J/\psi\pi^0\pi^0$ events.

data" sample of simulated generic $B\overline{B}$ events. The distribution of the normalized ΔE vs. normalized $M(B)$ for the sample of $B\overline{B}$ simulated events is shown in Figure 6.27. The $B\overline{B}$ combinatorial background is estimated to be 0.46 ± 0.11 events.

6.6.8 Consistency check for background estimation procedure

The background from $B^+ \to J/\psi\rho^+$ and $B^0 \to J/\psi K^0_S$, $K^0_S \to \pi^0\pi^0$ decays are credibly estimated because we used measured branching fractions. The estimation of combinatorial background from the Monte Carlo simulation, however, requires additional cross-checks, as this estimation depends on QQ physics model. We verified the quality of our background estimation procedure by predicting the number of events in 3 control regions of the ΔE vs. $M(B)$ plot shown in Figure 6.21. The 3 control regions are defined in Section 6.4.5. The results are listed in Table 6.4. We seem to overestimate the number of events below the signal box (Region 3). We can think of 2 possible factors contributing to the discrepancy:

1. $B \to J/\psi\rho$ and $B \to J/\psi\pi\pi$ decays are not in QQ, whereas the measured $B \to J/\psi X$ rate is saturated in QQ with $B \to J/\psi X_s$ decays. We added the contribution from $B \to J/\psi\rho$ and $B \to J/\psi\pi\pi$ without decreasing the total $B \to J/\psi X_s$ rate.

2. As discussed in Section 6.4.5, multi-body $B \to J/\psi K n\pi$ decays in QQ do not respect isospin symmetry, with the bias towards producing more neutral pions than is justified by isospin.

These shortcomings of the simulation do not pose a problem for our analysis because ΔE resolution is good enough to eliminate the background from $B \to J/\psi K\pi^0 X$ decays. The backgrounds from all the decays to $J/\psi\pi^0\pi$ final states have been carefully estimated.

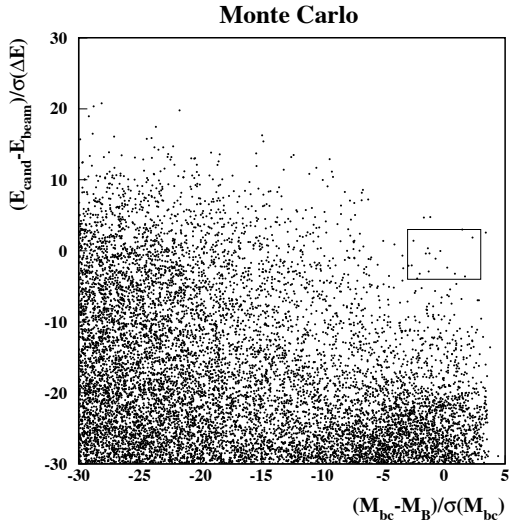

Figure 6.27: Combinatorial background from $B\overline{B}$ decays. The plot was obtained from a sample of simulated $B\overline{B}$ events with "35 times the data" statistics. Events containing $B^0 \to J/\psi\pi^0$ and $B^0 \to J/\psi K^0_S$, $K^0_S \to \pi^0\pi^0$ decays were removed from these samples. There are 16 events entering the signal box.

6.6.9 Combinatorial background estimation from fits to $M(B)$ distribution

Figure 6.28 shows the ARGUS function fit to the combinatorial background histograms obtained from the Monte Carlo simulation of $B\overline{B}$ and continuum events as well as off-$\Upsilon(4S)$ data. Figures 6.29 and 6.30 shows fits to $M(B)$ distribution in data. Signal is fit with a Gaussian shape determined from the Monte Carlo simulation. In Figure 6.29 the background is fit with the ARGUS shape $f(x) \propto x \cdot \sqrt{1-x^2} \cdot e^{\lambda(1-x^2)}$, where $x = M(B)/E_{beam}$; the parameter λ is fixed to the value obtained from the fit to simulated events and off-$\Upsilon(4S)$ data (Figure 6.28). In the left plot of Figure 6.30 the background is fit to the ARGUS shape with the parameter λ allowed to float. The background under the peak is $0.4^{+0.5}_{-0.3}$ ($0.5^{+0.2}_{-0.1}$) events for the fit with floating (fixed) λ. In Figure 6.30(right) the background is fit using a "flat with roll-off" function described in Section 6.4.6. In this case the background under the peak is 1.0 ± 0.3 events.

We take $0.4^{+0.5}_{-0.3}$ events as our estimation of the combinatorial background. This value was obtained in the fit to the ARGUS function with floating λ (Figure 6.30-left).

6.6.10 Statistical significance of the signal

We observed 10 $B^0 \to J/\psi\pi^0$ candidates with the estimated background of 1.0 ± 0.5 events. The Poisson probability of finding 10 or more events when 1.0 is expected is 1×10^{-7}; the corresponding probability of finding 10 or more events when $1.0 + 0.5 = 1.5$ are expected

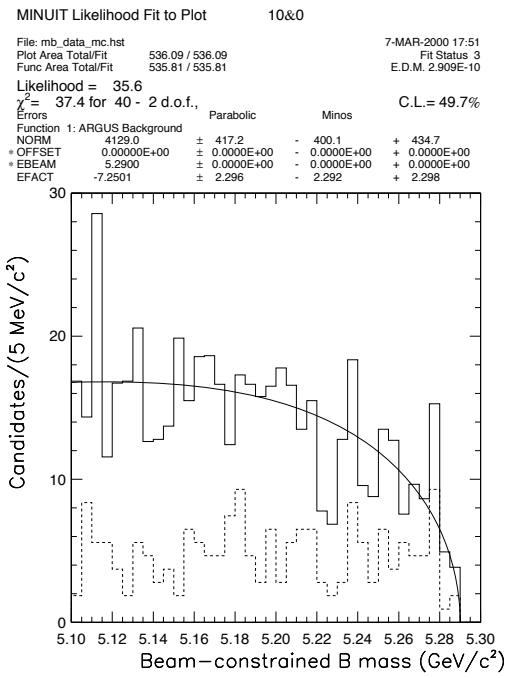

Figure 6.28: Fit of $M(B)$ distribution for continuum and combinatorial $B\overline{B}$ background to the ARGUS function. The histogram was obtained from the Monte Carlo simulation and off-$\Upsilon(4S)$ data. Continuum contribution is represented by the dashed line. Events containing $B^0 \to J/\psi\pi^0$, $B^+ \to J/\psi\rho^+$ and $B^0 \to J/\psi K^0_S$, $K^0_S \to \pi^0\pi^0$ decays were removed.

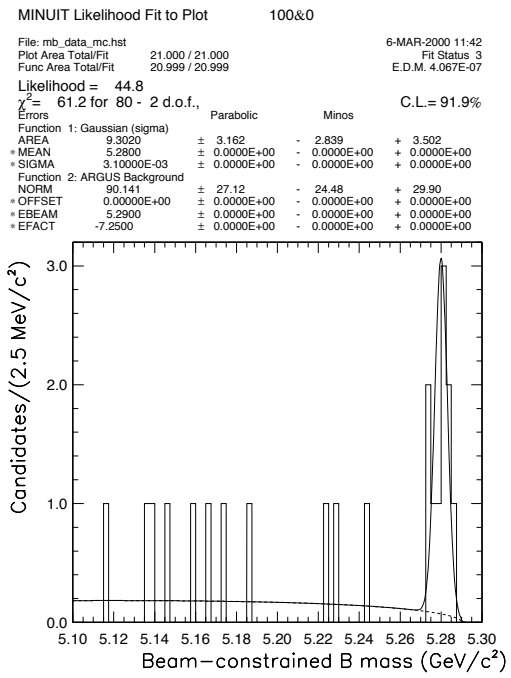

Figure 6.29: Fit to $M(B)$ distribution for $B^0 \to J/\psi\pi^0$ candidates in data. We use the ARGUS function to fit background; the background shape is fixed from a fit to the Monte Carlo event samples and off-$\Upsilon(4S)$ data (Figure 6.28).

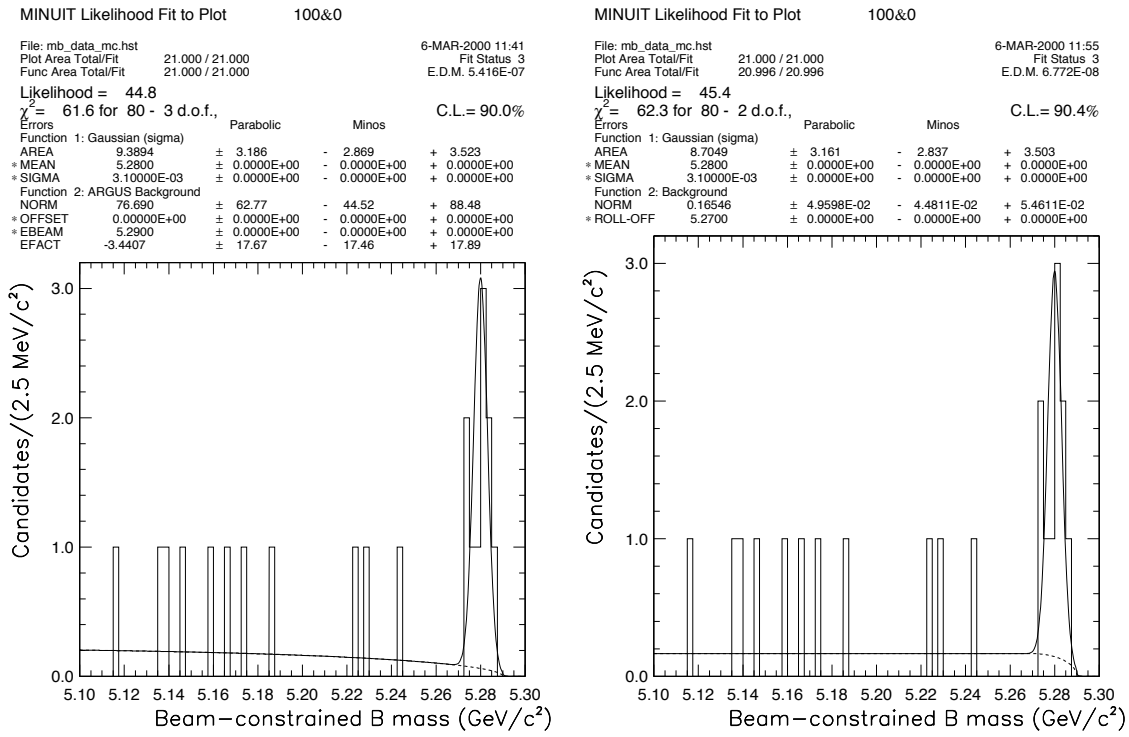

Figure 6.30: Fits to $M(B)$ distribution for $B^0 \to J/\psi\pi^0$ candidates in data. In the left plot we use the ARGUS function to fit background; the parameter λ is allowed to float. In the right plot we use "flat with roll-off" shape for background.

Table 6.4: Quality control of the background estimation procedure. We predict and compare with data the number of events in 3 control regions of the ΔE vs. $M(B)$ plots shown in Figure 6.21.

Source	Region 1	Region 2	Region 3
Continuum	97.9 ± 1.6	93.7 ± 1.6	4.0 ± 0.3
$B^0 \to J/\psi K^0_S,\ K^0_S \to \pi^0\pi^0$	35.3 ± 4.6	17.9 ± 2.4	15.4 ± 2.1
$B^+ \to J/\psi\rho^+$	16.4 ± 9.9	8.1 ± 3.7	8.1 ± 6.5
$B^+ \to J/\psi(\pi^+\pi^0)_{\rm non-res}$	15.1 ± 4.3	10.6 ± 3.0	4.5 ± 1.3
$B^0 \to J/\psi(\pi^0\pi^0)_{\rm non-res}$	9.8 ± 3.7	6.6 ± 2.5	3.2 ± 1.2
$B^0 \to J/\psi\pi^0$	1.3 ± 0.4	0.6 ± 0.2	0.7 ± 0.2
the rest of $B\overline{B}$	311.3 ± 3.0	274.7 ± 2.8	35.1 ± 1.0
Total predicted $N^{\rm pred}$	487 ± 13	413 ± 7	72 ± 7
Observed $N^{\rm obs}$	493	447	45
$N^{\rm obs}/N^{\rm pred} - 1$	$(+1 \pm 5)\%$	$(+8 \pm 5)\%$	$(-38 \pm 11)\%$

is 4×10^{-6}. The Poisson probability of the background fluctuation to 10 or more events is smaller than 0.27% when the expected background mean is less than 3.4 events. The 68% C.L. interval for the signal mean [49] is $9.0^{+3.8}_{-3.2}$ events.

6.7 Systematic uncertainties

- The number of produced $B\overline{B}$ pairs is known with a relative uncertainty of **2%** [96]. We assumed equal production of B^+B^- and $B^0\overline{B}^0$ pairs at the $\Upsilon(4S)$ resonance [4] and did not assign a systematic error for this assumption. The measured branching fractions may be corrected if the ratio is found to be different.

- $\mathcal{B}(J/\psi \to \ell^+\ell^-)$: **1.5%**. We used $\mathcal{B}(J/\psi \to \ell^+\ell^-) = (5.894 \pm 0.086)\%$ [50]. Lepton universality, $\mathcal{B}(J/\psi \to e^+e^-) = \mathcal{B}(J/\psi \to \mu^+\mu^-)$, is assumed in the calculation of this world average value.

- $\mathcal{B}(\chi_{c1} \to J/\psi\gamma)$: **5.9%** [47].

- $\mathcal{B}(K^0 \to K^0_S \to \pi^+\pi^-)$: **0.4%** [47].

- $\mathcal{B}(K^0 \to K^0_S \to \pi^0\pi^0)$: **0.9%** [47].

- Tracking efficiency: **1%** per track [97].

- $K^0_S \to \pi^+\pi^-$ finding: **2%** in addition to tracking efficiency systematics [98].

- $K^0_S \to \pi^0\pi^0$ finding: **5%** in addition to uncertainty on $K^0_S \to \pi^+\pi^-$ finding efficiency (Appendix E).

- Lepton identification efficiency: **3%** per lepton [99, 27]. Cross-checks for the J/ψ yields are described in Appendix F.

- Statistics of the simulated signal event samples: **0.6–1.0%** depending on the mode.

- Background subtraction: **0.01–5.0%** depending on the mode.
- π^0 finding efficiency in $B^0 \to J/\psi\pi^0$ analysis: **5%**. From recent π^0 efficiency studies [100] a 2% systematic uncertainty is justifiable if we select photons in good barrel region of the calorimeter. According to the Monte Carlo simulation, both daughter photons are detected in good barrel for 84% of π^0's from $B^0 \to J/\psi\pi^0$ decay. Taking systematic uncertainty to be 2% for good barrel π^0's and 10% for the π^0's detected in other regions of calorimeter, we obtain $2\%\cdot 0.84 + 10\%\cdot 0.16 = 3.3\%$. We conservatively assigned traditional 5% uncertainty on the π^0 reconstruction efficiency.
- γ efficiency in $\chi_{c1} \to J/\psi\gamma$ reconstruction: **2.5%** [100, 27].

The relative systematic uncertainty on $\mathcal{B}(B^0 \to J/\psi K^0)$ measurement common to both K^0_S modes amounts to 6.7%. The total relative systematic error is 6.7% for $K^0_S \to \pi^+\pi^-$ and 8.5% for $K^0_S \to \pi^0\pi^0$. We combined $K^0_S \to \pi^0\pi^0$ and $K^0_S \to \pi^+\pi^-$ modes and calculated $\mathcal{B}(B^0 \to J/\psi K^0)$ taking into account common systematic uncertainties [101].

The total relative systematic uncertainties on $\mathcal{B}(B^0 \to \chi_{c1}K^0)$ and $\mathcal{B}(B^0 \to J/\psi\pi^0)$ measurements are estimated to be 9%; the systematic uncertainties are much smaller than the statistical ones.

Chapter 7

Can CLEO measure $\sin 2\beta$?

7.1 Abstract

We present a sensitivity study for the $\sin 2\beta$ measurement with CLEO II.V data. The results came out to be too discouraging to justify a real measurement.

7.2 Historical context

The $\sin 2\beta$ measurements published at the time of writing this thesis are listed in Table 7.1. We started the analysis presented in this chapter in late 1998 when only the first

Table 7.1: Current status of the $\sin 2\beta$ measurements.

Year	Experiment	$\sin 2\beta$ value	Reference
1998	OPAL	$3.2^{+1.8}_{-2.0} \pm 0.5$	[72]
1998	CDF	$1.8 \pm 1.1 \pm 0.3$	[73]
2000	CDF	$0.79^{+0.41}_{-0.44}$	[74]
2000	ALEPH	$0.84^{+0.82}_{-1.04} \pm 0.16$	[75]
2001	BELLE	$0.58^{+0.32\ +0.09}_{-0.34\ -0.10}$	[76]
2001	BABAR	$0.34 \pm 0.20 \pm 0.05$	[77]

two measurements [72, 73] existed. BABAR and BELLE experiments had not yet started taking data. At that date a measurement of $\sin 2\beta$ with a precision of better than ± 1.0 would be respectable. Such a measurement coming from CLEO would have been completely unexpected. The end of the CLEO II.V data taking was still a few months away, so we decided to do a thorough sensitivity study before we embark on a real measurement. Shortly after we finished this study, CDF reported a new improved measurement of $\sin 2\beta$ [74].

7.3 Introduction

Quantum mechanics of the $\Upsilon(4S) \to B^0\overline{B}^0$ decays precludes an observation of the time-integrated mixing-induced CP violation. One has to measure the B meson decay

time, and this is not easy to do at a symmetric B factory because of the low energy release in the $\Upsilon(4S)$ decay. To measure $\sin 2\beta$ at CLEO, Karl Berkelman proposed a method requiring measurement of the vertex positions of both $B \to J/\psi K^0_S$ and a flavor-tagging B meson [102]. In this Chapter we investigate a new method proposed by Andy Foland in [103]. This method requires a measurement of the vertex position of only the $B \to J/\psi K^0_S$ decay. To measure CP violation, one observes a decay at time t_{CP} to a CP eigenstate f, without observing the decay time of the other B meson in the event. The decay time distribution for the events where the flavor-tagging B meson decayed as B^0 ($\overline{B}^0$) is given by the equation

$$R_{\pm}(t_{CP}) \quad \propto \quad e^{-\frac{t_{CP}}{\tau}} \left\{ 1 \mp \frac{\mathrm{Im}(\lambda)}{\sqrt{1+x_d^2}} \left[\sin\left(x_d \left(\frac{t_{CP}}{\tau} - \frac{\tan^{-1} x_d}{x_d} \right) \right) \right] \right\}, \qquad (7.1)$$

where $x_d \equiv \Delta M_{B^0}/\Gamma_{B^0}$, $\lambda \equiv q/p \times \overline{A}_f/A_f$ (Section 6.2), and we assume $|\lambda|$=1. For $B \to J/\psi K^0_S$, $B \to \psi(2S)K^0_S$, $B^0 \to \chi_{c1} K^0_S$ decays $\mathrm{Im}(\lambda) = \sin 2\beta$, whereas $\mathrm{Im}(\lambda) = -\sin 2\beta$ for $B \to J/\psi K_L$ and $B^0 \to J/\psi\pi^0$ [1] decays because these final states have the opposite sign of CP.

In order to measure $\sin 2\beta$, we have to reconstruct neutral B meson decays, tag the flavor of the other B meson in the event, and then try to distinguish between dashed and dotted-line decay time distributions shown in Figure 7.1.

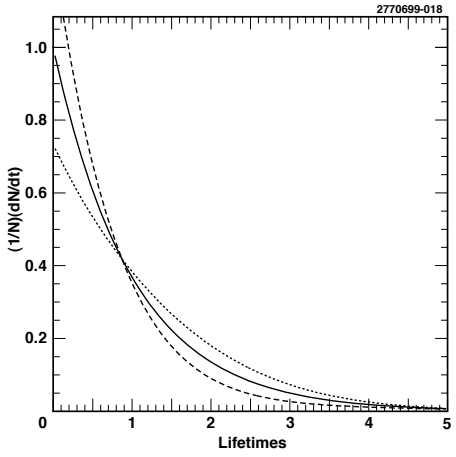

Figure 7.1: Effect of CP violation on decay time distributions of $J/\psi K^0_S$ final state. The solid line shows the case $\sin 2\beta$=0; the dotted (dashed) line shows the distribution of the decay times when the opposite B is tagged as a $B^0(\overline{B^0})$, for $\sin 2\beta$=0.7.

In this study we try to be realistic, but when in doubt we would rather be on the optimistic side because we do not want to kill a promising measurement by an overly pessimistic sensitivity study.

[1] Strictly speaking, $\mathrm{Im}(\lambda) \neq -\sin 2\beta$ for $B^0 \to J/\psi\pi^0$ if the penguin diagram contribution cannot be neglected (Section 6.2). We ignore this complication in our sensitivity study.

7.4 Strategy for $\sin 2\beta$ measurement

7.4.1 Signal event reconstruction

The CLEO II configuration does not have a silicon vertex detector necessary for the precise measurement of the B meson decay vertex. We therefore can only use CLEO II.V data for the $\sin 2\beta$ measurement. Combining the following modes: $B^0 \to J/\psi K^0_S$ ($K^0_S \to \pi^+\pi^-$ and $K^0_S \to \pi^0\pi^0$), $B^0 \to \psi(2S)K^0_S$, $B^0 \to \chi_{c1}K^0_S$, and $B^0 \to J/\psi\pi^0$, we estimate that in full CLEO II.V data sample (6.1 fb^{-1} of $\Upsilon(4S)$ data) we can reconstruct approximately 140 signal events with a background of around 2 events. Event displays for one such signal event are shown in Figures 7.2 and 7.3. In principle, $B^0 \to J/\psi K^0_L$ mode could also be used [31]. In addition, one can increase the $J/\psi \to \ell^+\ell^-$ reconstruction efficiency by about 15% by dropping the lepton identification requirement altogether for one of the lepton candidates. However this will entail an increase in background. We chose the background-free way because the method we employ to determine $\sin 2\beta$ becomes less robust in the presence of backgrounds. We can deal with a couple of background events at the stage of the systematic uncertainty study by repeating the fit many times, each time excluding random events from the sample.

7.4.2 Decay time measurement

The size of the CESR beam spot is known from the machine optics to be only 6 μm in the vertical (**y**) direction. The mean of the beam spot position in **y** direction for a particular run is measured with a precision of 3 μm using $e^+e^- \to \mu^+\mu^-$ and Bhabha scattering events. The remarkable flatness of the beam in **y** has already been successfully used to measure charm meson lifetimes [104]. We employ the same method to determine the proper time of the B meson decay (Figure 7.4).

7.4.3 Flavor tagging

Once we have reconstructed a signal B decay (for example, $B^0 \to J/\psi K^0_S$), we use the rest of the tracks and showers to tag the flavor of the other B meson in the event. Our flavor tagger [105] employs a neural net to optimally combine a set of quantities that discriminate between B^0 and $\overline{B}^0$. If a high-momentum lepton or a charged kaon is present in the event, then its charge is the most powerful tagging variable. A useful variable to describe the effectiveness of a combination of flavor estimators is the effective tagging efficiency ϵD^2, defined as a sum of ϵD^2 over all tagging variables. For each variable, ϵ is the efficiency and $D = 1 - 2w$ is the dilution, where w is the mistag fraction. The statistical uncertainty of the $\sin 2\beta$ measurement is proportional to $1/\sqrt{\epsilon D^2}$. In this study we used the value $\epsilon D^2 = 0.28$, which was determined from the Monte Carlo simulation. Later the flavor tagger was calibrated with data, and the effective tagging efficiency ϵD^2 was found to be 0.22 ± 0.04 for CLEO II and 0.21 ± 0.07 for CLEO II.V data [105]. For comparison, BELLE experiment measured $\epsilon D^2 = 0.270^{+0.021}_{-0.022}$ [76] for their flavor tagger, whereas BABAR reported $\epsilon D^2 = 0.267 \pm 0.016$ [77].

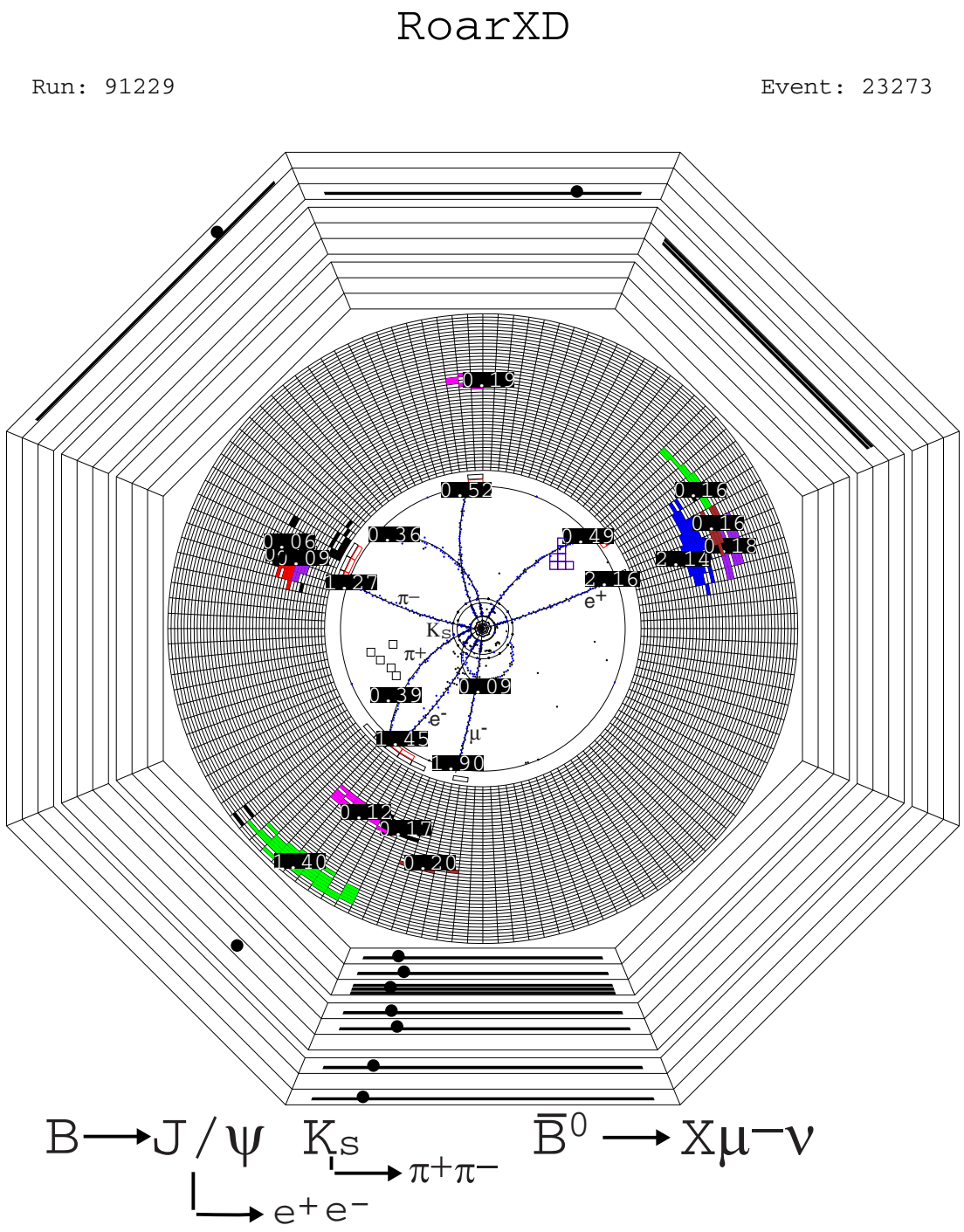

Figure 7.2: Event display for an event containing $B \to J/\psi K_S^0$ decay. Opening angle of the $J/\psi \to e^+e^-$ decay is 132°, which is about average.

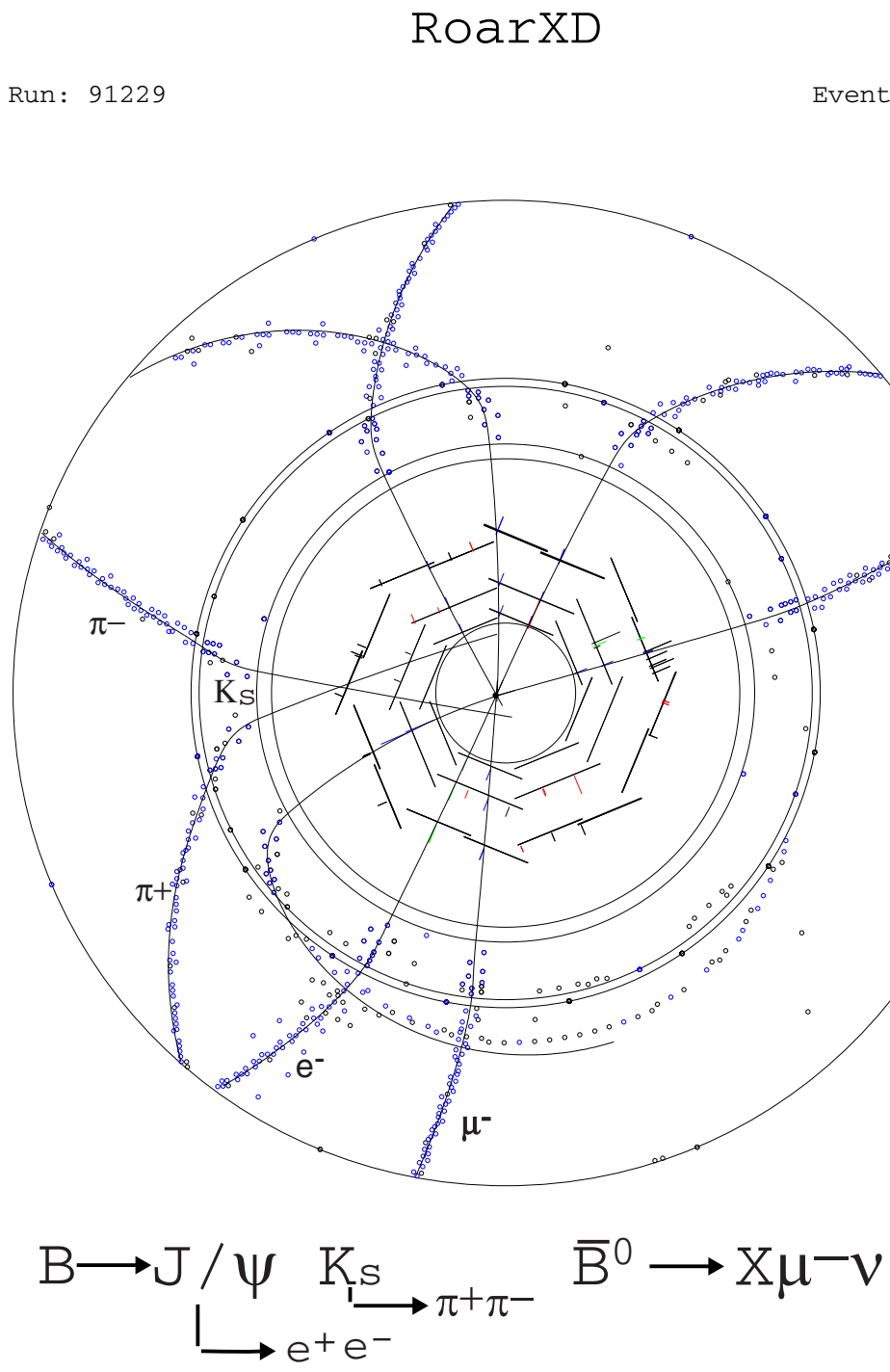

Figure 7.3: Fish-eye view of the event shown in Figure 7.2. It is interesting to note that all seven non-K_S^0 tracks have 2 silicon detector hits per view and that there are no noise hits on the $r-\phi$ side of the 1st silicon layer.

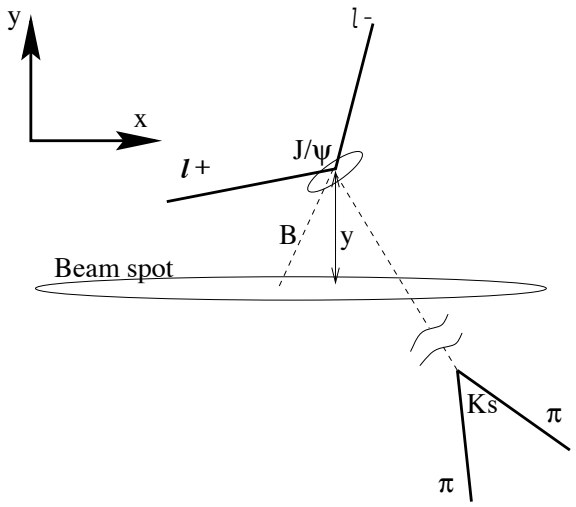

Figure 7.4: The schematics of the measurement of the **y** position of the $\ell^+\ell^- K^0_S$ vertex with respect to the beam spot which allows us to determine the proper time of the B meson decay using the formula $ct = \frac{m_B}{|p_y(B)|}y$.

7.4.4 Final fit

An unbinned likelihood fit method is employed to make the optimal use of the available information.

7.5 Study of B vertex position resolution

7.5.1 `CLEOG` Monte Carlo sample

In this study, for simplicity, we pretend that all signal events come from $B \to J/\psi K^0_S$, $K^0_S \to \pi^+\pi^-$ mode. We generated 30,000 `CLEOG` Monte Carlo events with each event having the $B \to J/\psi K^0_S$, $J/\psi \to \ell^+\ell^-$, $K^0_S \to \pi^+\pi^-$ decay chain. The other B meson in the event was forced to decay into two neutrinos. The sample was generated with the average beam energy of 5289 MeV to agree with CLEO II.V data. The distribution of the event-by-event expected mean B meson flight distance ($\gamma\beta c\tau$) is shown in Figure 7.5. The mean **y** axis projection of the B meson flight distance equals $9/16 \times \gamma\beta c\tau$ [106]. The average of the mean **y** projection distribution is only 15 μm. The geometrical factor 9/16 was calculated taking into account $\sin^2\theta$ distribution of $\Upsilon(4S) \to B\overline{B}$ events and assuming unpolarized beams, i.e. flat ϕ distribution. The small effect of a finite beam crossing angle was neglected. This geometrical factor can be as large as 3/4 if the beams are 100% polarized with the e^+ and e^- spins both pointing up or down [106].

7.5.2 Vertex reconstruction

We find the 3-dimensional B meson decay vertex [107] using the $\ell^+\ell^-$ tracks from the J/ψ decay as well as the K^0_S pseudo-track. The average K^0_S flight distance for

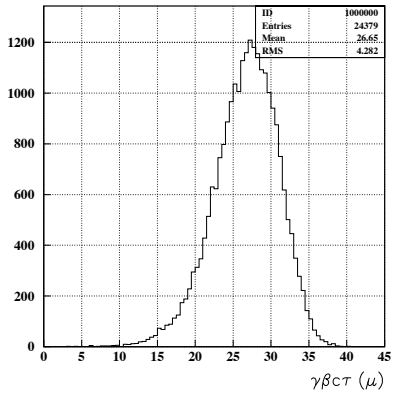

Figure 7.5: Event-by-event expected mean B meson flight distance ($\gamma\beta c\tau$) in microns. If all the runs had the same energy and there were no beam energy spread, then this distribution would have been a δ-function.

$B^0 \to J/\psi K^0_S$ decay is 9 cm, therefore most K^0_S's decay outside the silicon detector. That is why the K^0_S pseudo-track does not help much in the measurement of the B decay vertex (Figure 7.6). The average opening angle of the $J/\psi \to \ell^+\ell^-$ decay is about 130° (Figures 7.2 and 7.3). The precision of the **y** position measurement for the $J/\psi \to \ell^+\ell^-$ decay vertex strongly depends on the orientation of the J/ψ decay with respect to the **y** axis (Figure 7.7). Figure 7.8 shows the projection of the measured B flight distance on y axis: $[y(B \text{ vertex}) - y(\text{beam})] \times \text{sign}(p_y(B))$. To obtain the data histogram (Figure 7.8-left), we reconstructed the following decays in the CLEO II.V data: $B \to J/\psi K$, $B \to J/\psi K^*$, $B \to \psi(2S)K$, and $B \to \chi_{c1}K$. The right plot in Figure 7.8 was obtained from $B^0 \to J/\psi K^0_S$ `CLEOG` Monte Carlo sample. Only $\ell^\pm$ tracks were used to measure the vertex position in the data and in the Monte Carlo simulation. To produce this figure, we required that at least one of the $\ell^\pm$ tracks has silicon detector information, that the reported uncertainty on the **y** projection measurement is less than 100 μm, and χ^2 probability for the vertex fit is higher than 1%.

7.5.3 Check of vertex resolution with $\gamma\gamma \to \ell^+\ell^-$ data

In order to check with data the $J/\psi \to \ell^+\ell^-$ vertex resolution, Andy Foland studied two-photon production of lepton pairs [127]. There are copious $\gamma\gamma \to \ell^+\ell^-$ data for the lepton pairs of mass and momentum similar to the J/ψ decays we are looking for. Two-photon events are known to have zero lifetime, which makes this sample ideal for the studies of the vertex position resolution. For each event we formed the two-track vertex and compared the measured value of **y** to the known beam position. We found the vertex resolution to be consistent with the Monte Carlo simulation and with the values we use for our sensitivity estimation.

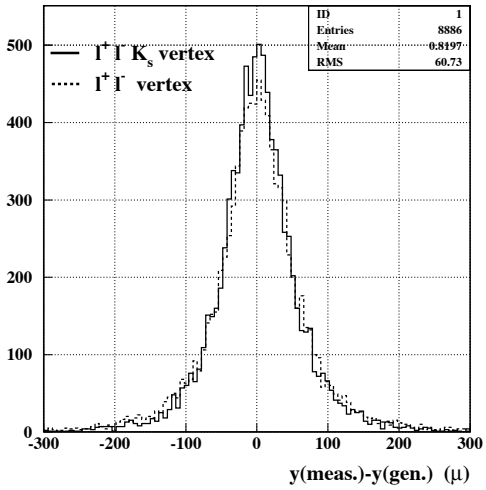

Figure 7.6: B vertex **y** position resolution. The K^0_S pseudo-track was used along with $\ell^+\ell^-$ tracks to find the vertex for the solid-line histogram, whereas only $\ell^+\ell^-$ tracks were used for the dashed-line distribution.

7.5.4 Parametrization of the proper decay time uncertainty

Having measured the **y** position of the $\ell^+\ell^- K^0_S$ vertex with respect to the beam spot, we can calculate the proper time of the B meson decay using the formula

$$t = \frac{m_B}{c|p_y(B)|} y. \tag{7.2}$$

The event-by-event uncertainty of this measurement is given by

$$\frac{\sigma_t}{t} = \sqrt{\frac{\sigma_y^2(B) + \sigma_y^2(\text{beam})}{y^2} + \left(\frac{\sigma_{p_y}}{|p_y(B)|}\right)^2} \tag{7.3}$$

where $\sigma_y(B)$ is the reported error on **y** position of B vertex calculated using track error matrices, $\sigma(\text{beam}) \approx 10$ μm is the uncertainty on the **y** position of the e^+e^- interaction point, and σ_{p_y} is the reported error on the measurement of the **y**-component of the B meson momentum. The error on **y** position of the B vertex dominates the uncertainty on the B decay proper time measurement. Figure 7.9 shows the σ_t distribution for the data and the Monte Carlo simulation. To produce this figure, we required that at least one of the $\ell^\pm$ tracks has silicon detector information, and that the χ^2 probability for the vertex fit is higher than 1%.

If the reported errors σ_t calculated using track error matrices perfectly represented the uncertainty on the B meson proper decay time measurement, then the distribution of pulls in Figure 7.10 would be a perfect unit Gaussian. We reflect the imperfections of the reported σ_t by allowing σ_t to be multiplied by a global scale factor S. We also assume

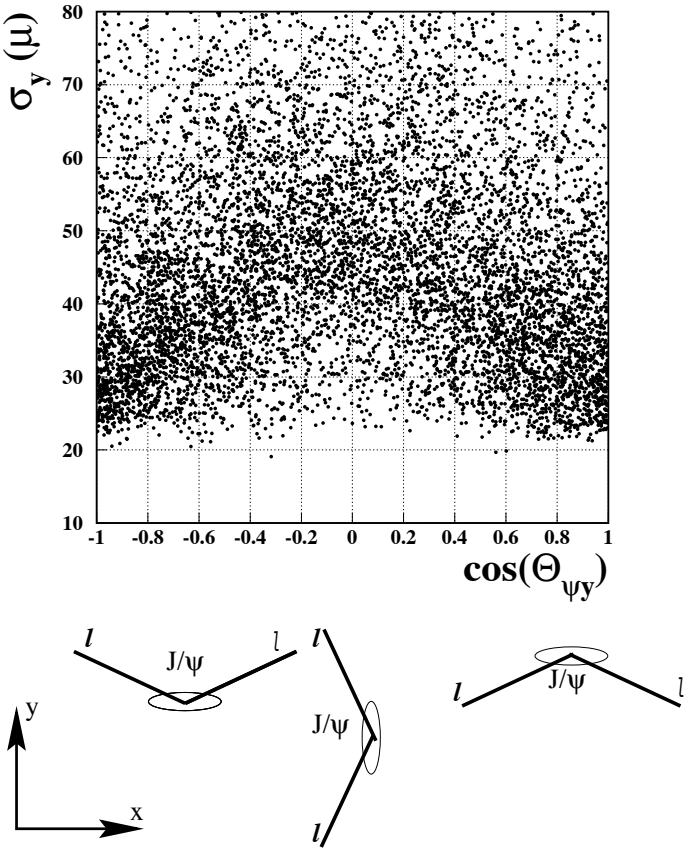

Figure 7.7: Top plot shows the dependence of the J/ψ vertex $\mathbf{y}$ position resolution on the orientation of $J/\psi \to \ell^+\ell^-$ decay. Bottom plot shows different orientations of $J/\psi \to \ell^+\ell^-$ decay. Left one corresponds to $\cos(\theta_{\psi y}) = -1$, central — $\cos(\theta_{\psi y}) = 0$, right — $\cos(\theta_{\psi y}) = +1$

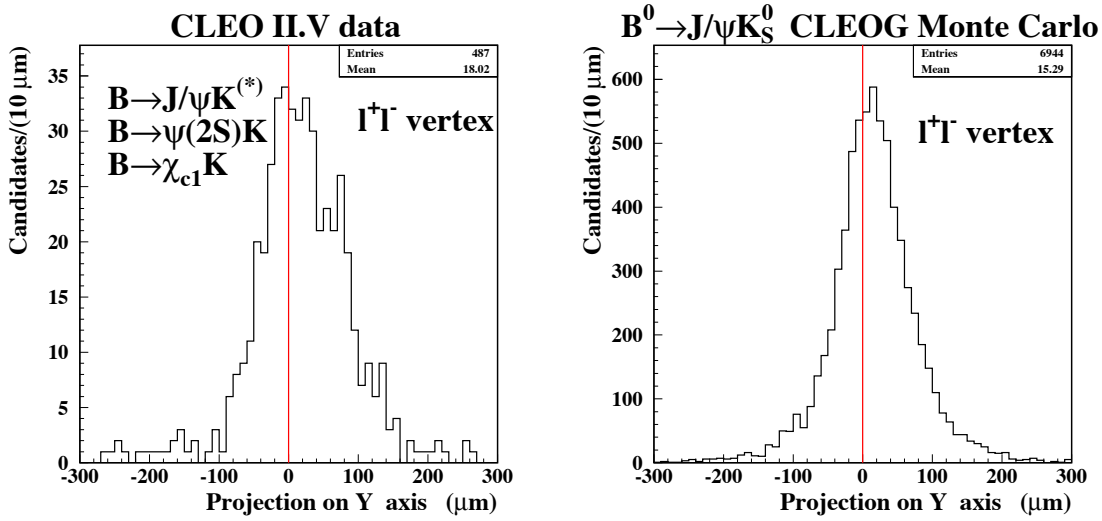

Figure 7.8: Projection of the measured B flight distance on **y** axis. Left plot was obtained using fully reconstructed B decays to charmonia in CLEO II.V data. Right plot is for $B \to J/\psi K^0_S$ `CLEOG` Monte Carlo sample. Only $\ell^\pm$ tracks were used to measure the vertex position.

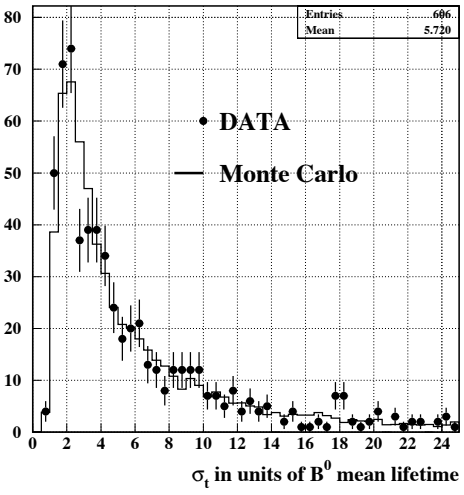

Figure 7.9: Reported error on B meson proper decay time measurement in the units of mean B^0 lifetime ($c\tau = 468\mu$m). Points were obtained using fully reconstructed B decays to charmonia from CLEO II.V data. Solid-line histogram was obtained using a sample of simulated $B \to J/\psi K^0_S$ events. The histogram extracted from the simulation was scaled to the same area as the data histogram. Only $\ell^\pm$ tracks were used to measure the vertex position.

that for a small fraction of events f_{mis} the reported error σ_t should not be trusted and uncertainty σ_{mis} should be used instead. We extract the values of S, f_{mis}, σ_{mis} from the simulation using the unbinned likelihood fit that maximizes the function

$$\mathcal{L}(S, f_{mis}, \sigma_{mis}) = \prod_i [(1 - f_{mis}) G(t_i(meas) - t_i(gen) | S\sigma_{t,i}) + \\ + f_{mis} G(t_i(meas) - t_i(gen) | \sigma_{mis})]$$

where $G(t|\sigma) \equiv 1/(\sqrt{2\pi}\sigma)\exp(-t^2/2\sigma^2)$. We obtain $S = 1.1$, $f_{mis} = 2.5\%$, and $\sigma_{mis} = 15$ (measured in units of mean B^0 lifetime).

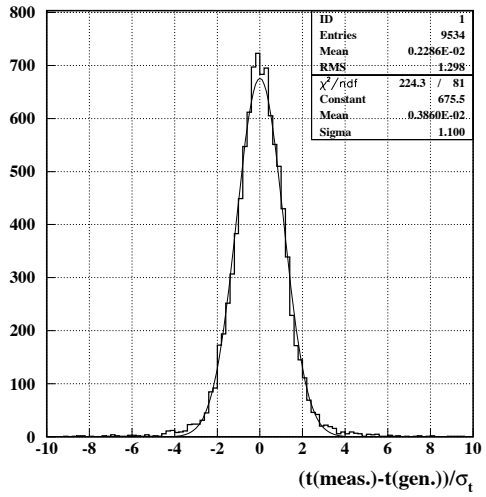

Figure 7.10: Pulls of the B meson proper decay time measurement with a sample of simulated events. Fit to a Gaussian is shown.

7.6 Samples of simulated CLEO II.V data

We estimated that using all CLEO II.V data we expect to reconstruct $\simeq 140$ B mesons decaying into $J/\psi K^0_S$ ($K^0_S \to \pi^+\pi^-$ and $K^0_S \to \pi^0\pi^0$), $\psi(2S)K^0_S$, $\chi_{c1}K^0_S$, or $J/\psi\pi^0$. Approximately 120 events will survive the minimal vertex quality cuts: at least one of the $\ell^\pm$ tracks should have silicon detector information, χ^2 probability for the vertex fit should be higher than 1%, and reported $\sigma_t < 25$.

We generate multiple samples of simulated CLEO II.V data (toy Monte Carlo samples). Each sample has 120 events. One B^0 or $\overline{B}^0$ meson in the event decays to $J/\psi K^0_S$. The other B meson is either B^0 or $\overline{B}^0$ with equal probability. The decay time t_i for $B \to J/\psi K^0_S$ is generated for each event according to the distribution (see Equation 7.1)

$$e^{-t_i}\{1 \mp \frac{\sin 2\beta}{\sqrt{1+x_d^2}}[\sin(x_d(t_i - \frac{\tan^{-1} x_d}{x_d}))]\} \qquad (7.4)$$

where the sign in front of the $\sin 2\beta$ term depends on whether the tagging B meson decayed as B^0 or $\overline{B}^0$. Then the reported uncertainty on the decay time measurement $\sigma_{t,i}$ is generated randomly according to the histogram shown in Figure 7.11. For $(1-f_{mis}) = 97.5\%$ of events,

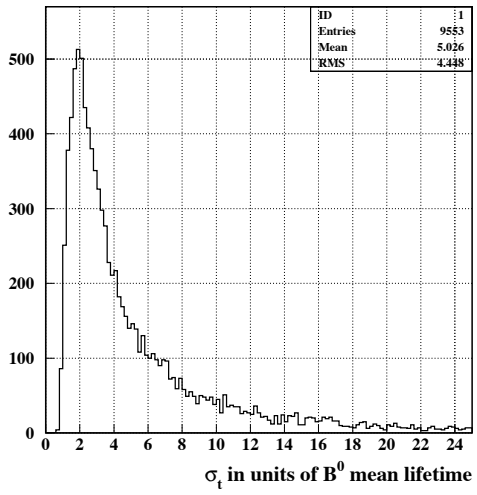

Figure 7.11: Reported error on B meson proper decay time measurement in the units of mean B^0 lifetime ($c\tau = 468\mu$m). This histogram was extracted from the `CLEOG` Monte Carlo sample and was used in the production of the toy Monte Carlo samples.

we smear the generated decay time using Gaussian distribution with $\sigma = S\sigma_{t,i}$ (S=1.1), and for $f_{mis} = 2.5\%$ of events we smear the time using a Gaussian with $\sigma_{mis} = 15$. The last step is to randomly assign $P(B^0)$, the probability that the other B meson decayed as B^0 (as opposed to $\overline{B}^0$), given the tagging information. This is accomplished using the distribution shown in Figure 7.12, and the resulting distribution of $P(B^0)$ is shown in Figure 7.13.

7.7 Unbinned likelihood fit

There are 3 input variables in our fit:

1. t — measured proper time of the $B \to J/\psi K^0_S$ decay,
2. σ_t — reported error on the $B \to J/\psi K^0_S$ decay time measurement,
3. $P(B^0)$ — probability that the other B meson decayed as B^0 (as opposed to $\overline{B}^0$).

The parameters we fix in the fit are:

1. B^0 lifetime $c\tau = 468\mu$m (PDG'98 value [47]),
2. $x_d \equiv \Delta M_{B^0}/\Gamma_{B^0} = 0.723$ (PDG'98 value [47]),

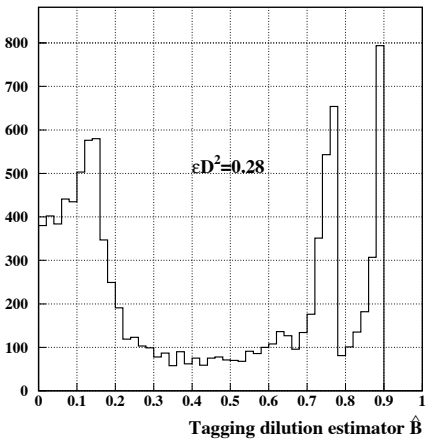

Figure 7.12: Flavor tagging dilution estimator [105]. This histogram was used for production of the toy Monte Carlo samples.

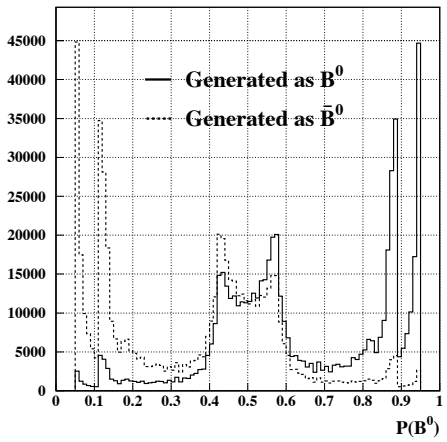

Figure 7.13: $P(B^0)$ - assigned probability that the other B meson decayed as B^0 (as opposed to $\overline{B}^0$). Solid (dashed) line represents the case when there was true $B^0(\overline{B}^0)$ on the other side.

3. $S = 1.1$ — global scaling factor for σ_t,

4. $\sigma_{mis} = 15$ — error on the decay time measurement for the events with underestimated decay time uncertainty,

5. $f_{mis} = 0.025$ — fraction of events with underestimated decay time uncertainty.

The output of the fit is the measured value of $\sin 2\beta$.

Description of the fit starts with a simple hypothetical case of perfect detector with perfect flavor tagging and then progresses to the real fit.

7.7.1 Perfect detector, perfect flavor tagging

With perfect flavor tagging, $P(B^0)$ equals to either 1.0 or 0.0 depending on whether the other B in the event decayed as B^0 or $\overline{B^0}$.

The probability density function (PDF) in this case is given by (see Equation 7.1)

$$R_{\pm}(t|\sin 2\beta) \quad = \quad e^{-t}\{1 \mp \frac{\sin 2\beta}{\sqrt{1+x_d^2}}[\sin(x_d(t - \frac{\tan^{-1} x_d}{x_d}))]\}. \tag{7.5}$$

The subscripts on $R_{\pm}$ denote the cases when the other B meson decayed as $B^0(\overline{B}^0)$. When $B^0 \to J/\psi\pi^0$ mode is used, additional minus sign should be placed in front of $\sin 2\beta$ in Equation 7.5 to account for opposite CP parity of this final state.

7.7.2 Perfect detector, imperfect flavor tagging

In this case $P(B^0)$ has some value between 0 and 1 (Figure 7.13). The PDF is given by

$$\begin{aligned} R(t|\sin 2\beta) &= e^{-t}\{1-[P(B^0)-P(\overline{B}^0)]\cdot\frac{\sin 2\beta}{\sqrt{1+x_d^2}}[\sin(x_d(t-\frac{\tan^{-1}x_d}{x_d}))]\} \\ &= e^{-t}\{1-[2\cdot P(B^0)-1]\cdot\frac{\sin 2\beta}{\sqrt{1+x_d^2}}[\sin(x_d(t-\frac{\tan^{-1}x_d}{x_d}))]\} \end{aligned} \tag{7.6}$$

The likelihood function to maximize is product of PDF's for all the events:

$$\mathcal{L}(\sin 2\beta) = \prod_i R(t_i|\sin 2\beta) \tag{7.7}$$

7.7.3 Imperfect detector, imperfect flavor tagging

For imperfect detector we have to convolute the PDF in Equation 7.6 with the Gaussian detector resolution. Then the likelihood function becomes

$$\mathcal{L}(\sin 2\beta) = \prod_i \int_0^\infty R(t'|\sin 2\beta)\times\left[\underbrace{(1-f_{\rm mis})G(t_i-t'|S\sigma_{t,i})}_{\text{correctly measured}}+\underbrace{f_{\rm mis}G(t_i-t'|\sigma_{\rm mis})}_{\text{mis-measured fraction}}\right]dt'$$

where $R(t|\sin 2\beta)$ is given by Equation 7.6.
It is useful to analytically calculate the following three integrals [108]:

$$\int_0^\infty e^{-t'}\frac{1}{\sqrt{2\pi}\sigma}\exp\left(-\frac{(t-t')^2}{2\sigma^2}\right)dt' = \frac{1}{2}\exp\left[\frac{\sigma^2}{2}-t\right]\mathrm{Erfc}\left[\frac{1}{\sqrt{2}}\left(\sigma-\frac{t}{\sigma}\right)\right],$$

$$\int_0^\infty e^{-t'}\sin xt'\frac{1}{\sqrt{2\pi}\sigma}\exp\left(-\frac{(t-t')^2}{2\sigma^2}\right)dt' = \frac{1}{2}\exp\left(-\frac{t^2}{2\sigma^2}\right)\mathrm{Im}\left[W\left(\frac{x\sigma}{\sqrt{2}}+\frac{i}{\sqrt{2}}(\sigma-\frac{x}{\sigma})\right)\right],$$

$$\int_0^\infty e^{-t'}\cos xt'\frac{1}{\sqrt{2\pi}\sigma}\exp\left(-\frac{(t-t')^2}{2\sigma^2}\right)dt' = \frac{1}{2}\exp\left(-\frac{t^2}{2\sigma^2}\right)\mathrm{Re}\left[W\left(\frac{x\sigma}{\sqrt{2}}+\frac{i}{\sqrt{2}}(\sigma-\frac{x}{\sigma})\right)\right].$$

Erfc(x) is the complementary error function

$$\mathrm{Erfc}(x) = 1-\mathrm{Erf}(x) = 1-\frac{2}{\sqrt{\pi}}\int_0^x \exp(-t^2)dt.$$

W(z) is the complex error function

$$\mathrm{W}(z) = e^{-z^2}\left[1+\frac{2i}{\sqrt{\pi}}\int_0^z e^{t^2}dt\right] = e^{-z^2}\left[1-\mathrm{Erf}(-iz)\right] = e^{-z^2}\mathrm{Erfc}(-iz).$$

The likelihood function we have to maximize is given by the following formula

$$\mathcal{L}(\sin 2\beta) = \prod_i \left[\underbrace{(1-f_{\rm mis}) R_{smeared}(t_i, S\sigma_{t,i}|\sin 2\beta)}_{\text{correctly measured}} + \underbrace{f_{\rm mis} R_{smeared}(t_i, \sigma_{mis}|\sin 2\beta)}_{\text{mis-measured fraction}} \right],$$

where

$$\begin{aligned} & R_{smeared}(t,\sigma|\sin 2\beta) = \\ = \;& \exp\left(\frac{\sigma^2}{2} - t\right) \mathrm{Erfc}\left[\frac{1}{\sqrt{2}}\left(\sigma - \frac{t}{\sigma}\right)\right] - \sin 2\beta \frac{(2P(B^0)-1)}{1+x_d^2} \exp\left(-\frac{t^2}{2\sigma^2}\right) \times \\ \times \;& \left\{ \mathrm{Im}\left[W\left(\frac{x\sigma}{\sqrt{2}} + \frac{i}{\sqrt{2}}(\sigma - \frac{x}{\sigma})\right)\right] - x_d \cdot \mathrm{Re}\left[W\left(\frac{x\sigma}{\sqrt{2}} + \frac{i}{\sqrt{2}}(\sigma - \frac{x}{\sigma})\right)\right]\right\}. \end{aligned}$$

7.8 Mean-time method

As a cross-check for the unbinned likelihood fit, we used another method to determine $\sin 2\beta$. As can be inferred from Figure 7.1, the mean decay time will be different for the events in which the tagging B meson decayed as B^0 or $\overline{B^0}$ [103]:

$$\bar{t}_\pm = \tau(1 \mp \frac{x_d \sin 2\beta}{(1+x_d^2)^2}).$$

The difference in the mean times is proportional to $\sin 2\beta$. Numerically, the corresponding difference in the mean decay lengths is $18 \times \sin 2\beta$ μm in the $\Upsilon(4S)$ frame. When the smearing is symmetric, the means are not systematically shifted. Therefore, if the flavor tagging were perfect, we could use the following formula to evaluate $\sin 2\beta$:

$$\tau \frac{2x_d \sin 2\beta}{(1+x_d^2)^2} = \underbrace{\frac{\sum \frac{t_i}{\tau^2+(S\sigma_{t,i})^2}}{\sum \frac{1}{\tau^2+(S\sigma_{t,i})^2}}}_{\mathrm{B^0tag}} - \underbrace{\frac{\sum \frac{t_j}{\tau^2+(S\sigma_{t,j})^2}}{\sum \frac{1}{\tau^2+(S\sigma_{t,j})^2}}}_{\overline{\mathrm{B^0}}\mathrm{tag}} \tag{7.8}$$

Note that we weight each measured decay proper time t_i by the squared proper time measurement uncertainty. For the flavor tagging with dilution D the Equation 7.8 should be substituted by

$$D \cdot \tau \frac{2x_d \sin 2\beta}{(1+x_d^2)^2}) = \underbrace{\frac{\sum \frac{t_i}{\tau^2+(S\sigma_{t,i})^2}}{\sum \frac{1}{\tau^2+(S\sigma_{t,i})^2}}}_{\mathrm{P(B^0)>0.5}} - \underbrace{\frac{\sum \frac{t_j}{\tau^2+(S\sigma_{t,j})^2}}{\sum \frac{1}{\tau^2+(S\sigma_{t,j})^2}}}_{\mathrm{P(B^0)<0.5}}.$$

In our analysis we estimate the flavor tagging dilution on the event-by-event basis using the dilution estimator $\hat{B} = |P(B^0) - P(\overline{B^0})|$ (Figure 7.12). The formula

$$\{\sin 2\beta\}_k = \frac{1}{\hat{B}_k} \cdot \frac{(1+x_d^2)^2}{2x_d \cdot \tau} \left[\underbrace{\frac{\sum \frac{t_i}{\tau^2+(S\sigma_{t,i})^2}}{\sum \frac{1}{\tau^2+(S\sigma_{t,i})^2}}}_{\mathrm{P(B^0)>0.5}} - \underbrace{\frac{\sum \frac{t_j}{\tau^2+(S\sigma_{t,j})^2}}{\sum \frac{1}{\tau^2+(S\sigma_{t,j})^2}}}_{\mathrm{P(B^0)<0.5}} \right] \tag{7.9}$$

is used the to find the value of $\sin 2\beta$ for each bin of the $\hat{B}$ distribution, and then the measurements are combined using the appropriate weighting.

7.9 Results

We have generated 10,000 toy Monte Carlo samples with $\sin 2\beta = +0.8$. Each sample has 120 events and is designed to represent CLEO II.V data. The results of the unbinned likelihood fit to these toy Monte Carlo samples are shown in Figures 7.14 and 7.15. The average expected statistical uncertainty of our $\sin 2\beta$ measurement with an unbinned likelihood fit is 1.8. The experiment-by-experiment RMS spread of the expected uncertainty distribution is 0.3.

We also generated the Monte Carlo samples with $\sin 2\beta = +0.4, 0.0, -0.4, -0.8$. We ran the likelihood fit on these samples and verified that the resulting average expected uncertainty of the $\sin 2\beta$ measurement does not depend on the input value of $\sin 2\beta$.

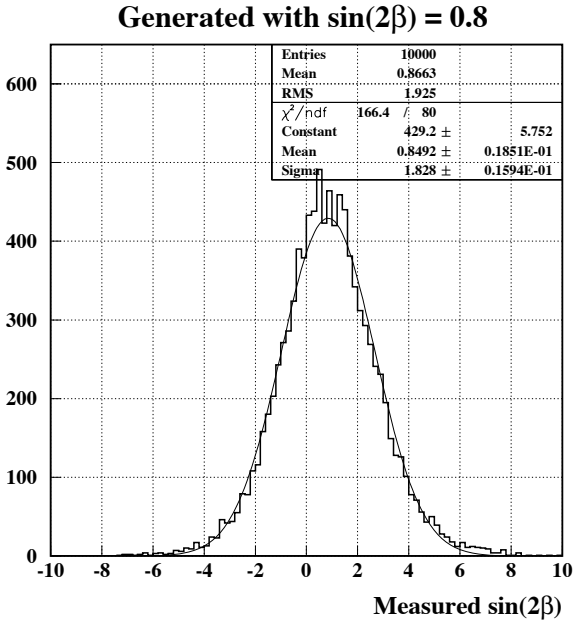

Figure 7.14: The values of $\sin 2\beta$ measured in each of 10,000 toy Monte Carlo experiments simulating CLEO II.V data. The events were generated using $\sin 2\beta = 0.8$.

The results obtained by the mean-time method for the same toy Monte Carlo samples are shown in Figure 7.16. Comparing Figures 7.14 and 7.16, one can infer that the full likelihood fit method wins 15% in sensitivity compared to the mean-time method. The likelihood fit is able to resolve the difference in shapes of the decay time distributions (Equation 7.1 and Figure 7.1), whereas mean-time method is sensitive only to the difference in means of the two distributions. Therefore with better vertex resolution and increased

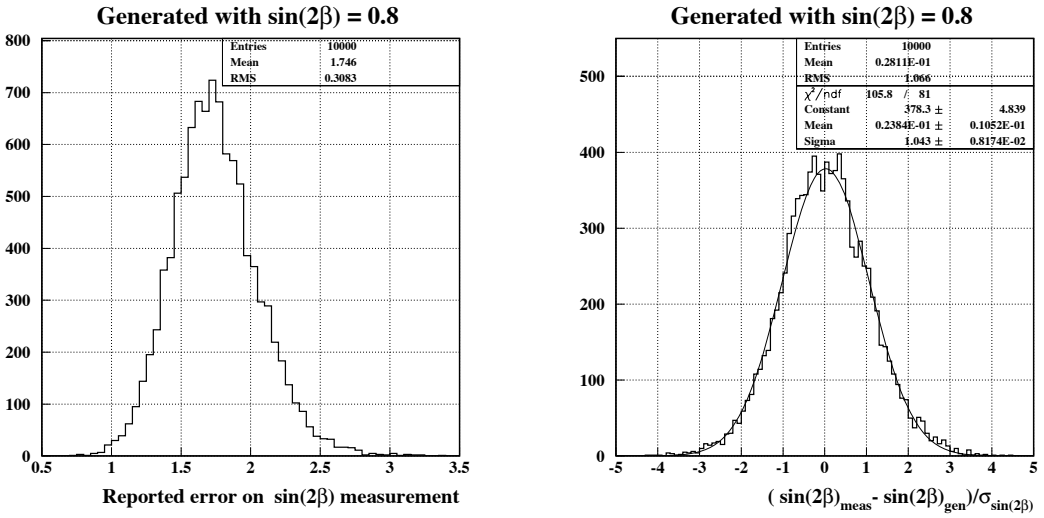

Figure 7.15: Left plot shows errors on the measured value of $\sin 2\beta$ reported by the likelihood fit in each of 10,000 toy Monte Carlo experiments simulating CLEO II.V data. Right plot shows the pulls of the $\sin 2\beta$ measurements. Right (left) MINOS [109] error was used depending on whether the measured $\sin 2\beta$ was bigger (smaller) than the generated one.

statistics the likelihood fit will be more and more advantageous compared to the mean-time method.

7.10 Conclusion: No

From the study presented we conclude that if someone does measure $\sin 2\beta$ with the precision better than ± 1.0 using CLEO II.V data, then we (Andy Foland and A. E.) will have to eat our hats.

7.11 Outlook: CLEO III and beyond

What if we had 30 fb^{-1} of data and our vertex detector were better than the one we have now? As the full `CLEOG` simulation of the CLEO III detector was not available at the time we performed this analysis, we used `TRACKERR` program [110] to study the vertex resolution for CLEO III. We have also performed the same study for the CLEO III detector with the proposed silicon detector upgrade [111] which we call CLEO III.V in this note. In Figure 7.17 we compare the distributions of the reported errors on B meson proper decay time measurement for CLEO II.V obtained using `CLEOG` and `TRACKERR`. One can see that `TRACKERR` is more optimistic than `CLEOG`, but for our purposes the agreement is not bad at all.

To obtain the σ_t distributions shown in Figure 7.18 we have generated the Monte Carlo samples similar to the one described in Section 7.5.1 with the average run beam

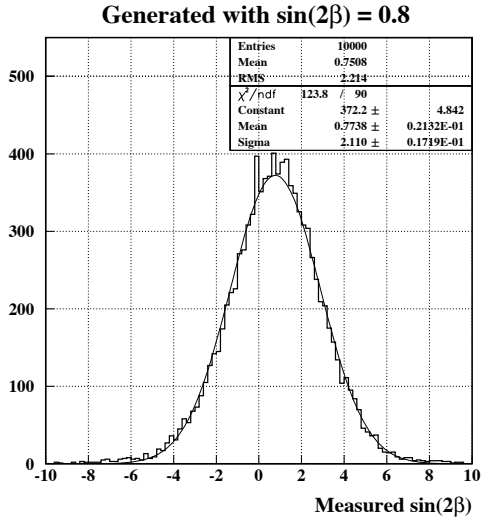

Figure 7.16: The values of $\sin 2\beta$ measured using mean-time method in each of 10,000 toy Monte Carlo experiments simulating CLEO II.V data. The events were generated using $\sin 2\beta = 0.8$.

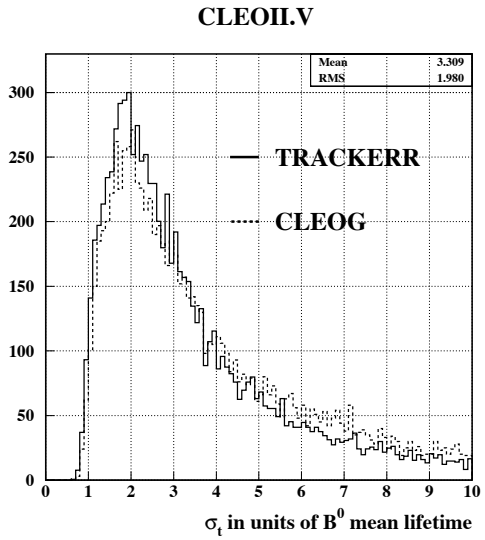

Figure 7.17: Reported error on B meson proper decay time measurement in the units of mean B^0 lifetime. Solid-line histogram was obtained using `CLEOG` Monte Carlo simulation of the CLEO II.V data, dashed-line histogram was obtained using `TRACKERR` Monte Carlo simulation of the CLEO II.V data.

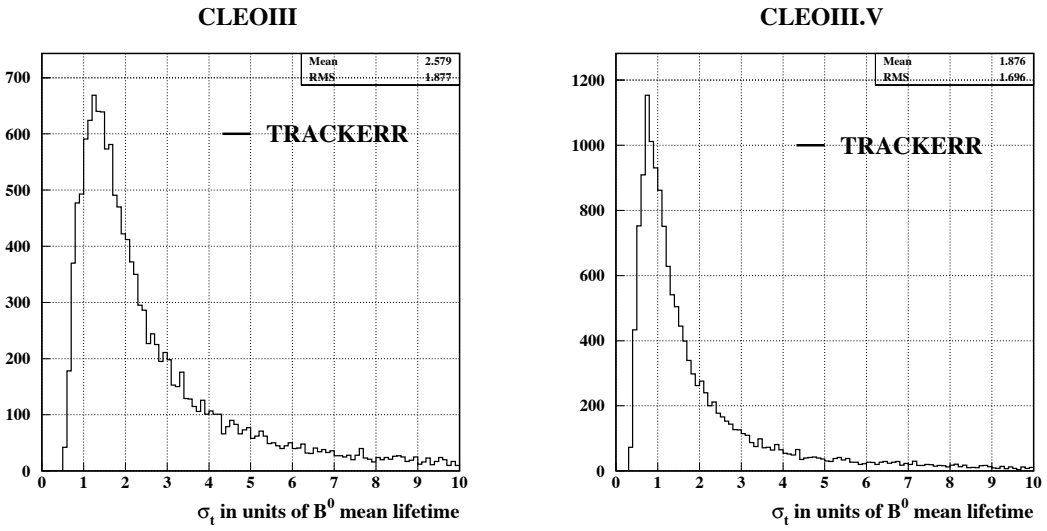

Figure 7.18: Reported error on B meson proper decay time measurement in the units of mean B^0 lifetime. Both histograms were obtained using `TRACKERR` parametrization. Left histogram is for CLEO III. Right histogram is for CLEO III with the upgraded silicon vertex detector [111]. These histograms were used in production of the toy Monte Carlo samples.

energy of 5290 MeV and using `TRACKERR` instead of `CLEOG`.

Then we have generated 10,000 toy Monte Carlo samples with $\sin 2\beta = 0.8$. Each sample has 600 events which corresponds roughly to 30 fb^{-1} of data. Decay time smearing was performed using the histograms shown in Figure 7.18. We used the same tagging probability distributions (Figures 7.12 and 7.13) as in the CLEO II.V study.

The results of the unbinned likelihood fit to the toy Monte Carlo samples simulating CLEO III and CLEO III.V data are shown in Figures 7.19 and 7.20. The average expected statistical uncertainty of our $\sin 2\beta$ measurement with an unbinned likelihood fit is 0.5 for CLEO III and 0.4 for CLEO III.V sample. The experiment-by-experiment RMS spread of the expected uncertainty distribution is 0.04 for CLEO III and 0.03 for CLEO III.V.

The results obtained by the mean-time method for the same toy Monte Carlo samples are shown in Figure 7.21. The full unbinned likelihood fit (Figure 7.19) wins 33% (46%) in sensitivity compared to mean-time method for CLEO III (CLEO III.V). The likelihood fit did only 15% better than the mean-time method for simulated CLEO II.V data (see Figures 7.14 and 7.16).

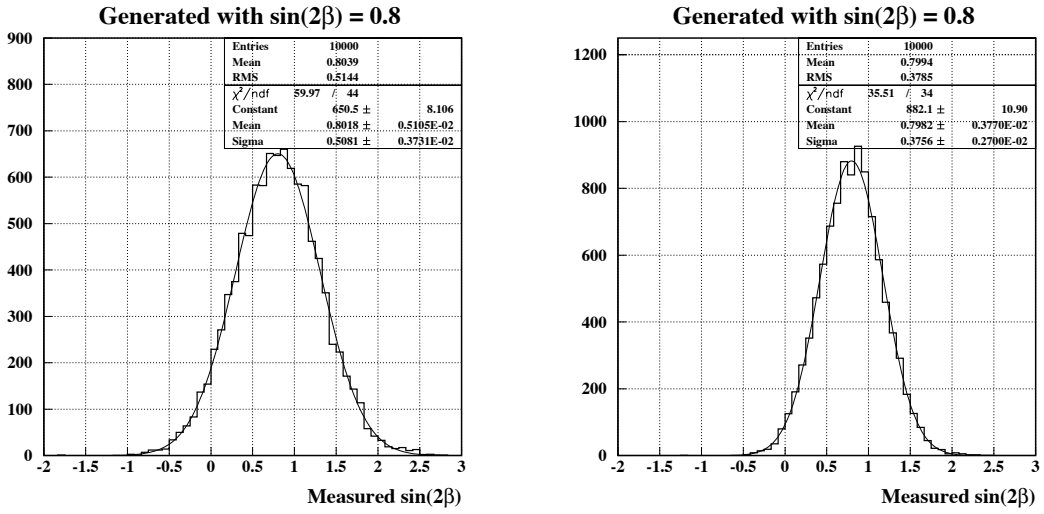

Figure 7.19: The $\sin 2\beta$ values measured in each of 10,000 toy Monte Carlo experiments simulating CLEO III (left) and CLEO III.V data (right). The events were generated using $\sin 2\beta = 0.8$. We generated 600 events in each toy Monte Carlo experiment, which corresponds to approximately 30 fb^{-1} of data.

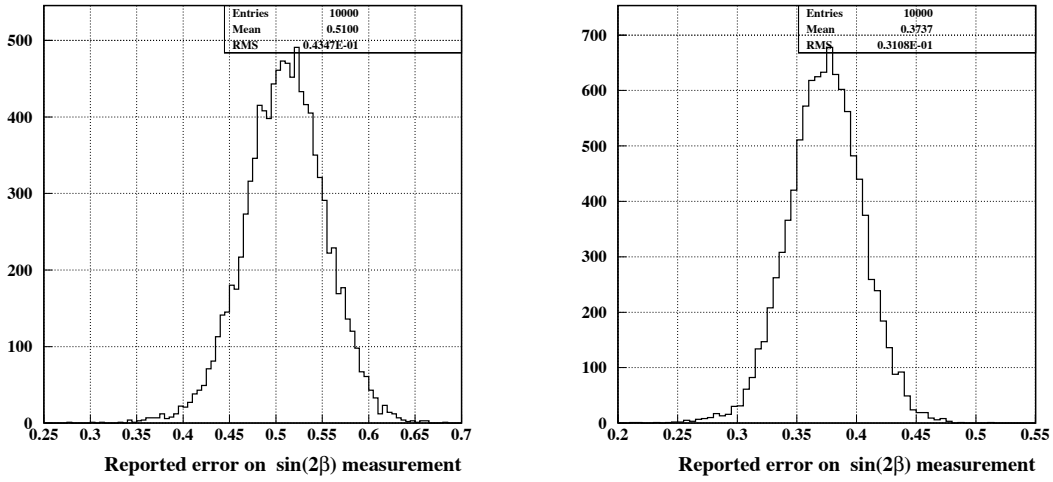

Figure 7.20: MINOS errors on the measured value of $\sin 2\beta$ reported by the unbinned likelihood fit in each of 10,000 toy Monte Carlo experiments simulating CLEO III (left) and CLEO III.V data (right).

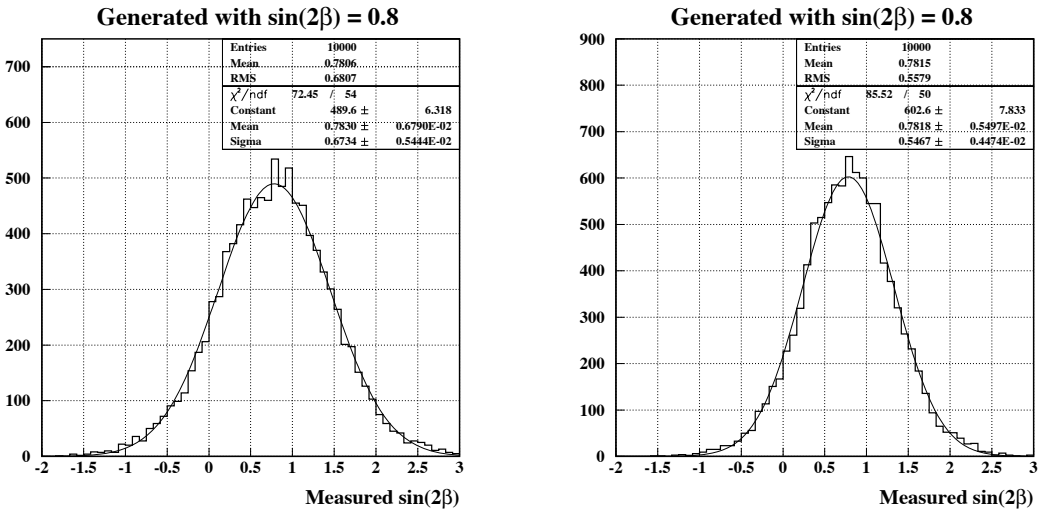

Figure 7.21: The $\sin 2\beta$ values measured with the mean-time method in each of 10,000 toy Monte Carlo experiments simulating CLEO III (left) and CLEO III.V data (right).

Chapter 8

Search for CP violation in $B^{\pm} \to J/\psi\, K^{\pm}$ and $B^{\pm} \to \psi(2S)\, K^{\pm}$ decays

8.1 Abstract

We present a search for direct CP violation in $B^{\pm} \to J/\psi\, K^{\pm}$ and $B^{\pm} \to \psi(2S)\, K^{\pm}$ decays. In a sample of 9.7×10^6 $B\overline{B}$ meson pairs, we have fully reconstructed 534 $B^{\pm} \to J/\psi\, K^{\pm}$ and 120 $B^{\pm} \to \psi(2S)\, K^{\pm}$ candidates with very low background. We have measured the CP-violating charge asymmetry to be $(+1.8 \pm 4.3[\text{stat}] \pm 0.4[\text{syst}])\%$ for $B^{\pm} \to J/\psi\, K^{\pm}$ and $(+2.0 \pm 9.1[\text{stat}] \pm 1.0[\text{syst}])\%$ for $B^{\pm} \to \psi(2S)\, K^{\pm}$.

8.2 Introduction

Direct CP violation is revealed when the amplitude for a decay and its CP-conjugate process have different magnitudes. Direct CP violation can be observed both in charged and in neutral B meson decays. At least two interfering amplitudes with different CP-odd (weak) and CP-even (strong or electromagnetic) phases are the necessary ingredients for direct CP violation. The magnitude of CP asymmetry is given by

$$\mathcal{A}_{CP} \equiv \frac{\Gamma(\overline{B} \to \overline{f}) - \Gamma(B \to f)}{\Gamma(\overline{B} \to \overline{f}) + \Gamma(B \to f)} = \frac{2|A_1||A_2|\sin(\phi_1 - \phi_2)\sin(\delta_1 - \delta_2)}{|A_1|^2 + |A_2|^2 + 2|A_1||A_2|\cos(\phi_1 - \phi_2)\cos(\delta_1 - \delta_2)}.$$

The maximal 100% asymmetry is attained when the interfering amplitudes have equal magnitudes: $|A_1| = |A_2|$, and the relative weak and strong phases are both equal to $\pi/2$: $|\phi_1 - \phi_2| = |\delta_1 - \delta_2| = \pi/2$.

In Standard Model the asymmetry we are trying to measure is well below the attainable statistical precision of 4%. The same reasoning which accords "gold-plated" status for the $\sin 2\beta$ measurement to the $B^0(\overline{B}^0) \to J/\psi K^0_S$ mode also leaves no hope for significant direct CP violation in $B^{\pm} \to J/\psi\, K^{\pm}$ decays. For the decays governed by the $b \to c\bar{c}s$ quark transition, such as $B^{\pm} \to J/\psi\, K^{\pm}$ and $B^0(\overline{B}^0) \to J/\psi\, K^0_S$, there are

interfering Standard Model tree and penguin amplitudes (Figure 8.1) which could have a significant relative strong phase. The penguin amplitude (Figure 8.1-middle) is expected to be small compared to the tree process (Figure 8.1-left). However, even if the penguin contribution and the relative tree-penguin strong phase turn out to be large, the weak phase just is not there to create a sizable CP asymmetry [71]. We can write the amplitude of the $b \to c\bar{c}s$ transition as a sum of tree ($T_{c\bar{c}s}$) and penguin ($P_{\{u,c,t\}}$) contributions: $A(c\bar{c}s) = V_{cb}V_{cs}^*(T_{c\bar{c}s} + P_c) + V_{ub}V_{us}^* P_u + V_{tb}V_{ts}^* P_t$. Using the constraint provided by the unitarity of the Cabibbo-Kobayashi-Maskawa matrix, $V_{cb}V_{cs}^* + V_{ub}V_{us}^* + V_{tb}V_{ts}^* = 0$, we can recast the expression for the $A(c\bar{c}s)$ as $A(c\bar{c}s) = V_{cb}V_{cs}^*(T_{c\bar{c}s} + P_c - P_u) + V_{tb}V_{ts}^*(P_t - P_u)$. The relative weak phase between the two terms is very small[1]: $\arg\left(V_{cb}V_{cs}^*/V_{tb}V_{ts}^*\right) \simeq \lambda^2\eta + \pi$, where $\lambda \equiv \sin\theta_C \approx 0.22$ and $\eta \approx 0.3$ [112].

A large value of $\mathcal{A}_{CP}$ which is measurable with the current CLEO data set can be generated in a model described in [113]. The authors discuss a particular two-Higgs doublet model without natural flavor conservation, in which the top quark is the only fermion which receives its mass from the vacuum expectation value of the second Higgs doublet. The charged Higgs sector of this model contains additional CP-violating phases. In this model the $b \to c\bar{c}s$ transition receives a contribution from a charged-Higgs-mediated tree diagram shown in Figure 8.1(right). This diagram comes with its own CP-violating phase. A relative strong phase can be generated because final state interactions could be quite different for the transitions mediated by spin-1 ($W^{\pm}$) and spin-0 ($H^{\pm}$) particles. The authors of [113] suggest that a CP asymmetry of $\mathcal{O}(10\%)$ in $B^{\pm} \to J/\psi\, K^{\pm}$ decays is possible if the relative strong phase is not too small.

There exist other possible New Physics scenarios for generating CP asymmetry in $B^{\pm} \to \psi^{(\prime)}K^{\pm}$ decays. In order to constrain any of the New Physics models, however, we need to know the relative strong phases, which are difficult to determine.

An observation of CP asymmetry in $B^{\pm} \to J/\psi\, K^{\pm}$ decay at a few per cent or larger level will be a clear evidence for sources of CP violation beyond the Standard Model. Such an observation will also mean that a measurement of the CP asymmetry in $B^0(\overline{B}^0) \to J/\psi\, K_S^0$ decay no longer determines $\sin 2\beta$.

CDF used $B^{\pm} \to J/\psi\, K^{\pm}$ sample to determine tagging dilutions in their measurement of $\sin 2\beta$ [74]; zero charge asymmetry in $B^{\pm} \to J/\psi\, K^{\pm}$ was assumed. The flavor-tagging method developed by CDF is likely to be used in the future precise measurements of $\sin 2\beta$ at the Tevatron and LHC colliders. This provides another reason to establish experimental limits on the CP asymmetry in $B^{\pm} \to J/\psi\, K^{\pm}$.

If some mechanism causes direct CP violation to occur in $B^{\pm} \to J/\psi\, K^{\pm}$ decays, then the same mechanism could generate a CP asymmetry in the $B^{\pm} \to \psi(2S)\, K^{\pm}$ mode. Final state strong interactions, however, could be quite different for $J/\psi\, K$ and $\psi(2S)\, K$ states; we therefore measured CP-violating charge asymmetries separately for $B^{\pm} \to J/\psi\, K^{\pm}$ and $B^{\pm} \to \psi(2S)\, K^{\pm}$ decay modes.

[1] The CP asymmetry is proportional to the sine of the relative weak phase.

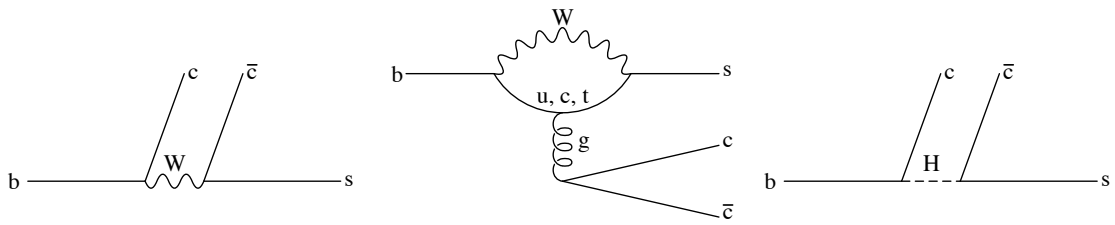

Figure 8.1: Standard Model tree (left) and penguin (middle) diagrams for the $b \to c\bar{c}s$ transition. The right plot shows the New Physics charged-Higgs mediated diagram.

8.3 Analysis summary and results

8.3.1 Selection of $B^{\pm}$ candidates and charge asymmetry measurement

For this measurement we used 9.2 fb^{-1} of e^+e^- data taken at the $\Upsilon(4S)$ resonance and 4.6 fb^{-1} taken 60 MeV below the $\Upsilon(4S)$ resonance. In $\Upsilon(4S)$ decays B^+ mesons are born only in pairs with B^- mesons, therefore B^+ and B^- mesons are produced in equal numbers.

The J/ψ mesons were detected through their dilepton decays; for $\psi(2S)$ reconstruction we used both $\psi(2S) \to \ell^+\ell^-$ and $\psi(2S) \to J/\psi\pi^+\pi^-$ decay modes. We required the normalized $\mu^+\mu^-$ mass to be from -4 to 3 for $J/\psi \to \mu^+\mu^-$ candidates (Figure 2.16) and from -3 to 3 for $\psi(2S) \to \mu^+\mu^-$. We required the normalized $e^+(\gamma)e^-(\gamma)$ mass to be from -10 to 3 for $J/\psi \to e^+e^-$ candidates (Figure 2.16) and from -3 to 3 for $\psi(2S) \to e^+e^-$. For each $\psi^{(\prime)} \to \ell^+\ell^-$ candidate, we performed a fit constraining its mass to the world average value. We selected the $\psi(2S) \to J/\psi\,\pi^+\pi^-$ candidates by requiring the absolute value of the normalized $J/\psi\,\pi^+\pi^-$ mass to be less than 3 and by requiring the $\pi^+\pi^-$ invariant mass to be greater than 400 MeV/c^2. The average $J/\psi\,\pi^+\pi^-$ mass resolution is approximately 3 MeV/c^2. To avoid soft-pion combinatorics, we selected a single $\psi(2S) \to J/\psi\pi^+\pi^-$ candidate in a given event based on the smallest absolute value of the $J/\psi\pi^+\pi^-$ normalized mass. For each $\psi(2S) \to J/\psi\,\pi^+\pi^-$ candidate, we performed a fit constraining its mass to the world average value. Well-measured tracks consistent with originating at the e^+e^- interaction point were selected as the $K^{\pm}$ candidates. In order avoid any additional charge-correlated systematic bias in the $K^{\pm}$ selection, we did not impose any particle identification requirements on the $K^{\pm}$ candidates. Very rarely, when $\mu^{\pm}$ and $K^{\pm}$ tracks are swapped, we reconstruct $B^{\pm} \to J/\psi K^{\pm}$, $J/\psi \to \mu^+\mu^-$ as $B^{\pm} \to \psi(2S)K^{\pm}$. We therefore veto a $B^{\pm} \to \psi(2S)K^{\pm}$ candidate if it is reconstructed from the same physical tracks as a $B^{\pm} \to J/\psi K^{\pm}$ candidate.

To select $B^{\pm} \to J/\psi\, K^{\pm}$ and $B^{\pm} \to \psi(2S)\, K^{\pm}$ candidates, we required $|\Delta E|/\sigma(\Delta E) < 3$ and $|M(B) - M_B|/\sigma(M) < 3$. The average resolution in ΔE is 10 MeV (8 MeV) for the $B^{\pm} \to J/\psi\, K^{\pm}$ ($B^{\pm} \to \psi(2S)\, K^{\pm}$) candidates. The resolution in $M(B)$ for the $B^{\pm} \to \psi^{(\prime)}\, K^{\pm}$ candidates is 2.7 MeV/c^2 and is dominated by the beam energy spread. The $M(B)$ distributions for the $B^{\pm} \to J/\psi\, K^{\pm}$ and $B^{\pm} \to \psi(2S)\, K^{\pm}$ candidates passing the $|\Delta E|/\sigma(\Delta E) < 3$ requirement are shown in Figure 8.2.

The CP-violating charge asymmetry in $B^{\pm} \to J/\psi\, K^{\pm}$ decays is defined as a

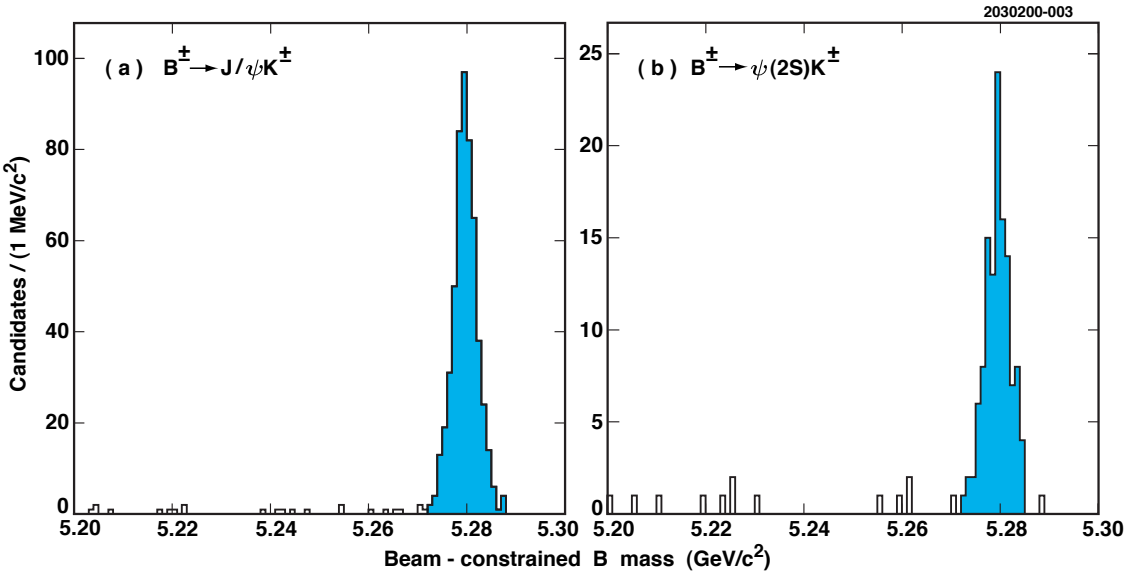

Figure 8.2: Beam-constrained B mass distribution for (a) $B^\pm \to J/\psi\, K^\pm$ and (b) $B^\pm \to \psi(2S)\, K^\pm$ candidates passing the $|\Delta E|/\sigma(\Delta E) < 3$ requirement. The shaded parts of the histograms represent the 534 $B^\pm \to J/\psi\, K^\pm$ and 120 $B^\pm \to \psi(2S)\, K^\pm$ candidates that pass the $|M(B) - M_B|/\sigma(M) < 3$ requirement.

branching fraction asymmetry

$$\mathcal{A}_{CP} \equiv \frac{\mathcal{B}(B^- \to J/\psi\, K^-) - \mathcal{B}(B^+ \to J/\psi\, K^+)}{\mathcal{B}(B^- \to J/\psi\, K^-) + \mathcal{B}(B^+ \to J/\psi\, K^+)}\,.$$

In this definition we adopted the sign convention from [114]. The same definition is used for $B^\pm \to \psi(2S)\, K^\pm$ mode.

Table 8.1 lists signal yields together with observed charge asymmetries. More details the selection of the $B^\pm$ signal candidates can be found in Section 8.4.1; several cross-checks of the selection procedure are described in Section 8.4.2.

Table 8.1: Number of selected candidates, the observed charge asymmetry, and the corrected asymmetry ($\mathcal{A}_{CP}$). The first uncertainty on $\mathcal{A}_{CP}$ is statistical, the second one is systematic.

Mode	$N(B^\pm)$	$N(B^-)$	$N(B^+)$	$\frac{N(B^-)-N(B^+)}{N(B^-)+N(B^+)}$	$\mathcal{A}_{CP}$
$B^\pm \to J/\psi\, K^\pm$	534	271	263	$(+1.5 \pm 4.3)\%$	$(+1.8 \pm 4.3 \pm 0.4)\%$
$B^\pm \to \psi(2S)\, K^\pm$	120	61	59	$(+1.7 \pm 9.1)\%$	$(+2.0 \pm 9.1 \pm 1.0)\%$

8.3.2 Bias corrections and systematic uncertainties

Background. — From fits to the beam-constrained mass distributions (Figure 8.2), we estimated the combinatorial background to be $3.5^{+2.8}_{-1.7}$ ($1.7^{+2.0}_{-1.0}$) events for $B^\pm \to J/\psi\, K^\pm$ ($B^\pm \to \psi(2S)\, K^\pm$) mode. The background from $B^\pm \to \psi^{(\prime)}\, \pi^\pm$ decays must be added

because $B^\pm \to \psi^{(\prime)}\, \pi^\pm$ candidates contribute to the beam-constrained mass peaks. Using simulated events, we estimated the background from $B^\pm \to \psi^{(\prime)}\, \pi^\pm$ decays to be 1.5 ± 0.5 events for $B^\pm \to J/\psi\, K^\pm$ and 0.1 event for $B^\pm \to \psi(2S)\, K^\pm$ mode. We assumed the branching ratio of $\mathcal{B}(B^\pm \to J/\psi\, \pi^\pm)/\mathcal{B}(B^\pm \to J/\psi\, K^\pm) = (5.1 \pm 1.4)\%$ [48]; the same value was assumed for $B^\pm \to \psi(2S)\, \pi^\pm$ decays. Total background is therefore estimated to be 5^{+3}_{-2} events for $B^\pm \to J/\psi\, K^\pm$ and 2^{+2}_{-1} events for $B^\pm \to \psi(2S)\, K^\pm$ mode. As a check, we used samples of simulated events together with the data collected below the $B\overline{B}$ production threshold and estimated total background to be 3.3 ± 0.8 events for $B^\pm \to J/\psi\, K^\pm$ and 3.7 ± 0.9 events for $B^\pm \to \psi(2S)\, K^\pm$ mode. We verified that the simulation accurately reproduced the rate and distribution of candidates in the data in the ΔE vs. $M(B)$ plane near, but not including, the signal region. More details on the background estimation can be found in Sections 8.4.3 and 8.4.4. Backgrounds are expected to be CP-symmetric. We measured the charge asymmetry for the candidates in the sideband regions of the ΔE and $M(B)$ distributions to be $(+2.2 \pm 4.1)\%$ for $B^\pm \to J/\psi\, K^\pm$ and $(-1.2 \pm 6.4)\%$ for $B^\pm \to \psi(2S)\, K^\pm$. We also verified that our final result does not critically depend on the assumption of zero CP asymmetry for background events (Section 8.4.5). We assumed that the number of background events entering our sample follows a Poisson distribution with a mean of 5 events for $B^\pm \to J/\psi\, K^\pm$ and 4 events for $B^\pm \to \psi(2S)\, K^\pm$ mode. We also assumed that the CP-violating charge asymmetry for the background is +30%. Using Monte Carlo techniques, we found that background with such properties introduces a +0.3% (+1.0%) bias in our $\mathcal{A}_{CP}$ measurement for the $B^\pm \to J/\psi\, K^\pm$ ($B^\pm \to \psi(2S)\, K^\pm$) mode. We assigned a systematic uncertainty on $\mathcal{A}_{CP}$ of 0.3% for $B^\pm \to J/\psi\, K^\pm$ and 1.0% for $B^\pm \to \psi(2S)\, K^\pm$.

Difference in K^+ vs. K^- detection efficiencies. — The flavor of the B meson is tagged by the charged kaon; therefore, we searched for charge-correlated systematic bias associated with the $K^\pm$ detection and its momentum measurement. The cross sections for nuclear interactions are larger for negative than for positive kaons from $B^\pm \to \psi^{(\prime)}\, K^\pm$ decays. We used two methods to evaluate the difference in K^+ vs. K^- detection efficiencies. In the first method, we performed[2] an analytic calculation of the expected asymmetry, combining the data on the nuclear interaction cross sections for K^+ and K^- mesons [48] with the known composition of the CLEO detector material. In the second method, we used the GEANT-based simulation of the CLEO detector response, processing the simulated events in a similar manner as the data. Both methods are in excellent agreement that the K^+ reconstruction efficiency is approximately 0.6% higher than the K^- reconstruction efficiency. The corresponding charge-correlated detection efficiency asymmetry is therefore -0.3%. We applied a +0.3% correction to the measured values of $\mathcal{A}_{CP}$ both for $B^\pm \to J/\psi\, K^\pm$ and for $B^\pm \to \psi(2S)\, K^\pm$ modes. We assigned 100% of the correction as a systematic uncertainty. More details can be found in Section 8.4.7.

Charge asymmetry for inclusive tracks. — For this study we selected inclusive tracks satisfying the same track quality criteria as were used for the $K^\pm$ candidates in the $B^\pm \to \psi^{(\prime)}\, K^\pm$ reconstruction. The kaon momentum in the laboratory frame is between 1.2 and 1.4 GeV/c for the $B^\pm \to \psi(2S)\, K^\pm$ mode and between 1.55 and 1.85 GeV/c for the $B^\pm \to J/\psi\, K^\pm$ mode. We have found more positive than negative tracks in these

[2] We thank Tony Hill for providing us with the results of his study.

two momentum ranges. For all tracks with momentum between 1.2 and 1.4 GeV/c, we have observed a charge asymmetry of $(N^- - N^+)/(N^- + N^+) = (-0.23 \pm 0.03)\%$; the corresponding number for tracks with momentum between 1.55 and 1.85 GeV/c is $(-0.17 \pm 0.04)\%$. The sign and the magnitude of the observed asymmetry are accounted for by the expected differences in K^+ vs. K^- and p vs. $\overline{p}$ detection efficiencies: slightly more K^- and $\overline{p}$ undergo nuclear interactions compared to K^+ and p. More details can be found in Section 8.4.8. Collisions of particles with the nuclei in the detector material occasionally result in recoil protons, but almost never in recoil antiprotons. To fake a K^+ candidate, a recoil proton must have a momentum of at least 1.2 GeV/c and its track should be consistent with originating at the e^+e^- interaction point. The possible random combinations of a J/ψ and a recoil proton would be accounted for in our background estimation. If a recoil proton results from an interaction of a $K^\pm$ from the signal $B^\pm \to \psi^{(\prime)}K^\pm$ decay, then the possible bias caused by these protons would be accounted for in our study of the high-statistics samples of simulated $K^\pm$ interactions described in the previous paragraph and Section 8.4.7. Besides increasing our confidence that the track reconstruction procedure does not introduce significant charge-correlated bias, the measurement of charge asymmetry for inclusive tracks in data also confirms that the number of recoil protons entering the pool of K^+ candidates is negligible even before the reconstruction of the full $B^\pm \to \psi^{(\prime)}\, K^\pm$ decay chain.

Bias in K^+ vs. K^- momentum measurement. — This bias will separate the $\Delta E \equiv E(B^\pm) - E_{\rm beam}$ peaks for B^+ and B^- candidates so that the requirement on ΔE can manifest a preference for the B candidates of a certain sign. We measured the difference in mean ΔE for the B^+ and B^- candidates to be 0.6 ± 0.8 MeV. This result is consistent with zero and very small compared to the approximately ± 30 MeV window used in the ΔE requirement. We also used high-momentum muon tracks from $e^+e^- \to \mu^+\mu^-$ events (Appendix C) as well as samples of D^0 and $D^\pm_{(s)}$ meson decays [114] to put stringent limits on possible charge-correlated bias in the momentum measurement. We conclude that the bias in K^+ vs. K^- momentum reconstruction is negligible for our CP-violation measurement. More details can be found in Section 8.4.9.

8.3.3 Results

In conclusion, we have measured the CP-violating charge asymmetry to be $(+1.8 \pm 4.3[\text{stat}] \pm 0.4[\text{syst}])\%$ for $B^\pm \to J/\psi\, K^\pm$ and $(+2.0 \pm 9.1[\text{stat}] \pm 1.0[\text{syst}])\%$ for $B^\pm \to \psi(2S)\, K^\pm$. These values of $\mathcal{A}_{CP}$ include a $+0.3\%$ correction due to a slightly higher reconstruction efficiency for the positive kaons. Apart from being yet another failed attempt to rock the Standard Model boat, this measurement provides the first experimental test of the assumption that direct CP violation is negligible in $B \to \psi^{(\prime)}\, K$ decays.

8.4 More details on the analysis

8.4.1 Selection of $B^\pm \to J/\psi\, K^\pm$ and $B^\pm \to \psi(2S)\, K^\pm$ candidates

The distributions of the normalized ΔE vs. normalized $M(B)$ for $B^\pm \to J/\psi K^\pm$ and $B^\pm \to \psi(2S)K^\pm$ candidates are shown in Figure 8.3. We multiplied the reported ΔE uncertainties by a scale factor of 1.1 to make the normalized ΔE distribution look more

like a unit Gaussian for the simulated signal events. There are 534 (120) candidates in the signal box for $B^{\pm} \to J/\psi K^{\pm}$ ($B^{\pm} \to \psi(2S)K^{\pm}$) mode. One can count approximately 20 $B^{\pm} \to J/\psi\pi^{\pm}$ candidates above the signal box in Figure 8.3(left). All $B^{\pm} \to J/\psi K^{\pm}$ and $B^{\pm} \to \psi(2S)K^{\pm}$ signal candidates come from different events, even though we did not attempt to select a single candidate in a given event.

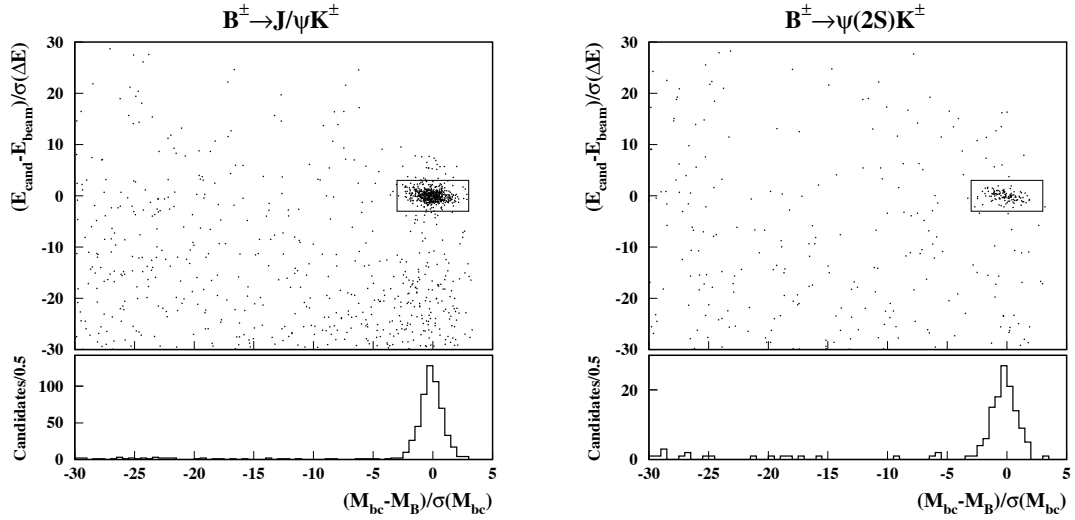

Figure 8.3: Normalized ΔE vs. normalized $M(B)$ for $B^{\pm} \to J/\psi K^{\pm}$ (left) and $B^{\pm} \to \psi(2S)K^{\pm}$ (right) candidates in data. There are 534 (120) candidates in the signal box for the $B^{\pm} \to J/\psi K^{\pm}$ ($B^{\pm} \to \psi(2S)K^{\pm}$) mode. The lower parts of the plots show the normalized beam-constrained mass distributions for the candidates passing the 3σ cut on normalized ΔE.

8.4.2 Cross-checks for signal candidate selection

To normalize or not to normalize?

In the real analysis we selected $B^{\pm} \to \psi^{(\prime)}K^{\pm}$ signal candidates using normalized $M(B)$ and ΔE variables. As a cross-check, we selected signal candidates using unnormalized $M(B)$ and ΔE. We applied the following selection criteria, approximately corresponding to 3σ signal box in ΔE vs. $M(B)$ plane, as determined from simulation: $|M(B) - M_B| <$ 8.1 MeV, $|\Delta E| < 30$ MeV for $J/\psi K^{\pm}$ and $|\Delta E| < 24$ MeV for $\psi(2S)K^{\pm}$. The results are listed in Table 8.2. The quoted statistical uncertainty in the shift of the measured $\mathcal{A}_{CP}$ was obtained using toy Monte Carlo simulation. We did not assign any systematic uncertainty.

Table 8.2: Number of selected candidates and the observed charge asymmetry for the case when we select $B^{\pm}$ candidates using unnormalized ΔE and $M(B)$ variables.

Mode	$N(B^{\pm})$	$N(B^{-})$	$N(B^{+})$	shift in $\mathcal{A}_{CP}$
$J/\psi K^{\pm}$	523 (515 common)	262	261	$(-1.3 \pm 1.0[\text{stat}])\%$
$\psi(2S)K^{\pm}$	121 (120 common)	61	60	negligible

Particle identification for charged kaons

In the real analysis we did not apply any particle identification requirements to charged kaons. As a cross-check, we required that all $K^{\pm}$ candidates have good dE/dx information, and that the dE/dx measurements lie within 3 standard deviations of the values expected for kaons. These cuts removed 8 out of 526 $B^{\pm} \to J/\psi K^{\pm}$ signal candidates; all 120 $B^{\pm} \to \psi(2S)K^{\pm}$ pass these kaon particle identification cuts. The results are listed in Table 8.3. The quoted statistical uncertainty in the shift of the measured $\mathcal{A}_{CP}$ was obtained using toy Monte Carlo simulation. We did not assign any systematic uncertainty.

Table 8.3: Number of selected candidates and the observed charge asymmetry for the case when we particle identification requirements are applied to charged kaons.

Mode	$N(B^{\pm})$	$N(B^{-})$	$N(B^{+})$	shift in $\mathcal{A}_{CP}$
$J/\psi K^{\pm}$	526(−8)	268(−3)	258(−5)	$(+0.4 \pm 0.5[\text{stat}])\%$
$\psi(2S)K^{\pm}$	120 (no change)	59	61	no shift

8.4.3 Background estimation from Monte Carlo simulation and off-$\Upsilon(4S)$ data

In this section we estimate backgrounds using samples of simulated events and off-$\Upsilon(4S)$ data. Table 8.4 lists various background contributions and total background estimates.

Table 8.4: Estimated backgrounds for $B^{\pm} \to J/\psi K^{\pm}$ and $B^{\pm} \to \psi(2S)K^{\pm}$ candidates. Uncertainties in the total number of background events include 20% systematic uncertainty assigned from our consistency checks described below.

Background source	$B^{\pm} \to J/\psi K^{\pm}$	$B^{\pm} \to \psi(2S)K^{\pm}$
Continuum	0.49 ± 0.15	0.66 ± 0.15
$B^{\pm} \to \psi^{(\prime)}\pi^{\pm}$	1.51 ± 0.45	0.08
The rest of $B\overline{B}$	1.26 ± 0.19	$2.94^{+0.54}_{-0.33}$
Total background	3.3 ± 0.8	3.7 ± 0.9

Background from continuum events

Continuum background was estimated from off-$\Upsilon(4S)$ data and "5 times the on-$\Upsilon(4S)$ data" sample of simulated generic continuum events. Continuum background is very low. In order to get more statistics for continuum background evaluation, we relaxed

$J/\psi \to \ell^+\ell^-$ and $\psi(2S) \to \ell^+\ell^-$ mass requirements. We required the absolute value of the normalized $\psi^{(\prime)}$ mass to be less than 20 both for $\psi^{(\prime)} \to e^+e^-$ and for $\psi^{(\prime)} \to \mu^+\mu^-$ modes. The continuum background is estimated to be 0.49 ± 0.15 events for $B^\pm \to J/\psi K^\pm$ and 0.66 ± 0.15 events for $B^\pm \to \psi(2S)K^\pm$.

Background from $B^\pm \to \psi^{(\prime)}\pi^\pm$ decays

The branching fraction $\mathcal{B}(B^\pm \to \psi(2S)\pi^\pm)$ has yet to be measured, therefore we assumed $\frac{\mathcal{B}(B^\pm \to \psi(2S)\pi^\pm)}{\mathcal{B}(B^\pm \to \psi(2S)K^\pm)} = \frac{\mathcal{B}(B^\pm \to J/\psi\pi^\pm)}{\mathcal{B}(B^\pm \to J/\psi K^\pm)} = (5.1 \pm 1.4)\%$ [48]. The distributions of the normalized ΔE for the simulated $B^\pm \to \psi^{(\prime)}K^\pm$ and $B^\pm \to \psi^{(\prime)}\pi^\pm$ events are shown in Figure 8.4. Softer $K^\pm/\pi^\pm$ track makes for better separation of ΔE peaks for $B^\pm \to \psi(2S)K^\pm/\pi^\pm$ modes. Using high-statistics samples of simulated $B^\pm \to J/\psi\pi^\pm$ and $B^\pm \to \psi(2S)\pi^\pm$ events, we estimated the background from $B^\pm \to J/\psi\pi^\pm$ decays to be 1.51 ± 0.45 events, where quoted error reflects the branching ratio uncertainty. The background from $B^\pm \to \psi(2S)\pi^\pm$ decays is estimated to be 0.08 events.

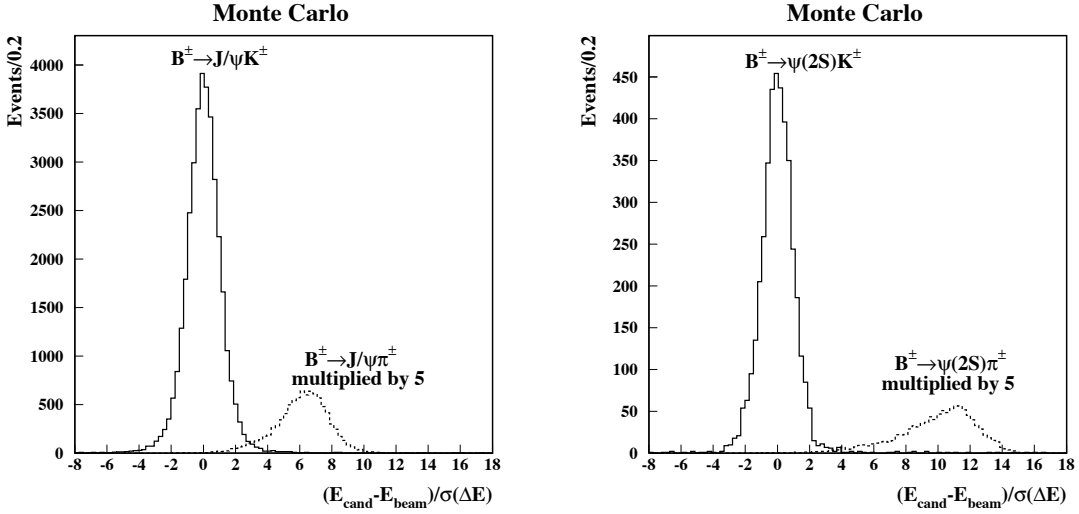

Figure 8.4: Normalized ΔE distributions for $B^\pm \to \psi^{(\prime)}K^\pm/\pi^\pm$ decays reconstructed as $B^\pm \to \psi^{(\prime)}K^\pm$. A 3σ cut on normalized beam-constrained mass has been imposed. We assumed $\mathcal{B}(B^\pm \to \psi(2S)\pi^\pm)/\mathcal{B}(B^\pm \to \psi(2S)K^\pm) = \mathcal{B}(B^\pm \to J/\psi\pi^\pm)/\mathcal{B}(B^\pm \to J/\psi K^\pm) = 5\%$ [48].

$B \to J/\psi\rho$ background

The background from $B \to J/\psi\rho$ was found to be negligible (Section 5.4.3).

Background from the rest of $B\overline{B}$ events

To study the background from generic $B\overline{B}$ decays, we used a high-statistics sample of simulated generic $B\overline{B}$ events corresponding to "35 times the data". The $B\overline{B}$ background is estimated to be 1.26 ± 0.19 events for $B^\pm \to J/\psi K^\pm$ and $2.94^{+0.54}_{-0.33}$ events for $B^\pm \to \psi(2S)K^\pm$. These values do not include contributions from $B^\pm \to \psi^{(\prime)}\pi^\pm$ decays.

Consistency checks for background estimation procedure

We verified the quality of our background estimation procedure by predicting the number of events in 3 control regions of the ΔE vs. $M(B)$ plots shown in Figure 8.3. The 3 control regions are defined in Section 6.4.5. The results for $B^\pm \to J/\psi K^\pm$ and $B^\pm \to \psi(2S)K^\pm$ modes are listed in Table 8.5. Based on this study, we assigned 20% systematic uncertainty in the estimated number of background events both for $B^\pm \to J/\psi K^\pm$ and for $B^\pm \to \psi(2S)K^\pm$ mode.

Table 8.5: Quality control of the background estimation. We predict and compare with data the number of events in 3 control regions of the ΔE vs. $M(B)$ plots shown in Figure 8.3.

Source	Region 1	Region 2	Region 3
	$B^\pm \to J/\psi K^\pm$		
Continuum	92 ± 2	87 ± 2	5.5 ± 0.5
$B^\pm \to J/\psi\pi^\pm$	27 ± 8	1 ± 0.3	26 ± 8
$B^\pm \to J/\psi K^\pm$	30 ± 1	14 ± 1	16 ± 1
the rest of $B\overline{B}$	399 ± 3	238 ± 3	157 ± 2
Total predicted $N^{\rm pred}$	548 ± 9	340 ± 4	205 ± 8
Observed $N^{\rm obs}$	591	400	187
$N^{\rm obs}/N^{\rm pred} - 1$	$(+8 \pm 5)\%$	$(+18 \pm 6)\%$	$(-9 \pm 8)\%$
	$B^\pm \to \psi(2S)K^\pm$		
Continuum	59 ± 1	53 ± 1	5.2 ± 0.4
$B^\pm \to \psi(2S)\pi^\pm$	7 ± 2	0.5 ± 0.1	6 ± 2
$B^\pm \to \psi(2S)K^\pm$	19 ± 2	13 ± 1	6 ± 1
the rest of $B\overline{B}$	166 ± 5	130 ± 4	35 ± 2
Total predicted $N^{\rm pred}$	251 ± 6	197 ± 4	52 ± 3
Observed $N^{\rm obs}$	245	204	40
$N^{\rm obs}/N^{\rm pred} - 1$	$(-2 \pm 7)\%$	$(+4 \pm 8)\%$	$(-23 \pm 13)\%$

8.4.4 Background estimation from fits to $M(B)$ distributions

We performed an independent background estimation from the fits to beam-constrained mass distributions (Figure 8.5). Signal was fit with a Gaussian shape determined from simulation. The background was fit with ARGUS shape [83] $f(x) \propto x \cdot \sqrt{1-x^2} \cdot e^{\lambda(1-x^2)}$, where $x = M(B)/E_{beam}$; the parameter λ was allowed to float. We determined the background for $B^\pm \to J/\psi\, K^\pm$ ($B^\pm \to \psi(2S)\, K^\pm$) mode to be $3.5^{+2.8}_{-1.7}$ ($1.7^{+2.0}_{-1.0}$) events. Background from $B^\pm \to \psi^{(\prime)}\, \pi^\pm$ decays (Section 8.4.3) must be added because $B^\pm \to \psi^{(\prime)}\, \pi^\pm$

candidates contribute to the beam-constrained mass peak. Therefore total background for $B^{\pm} \to J/\psi\, K^{\pm}$ ($B^{\pm} \to \psi(2S)\, K^{\pm}$) is estimated to be $5.0^{+3.2}_{-1.8}$ ($1.8^{+2.0}_{-1.0}$) events.

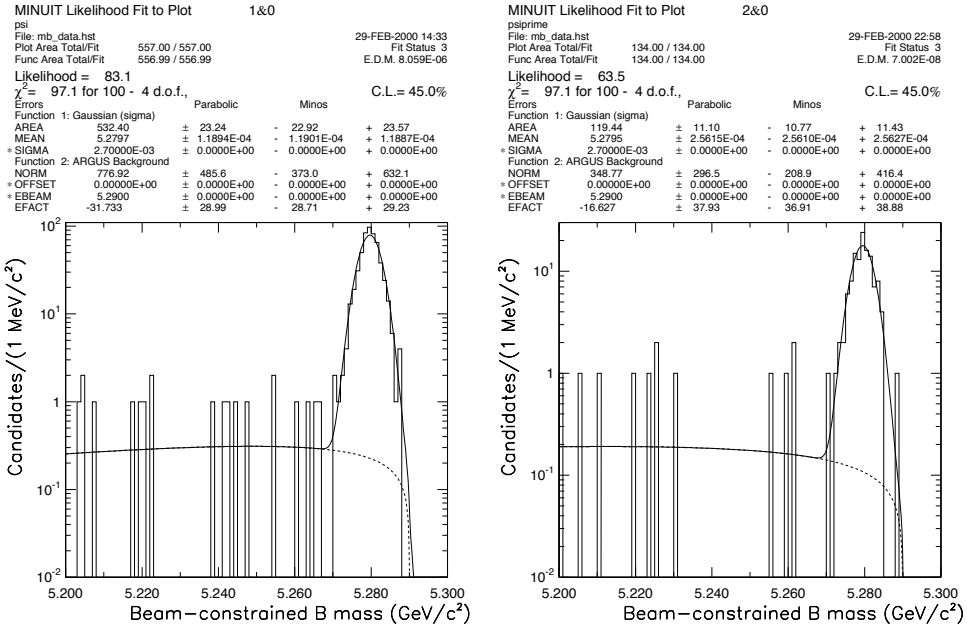

Figure 8.5: Fits to beam-constrained mass distribution for $B^{\pm} \to J/\psi\, K^{\pm}$ (left) and $B^{\pm} \to \psi(2S)\, K^{\pm}$ (right) candidates.

8.4.5 Systematic uncertainty associated with background

We expect the background to be CP-symmetric. To support this prejudice, we measured the charge asymmetries for the candidates in the sideband regions of the ΔE vs. $M(B)$ distributions shown in Figure 8.3. Table 8.6 lists event yields outside the signal regions in Figure 8.3 together with associated charge asymmetries.

Table 8.6: Event yields outside the signal regions in Figure 8.3 together with associated charge asymmetries.

Mode	$N^{\pm}$	N^{-}	N^{+}	$\frac{N^- - N^+}{N^- + N^+}$
$J/\psi\, K^{\pm}$	591	302	289	$(+2.2 \pm 4.1)\%$
$\psi(2S)\, K^{\pm}$	245	121	124	$(-1.2 \pm 6.4)\%$

To show that the final result does not critically depend on the assumption that background is CP-symmetric, we studied what would happen if we make an outrageous assumption that the background has an intrinsic CP asymmetry of +30%. We generated toy Monte Carlo experiments with the following assumptions:

- Total number of signal+background events is 534 for $B^{\pm} \to J/\psi K^{\pm}$ and 120 for $B^{\pm} \to \psi(2S) K^{\pm}$.

- Number of background events follows Poisson distribution with the mean of 5 for $B^{\pm} \to J/\psi K^{\pm}$ and 4 for $B^{\pm} \to \psi(2S) K^{\pm}$ mode.
- Signal is CP-symmetric.
- Background has an intrinsic CP asymmetry of +30%.

CP asymmetry distributions for 100,000 toy Monte Carlo experiments are shown in Figure 8.6. The 30% CP-asymmetric background introduces a 0.3% (1.0%) bias in $\mathcal{A}_{CP}$ measurement for $B^{\pm} \to J/\psi\, K^{\pm}$ ($B^{\pm} \to \psi(2S)\, K^{\pm}$) mode.

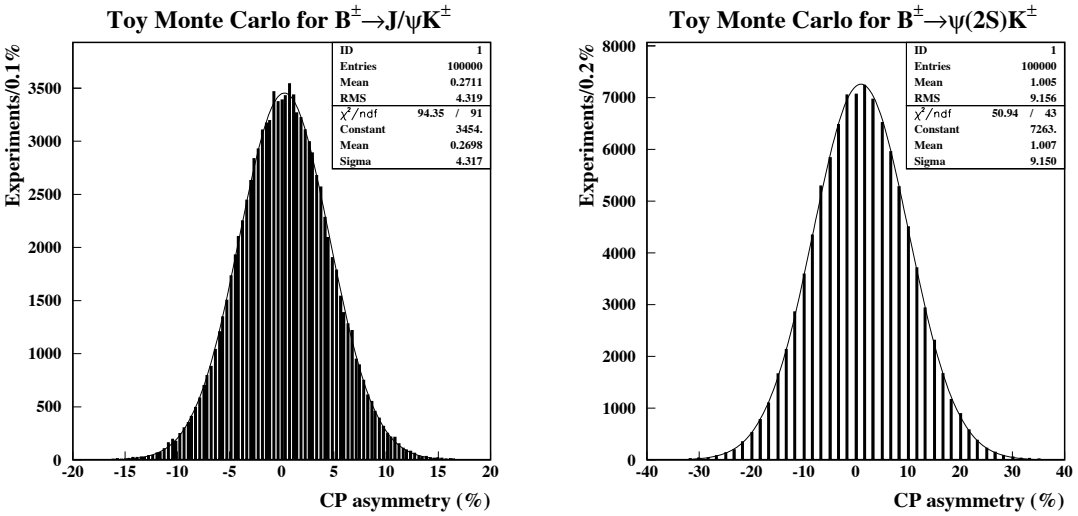

Figure 8.6: CP asymmetry in each of 100,000 toy Monte Carlo experiments generated to probe the bias in $\mathcal{A}_{CP}$ measurement due to the presence of background with an intrinsic CP asymmetry of +30%. The left plot is for $B^{\pm} \to J/\psi K^{\pm}$, whereas the right plot is for $B^{\pm} \to \psi(2S) K^{\pm}$ mode.

As a systematic uncertainty in $\mathcal{A}_{CP}$ measurement we assigned 0.3% for $B^{\pm} \to J/\psi\, K^{\pm}$ and 1.0% for $B^{\pm} \to \psi(2S)\, K^{\pm}$ mode.

8.4.6 Overview of charge-correlated systematic effects

We only need to study the charge-correlated systematic bias of the CLEO detector response for the kaons with momentum ranging from 1.2 GeV/c to 1.9 GeV/c (Figure 8.7-left). Note that in our analysis we did not impose any particle identification requirements (dE/dx, time-of-flight, lepton veto) on charged kaon candidates. That makes for an easier systematic uncertainty study. Two excellent studies of the charge-correlated systematic effects have recently been performed for the CP-violation searches in rare B meson decays [114] and in charm decays [115].

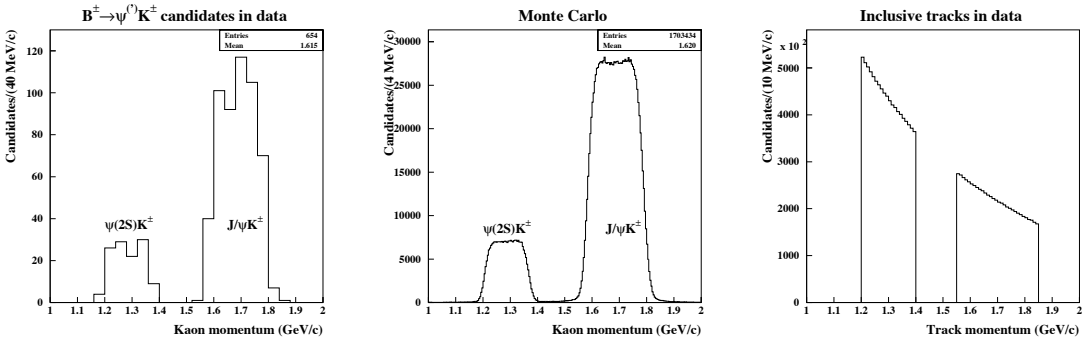

Figure 8.7: Left plot shows the momentum of the kaons for 534 $B^{\pm} \to J/\psi K^{\pm}$ and 120 $B^{\pm} \to \psi(2S)K^{\pm}$ signal candidates in data. Middle plot shows the momentum of the tracks in the high-statistics sample of simulated $B^{\pm} \to \psi^{(\prime)}K^{\pm}$ events described in Section 8.4.7. Right plot shows the momentum distribution of the inclusive tracks selected from data and used in the check described in Section 8.4.8.

8.4.7 Expected difference in K^+ vs. K^- detection efficiencies

Pen-and-paper calculation

This calculation was performed by Tony Hill (see [115]). The cross sections of nuclear interactions are quite different for the positive and negative kaons from $B^{\pm} \to \psi^{(\prime)}K^{\pm}$ decays (Figure 8.8). The momentum dependence of the expected reconstruction

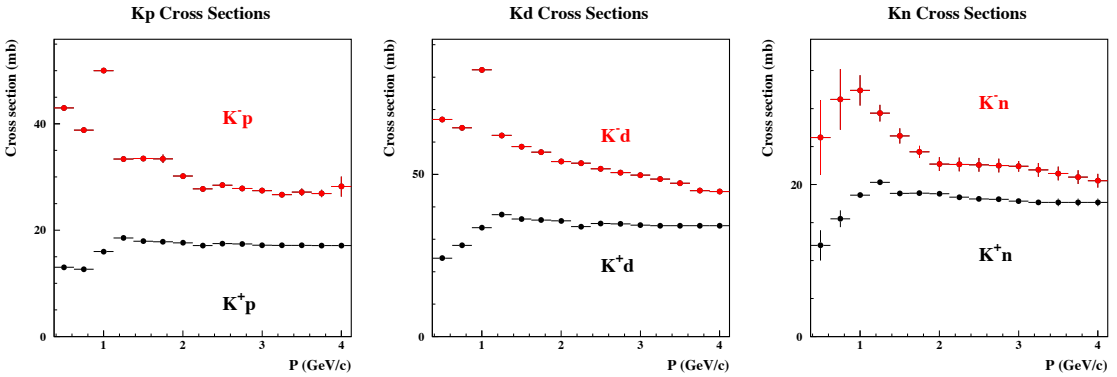

Figure 8.8: Total cross sections for $K^{\pm}\{\text{proton, deuteron, neutron}\}$ collisions as a function of incident kaon momentum. The data were provided by Particle Data Group.

efficiency asymmetry is shown in Figure 8.9. The cross section data were provided by Particle Data Group [47]. The composition of CLEO II.V detector material was obtained from published papers and private communications with detector experts; no `CLEOG` detector description information was used. The tracks were assumed to traverse the detector at $\theta = 45^{\circ}$ with respect to the beam axis. The layers of material accounted for in this calculation include beam pipe, silicon detector, intermediate drift chamber (`VD`), and up to the 4th layer

of the main drift chamber (DR): if the nuclear interaction happened inside this cylindrical volume, then the track is unlikely to be found. The calculations were performed for three values of the the proton to neutron ratio Z/N in the inner detector material:

1. Real CLEO II.V inner detector ($Z/N \approx 1$). True Z/N values were used for the layers of material traversed by the tracks.
2. $N/Z = 0$ – inner detector made of protons.
3. $Z/N = 0$ – inner detector made of neutrons.

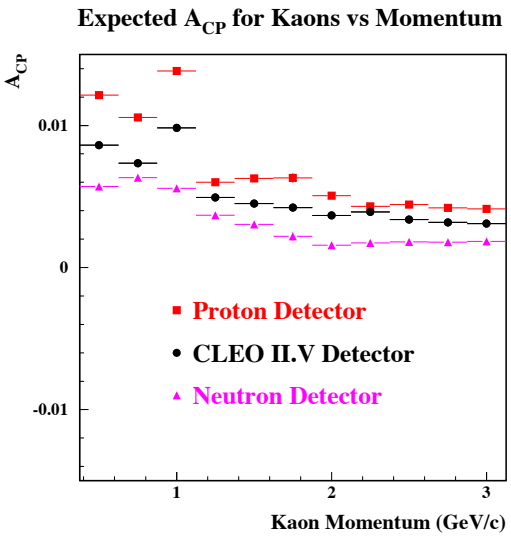

Figure 8.9: Expected charged-correlated detection efficiency asymmetry for $K^{\pm}$. Shown are the results of the analytic calculations performed for the three values of the proton to neutron ratio in the detector material. In this calculation $\mathcal{A}_{CP}$ is positive if reconstruction efficiency is higher for K^+ than for K^- mesons.

Note that the value of the calculated charged-correlated detection efficiency asymmetry is linearly dependent on the amount of material. In CLEO II we had approximately 30% less material inside DR compared to CLEO II.V detector configuration (Figure 5.10).

Detection asymmetry predicted by CLEO Monte Carlo simulation

We have produced approximately 1 million 2-track CLEOG simulated events: $\Upsilon(4S) \to B^+B^-$ events were generated, then we forced the decays $B^{\pm} \to \psi^{(\prime)} K^{\pm}$, $\psi^{(\prime)} \to \nu\nu$. Therefore, one K^+ and one K^- are the only "visible" particles produced in each event. We selected the reconstructed tracks satisfying the same track-quality requirements as were imposed on the $K^{\pm}$ tracks in the analysis. The momentum spectrum of the selected tracks is shown in Figure 8.7-middle.

To compare the Monte Carlo simulation prediction with the results of calculations presented in Figure 8.9, we take only CLEO II.V simulated events and count all the selected tracks with the momenta ranging from 1.1 GeV/c to 1.9 GeV/c. We obtain: $\frac{N^+ - N^-}{N^+ + N^-} = \frac{565{,}501 - 560{,}880}{565{,}501 + 560{,}880} = (0.41 \pm 0.09)\%$, which is in excellent agreement with the calculations performed by Dr. Hill (Figure 8.9). Letting in CLEO II simulated events, we obtain $\frac{N^+ - N^-}{N^+ + N^-} = \frac{853{,}521 - 847{,}558}{853{,}521 + 847{,}558} = (0.35 \pm 0.08)\%$. We checked that this result is stable if we vary track momentum cuts, require that the tracks are tagged as true kaons, or require that at most 2 good-quality tracks are reconstructed in each event. These cross-checks confirm that the sample of reconstructed tracks does not contain a significant number of recoil protons produced by the kaons from the signal decays. Also, these recoil protons would increase the charge-correlated detection asymmetry, so that the value measured in the Monte Carlo simulation would no longer agree with the value obtained in the pen-and-paper calculation.

To make sure that the reconstruction of the full $B^{\pm} \to \psi^{(\prime)} K^{\pm}$ decay chain does not introduce any additional charge-correlated bias, we have also generated 1.4×10^6 simulated B^+B^- events where one of the B mesons decays into neutrinos (to save computer time), while the other B mesons decays into $\psi^{(\prime)} K^{\pm}$ final state. In this Monte Carlo sample we reconstructed 578,898 $B^{\pm} \to \psi^{(\prime)} K^{\pm}$ candidates and determined the charge-correlated detection asymmetry value to be in line with expectations: $\frac{N(B^+ \to \psi^{(\prime)} K^+) - N(B^- \to \psi^{(\prime)} K^-)}{N(B^+ \to \psi^{(\prime)} K^+) + N(B^- \to \psi^{(\prime)} K^-)} = \frac{290{,}382 - 288{,}516}{290{,}382 + 288{,}516} = (0.32 \pm 0.13)\%$.

8.4.8 Charge asymmetry for inclusive tracks in data

We used all the CLEO II and CLEO II.V on-resonance hadronic events passing the same event selection requirements as used in $B^{\pm} \to \psi^{(\prime)} K^{\pm}$ reconstruction. In these events we selected the tracks satisfying the same track quality requirements as were imposed on $K^{\pm}$ tracks in the $B^{\pm} \to \psi^{(\prime)} K^{\pm}$ reconstruction. The momenta of the tracks were restricted to the following two ranges (Figure 8.7-right): 1.20 GeV/c $< |p| <$ 1.40 GeV/c and 1.55 GeV/c $< |p| <$ 1.85 GeV/c. The results of the track counting are listed in Table 8.7.

Table 8.7: Comparison of number of positive and negative tracks found in on-resonance hadronic events.

Momentum range	$N^{\pm}$	N^+	N^-	$\frac{N^+ - N^-}{N^+ + N^-}$
1.20$< \|p\| <$ 1.40 GeV/c	8,753,542	4,386,764	4,366,778	$(2.28 \pm 0.34) \cdot 10^{-3}$
1.55$< |p| <$1.85 GeV/c	6,549,635	3,280,340	3,269,295	$(1.69 \pm 0.39) \cdot 10^{-3}$

Can we make sense of the sign and the magnitude the observed 0.2% charge asymmetry? The Monte Carlo simulation predicts the following composition of the inclusive track sample used in the study: 61% of $\pi^{\pm}$, 23% of $K^{\pm}$, 5% of p or $\overline{p}$, 6% of $\mu^{\pm}$, and 5% of $e^{\pm}$. If the inner detector is composed of an equal number of protons and neutrons, then, by virtue of isospin symmetry, the detection efficiency should not depend on the pion's charge. Dr. Hill's calculations [115] (similar to those for kaons in Section 8.4.7) indeed predict a negligible (even at 0.1% level) charge asymmetry for pions. The asymmetry for leptons should also be negligible (note that no particle identification requirements were imposed). The expected asymmetry for kaons is approximately 0.4% (Figure 8.9): detection efficiency

is higher for K^+. Using Hill's method described in Section 8.4.7, we also calculated the expected asymmetry for p vs. $\overline{p}$ detection to be approximately 2.5%: detection efficiency is higher for p. We obtain the following expected value of the asymmetry for inclusive tracks $0.4\% \times 0.23(K^{\pm}) + 2.5\% \times 0.05(p^{\pm}) \approx 0.2\%$, which is in agreement with the measured value. There does not seem to be much room for additional asymmetry from recoil protons.

8.4.9 Bias in K^+ vs. K^- momentum measurement.

This bias will move apart the ΔE peaks for B^+ and B^- candidates, and therefore the ΔE cut can manifest a preference for the B candidates of a certain sign.

Limit from a study of $D_{(s)}$ decays

In [114] a high-statistics sample of $D_{(s)}$ mesons was used to study charge-correlated systematics in the momentum measurement for the tracks with the momenta ranging from 2 GeV/c to 3 GeV/c. No statistically significant bias was observed, and a conservative upper limit on a systematic charge-correlated momentum shift was derived: $|p^+ - p^-| < 0.4$ MeV/c. The ΔE resolution for $B^{\pm} \to \psi^{(\prime)} K^{\pm}$ candidates is approximately 10 MeV/c, and we select all the candidates inside a $\pm 3\sigma$ window. Therefore $\mathcal{O}(0.1$ MeV/$c)$ charge-correlated bias in the momentum measurement should not be a problem for our analysis.

Measurement of ΔE peak positions for B^+ and B^- candidates in data

We have also measured the separation of the ΔE peaks for B^+ and B^- candidates directly in data. We used an unbinned likelihood fit procedure analogous to the one employed for the B mass measurement (Chapter 5). There are 2 inputs in our fit:

1. $(\Delta E)_i$ – the measured value of ΔE for a particular $B^{\pm} \to \psi^{(\prime)} K^{\pm}$ candidate
2. σ_i – the reported uncertainty on the ΔE measurement for a particular $B^{\pm} \to \psi^{(\prime)} K^{\pm}$ candidate. Note that we have already scaled up the reported error by a factor of 1.1 to make $\Delta E/\sigma(\Delta E)$ distribution closer to a unit Gaussian for the simulated signal events: $\sigma(\Delta E) = 1.1 \cdot \sigma_{\Delta E}^{\text{reported}}$.

There are 2 outputs in our fit:

1. $\overline{\Delta E}$ – the mean value of ΔE;
2. S – the global scale factor multiplying $\sigma(\Delta E)$.

The likelihood function to maximize is the product of PDF's for all the selected signal candidates:

$$\mathcal{L}(\overline{\Delta E}; S) = \prod_i \frac{G((\Delta E)_i - \overline{\Delta E} | S\sigma_i)}{\int_{-3\sigma_i}^{+3\sigma_i} G(\Delta E - \overline{\Delta E} | S\sigma_i) d(\Delta E)}, \tag{8.1}$$

where $G(x|\sigma) \equiv 1/(\sqrt{2\pi}\sigma) \exp(-x^2/2\sigma^2)$.

First, we performed a fit using all 654 $B^{\pm} \to \psi^{(\prime)} K^{\pm}$ candidates, then we fitted the B^+ and B^- subsamples separately. The results of the fits are listed in Table 8.8. From Table 8.8 we obtain:

Table 8.8: Results of the unbinned likelihood fit to ΔE distribution.

	Number of candidates	$\overline{\Delta E}$ returned by fit	S returned by fit
$B^{\pm} \to \psi^{(\prime)} K^{\pm}$	654	-0.16 ± 0.38 MeV	1.004 ± 0.030
$B^{+} \to \psi^{(\prime)} K^{+}$	322	$+0.16 \pm 0.54$ MeV	1.000 ± 0.042
$B^{-} \to \psi^{(\prime)} K^{-}$	332	-0.46 ± 0.53 MeV	1.006 ± 0.042

- The separation of the means of the ΔE peaks for the B^+ and B^- candidates is consistent with zero: $\chi^2/dof = \left[\left(\frac{0.16+0.16}{0.54}\right)^2 + \left(\frac{-0.46+0.16}{0.53}\right)^2\right]/2 = 0.67/2$. In any case, any possible charge-correlated difference in ΔE peak position is tiny compared to the ΔE cut window ($\approx \pm 30$ MeV)
- The widths of the ΔE peaks for the B^+ and B^- candidates are the same.

Limit from a study of $e^+e^- \to \mu^+\mu^-$ events

In Appendix C we presented a study of the charge-correlated bias in the momentum measurement using $e^+e^- \to \mu^+\mu^-$ events. In this study we probed the difference of the reconstructed transverse momenta of μ^+ and μ^- tracks ($p_t^+ - p_t^-$); this study tells us about the average false curvature in the CLEO detector. We also probed the dependence of the measured sum of the μ^+ and μ^- momenta ($p^+ + p^-$) on the ϕ and θ angle of the μ^+ track; this study tells us about false curvature which depends on ϕ and θ of the track. As a check, we repeated our $B^{\pm} \to \psi^{(\prime)} K^{\pm}$ candidate selection changing the measured $K^{\pm}$ momenta according to the following four expressions derived from the study of the $e^+e^- \to \mu^+\mu^-$ events:

1. $p^{K^{\pm}}_{new} = p^{K^{\pm}}_{old} \cdot (1 \mp p^{K^{\pm}}_{t,old} \cdot 1.4 \cdot 10^{-4} (\mathrm{GeV}/c)^{-1})$
2. $p^{K^{\pm}}_{new} = p^{K^{\pm}}_{old} \cdot (1 \mp \frac{p^{K^{\pm}}_{old}}{5.3\ \mathrm{GeV}} \cdot \frac{0.03\ \mathrm{GeV}}{10.6\ \mathrm{GeV}} \cdot \sin\phi)$
3. $p^{K^{\pm}}_{new} = p^{K^{\pm}}_{old} \cdot (1 \mp \frac{p^{K^{\pm}}_{old}}{5.3\ \mathrm{GeV}} \cdot \frac{0.03\ \mathrm{GeV}}{10.6\ \mathrm{GeV}} \cdot \cos\phi)$
4. $p^{K^{\pm}}_{new} = p^{K^{\pm}}_{old} \cdot (1 \pm \frac{p^{K^{\pm}}_{old}}{5.3\ \mathrm{GeV}} \cdot \frac{0.015\ \mathrm{GeV}}{10.6\ \mathrm{GeV}} \cdot \frac{\cos\theta}{0.8})$.

In the worst case, we lost two (one of each sign) out of 654 $B^{\pm} \to \psi^{(\prime)} K^{\pm}$ signal candidates. We conclude that the charge-correlated bias in the momentum measurement is negligible for our analysis.

Appendix A

π^0 study for $B \to \chi_{c1,2}X$ analysis

In Chapter 3 we determine χ_{c1} and χ_{c2} yields in the fits to $M(J/\psi\gamma) - M(J/\psi)$ distributions (Figure 3.1). The χ_{c1} and χ_{c2} signal shapes are obtained from the Monte Carlo simulation (Figure 3.4), therefore we rely on accurate simulation of the calorimeter response. We have studied π^0's in the data and the simulation to estimate the systematic uncertainties associated with the χ_{c1} and χ_{c2} signal shapes. We select isolated photon showers using the same cuts as were used to select the photons in $\chi_{c1,2} \to J/\psi\gamma$ reconstruction. The energy of the showers is further restricted to be between 300 and 600 MeV corresponding to the energy range for photons from $\chi_{c1,2} \to J/\psi\gamma$ decays. We use all CLEO II and CLEO II.V on- and off-$\Upsilon(4S)$ data as well as a sample of simulated generic continuum events. We checked that the energy spectra of the photons which we select in the data and the Monte Carlo samples are in excellent agreement. The resulting π^0 mass distributions are shown in Figure A.1.

A.1 Mean of π^0 mass peak

To extract the π^0 mass lineshape from the simulation, we fit the distribution in Figure A.1 (top right) with a 4th order Chebyshev polynomial. We exclude the peak region from the fit, then subtract the background, and smooth the resulting histogram in `MN_FIT`. We fit the π^0 mass distribution in data (Figure A.1-top left) using a 4th order Chebyshev polynomial as a background shape and the template extracted from the simulation as a signal shape. The horizontal offset of the π^0 mass template extracted from the simulation is allowed to float in the fit. We determine that the π^0 mass peak is shifted by -0.2 MeV/c^2 in the data with respect to the simulation (see also bottom plot in Figure A.1). We also perform the fits breaking data into 26 individual datasets (4S2-4ST). As an example, the fit to 4SL data is shown in Figure A.2. The resulting shifts of the π^0 mass peak in the data with respect to the simulation are plotted in Figure A.3 (left). Weighting the datasets by the π^0 yield, we obtain the RMS spread of the shifts to be 0.46 MeV/c^2. A 0.2 MeV/c^2 shift of the π^0 mass peak corresponds, on average, to a 0.6 MeV shift in the energy of each photon.

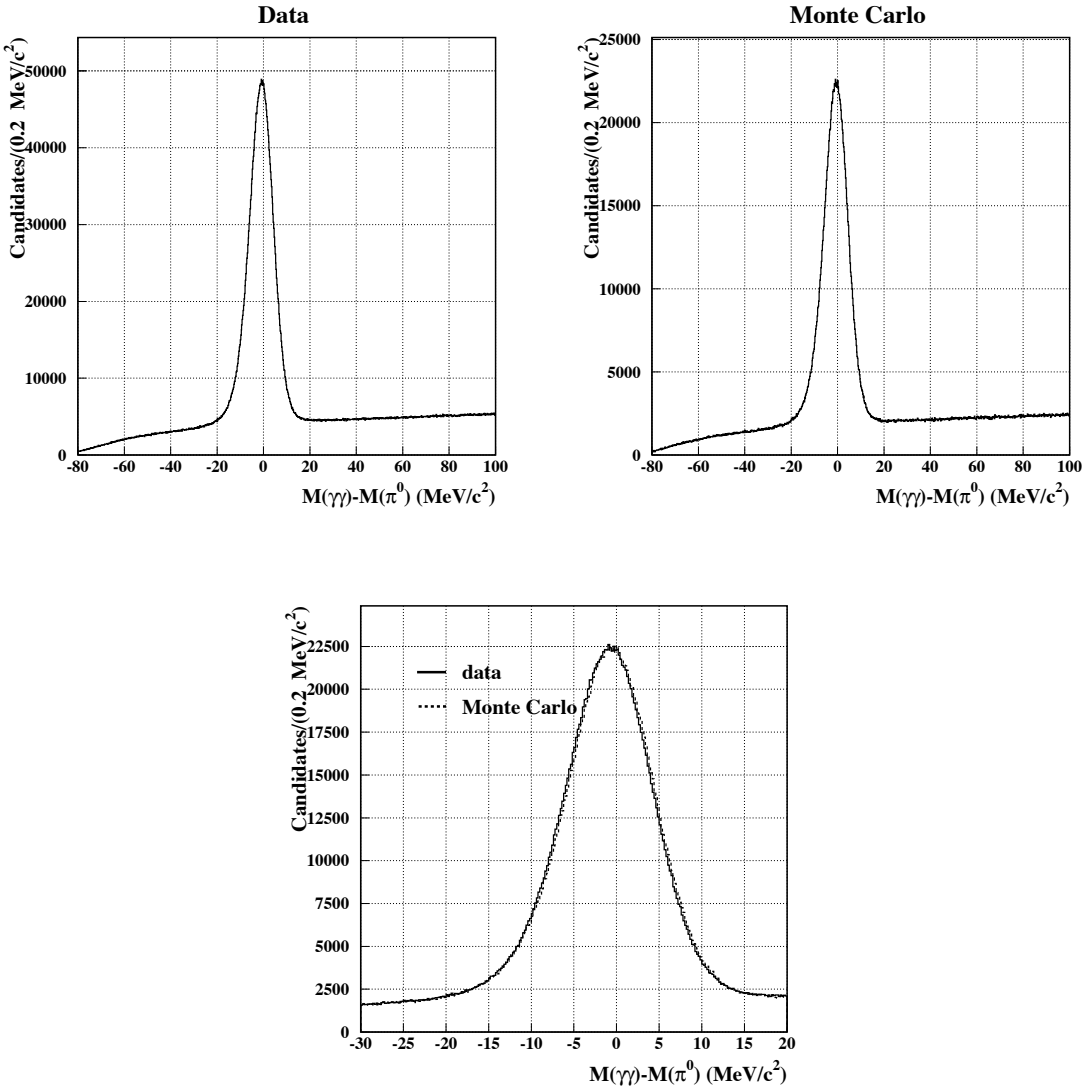

Figure A.1: The $M(\gamma\gamma) - M(\pi^0)$ distributions for the inclusive π^0 candidates used in the study. Both photon showers are required to be in good barrel region and have an energy between 300 and 600 MeV. Top left plot is for the data, top right one is for the simulation. Bottom plot shows overlay of the distributions in the data and the simulation with the histograms normalized to the same area.

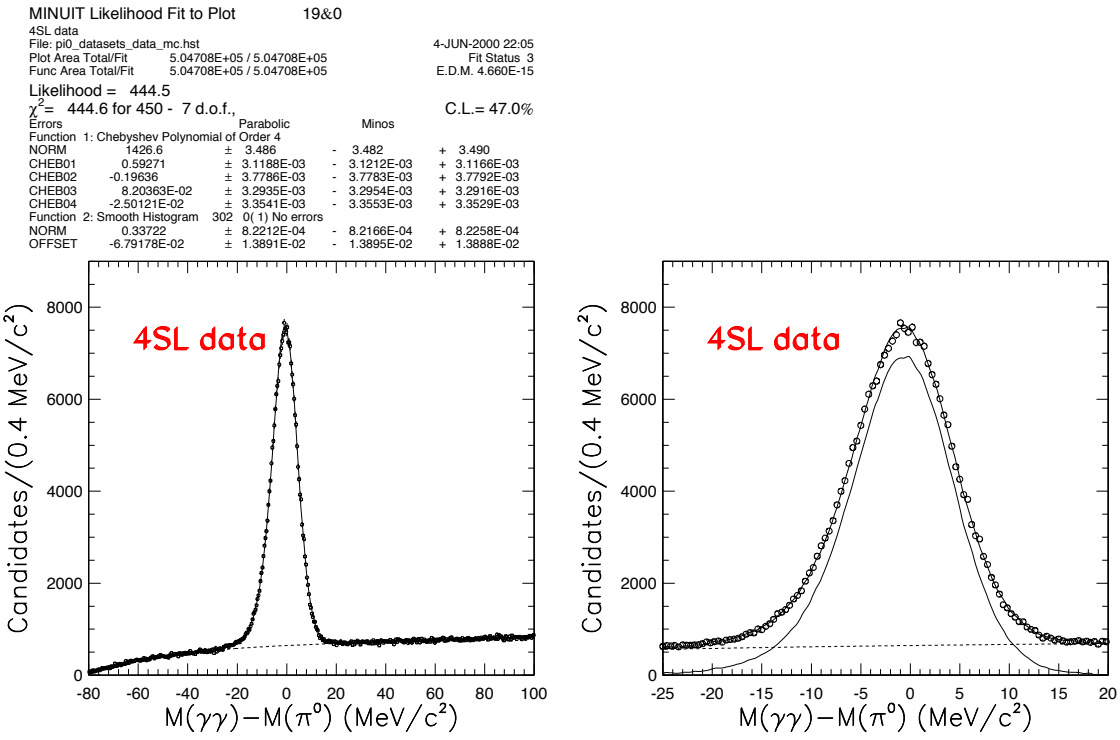

Figure A.2: The fit to $M(\gamma\gamma) - M(\pi^0)$ distributions for 4SL dataset. A polynomial is used to fit background, whereas the template histogram extracted from the simulation is used for signal. Both photon showers are required to be in the good barrel region of the calorimeter and have an energy between 300 and 600 MeV.

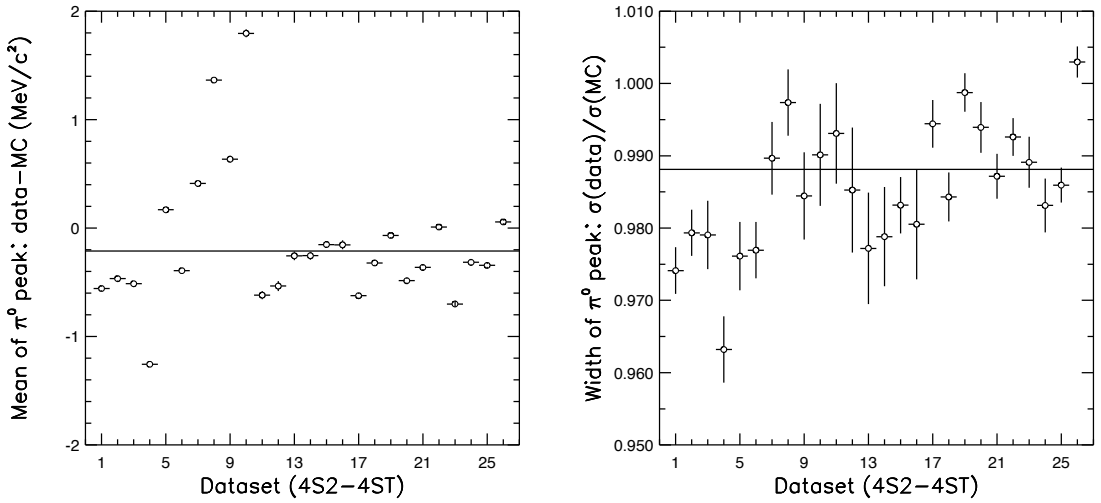

Figure A.3: Variation of π^0 mass peak mean (left) and width (right) over the individual datasets (4S2-4ST). The average for all the datasets combined is represented by a horizontal line.

A.2 Width of π^0 mass peak

To study the π^0 mass resolution, we use a Crystal Ball function as a signal shape. Crystal Ball function is a "Gaussian with low-side tail", defined as:

$$f(M|A,M^*,\sigma,\alpha,n) = \begin{cases} A \cdot exp\left(-\frac{M_d^2}{2\sigma^2}\right) & \text{if } \mathrm{M_d} \geq -\alpha\sigma, \\ A \cdot \frac{exp(-\alpha^2/2)}{\left(1-\frac{\alpha}{n}\frac{M_d}{\sigma}-\frac{\alpha^2}{n}\right)^n} & \text{if } \mathrm{M_d} < -\alpha\sigma, \end{cases} \tag{A.1}$$

where $M_d \equiv M - M^*$, $M \equiv M(\gamma\gamma)$, M^* is the mass peak value. Parameters α and N are fixed form the fit to the simulated event samples, whereas mean and σ are allowed to float. The resulting shifts of the π^0 mass peak in the data with respect to the simulation are identical to the shifts obtained in the fits to the template extracted from the simulation. The π^0 peak in the simulation is on average 1% wider than in the data. The distribution of the relative peak width vs. the dataset is shown in Figure A.3 (right). RMS spread of the width ratio over the datasets is 0.9%.

The π^0 mass resolution $\sigma_{\rm tot}$ for the π^0 candidates used in this study can be separated into angular part $\sigma_{\rm ang}$ and energy part $\sigma_{\rm E}$ as $\sigma_{\rm tot} = \sqrt{\sigma_{\rm ang}^2 + \sigma_{\rm E}^2}$, where $\sigma_{\rm ang} = 0.86\sigma_{\rm tot}$ and $\sigma_{\rm E} = 0.51\sigma_{\rm tot}$. To increase the π^0 mass peak width by 1%, one has to degrade the the photon energy resolution by 4%.

Appendix B

Position of $J/\psi \to \ell^+\ell^-$ mass peaks: data vs. Monte Carlo simulation

This study was performed as a part of the B meson mass measurement (Chapter 5). We used a sample of inclusive $J/\psi \to \ell^+\ell^-$ decays reconstructed from all CLEO II and CLEO II.V $\Upsilon(4S)$ data. The momentum spectrum of the muons from inclusive J/ψ decays is shown in Figure B.1.

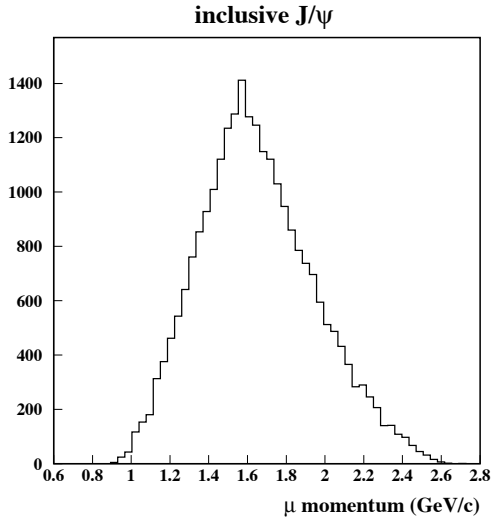

Figure B.1: Reconstructed momentum of the J/ψ daughter muons for inclusive J/ψ's in the sample of simulated generic $B\overline{B}$ events.

We fitted $M(\mu^+\mu^-) - M_{J/\psi}$ and $M(e^+(\gamma)e^-(\gamma)) - M_{J/\psi}$ distributions in the region from -0.650 GeV/c^2 to $+0.200$ GeV/c^2. We also fitted normalized mass distributions $[M(\mu^+\mu^-) - M_{J/\psi}]/\sigma(M)$ and $[M(e^+(\gamma)e^-(\gamma)) - M_{J/\psi}]/\sigma(M)$ in the region from -55 to $+20$. As a background shape we used 2nd order Chebyshev polynomial. As signal shape templates we used histograms extracted from a high-statistics sample of simulated $J/\psi \to$

$\ell^+\ell^-$ events generated with the J/ψ mass of 3096.88 MeV/c^2 [47]. The normalization as well as the x coordinate of the signal template were floated in the fit. The lepton tracks were fit with the pion Kalman hypothesis both in the data and in the Monte Carlo simulation. The statistics of the Monte Carlo sample correspond to "31 times the data".

B.1 $J/\psi \to \mu^+\mu^-$

We checked that the detector response simulation does not introduce systematic bias to the measured position of the $J/\psi \to \mu^+\mu^-$ mass peak. Unlike electrons, muons do not radiate in the detector material. The ionization energy loss by muons should be correctly taken into account by the Billoir fitter. Therefore if we switch off the final state radiation (inner bremsstrahlung) in the $J/\psi \to \mu^+\mu^-$ decay, then we expect the measured $\mu^+\mu^-$ invariant mass to be symmetrically distributed around the nominal J/ψ mass value (Figure 2.8). This is indeed the case, and we measured the mean of the reconstructed $\mu^+\mu^-$ mass peak to be within 0.03 MeV/c^2 from the nominal J/ψ mass regardless of whether the muon or pion Kalman fit hypothesis was used to fit the muon tracks.

The fits to the mass distributions for $J/\psi \to \mu^+\mu^-$ are shown in Figure B.2; the results of these fits are listed in Table B.1. To appreciate how small a 0.5 MeV/c^2 shift of the $J/\psi \to \mu^+\mu^-$ mass peak position is, we note that if the magnetic field value were perfectly known, but the track fitter had not taken into account the ionization energy loss of the muons in the detector material, then the $J/\psi \to \mu^+\mu^-$ peak would be shifted by about -5 MeV/c^2.

Table B.1: Results of the fits comparing $J/\psi \to \mu^+\mu^-$ mass peak positions in the data and the Monte Carlo simulation. The value of the "shift" parameter shows by how much the fit wants to slide the histogram extracted from the simulation to match the data.

	$M(\mu\mu) - M_{J/\psi}$ fit	$[M(\mu\mu) - M_{J/\psi}]/\sigma(M_{\mu\mu})$ fit		
	shift (MeV)	shift ($10^{-2} \cdot \sigma$)	average $\sigma(M_{\mu\mu})$	shift (MeV)
all data	$+0.49 \pm 0.18$	$+5.2 \pm 1.7$	10.5 MeV	$+0.55 \pm 0.18$
CLEO II	$+0.38 \pm 0.34$	$+3.6 \pm 3.0$	12.1 MeV	$+0.44 \pm 0.36$
CLEO II.V	$+0.59 \pm 0.20$	$+6.1 \pm 2.1$	9.7 MeV	$+0.59 \pm 0.20$

B.2 $J/\psi \to e^+e^-$

The fits to the mass distributions for $J/\psi \to e^+e^-$ are shown in Figure B.3; the results of these fits are listed in Table B.2. Note that the exclusion of the right-hand side of the $J/\psi \to e^+e^-$ peak from the fit makes the fit more sensitive to the deficiencies of the Monte Carlo simulation of the radiative tail, thus providing better check for possible shortcomings of `CLEOG` material description.

In order to further increase the sensitivity of the fit to the simulation of the $J/\psi \to e^+e^-$ radiative tail, we got rid of the bremsstrahlung photon addition, i.e. we used only the e^+e^- invariant mass (Figure B.4). The results of the fits are given in Table B.3.

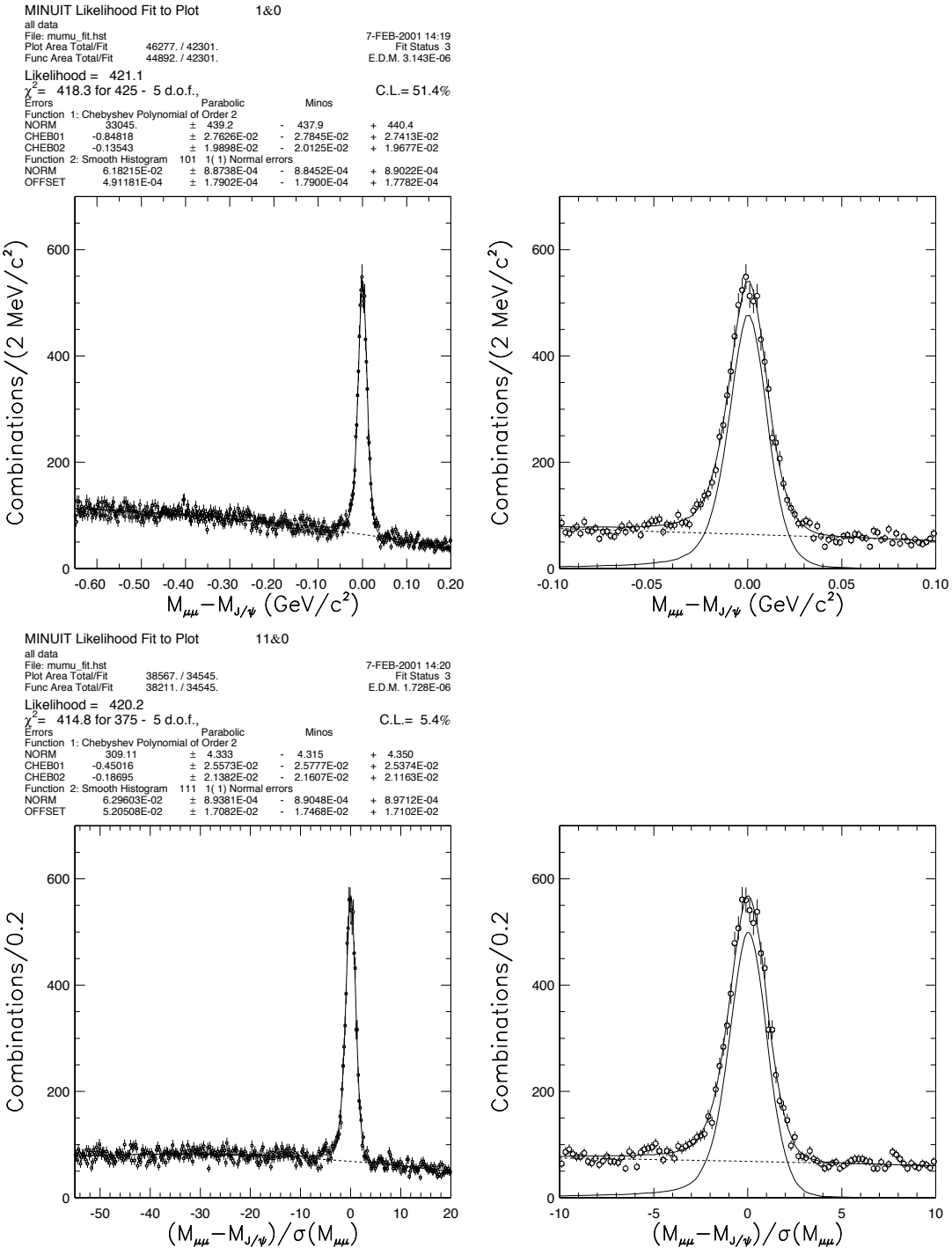

Figure B.2: Fits to $M(\mu^+\mu^-) - M_{J/\psi}$ (top) and $[M(\mu^+\mu^-) - M_{J/\psi}]/\sigma(M)$ (bottom) distributions. Right plots show the close-up of the J/ψ peak region; signal and background fit functions are overlaid.

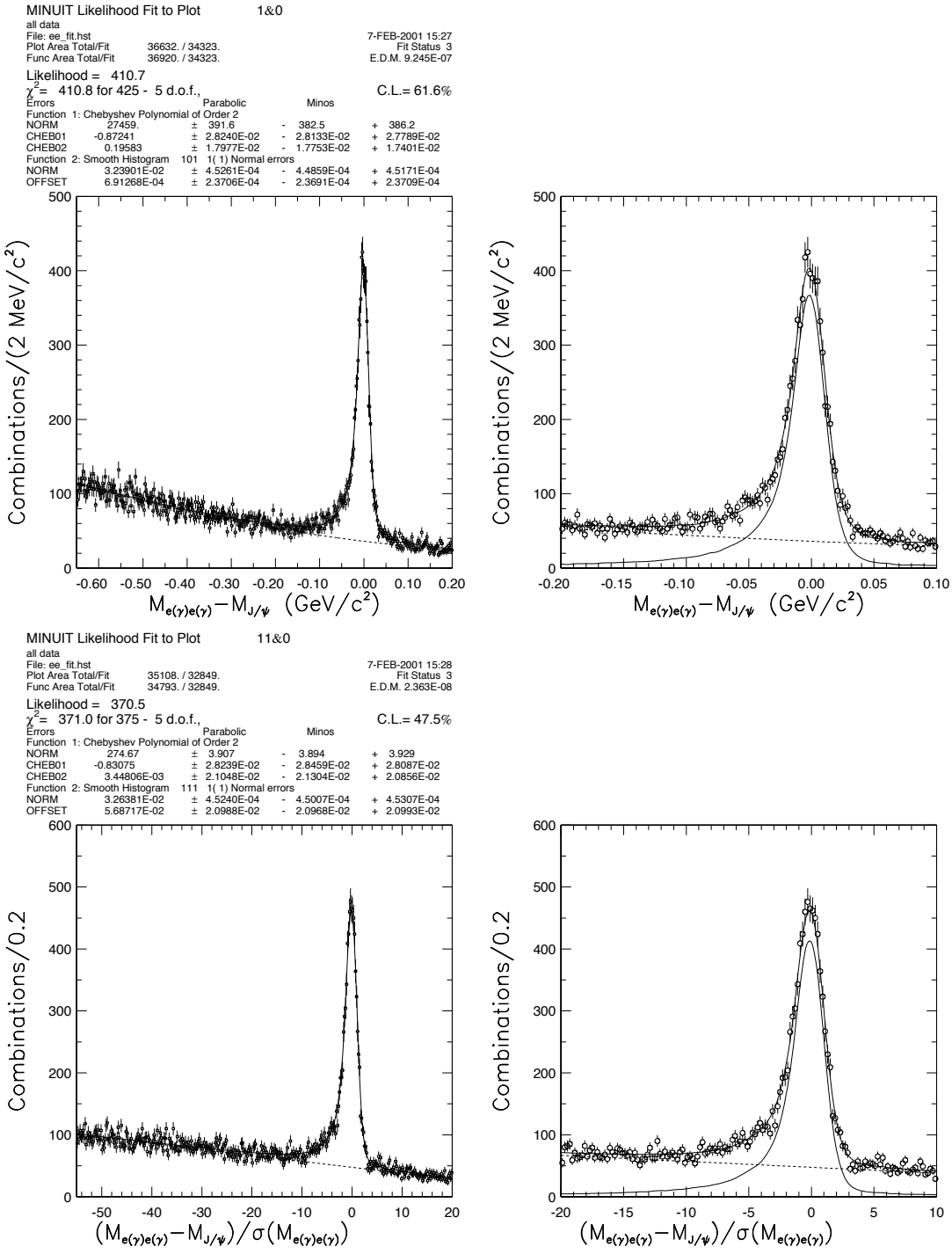

Figure B.3: Fits to $M(e^+e^-) - M_{J/\psi}$ (top) and $[M(e^+(\gamma)e^-(\gamma)) - M_{J/\psi}]/\sigma(M)$ (bottom) distributions. Right plots show the close-up of the J/ψ peak region; signal and background fit functions are overlaid.

Table B.2: Results of the fits comparing $J/\psi \to e^+e^-$ mass peak positions in the data and the Monte Carlo simulation. The value of the "shift" parameter shows by how much the fit wants to slide the histogram extracted from the simulation to match the data.

	$M(e(\gamma)e(\gamma)) - M_{J/\psi}$ fit	$[M(e(\gamma)e(\gamma)) - M_{J/\psi}]/\sigma(M_{e(\gamma)e(\gamma)})$ fit		
	shift (MeV)	shift $(10^{-2}\cdot\sigma)$	average $\sigma(M_{e(\gamma)e(\gamma)})$	shift (MeV)
all data	$+0.69 \pm 0.24$	$+5.7 \pm 2.1$	12.0 MeV	$+0.68 \pm 0.25$
all data	region 0 to 30 MeV excluded from fit $+1.40 \pm 0.67$	region 0 to 3 excluded from fit $+7.8 \pm 5.9$		

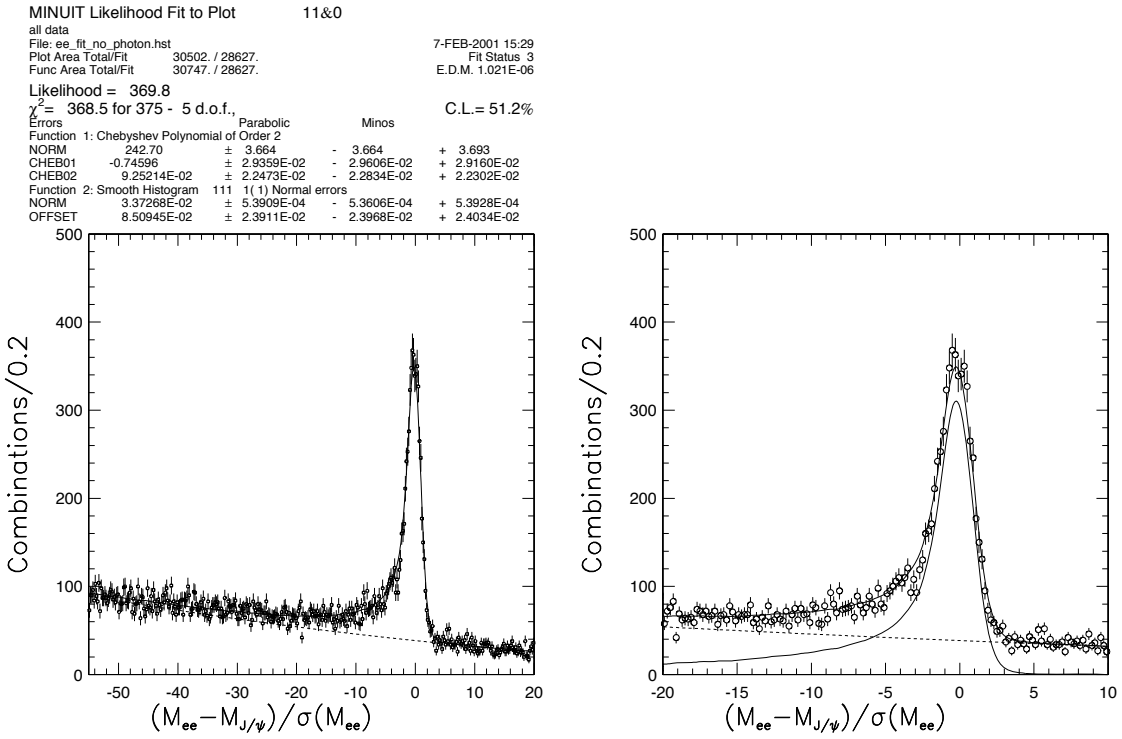

Figure B.4: Fit to $[M(e^+e^-) - M_{J/\psi}]/\sigma(M)$ distribution. Bremsstrahlung photon candidates have not been added. Right plot shows the close-up of the J/ψ peak region; signal and background fit functions are overlaid.

Table B.3: Results of the fits comparing $J/\psi \to e^+e^-$ mass peak positions in the data and the Monte Carlo simulation. The bremsstrahlung photon candidates were not added.

	$M(ee) - M_{J/\psi}$ fit	$[M(ee) - M_{J/\psi}]/\sigma(M_{ee})$ fit
	shift (MeV)	shift $(10^{-2}\cdot\sigma)$
all data	$+1.11 \pm 0.26$	$+8.5 \pm 2.4$
all data	region 0 to 30 MeV excluded from fit $+1.00 \pm 0.72$	region 0 to 3 excluded from fit $+7.3 \pm 6.3$

Appendix C

Study of detector misalignment with $e^+e^- \to \mu^+\mu^-$ events

Because of detector misalignments, the measured curvature of a track can have an offset $CU_{\rm meas.} = CU_{\rm true} + \delta$. For example, the $r-\phi$ rotation of VD with respect to DR will introduce ϕ-independent false curvature. Due to this effect, a non-zero false curvature will be assigned to an infinite-momentum track, and measured momenta will be different for positive and negative tracks of the same true momenta. There could also be a momentum measurement bias which depends on azimuthal and polar angle of the track. One can think of this bias as of false curvature which depends on the angles ϕ and θ of the track.

High momentum tracks have small curvature, and therefore their momentum measurement is most sensitive to the false curvature effect. We probed the magnitude of this effect by comparing reconstructed transverse momenta of positive and negative muon tracks in $e^+e^- \to \mu^+\mu^-$ events. The selected events should be classified as $e^+e^- \to \mu^+\mu^-$, have good bunch matching to reject cosmic muons, have exactly two muon candidates (DPTHMU > 5) of opposite charge; there should not be any unmatched calorimeter showers with an energy higher than 10 MeV. For the data with non-zero beam crossing angle, we calculated muon momenta in the boosted $\Upsilon(4S)$ rest frame using the crossing angle value reported by CESR.

Typical distributions of the difference in reconstructed transverse momenta between positive and negative muons in $e^+e^- \to \mu^+\mu^-$ events are shown in Figure C.1. We fitted these distributions to a double Gaussian with the same mean; the results of the fits for different data sets are listed in Table C.1. The $p_t^+ - p_t^-$ resolution, listed in the 3rd column of Table C.1, was calculated as a weighted average of σ's of the two Gaussians. The right column in Table C.1 lists the value of $< \frac{\delta}{p_t^\mu \cdot CU(\mu)} > = < \frac{1}{(p_t^+ + p_t^-)/2} \cdot \frac{(p_t^+ - p_t^-)}{(p_t^+ + p_t^-)} >$ used in parametrization of the false curvature effect.

We also fitted the sum of muon momenta, taking into account variation in run energy: $(|p(\mu^+)| + |p(\mu^-)| - 2E_{beam})$. We studied the dependence of the peak position on ϕ and θ angles of the μ^+ track. The distributions for the observed variations around the average peak position are shown in Figure C.2. Note that starting with 4SN data set, Pablo Hopman introduced an improved VD alignment procedure, which takes into account beam crossing angle. This procedure significantly reduced the detector misalignment revealed in Figure C.2.

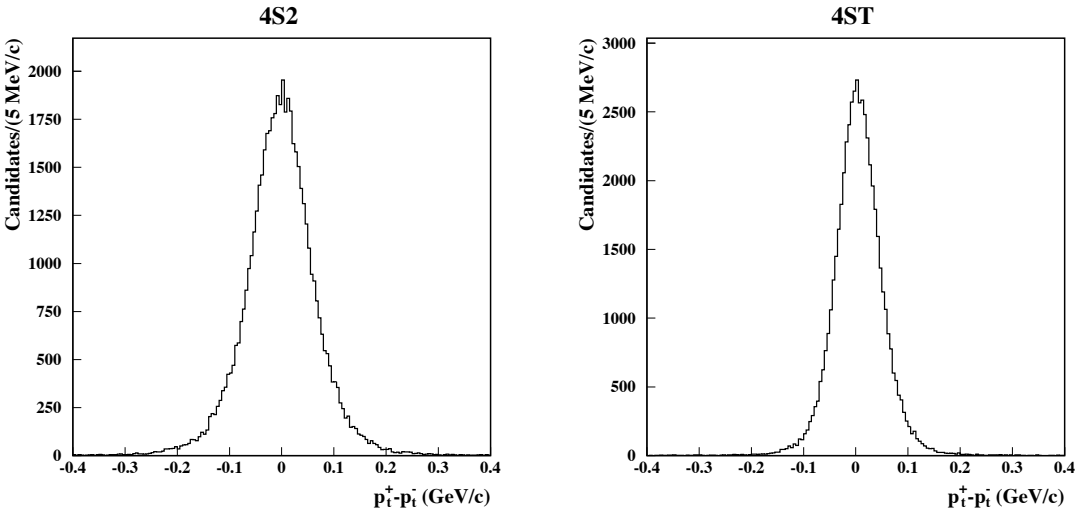

Figure C.1: Difference in reconstructed transverse momenta for positive and negative muons in $e^+e^- \to \mu^+\mu^-$ events. Left plot represents `4S2` data, right plot – `4ST` data.

Table C.1: Results of the fits to $p_t^+ - p_t^-$ and $\frac{1}{(p_t^+ + p_t^-)/2} \cdot \frac{(p_t^+ - p_t^-)}{(p_t^+ + p_t^-)}$ distributions obtained using $e^+e^- \to \mu^+\mu^-$ events in different data sets.

Data set	Number of $\mu^+\mu^-$ events used ($\times 10^3$)	$< \sigma_{\Delta p_t} >$ (MeV/c)	Mean $p_t^+ - p_t^-$ (MeV/c)	Mean $\frac{1}{(p_t^+ + p_t^-)/2} \cdot \frac{(p_t^+ - p_t^-)}{(p_t^+ + p_t^-)}$ $\times 10^{-5}$(GeV/c)$^{-1}$
`4S2`	54	68	-2.1 ± 0.3	-5.8 ± 0.7
`4S3`	19	68	$+1.5 \pm 0.5$	$+3.4 \pm 1.2$
`4S5`	18	60	$+1.5 \pm 0.4$	$+3.4 \pm 1.1$
`4S7`	18	60	0.0 ± 0.4	$+0.9 \pm 1.1$
`4S9`	21	63	$+0.6 \pm 0.4$	$+1.4 \pm 1.0$
`4SC`	16	65	$+5.4 \pm 0.5$	$+13.5 \pm 1.2$
`4SD`	11	63	$+4.1 \pm 0.6$	$+9.3 \pm 1.4$
`4SG`	18	69	$+0.0 \pm 0.5$	-0.3 ± 1.2
`4SJ`	20	48	$+4.9 \pm 0.3$	$+12.2 \pm 0.8$
`4SK`	24	48	$+8.9 \pm 0.3$	$+20.0 \pm 0.7$
`4SN`	37	48	$+5.6 \pm 0.2$	$+13.8 \pm 0.6$
`4SP`	113	46	$+5.0 \pm 0.1$	$+12.4 \pm 0.3$
`4SS`	46	46	$+5.2 \pm 0.2$	$+13.2 \pm 0.5$
`4ST`	54	47	$+4.8 \pm 0.2$	$+12.1 \pm 0.5$

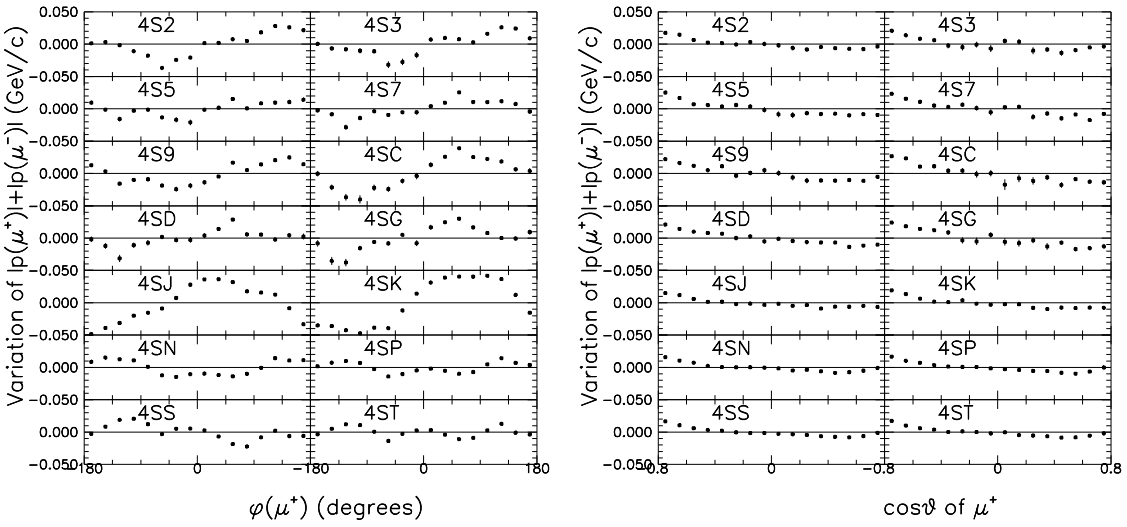

Figure C.2: Variation of the $|p(\mu^+)| + |p(\mu^-)|$ peak position around its average value depending on the azimuth (left plot) and the $\cos\theta$ (right plot) of the μ^+ track.

Appendix D

Study of high-momentum π^0's for $B^0 \to J/\psi\pi^0$ reconstruction

The π^0 momentum distribution in $B^0 \to J/\psi\pi^0$ decays is shown in Figure D.1. We

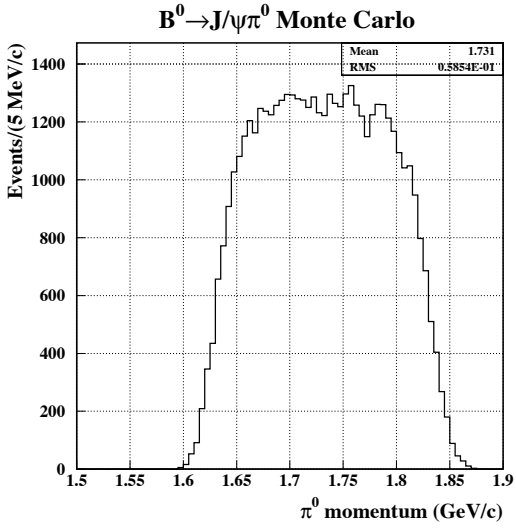

Figure D.1: π^0 laboratory momentum in $B^0 \to J/\psi\pi^0$ decays. The generator-level information is shown.

performed a study of π^0's in the momentum range of interest for this analysis. For this study, we used spherically-looking hadronic events in all CLEO II and CLEO II.V data; on and off-$\Upsilon(4S)$ data were used. We also used a sample of simulated generic continuum events. We selected inclusive π^0's using the same selection criteria as in $B^0 \to J/\psi\pi^0$ analysis. The π^0 momenta were restricted to be from 1.60 to 1.85 GeV/c (Figure D.1). Figure 1.4 shows one quadrant of the CLEO detector. In "good barrel" region of the calorimeter ($|\cos\theta_\gamma| < 0.71$) photons do not pass through the DR endplate; the rest of the barrel calorimeter is called "bad

barrel". We grouped the π^0 candidates into 6 categories according to the calorimeter region where each daughter photon was detected and compared normalized π^0 mass distributions in CLEO II and CLEO II.V data (Figure D.2-left) and simulated event samples (Figure D.2-right). These plots convinced us that in the search for $B^0 \to J/\psi\pi^0$ we should not throw away photon candidates from bad barrel and endcap regions. According to our Monte Carlo simulation, at least one daughter photon is detected outside the good barrel for 16% of π^0's from $B^0 \to J/\psi\pi^0$ decay. There is a problem with calorimeter energy calibration in bad

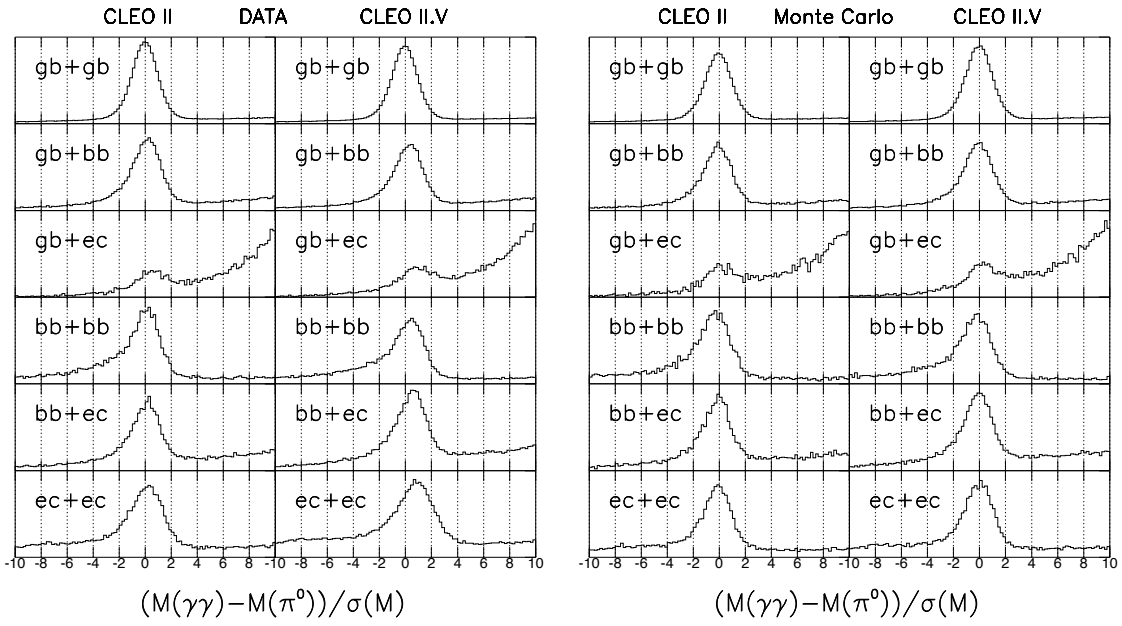

Figure D.2: Normalized π^0 mass distributions for inclusive π^0's with momenta between 1.60 and 1.85 GeV/c. We divide π^0 candidates according to the calorimeter region where each daughter photon was detected: "gb"≡"good barrel", "bb"≡"bad barrel", and "ec"≡"end cap". We compare the distributions for CLEO II (left column) and CLEO II.V (right column). The left plot is for data; the right one is for the Monte Carlo simulation.

barrel and endcap regions in CLEO II.V data (Figure D.2-left); no such problem is seen in the Monte Carlo simulation (Figure D.2-right). This problem is minor, however, because our π^0 mass window cut is quite wide ($-5 < (M(\gamma\gamma) - M_{\pi^0})/\sigma(M) < 4$), and we perform a mass-constraint fit for the π^0 candidates. If we consider π^0's in all calorimeter regions, then CLEO II and CLEO II.V data are almost indistinguishable. In Figure D.3(left) we compare π^0 lineshapes in CLEO II and CLEO II.V data; the histograms were scaled by the ratio of integrated luminosities. In Figure D.3(right) we compare π^0 lineshapes in the data and in the simulation; the histograms were scaled to have the same area.

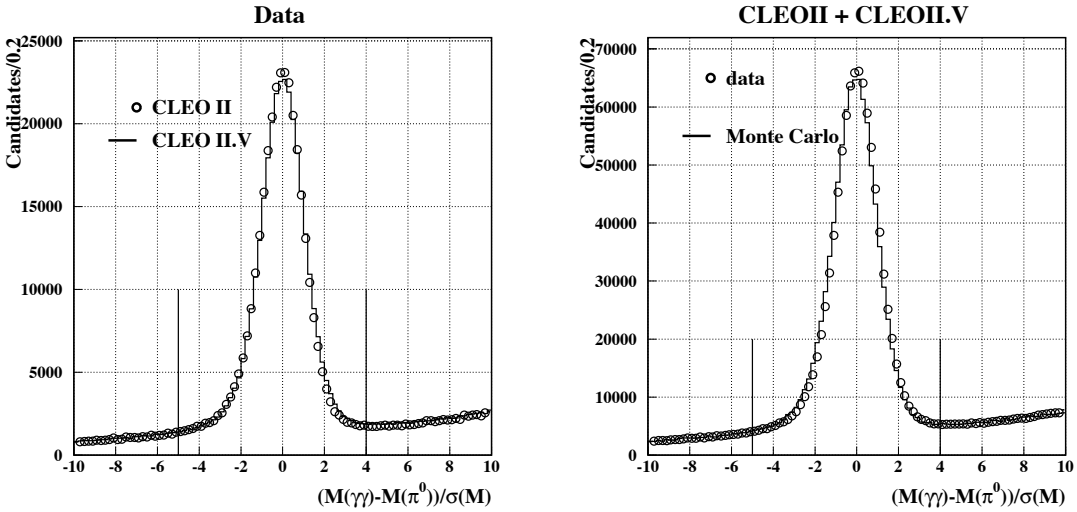

Figure D.3: Normalized π^0 mass distributions for inclusive π^0's with momenta between 1.60 and 1.85 GeV/c. Photons were detected in all calorimeter regions. In the left plot we overlay the histograms obtained from CLEO II (circles) and CLEO II.V (solid line) data; these histograms were scaled by the ratio of integrated luminosities. In the right plot we overlay the histograms obtained from the data (circles) and the Monte Carlo simulation (solid line); these histograms were scaled to have the same area. Vertical lines represent the cut used in $B^0 \to J/\psi\pi^0$ analysis.

Appendix E

How to reconstruct $K^0_S \to \pi^0\pi^0$

K^0_S's are used in many analyses and some analyses would welcome the 15% efficiency boost from $K^0_S \to \pi^0\pi^0$ mode even if this mode is not quite as clean as $K^0_S \to \pi^+\pi^-$. One example of such an analysis is $B^0 \to J/\psi K^0_S$ reconstruction, important for CP violation studies. Originally we developed a technique for $K^0_S \to \pi^0\pi^0$ finding to augment the statistics of the $B^0 \to J/\psi K^0_S$ sample used for the projected $\sin 2\beta$ measurement at CLEO. Unfortunately, the CLEO $\sin 2\beta$ measurement has passed away (Chapter 7). We find it useful, however, to describe the developed procedure.

We studied the K^0_S's from $B^0 \to J/\psi K^0_S$ decays. The technique is applicable, however, to reconstruction of K^0_S's from other decays. The K^0_S momentum and flight distance distributions for $B^0 \to J/\psi K^0_S$ are shown in Figure E.1. Unless otherwise stated, all the plots in this section were produced using tagged $K^0_S \to \pi^0\pi^0$ candidates reconstructed from a sample of simulated $B^0 \to J/\psi K^0_S$ events.

For $K^0_S \to \pi^0\pi^0$ reconstruction we selected photon showers requiring the shower energy to be greater than 30 MeV for good barrel ($|\cos\theta_\gamma| < 0.71$) and greater than 50 MeV for the rest of the calorimeter.

E.1 What if we use the e^+e^- interaction point as a photon origin?

By e^+e^- interaction point we mean run-by-run beam spot in $r-\phi$ plane and event-by-event reconstructed vertex along the z-axis. Calorimeter provides us with energy and position measurements of a photon shower. To reconstruct the photon momentum, we need to make an assumption about the production point of this photon. In the beginning, for lack of better knowledge, we pretend that all the photons come from the e^+e^- interaction point. In this case we obtain badly distorted π^0 and K^0_S mass distributions (Figure E.2). Photon-shower covariance matrices cannot be trusted when the e^+e^- interaction point is assumed as a photon origin. Therefore it is impossible to perform kinematic fits constraining π^0 and K^0_S masses. Remarkably, the reconstructed K^0_S flight direction is very accurate (Figure E.3). For example, missing true K^0_S flight direction by 0.02 radians (Figure E.3) for a K^0_S that flew 20 cm (Figure E.1-right), translates into an error of 0.4 cm in the K^0_S vertex position;

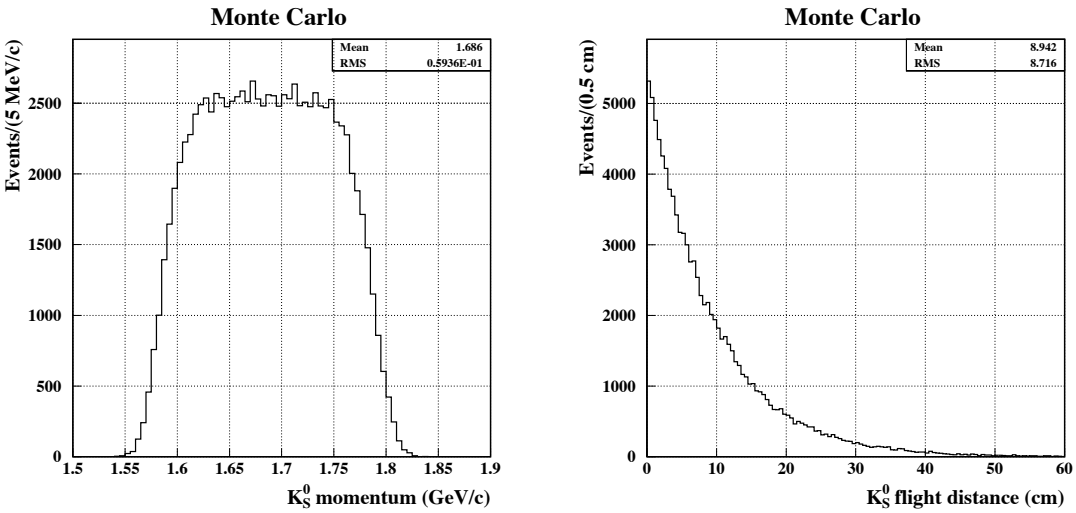

Figure E.1: K^0_S laboratory momentum (left) and flight distance (right) in $B^0 \to J/\psi K^0_S$ decays. The generator-level information is shown.

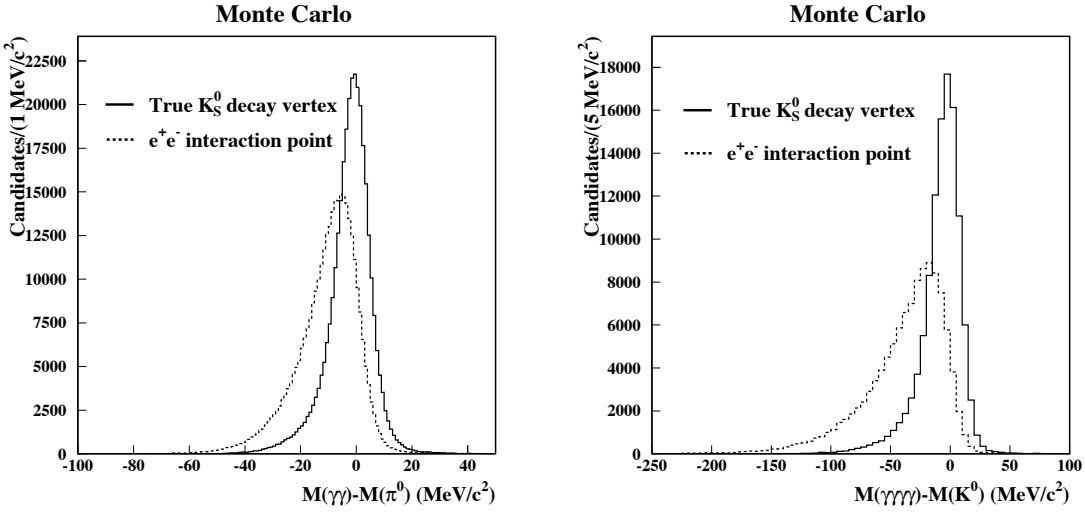

Figure E.2: π^0 (left plot) and K^0_S (right plot) mass distributions for $K^0_S \to \pi^0\pi^0$ from $B^0 \to J/\psi K^0_S$ decays. To calculate the photon directions, we used true K^0_S decay vertex from QQ (solid line) and e^+e^- interaction point (dashed line) as a photon origin.

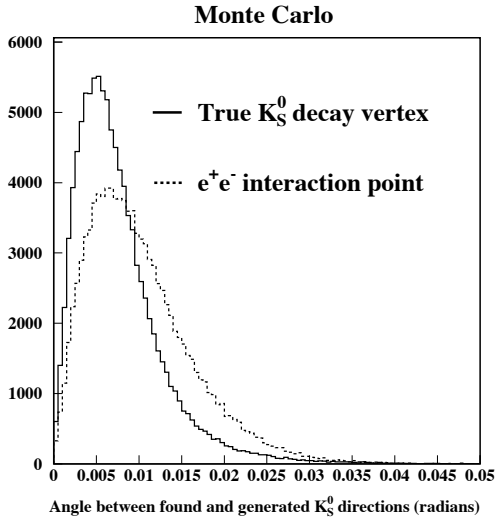

Figure E.3: The angle between the reconstructed and generated K^0_S momentum vectors. The K^0_S momentum vector was calculated as sum of momenta of the four photons. To calculate the photon directions, we used true K^0_S decay vertex from QQ (solid line) and e^+e^- interaction point (dashed line) as a photon origin.

such an error is negligible compared to the achieved K^0_S flight distance resolution of 4.4 cm. Therefore we consider the K^0_S flight direction to be perfectly known.

E.2 $K^0_S \to \pi^0\pi^0$ vertex finding

Even if the K^0_S vertex position were perfectly known, the π^0 mass distribution would still have a low-side tail due to nonlinearities in photon energy measurements (Figure E.4). We fitted this distribution with the Crystal Ball function, "Gaussian with low-side tail", defined in Appendix A.2. The fit, shown in Figure E.4, returned the following parameters: peak position $M^* = M_{\pi^0} - 0.9$ MeV/c^2, $\sigma = 5.6$ MeV/c^2, $\alpha = 0.99$, and $n = 12.4$.

As mentioned in the previous section, the K^0_S flight direction can be considered perfectly measured. To find the K^0_S vertex position, we step along this direction, recalculating photon directions at each point on the way, until the following function of the two π^0 masses is maximized:

$$\mathcal{L}(M(\gamma_1\gamma_2), M(\gamma_3\gamma_4)|L(K^0_S)) = f[M(\gamma_1\gamma_2)] \times f[M(\gamma_3\gamma_4)]. \quad \text{(E.1)}$$

We denote K^0_S flight distance as $L(K^0_S)$. The parameters M^*, σ, α, and n of the Crystal Ball function $f(M)$ are fixed to the values obtained from the fit shown in Figure E.4. We let the two π^0's freely decide between themselves which point along the K^0_S flight direction they prefer, therefore we also allow negative flight distances. Figure E.5 shows the distribution

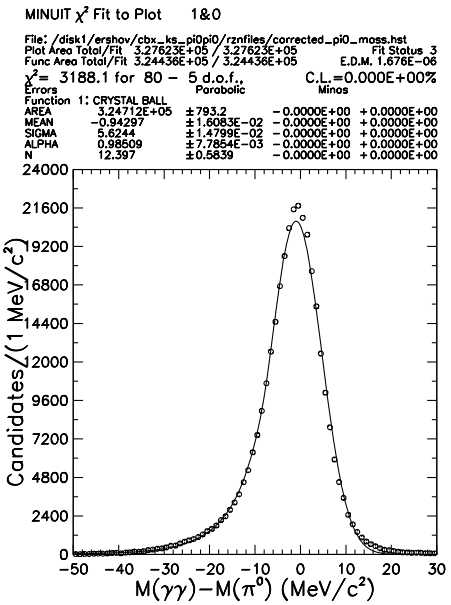

Figure E.4: π^0 mass distribution for $K^0_S \to \pi^0\pi^0$ in a sample of simulated $B^0 \to J/\psi K^0_S$ events. To calculate the photon directions, we used true K^0_S decay vertex from QQ as a photon origin. The distribution is fit with the Crystal Ball function.

of the found K^0_S flight distances as well as the distribution of the differences between found and true K^0_S flight distances. The K^0_S flight distance is found without a bias and with a resolution of 4.4 cm.

We recalculate the photon directions using the found K^0_S decay vertex. The resulting π^0 mass distribution is shown in Figure E.6. This distribution is narrower than the distribution shown in Figure E.4. This is not surprising: the distribution in Figure E.6 is not a δ-function only because two π^0's have to come to a compromise on the best K^0_S decay vertex.

E.3 Kinematic fits with π^0 and K^0 mass constraints

Now we can calculate photon covariance matrices. The energy and position resolutions of a shower in the calorimeter are parametrized in the shower reconstruction software. We also know that the photon origin is limited to a line (K^0_S flight direction), and a position along this line is known without a bias with 4.4 cm precision (Figure E.5-right). The directions of the four photons from K^0_S decay are strongly correlated because all four photons originate from the K^0_S decay vertex. Therefore we build a combined covariance matrix for the two π^0's, taking into account correlations in the photon directions. Then we perform a kinematic fit constraining both π^0 masses together in one fit. This final π^0 mass-constraint fit rectifies bias and slightly improves K^0_S mass resolution (compare left and right plots in Figure E.7). In Figure E.8 we compare the K^0_S mass distribution we have started from and the distribution we obtain after we find the K^0_S decay vertex and constrain the π^0 masses.

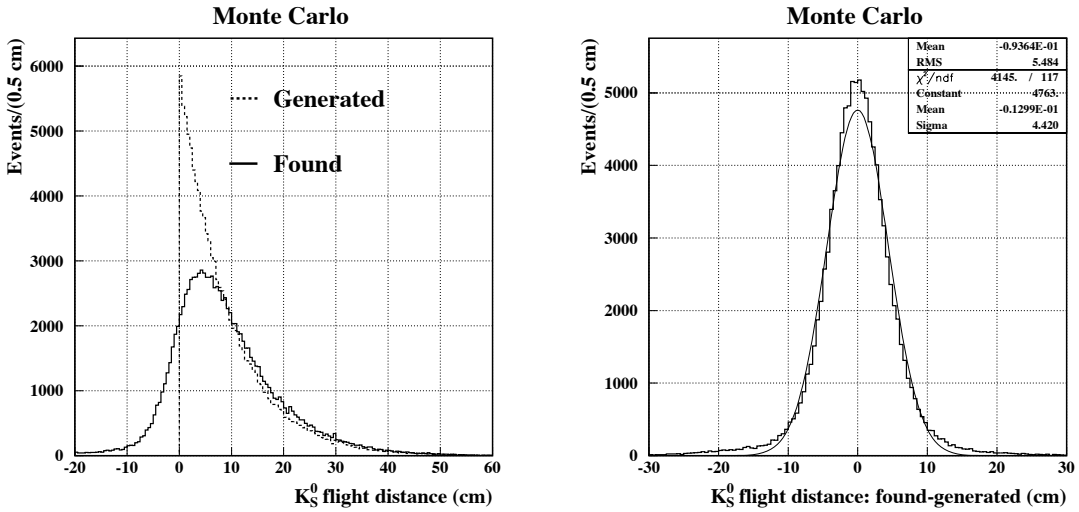

Figure E.5: The distributions of found and generated K^0_S flight distances are overlaid in the left plot. Right plot shows the difference between found and generated K^0_S flight distances.

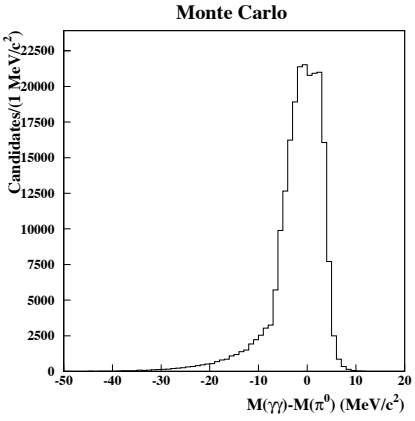

Figure E.6: π^0 mass distribution after the photon directions have been recalculated to the found K^0_S decay vertex. Note that the π^0 masses have already been used to find K^0_S decay vertex.

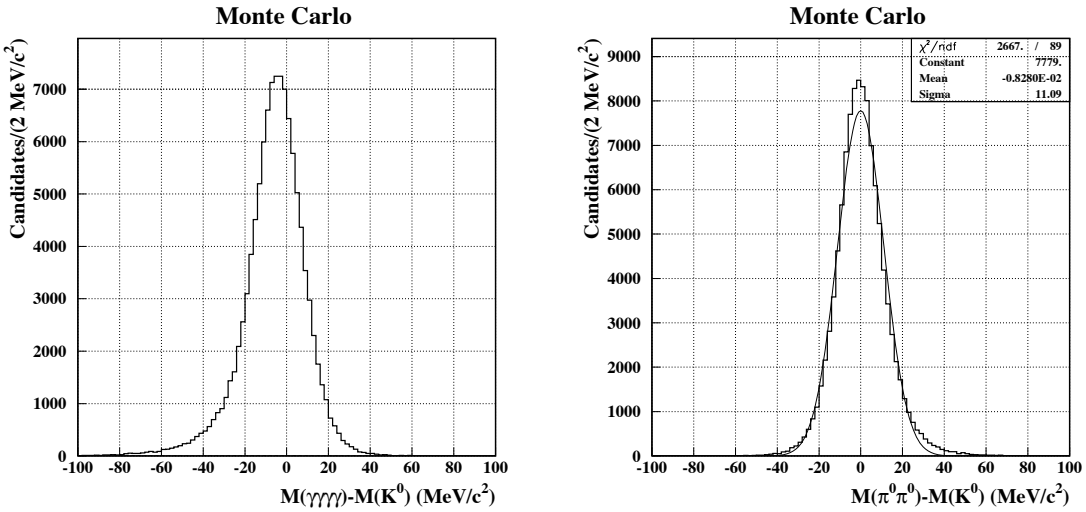

Figure E.7: K^0_S mass distributions after the photon directions have been recalculated to the found K^0_S decay vertex. Left and right plots show the distributions before and after final π^0 mass-constraint fit. The Gaussian fit to the right-hand K^0_S mass distribution yields 11 MeV/c^2 K^0_S mass resolution.

Now we can cut on the K^0_S mass. Figure E.9 shows the distribution of the reported K^0_S mass uncertainties and the distribution of the normalized K^0_S mass.
Next we perform a kinematic fit constraining K^0_S mass to its world average value. Now the K^0_S four-vector is ready to be used for the reconstruction of "upstream" decays. Figure E.10 shows the distribution of the reported K^0_S energy uncertainties and the distribution of the K^0_S energy pulls.

E.4 Step-by-step $K^0_S \to \pi^0\pi^0$ reconstruction procedure

1. Select photon showers.

2. Assume that all photons come from the e^+e^- interaction point.

3. Form π^0 candidates. In principle, no π^0 mass cut is necessary at this point; in practice, however, one may want to apply some very loose requirement in order to save computer time. In our $B^0 \to J/\psi K^0_S$ analysis we required $-80 < M(\gamma\gamma) - M_{\pi^0} < 40$ MeV/c^2 (Figure E.2-left).

4. Form $K^0_S \to \pi^0\pi^0$ candidates. Again, no K^0_S mass cut is necessary at this point. In our $B^0 \to J/\psi K^0_S$ analysis we required $-250 < M(\gamma\gamma\gamma\gamma) - M_{K^0} < 75$ MeV/c^2 (Figure E.2-right).

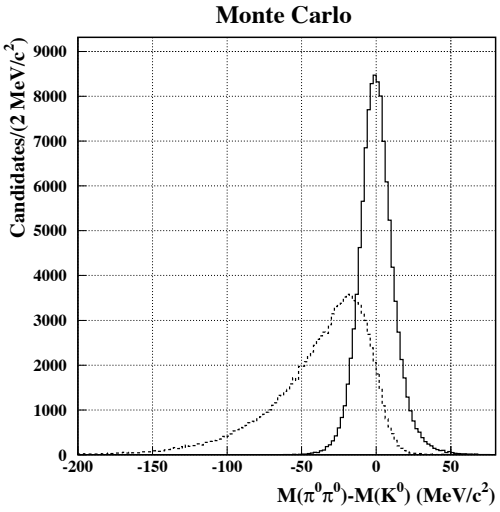

Figure E.8: Solid line represents K^0_S mass distribution after new K^0_S decay vertex is found and after final π^0 mass-constraint fit is performed. Dashed line represents the K^0_S mass distribution we have started from, when we used e^+e^- interaction point as a photon origin. The histograms are normalized to the same area.

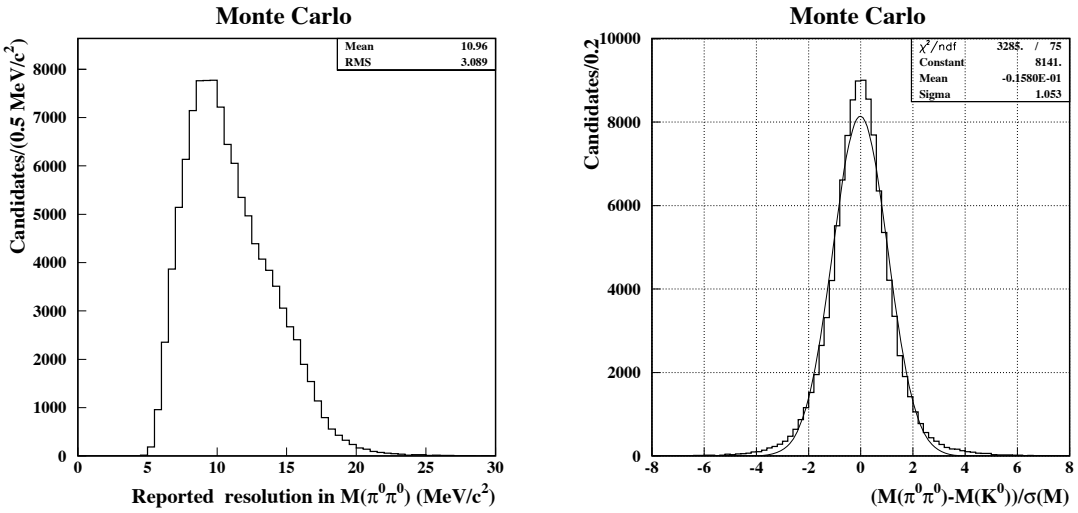

Figure E.9: Left plot shows reported event-by-event uncertainties in K^0_S mass. The normalized K^0_S mass distribution is shown in the right plot.

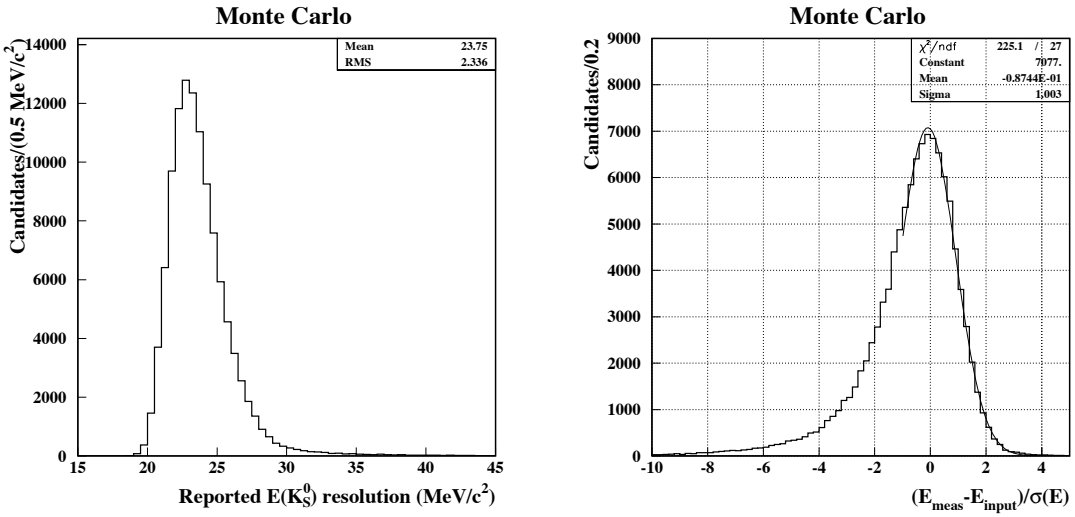

Figure E.10: Left plot shows reported event-by-event uncertainties in K^0_S energy. The normalized K^0_S energy distribution is shown in the right plot.

5. K^0_S flight direction is just the direction of the K^0_S momentum calculated as a sum of momenta of the four photons. Photon directions are calculated assuming the e^+e^- interaction point as a photon origin (see Figure E.3). One might think of thus calculated K^0_S flight direction as a line passing through the e^+e^- interaction point and the center of energy of the four photon showers in the calorimeter. Consider the K^0_S flight direction to be perfectly known.

6. For each K^0_S candidate, step along the K^0_S flight direction, allowing negative flight distances. At each step recalculate the directions of the four photons, assuming new K^0_S decay vertex. The point for which the following expression

$$\mathcal{L}(M(\gamma_1\gamma_2), M(\gamma_3\gamma_4)|L(K^0_S)) = f[M(\gamma_1\gamma_2)] \times f[M(\gamma_3\gamma_4)]$$

   is maximal is declared to be our best guess on K^0_S decay vertex (Figure E.5). Function $f(M(\gamma\gamma))$ in the above expression was obtained from a fit of a Crystal Ball shape to the π^0 mass distribution obtained from simulation (Figure E.4). If your K^0_S momenta differ significantly from ours, please derive your own template lineshape.

7. Cut on the found K^0_S flight distance $L(K^0_S)$. In our $B^0 \to J/\psi K^0_S$ analysis we required $-10 < L(K^0_S) < 60$ cm (Figure E.5).

8. Photon directions are recalculated using our best guess on K^0_S vertex. Now cut tighter on the π^0 mass. In our $B^0 \to J/\psi K^0_S$ analysis we required $-15 < M(\gamma\gamma) - M_{\pi^0} < 10$ MeV/c^2 (Figure E.6).

9. Recalculate photon-shower covariance matrices, assuming that the photon origin is limited to a line (K^0_S flight direction) and a position along this line is known without

a bias with the precision determined from the Monte Carlo simulation. In our analysis the K^0_S flight distance resolution is 4.4 cm (Figure E.5-right). Build a combined covariance matrix for the two π^0's taking into account correlations in the photon directions due to the common uncertain origin. Then perform a kinematic fit constraining both π^0 masses together in one fit.

10. After final π^0 mass-constraint fit, cut on K^0_S mass. In our $B^0 \to J/\psi K^0_S$ analysis we required the absolute value of the normalized K^0_S mass to be less than 3 (Figure E.9).

11. Perform kinematic fit constraining K^0_S mass to its world average value. Thus obtained K^0_S four-vector and covariance matrix are now ready to be used for the reconstruction of an "upstream" decay.

E.5 Reconstruction of inclusive $K^0_S \to \pi^0\pi^0$ in data

We tested our $K^0_S \to \pi^0\pi^0$ finder on inclusive K^0_S's in data. The K^0_S momenta were restricted to be from 1.55 to 1.85 GeV/c; this range corresponds to the K^0_S momentum range in $B^0 \to J/\psi K^0_S$ decays (Figure E.1-left). We required the found K^0_S flight distance to be between -10 and 60 cm (Figure E.5-left); we also required $-15 < M(\gamma\gamma) - M_{\pi^0} < 10$ MeV/c^2 (Figure E.6) with the photon directions recalculated to the found K^0_S vertex. We did not limit number of K^0_S candidates per event. In particular, a photon shower can be reconstructed as a part of several K^0_S candidates, each having its own decay vertex. The resulting K^0_S mass distribution is shown in Figure E.11(left). The right plot in Figure E.11 was obtained by requiring the K^0_S flight distance to be greater than 4 cm, which corresponds to approximately 1σ vertex separation cut. The purity of the signal can be further increased by cutting tighter on the π^0 mass. The fits to the K^0_S mass and normalized mass distributions in Figures E.12 and E.13 show good agreement between the data and the Monte Carlo simulation.

E.6 Systematic uncertainty on $K^0_S \to \pi^0\pi^0$ reconstruction efficiency

In our measurement of $\mathcal{B}(B^0 \to J/\psi K^0)$ described in Chapter 6 we used the Monte Carlo simulation to determine the reconstruction efficiency. The $K^0_S \to \pi^+\pi^-$ decays provide an excellent calibration sample for the study of systematic uncertainties associated with $K^0_S \to \pi^0\pi^0$ reconstruction. The branching ratio $\mathcal{B}(K^0_S \to \pi^+\pi^-)/\mathcal{B}(K^0_S \to \pi^0\pi^0)$ is measured with a relative accuracy of 1.3% [48]. For this study we used spherically-looking hadronic events in all CLEO II and CLEO II.V data; both on- and off-$\Upsilon(4S)$ data sets were used. We selected inclusive $K^0_S \to \pi^0\pi^0$ and $K^0_S \to \pi^+\pi^-$ candidates using the same K^0_S selection criteria as in $B^0 \to J/\psi K^0_S$ analysis. The K^0_S momenta were further restricted to be from 1.55 and 1.85 GeV/c; this range corresponds to the K^0_S momenta in $B^0 \to J/\psi K^0_S$ decays (Figure E.1-left). We calculated ratios of $K^0_S \to \pi^0\pi^0$ and $K^0_S \to \pi^+\pi^-$ yields — $R \equiv N(K^0_S \to \pi^0\pi^0)/N(K^0_S \to \pi^+\pi^-)$ — separately for data and the Monte Carlo simulation. Then we formed double ratio $R_{\rm data}/R_{\rm MC}$. This double ratio should be close to unity if

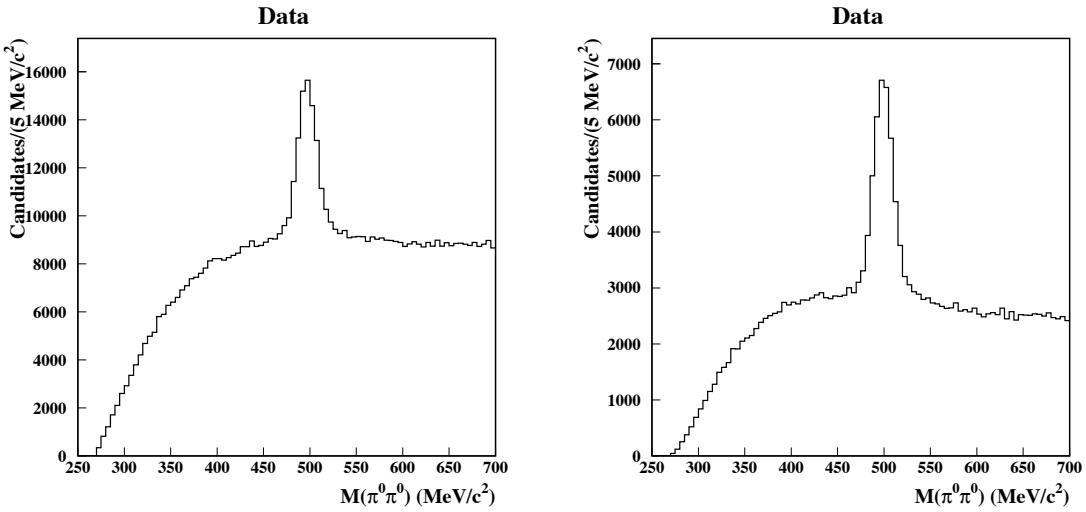

Figure E.11: Inclusive $K^0_S \to \pi^0\pi^0$ candidates reconstructed from data. The momenta of the candidates were restricted to be between 1.55 and 1.85 GeV/c. For the right plot we required the K^0_S flight distance to be greater than 4 cm ($\approx 1\sigma$).

our simulation correctly predicts ratio of $K^0_S \to \pi^0\pi^0$ and $K^0_S \to \pi^+\pi^-$ reconstruction efficiencies. Signal yields were extracted from the fits to $\pi\pi$ mass and normalized $\pi\pi$ mass distributions (see Figures E.12 and E.13). We averaged central values of double ratios of yields obtained from fits to $M(\pi\pi)$ and normalized $M(\pi\pi)$ distributions and assigned the largest deviation from the average as a systematic uncertainty. The results are listed in the Table E.1. We take the value of $R_{\rm data}/R_{\rm MC} - 1$ to be 5%. Therefore the systematic

Table E.1: Deviation from 1 of the double ratio of $K^0_S \to \pi^0\pi^0$ and $K^0_S \to \pi^+\pi^-$ yields ($R_{\rm data}/R_{\rm MC}$), where $R \equiv N(K^0_S \to \pi^0\pi^0)/N(K^0_S \to \pi^+\pi^-)$.

	$R_{\rm data}/R_{\rm MC} - 1$ (%)
CLEO II	$+5.3 \pm 0.2$(stat) ± 0.4(fit syst)
CLEO II.V	-2.0 ± 0.1(stat) ± 1.6(fit syst)

uncertainty in the Monte Carlo simulation prediction of the $K^0_S \to \pi^0\pi^0$ reconstruction efficiency equals 5% added in quadrature to the systematic uncertainty assigned for $K^0_S \to \pi^+\pi^-$ reconstruction efficiency.

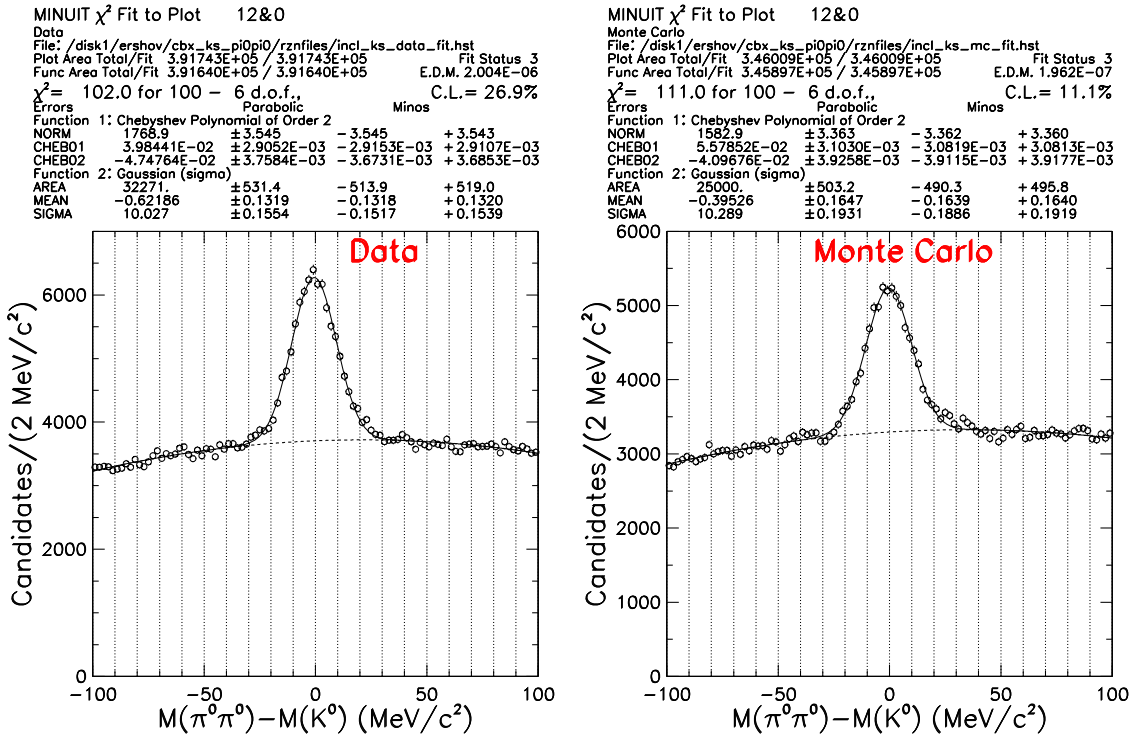

Figure E.12: Fit to the K^0_S mass distribution for inclusive $K^0_S \to \pi^0\pi^0$ candidates. We applied the same selection criteria as for the plot in Figure E.11(left). Left plot is for data, right one is for a sample of simulated events.

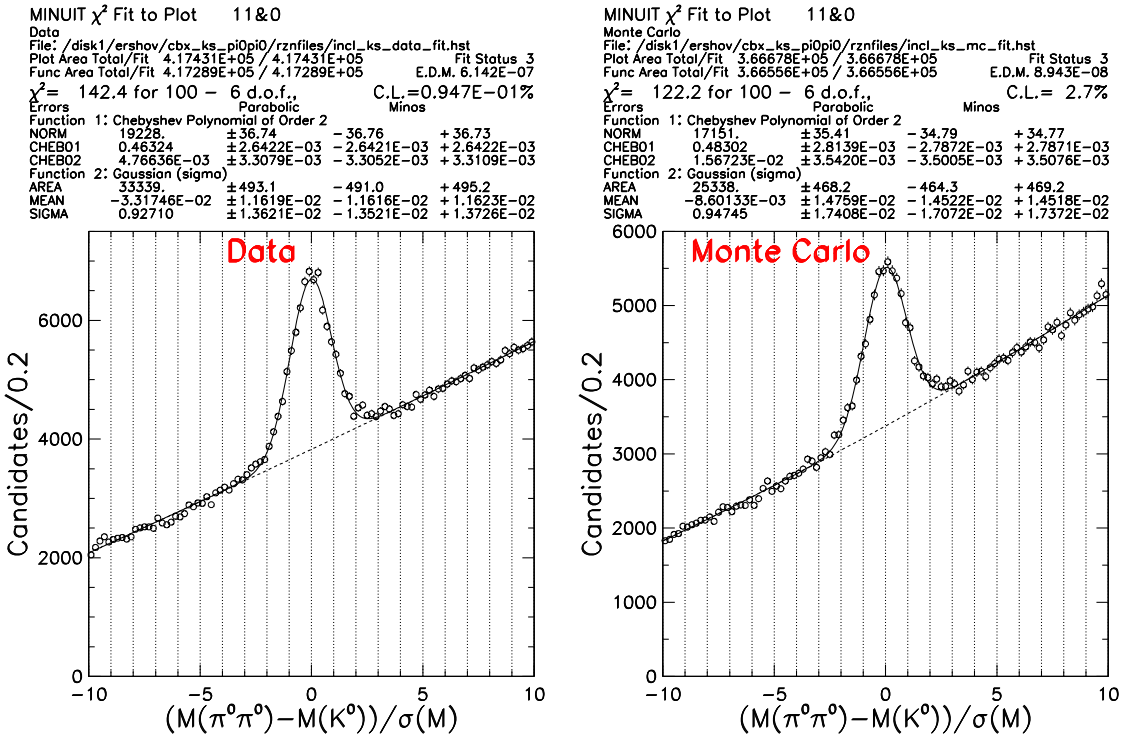

Figure E.13: Fit to the normalized K^0_S mass distribution for inclusive $K^0_S \to \pi^0\pi^0$ candidates. We applied the same selection criteria as for the plot in Figure E.11(left). Left plot is for data, right one is for a sample of simulated events.

Appendix F

Cross-checks of J/ψ yields

We compared the J/ψ yields in CLEO II and CLEO II.V data, and also compared the yields in data and the Monte Carlo simulation. For $J/\psi \to \mu^+\mu^-$ mode we additionally list the results obtained with the requirement that both muons pass the muon penetration requirement `DPTHMU` $>$ `3`. To determine J/ψ yields, we fitted $M(\mu^+\mu^-) - M_{J/\psi}$ and $M(e^+(\gamma)e^-(\gamma)) - M_{J/\psi}$ distributions in the region from -650 to $+200$ MeV/c^2. We also fitted normalized mass distributions $[M(\mu^+\mu^-) - M_{J/\psi}]/\sigma(M)$ and $[M(e^+(\gamma)e^-(\gamma)) - M_{J/\psi}]/\sigma(M)$ in the region from -55 to $+20$ (Figure F.1). We used 2nd order Chebyshev polynomial as background shape. We used histograms extracted from tagged J/ψ decays in a sample of simulated signal events as signal shape templates. The J/ψ yields in data were obtained by scaling the area of the template histogram extracted from simulation; no mass cuts were applied. We averaged central values of the J/ψ yields obtained from fits to the J/ψ mass and normalized mass distributions and assigned a deviation from the average as a systematic uncertainty. The J/ψ yields are listed in Table F.1.

Table F.1: $J/\psi \to \mu^+\mu^-$ and $J/\psi \to e^+e^-$ yields in data obtained by scaling the area of the template histogram extracted from simulation; no mass cuts were applied. The first uncertainty is statistical; the second one is assigned through comparison of yields obtained in fits to the J/ψ mass and normalized J/ψ mass distributions.

Mode	Data set	J/ψ yield
$J/\psi \to \mu^+\mu^-$	CLEO II	$2556 \pm 63 \pm 4$
	CLEO II.V	$5025 \pm 85 \pm 45$
$J/\psi \to \mu^+\mu^-$	CLEO II	$2165 \pm 56 \pm 7$
both μ with `DPTHMU` $>$ `3`	CLEO II.V	$4189 \pm 75 \pm 30$
$J/\psi \to e^+e^-$	CLEO II	$2985 \pm 70 \pm 7$
	CLEO II.V	$5750 \pm 98 \pm 10$

1. To check that the $J/\psi \to \mu^+\mu^-$ and $J/\psi \to e^+e^-$ reconstruction efficiencies are not significantly different in CLEO II and CLEO II.V data, we compared the J/ψ yields per $B\overline{B}$ pair in CLEO II and CLEO II.V data. The results are listed in Table F.2.

2. To check that our Monte Carlo simulation tracks the change in $J/\psi \to \mu^+\mu^-$ and

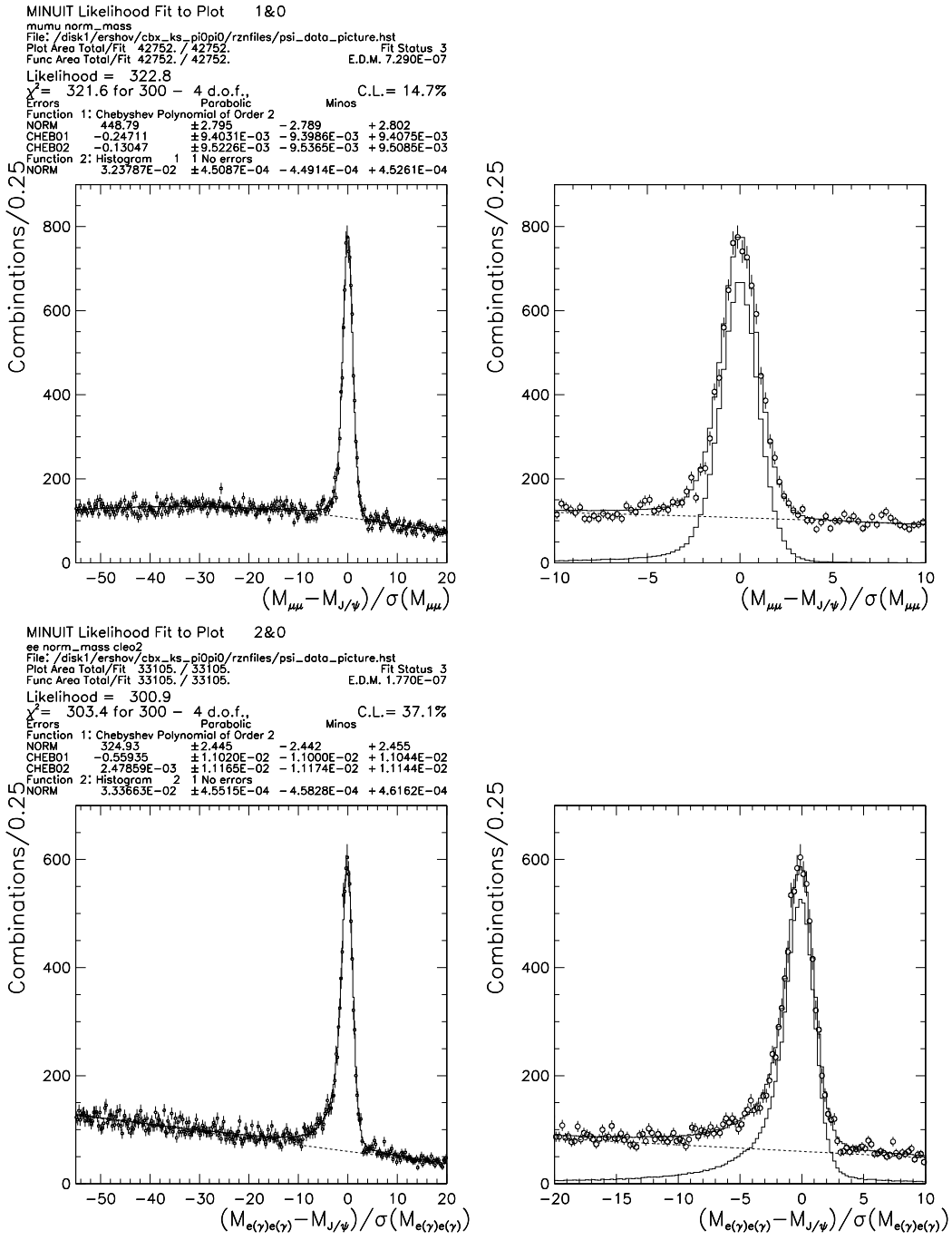

Figure F.1: Fits to $J/\psi \to \mu^+\mu^-$ (top row) and $J/\psi \to e^+e^-$ (bottom row) normalized mass distributions. As signal shape templates we used histograms extracted from the Monte Carlo simulation. Right plots show the close-up of the J/ψ peak region; signal and background fit functions are overlaid.

$J/\psi \to e^+e^-$ reconstruction efficiencies between CLEO II and CLEO II.V, we compared the J/ψ yields per $B\overline{B}$ pair divided by the J/ψ reconstruction efficiency determined from simulation. This is equivalent to the check that in CLEO II and CLEO II.V we get consistent values of $\mathcal{B}(B \to J/\psi X)$. The results are listed in Table F.2.

3. We checked that ratio of $J/\psi \to \mu^+\mu^-$ and $J/\psi \to e^+e^-$ reconstruction efficiencies is consistent between data and the Monte Carlo simulation. This is equivalent to the check that we get consistent values of $\mathcal{B}(B \to J/\psi X)$ using $J/\psi \to \mu^+\mu^-$ and $J/\psi \to e^+e^-$ modes. The results are listed in Table F.3.

In all the analyses presented in this thesis we assign a 6% uncertainty on the J/ψ reconstruction efficiency (3% per lepton). The study presented in this Appendix confirms that this uncertainty is quite conservative.

Table F.2: Comparison of the J/ψ yields per $B\overline{B}$ pair and in CLEO II and CLEO II.V data. We also compare the J/ψ yields per $B\overline{B}$ pair divided by the J/ψ reconstruction efficiency determined from simulation.

Mode	$\frac{N(J/\psi)/N(B\overline{B})\,\vert_{\rm CLEOII.V}}{N(J/\psi)/N(B\overline{B})\,\vert_{\rm CLEOII}} - 1$	$\frac{[N(J/\psi)/N(B\overline{B})]/\epsilon_{\rm MC}\,\vert_{\rm CLEOII.V}}{[N(J/\psi)/N(B\overline{B})]/\epsilon_{\rm MC}\,\vert_{\rm CLEOII}} - 1$
$J/\psi \to \mu^+\mu^-$	$(+2.7 \pm 3.1)\%$	$(-1.0 \pm 3.1)\%$
both μ with `DPTHMU` > 3	$(+1.1 \pm 3.3)\%$	$(-3.0 \pm 3.1)\%$
$J/\psi \to e^+e^-$	$(+0.6 \pm 2.9)\%$	$(-1.7 \pm 2.9)\%$

Table F.3: J/ψ yield divided by J/ψ reconstruction efficiency determined from simulation. We compare $J/\psi \to \mu^+\mu^-$ and $J/\psi \to e^+e^-$ modes.

Mode	$\frac{N(J/\psi)/\epsilon_{\rm MC}\,\vert_{J/\psi\to e^+e^-}}{N(J/\psi)/\epsilon_{\rm MC}\,\vert_{J/\psi\to \mu^+\mu^-}} - 1$
2nd μ can have `DPTHMU` $= 0$	$(+3.9 \pm 2.1)\%$
both μ with `DPTHMU` > 3	$(+2.4 \pm 2.1)\%$

List of References

[1] *The CLEO II detector*, CLEO Collaboration, Y. Kubota *et al.*, Nuclear Instruments and Methods A **320**, 66 (1992).

[2] *The CLEO II silicon vertex detector*, T.S. Hill, Nuclear Instruments and Methods A **418**, 32 (1998).

[3] *Measurements of the B semileptonic branching fraction with lepton tags*, CLEO Collaboration, B. Barish *et al.*, Physical Review Letters **76**, 1570 (1996).

[4] *Measurement of the relative branching fraction of* $\Upsilon(4S)$ *to charged and neutral B meson pairs*, CLEO Collaboration, J. P. Alexander *et al.*, Physical Review Letters **86**, 2737 (2001).

[5] *B momenta calibration in recompress and CLEO II.V*, V. Fadeyev and R. Stroynowski, internal CLEO note CBX 00-43 (2000).

[6] *A personal history of CESR and CLEO*, K. Berkelman, internal CLEO note CBX 95-87 (1995).

[7] *CESR - an electron positron colliding beam facility at Cornell*, M. Tigner, IEEENS-24, 1849 (1977).

[8] *Proposal for multibunch operation of CESR*, R. Littauer, CESR internal publication CBN 82-16 (1982); *Multibunch Operation of CESR*, R. Littauer, CESR internal publication CBN 85-7 (1987).

[9] *Proposal for CESR Mini-B*, R. Meller , CESR internal publication CON 90-17 (1990).

[10] *CESR status and plans*, D. Rubin, Proceedings of the 1995 IEEE Particle accelerator Conference, volume 1, page 481 (1995).

[11] *CESR performance and upgrade status*, S. Peck and D. Rubin, Proceedings of the 1999 IEEE Particle Accelerator Conference, volume 1, page 285 (1999).

[12] *Observation of the Dynamic Beta Effect at CESR with CLEO*, D. Cinabro *et al.*, Physics Letters **E57**, 1193 (1998).

[13] *Observation of the Hourglass Effect and Measurement of CESR Beam Parameters with CLEO*, D. Cinabro and K. Korbiak, CLEO internal publications CBX 00-22 and CBX 00-60 (2000).

[14] *Beam backgrounds at CLEO: Design and performance of the CESR high luminosity interaction region*, S. Henderson, Report CLNS-97-1528 (1997).

[15] Hitoshi Yamamoto, private communication.

[16] *Study of helium-based drift chamber gases*, K.K. Gan *et al.*, Nuclear Instruments and Methods A **374**, 27 (1996); *Tracking in Helium-Based Gases: Present and Future B Factories*, R. Briere, Proceedings of the Seventh International Symposium on Heavy Flavor Physics, Santa Barbara, CA, July, 1997.

[17] *A muon identification detector for B physics near* $e^+e^- \to B\overline{B}$ *threshold*, D. Bortoletto *et al.*, Nuclear Instruments and Methods A **320**, 114 (1992).

[18] *Billoir fitter for CLEO II*, R. Kutschke and A. Ryd, internal CLEO note CBX 96-20 (1996).

[19] *Track Fitting With Multiple Scattering: A New Method*, P. Billoir, Nuclear Instruments and Methods A **225**, 352 (1984).

[20] *The KNVF Secondary Vertex Finding Package*, C.P. Prescott, internal CLEO note CSN 97/353 (1997).

[21] *Rare B Meson Decays with* η' *or* η *Mesons*, A. Gritsan, Ph.D. dissertation, University of Colorado (2000).

[22] *The BaBar Physics Book*, BaBar Collaboration, edited by P.F Harrison and H.R. Quinn, report SLAC-R-504 (1998).

[23] *High-energy physics event generation with PYTHIA 5.7 and JETSET 7.4*, T. Sjöstrand, Comput. Phys. Commun. **82**, 74 (1994).

[24] *GEANT – Detector Description and Simulation Tool*, CERN Program Library Long Writeup W5013 (1993).

[25] *Study of the photon spectrum in the decay* $K^0_S \to \pi^+\pi^-\gamma$, H. Taureg *et al.*, Physics Letters **65B**, 92 (1976).

[26] *Observation of the radiative decay* $J/\psi \to e^+e^-\gamma$, E760 Collaboration, T.A. Armstrong *et al.*, Physical Review D **54**, 7067 (1996).

[27] *Inclusive and exclusive decays of B mesons to charmonium states at the* $\Upsilon(4S)$ *resonance*, S. Schrenk, Ph.D. dissertation, University of Minnesota (1994).

[28] *Inclusive decays of B mesons to charmonium*, CLEO Collaboration, R. Balest *et al.*, Physical Review D **52**, 2661 (1995).

[29] *Update on* $B \to J/\psi K$ *branching fractions*, R. Wanke, internal CLEO note CBX 96-87 (1996).

[30] *Measurement of the decay amplitudes and branching fractions of $B \to J/\psi K^*$ and $B \to J/\psi K$ decays*, CLEO Collaboration, C.P. Jessop *et al.*, Physical Review Letters **79**, 4533 (1997).

[31] *Observation of $B^0 \to \psi K^0_L$*, A. Foland, internal CLEO note CBX 97-70 (1997).

[32] *Two-photon production of charged pion and kaon pairs*, CLEO Collaboration, J. Dominick *et al.*, Physical Review D **50**, 3027 (1994); D. Acosta, internal CLEO note CBX 93-123 (1993).

[33] *Muon identification in CLEO II*, T. Skwarnicki, internal CLEO note CSN 90-301 (1990).

[34] *Inclusive J/ψ, $\psi(2S)$, and b-quark production in $p\overline{p}$ collisions at $\sqrt{s} = 1.8$ TeV*, CDF Collaboration, F. Abe *et al.*, Physical Review Letters **69**, 3704 (1992);
J/ψ and $\psi(2S)$ production in $p\overline{p}$ collisions at $\sqrt{s} = 1.8$ TeV, CDF Collaboration, F. Abe *et al.*, Physical Review Letters **79**, 572 (1997);
Production of J/ψ mesons from χ_c meson decays in $p\overline{p}$ collisions at $\sqrt{s} = 1.8$ TeV, CDF Collaboration, F. Abe *et al.*, Physical Review Letters **79**, 578 (1997);
J/ψ production in $p\overline{p}$ collisions at $\sqrt{s} = 1.8$ TeV, D0 Collaboration, S. Abachi *et al.*, Physics Letters B **370**, 239 (1996).

[35] *J/ψ suppression by quark-gluon plasma formation*, T. Matsui and H. Satz, Physics Letters B **178**, 416 (1986).

[36] For a short overview see, for example, *A brief history of J/ψ suppression*, H. Satz, talk given at Workshop on Quarkonium Production in Relativistic Nuclear Collisions, Seattle, WA, May 1998, `hep-ph/9806319`.

[37] For detailed reviews, see *Quarkonium production and decays*, G. A. Schuler, Report CERN-TH-7170-94, `hep-ph/9403387`; *Production of Heavy Quarkonium in High Energy Colliders*, E. Braaten, S. Fleming, and T. C. Yuan, Annual Review of Nuclear and Particle Science **46**, 197 (1996).

[38] *NRQCD: A Critical Review*, I. Z. Rothstein, talk given at 8th International Symposium on Heavy Flavor Physics (Heavy Flavors 8), Southampton, England, 1999, `hep-ph/9911276`.

[39] *Creation of Particle from Vacuum by a $V-A$ Current*, H. Yamamoto, internal CLEO note CBX 97-72 (1997).

[40] *Charmonium production in B decays*, J. H. Kühn, S. Nussinov, and R. Rückl, Zeitschrift für Physik C **5**, 117 (1980);
Clues on color suppression from $B \to J/\psi + X$, J. H. Kühn and R. Rückl, Physics Letters **135B**, 477 (1984); Physics Letters B **258**, 499 (1991).

[41] *QCD analysis of inclusive B decay into charmonium*, M. Beneke, F. Maltoni, and I. Z. Rothstein, Physical Review Letters **59**, 054003 (1999).

[42] *Rigorous QCD analysis of inclusive annihilation and production of heavy quarkonium*, G. T. Bodwin, E. Braaten, and G. P. Lepage, Physical Review D **51**, 1125 (1995). SPIRES found 504 citations of this paper on 16 May 2001.

[43] *P-wave charmonium production in B-meson decays*, G. T. Bodwin *et al.*, Physical Review D **46**, 3703 (1992).

[44] *Measurement of J/ψ and $\psi(2S)$ polarization in $p\overline{p}$ collisions at $\sqrt{s} = 1.8$ TeV*, CDF Collaboration, T. Affolder *et al.*, Physical Review Letters **85**, 2886 (2000).

[45] *Quantitative tests of color evaporation: charmonium production*, J. F. Amundson *et al.*, Physics Letters B **390**, 323 (1997).

[46] *Testing factorization of charmonium production*, G. A. Schuler, European Physical Journal C **8**, 273 (1999).

[47] *Review of particle physics*, Particle Data Group, C. Caso *et al.*, European Physical Journal C **3**, 1 (1998).

[48] *Review of particle physics*, Particle Data Group, D.E. Groom *et al.*, European Physical Journal C **15**, 1 (2000).

[49] *Unified approach to the classical statistical analysis of small signals*, G.J. Feldman and R.D. Cousins, Physical Review D **57**, 3873 (1998).

[50] *Determination of J/ψ leptonic branching fraction via $\psi(2S) \to \pi^+\pi^- J/\psi$*, BES Collaboration, J. Z. Bai *et al.*, Physical Review D **58**, 092006 (1998).

[51] *First Measurement of the Rate for the Inclusive Radiative Penguin Decay $b \to s\gamma$*, CLEO Collaboration, M. S. Alam *et al.*, Physical Review D **74**, 2885 (1995).

[52] *Observation of High Momentum η' Production in B Decay*, CLEO Collaboration, T. E. Browder *et al.*, Physical Review Letters **81**, 1786 (1998).

[53] *MN_FIT: A Fitting and Plotting Package Using MINUIT*, I.C. Brock, Report BONN-MS-99-02.

[54] *Clarification of the use of χ^2 and likelihood functions in fits to histograms*, S. Baker and R. D. Cousins, Nuclear Instruments and Methods A **221**, 437 (1984).

[55] *Goodness of fit for Poisson distributed data*, H. Nelson, internal CLEO note CBX 98-73 (1998).

[56] For example, see *Probability And Statistics In Particle Physics*, A. G. Frodesen, O. Skjeggestad, and H. Tofte, Bergen, Norway: Universitetsforlaget (1979).

[57] *Charmonium Spectroscopy From Inclusive ψ' and J/ψ Radiative Decays*, Crystal Ball Collaboration, J. Gaiser *et al.*, Physical Review D **34**, 711 (1986).

[58] *Update on the Search for $B \to \chi_{c2}X$ using the Full CLEO II Data Set*, A. Smith and R. Poling, internal CLEO note CBX 98-2 (1998).

[59] *Study of $B \to \psi(2S)K$ and $B \to \psi(2S)K^*(892)$ decays*, CLEO Collaboration, S.J. Richichi *et al.*, Physical Review D **63**, 031103 (2001).

[60] *Search for rare B meson decays into D_s^+ mesons*, ARGUS Collaboration, H. Albrecht *et al.*, Zeitschrift für Physik C **60**, 11 (1993).

[61] *D_s–lepton charge correlations in B meson decays: a study of the D_s meson production mechanism*, CLEO Collaboration, X. Fu *et al.*, contribution to International Europhysics Conference on High Energy Physics in Brussels, CLEO-CONF-95-11, EPS0169 (1995); *A study of lower vertex production of D_s mesons in B meson decays*, A.F. Cho, Ph.D. dissertation, Cornell University (1997).

[62] *Gluonic hadrons and charmless B decays*, F.E. Close, I. Dunietz, P.R. Page, S. Veseli, and H. Yamamoto, Physical Review D **57**, 5653 (1998).

[63] *Study of $B \to \phi X$ and search for $B \to \phi X_s$ from $b \to s$ gluon transitions*, T. Browder, internal CLEO note CBX 95-48 (1995).

[64] *Exclusive hadronic decays of B mesons*, ARGUS Collaboration, H. Albrecht *et al.*, Zeitschrift für Physik C **48**, 543 (1990).

[65] *Exclusive hadronic B decays to charm and charmonium final states*, CLEO Collaboration, M.S. Alam *et al.*, Physical Review D **50**, 43 (1994).

[66] *Measurement of the Υ mass*, W. W. MacKay *et al.*, Physical Review D **29**, 2483 (1984).

[67] *Exclusive decays and masses of the B mesons*, CLEO Collaboration, C. Bebek *et al.*, Physical Review D **36**, 1289 (1987).

[68] *Unitary symmetry and leptonic decays*, N. Cabibbo, Physical Review Letters **10**, 531 (1963);
CP Violation In The Renormalizable Theory Of Weak Interaction, M. Kobayashi and T. Maskawa, Progress of Theoretical Physics **49**, 652 (1973).

[69] *CP violation in B meson decays*, A. B. Carter and A. I. Sanda, Physical Review D **23**, 1567 (1981).

[70] *Notes on the observability of CP violations in B decays*, I. I. Bigi and A. I. Sanda, Nuclear Physics B **193**, 85 (1981).

[71] For a recent review, see *CP violation in and beyond the standard model*, Y. Nir, lectures given at 27th SLAC Summer Institute on Particle Physics, Stanford, California, `hep-ph/9911321`.

[72] *Investigation of CP violation in $B^0 \to J/\psi K_S^0$ decays at LEP*, OPAL collaboration, K. Ackerstaff *et al.*, European Physical Journal C **5**, 379 (1998).

[73] *Measurement of the CP-violation parameter $\sin(2\beta)$ in $B^0/\overline{B^0} \to J/\psi K_S^0$ decays*, CDF Collaboration, F. Abe *et al.*, Physical Review Letters **81**, 5513 (1998).

[74] *A measurement of* $\sin(2\beta)$ *from* $B^0 \to J/\psi K^0_S$ *with the CDF detector*, CDF Collaboration, T. Affolder *et al.*, Physical Review D **61**, 072005 (2000).

[75] *Study of the CP asymmetry of* $B^0 \to J/\psi K^0_S$ *decays in ALEPH*, ALEPH collaboration, R. Barate *et al.*, Physics Letters B **492**, 259 (2000).

[76] *Measurement of the CP violation parameter* $\sin 2\phi_1$ *in* B^0_d *meson decays*, BELLE Collaboration, A. Abashian *et al.*, Physical Review Letters **86**, 2509 (2001).

[77] *Measurement of CP-violating asymmetries in* B^0 *decays to CP eigenstates*, BABAR collaboration, B. Aubert *et al.*, Physical Review Letters **86**, 2515 (2001).

[78] *Study of the decays* $B^0 \to D^{(*)+} D^{(*)-}$, CLEO Collaboration, E. Lipeles *et al.*, Physical Review D **62**, 032005 (2000).

[79] *CP violating B decays in the standard model and supersymmetry*, M. Ciuchini *et al.*, Physical Review Letters **79**, 978 (1997).

[80] *Removing discrete ambiguities in CP asymmetry measurements*, Y. Grossman and H. R. Quinn, Physical Review D **56**, 7259 (1997).

[81] *Cascade mixing and the CP-violating angle beta*, B. Kayser, Proceedings of 32nd Rencontres de Moriond, Electroweak Interactions and Unified Theories, Les Arcs, France, 1997, p. 389, `hep-ph/9709382`.

[82] *B decay CP asymmetries, discrete ambiguities and new physics*, B. Kayser and D. London, Physical Review D **61**, 116012 (2000).

[83] *Search for hadronic* $b \to u$ *decays*, ARGUS Collaboration, H. Albrecht *et al.*, Physics Letters B **241**, 278 (1990).

[84] *Study of* $B \to \psi\rho$, CLEO Collaboration, M. Bishai *et al.*, Physics Letters B **369**, 186 (1996).

[85] *First evidence of* χ_c *production in B meson decays*, ARGUS Collaboration, H. Albrecht *et al.*, Physics Letters B **277**, 209 (1992).

[86] *An angular distribution cookbook*, R. Kutschke, never distributed but widely admired internal CLEO note.

[87] *Quark magnetic moments and* $E1$ *radiative transitions in charmonium*, G. Karl, S. Meshkov, and J. L. Rosner, Physical Review Letters **45**, 215 (1980).

[88] *Production and decay of P wave charmonium states in* $p\bar{p}$ *collisions*, A. D. Martin, M. G. Olsson, and W. J. Stirling, Physics Letters B **147**, 203 (1984).

[89] *A study of the reaction* $\psi' \to \gamma\gamma J/\psi$, Crystal Ball Collaboration, M. Oreglia *et al.*, Physical Review D **25**, 2259 (1982).

[90] *Angular distributions in the reactions* $p\bar{p} \to \chi_{1,2} \to \gamma\psi \to \gamma e^+ e^-$, R704 Collaboration, C. Baglin *et al.*, Physics Letters B **195**, 85 (1987).

[91] *Multipole amplitudes in parity changing one photon transitions of charmonium*, K. J. Sebastian, H. Grotch, and F. L. Ridener, Physical Review D **45**, 3163 (1992).

[92] *Study of the angular distribution of the reaction* $p\bar{p} \to \chi_{c2} \to J/\psi\gamma \to e^+e^-\gamma$, E760 Collaboration, T. A. Armstrong *et al.*, Physical Review D **48**, 3037 (1993).

[93] *Measurement of the decay amplitudes of* $B^0 \to J/\psi K^{*0}$ *and* $B_S^0 \to J/\psi\phi$ *decays*, CDF Collaboration, T. Affolder *et al.*, Physical Review Letters **85**, 4668 (2000).

[94] *Observation of* $B \to \psi\pi$ *decays*, CLEO Collaboration, J. Alexander *et al.*, Physics Letters B **341**, 435 (1995).

[95] *Measurement of the branching fraction* $\mathcal{B}(B_u^+ \to J/\psi\pi^+)$ *and search for* $B_c^+ \to J/\psi\pi^+$, CDF Collaboration, F. Abe *et al.*, Physical Review Letters **77**, 5176 (1996).

[96] *The* $\Upsilon(4S)$ *cross-section at CLEO*, D. Besson, internal CLEO notes CBX 92-23 and CBX 92-75 (1992).

[97] *Track-finding study using tau decays — re-revisited*, J. Urheim, internal CLEO note CBX 99-53 (1999).

[98] Jon Urheim's study of $\tau \to K^{*+}\nu$, $K^{*+} \to K^0\pi^+$ decays reported at CLEO meeting in June 1999.

[99] *Muon Identification Efficiencies for Full CLEO II.V Data*, M. Artuso and C. Boulahouache, internal CLEO note CBX 00-39 (2000);
Report of the Lepton Systematics Advisory Committee, B. Heltsley, internal CLEO note CBX 95-35 (1995);
Measurements of the inclusive semileptonic branching fraction of B mesons at the $\Upsilon(4S)$ *resonance*, R. Wang, Ph.D. dissertation, University of Minnesota (1994).

[100] *Search for rare decay* $B^0 \to D^{*0}\gamma$, V. Savinov, internal CLEO note CBX 99-38 (1999);
Search for the decay $\overline{B}^0 \to D^{*+}D^- + D^+D^{*-}$, D. Jaffe, internal CLEO note CBX 99-21 (1999);
$\Gamma(\eta \to 3\pi)/\Gamma(\eta \to \gamma\gamma)$ *and* $\eta/\pi^0/\gamma$ *systematics*, A. Gritsan, internal CLEO note CBX 99-72 (1999).

[101] *Combining measurements with correlated errors*, P. Avery, internal CLEO note CBX 95-55 (1995).

[102] *CP violation in neutral B decays on the* $\Upsilon(4S)$ *with symmetric energies*, K. Berkelman, Modern Physics Letters A **10**, 165 (1995).

[103] *Measurement of CP violation at the* $\Upsilon(4S)$ *without time ordering or* Δt, A. D. Foland, Physical Review D **60**, 111301 (1999).

[104] *Measurement of charm meson lifetimes*, CLEO Collaboration, G. Bonvicini *et al.*, Physical Review Letters **82**, 4596 (1999).

[105] *Flavor mixing and mixing-induced CP violation in the neutral B meson system*, A. Foland, Ph.D. dissertation, Cornell University (2000).

[106] Hitoshi Yamamoto, private communication.

[107] *Data Analysis and Kinematic Fitting with the KWFIT Library*, P. Avery, internal CLEO note CSN 98/355 (1998).

[108] *Table of integrals, series, and products,* I.S. Gradshteyn and I.M. Ryzhik.

[109] *'MINUIT' a system for function minimization and analysis of the parameter errors and correlations*, F. James and M. Roos, Comput. Phys. Commun. **10**, 343 (1975).

[110] *TRACKERR: a program for calculating tracking errors*, W. Innes, SLAC-BABAR-NOTE-121 (1993). Pablo Hopman has integrated `TRACKERR` into the CLEO software and provided us with the detector description files for different configurations of the CLEO detector.

[111] *Silicon Vertex Upgrade Proposal*, P. Hopman, undistributed internal CLEO note (1998). Pablo Hopman proposed to decrease the beam pipe radius to 1.5 cm and add an additional layer of thin silicon sensors close to the beam pipe.

[112] *Parametrization of the Kobayashi-Maskawa Matrix*, L. Wolfenstein, Physical Review Letters **51**, 1945 (1983).

[113] *Novel CP-violating effects in B decays from charged Higgs in a two-Higgs doublet model for the top quark*, G. Wu and A. Soni, Physical Review D **62**, 056005 (2000).

[114] *Measurement of charge asymmetries in charmless hadronic B meson decays*, CLEO Collaboration, S. Chen *et al.*, Physical Review Letters **85**, 525 (2000);
Charge-correlated systematic effects for high momentum tracks, J. Alexander, P. Gaidarev, A. Gritsan, J. Smith, and F. Würthwein, internal CLEO note CBX 99-67 (1999)

[115] *Cabibbo-suppressed $D^0 \to P^+P^-$ decays*, D. Asner, T. Hill, and H. Nelson, CBX note in preparation. Also, multiple private communications with Tony Hill.

[116] *How to reconstruct more clean J/ψ's*, A. Ershov, internal CLEO note CBX 99-31 (1999).

[117] *Study of χ_{c1} and χ_{c2} meson production in B meson decays*, A. Ershov, internal CLEO note CBX 00-53 (2000).

[118] *Study of χ_{c1} and χ_{c2} meson production in B meson decays*, CLEO Collaboration, S. Chen *et al.*, Physical Review D **63**, 31102 (2001).

[119] *First observation of the decay $B \to J/\psi\,\phi\,K$*, A. Ershov, internal CLEO note CBX 99-43 (1999).

[120] *First observation of the decay* $B \to J/\psi\,\phi\,K$, CLEO Collaboration, A. Anastassov *et al.*, Physical Review Letters **84**, 1393 (2000).

[121] *Measurement of the* B^0 *and* B^+ *meson masses from* $B^0 \to \psi^{(\prime)} K^0_S$ *and* $B^+ \to \psi^{(\prime)} K^+$ *decays*, A. Ershov, internal CLEO note CBX 99-64 (1999).

[122] *Measurement of the* B^0 *and* B^+ *meson masses from* $B^0 \to \psi^{(\prime)} K^0_S$ *and* $B^+ \to \psi^{(\prime)} K^+$ *decays*, CLEO Collaboration, S.E. Csorna *et al.*, Physical Review D **61**, 111101 (2000).

[123] *How to reconstruct* $K^0_S \to \pi^0\pi^0$. *Observation of* $B^0 \to J/\psi K^0_S$, $K^0_S \to \pi^0\pi^0$, A. Ershov, internal CLEO note CBX 00-09 (2000).

[124] *First observation of the decay* $B^0 \to \chi_{c1} K^0_S$, A. Ershov, internal CLEO note CBX 00-18 (2000).

[125] *First observation of the decay* $B^0 \to J/\psi\pi^0$, A. Ershov, internal CLEO note CBX 00-17 (2000).

[126] *Study of exclusive two-body* B^0 *meson decays to charmonium*, CLEO Collaboration, P. Avery *et al.*, Physical Review D **62**, 051101 (2000).

[127] *Can CLEO measure* $\sin 2\beta$*?*, A. Ershov and A. Foland, internal CLEO note CBX 99-29 (1999).

[128] *Search for CP violation in* $B^\pm \to J/\psi K^\pm$ *and* $B^\pm \to \psi(2S) K^\pm$ *decays*, A. Ershov, internal CLEO note CBX 00-02 (2000).

[129] *Search for CP violation in* $B^\pm \to J/\psi K^\pm$ *and* $B^\pm \to \psi(2S) K^\pm$ *decays*, CLEO Collaboration, G. Bonvicini *et al.*, Physical Review Letters **84**, 5940 (2000).